Computational Aeroacoustics via Linearized Euler Equations in the Frequency Domain

by

Kevin S. Huh

B.S. *honors* University of Illinois (1986)
S.M. Massachusetts Institute of Technology (1988)

Submitted to the Department of Aeronautics and Astronautics
in partial fulfillment of the requirements for the degree of

Doctor of Philosophy

at the

Massachusetts Institute of Technology

June 1993

Author .....
Department of Aeronautics and Astronautics
March 25, 1993

Certified by .....
Sheila E. Widnall
Abby Rockefeller Mauze Professor of Aeronautics and Astronautics
Thesis Supervisor

Certified by .....
Marten T. Landahl
Professor of Aeronautics and Astronautics
Thesis Committee Member

Certified by .....
Michael B. Giles
Professor of Aeronautics and Astronautics
Thesis Committee Member

Accepted by .....
Professor Harold Y. Wachman
Chairman, Departmental Graduate Committee

Computational Aeroacoustics via Linearized Euler Equations in the Frequency Domain

by

Kevin S. Huh

Submitted to the Department of Aeronautics and Astronautics
on March 25, 1993, in partial fulfillment of the
requirements for the degree of
Doctor of Philosophy

Abstract

A method of computing acoustic perturbation values is presented. The governing equations are derived directly from the Euler equations by assuming that acoustic values are a small, linear, unsteady perturbation upon a steady mean flow. The linearization limits the applications to those cases in which the square of the forced unsteadiness is not large, but since the linearization is only in the time sense the steady mean flow can be completely arbitrary.

The numerical method is based upon the Jameson [37] finite volume scheme and is globally conservative. The small length scales found in acoustics are efficiently discretized by a fourth order accurate compact scheme in the azimuthal direction and by a second order accurate central differencing scheme in the normal direction. The complete set of complex Euler equations are integrated in the pseudo–time plane using a Runge–Kutta integration method.

Analysis is presented which shows the accuracy of the method, and computational examples are provided for some model aeroacoustic problems. The computational results obtained indicate that the commonly used linear methods are applicable only when the given parameters (thickness, angle of attack, Mach number and compactness) are within a narrow range of validity, and beyond that range, a more sophisticated numerical method, such as the one included, is required.

Sound waves radiating from a thick airfoil in a nonuniform flow are diffracted by a varying mean velocity field. An airfoil at an angle of attack subjected to an unsteady load has associated with it a trailing vorticity sheet, and although the wake is itself silent, the wake influences the perturbation velocity field and the sound pressure near the airfoil. Furthermore the unsteady wake can extract energy from the mean flow to the perturbation vortical mode, and via the Kutta condition, the extraction may create a higher than expected overall sound field.

Thesis Supervisor: Sheila E. Widnall
Title: Abby Rockefeller Mauze Professor of Aeronautics and Astronautics

Acknowledgements

I would like to express my appreciation to my research advisor, Professor Sheila Widnall, for giving me the opportunity to work on this interesting project under her guidance. I would like to thank Dr. Agarwal at McDonnell Douglas for sponsoring this research and for his constant support of my professional development. Thanks are also in order for Professors Marten Landahl and Mike Giles. Their experiences and insights were helpful in all phases of the research.

I was fortunate that I had the love and support of my family and friends during my stay at MIT and elsewhere. Mom and dad, thank you for believing in me and for always encouraging me to do my very best. Sang Yoon and Jean, I'm lucky to have you for my brother and sister. You guys are the best.

As a graduate student one learns almost as much from his fellow students as he does from formal lectures, and my friends at MIT have made my stay there both enjoyable and rewarding. Thanks Stephane Mondoloni, Sasi Digavali, Alexandros Gioulekas, Fei Li, Joseph Wang, Didier Hazan, Reuben Rathnasingham, Will Gorgen, Mark Vidov, Harold Weigel, Mike Valdez, Errol Arkilic, Rudy King and Beth Grimaldi.

Diversity of thought can be an important asset, particularly if it allows you to travel, and I am grateful I had the chance to conduct research at both Cambridge and St. Louis. I am even more grateful I had the opportunity to meet the people there. Thanks Mark Shu, Mary Burgoon, Jeff Lewis, Hoby Chae, Don Kriesel, Linda Kral and John Donovan.

Finally, I would like to thank Lynn Matthews for always being there for me. I owe her so much.

This research was supported by McDonnell Douglas Independent Research and Development Program. Some computations were done on the MIT supercomputer facility.

Contents

List of Figures

List of Tables

Nomenclature

Roman Scalar Variables

SYMBOL	DEFINITION
a	characteristic length
CFD	computational fluid dynamics
CFL	Courant, Friedrichs, and Lewy
c	speed of sound
c_1, c_2, c_3, c_4	characteristics
D	energy source
D_p	directivity, $\sqrt{r}\lvert\tilde{p}\rvert$
dB	decibels
E	perturbation energy
e	total energy
e_i	internal energy
G	amplification factor
H	Hankel function
h	enthalpy or typical mesh size
$\Im$	imaginary part
i	$\sqrt{-1}$
J	determinant of Jacobian matrix or Bessel function of first kind
K	compactness ratio, $\frac{\nu M_0}{\beta^3}$
k	wave number in x direction
L	Lift

L_2 ..... root-mean-square, (L_2 norm)

l ..... wave number in y direction

M ..... Mach Number

p ..... pressure

p_{ij} ..... total stress tensor

$\Re$ ..... real part

Re ..... Reynolds number based on a

Re_x ..... Reynolds number based on chord position

r ..... distance from source, $\sqrt{x^2 + y^2}$

SPL ..... sound pressure level

s ..... entropy, or wrap-around spatial variable $s = r\theta$

T ..... temperature

T_{ij} ..... Lighthill stress tensor

t ..... time

t^* ..... pseudo-time

U ..... total velocity, $\sqrt{u^2 + v^2}$

u ..... x component of velocity

v ..... y component of velocity

W ..... power

x ..... independent spatial variable

Y ..... Bessel function of second kind

y ..... independent spatial variable

Greek Scalar Variables

SYMBOL	DEFINITION
α	angle of attack
β	Prandtl-Glauert factor, $\sqrt{1 - M_0^2}$
γ	ratio of specific heats, set to 1.4

δ ..... forward difference operator

δ_{ij} ..... Kronecker delta, $= 0$ if $i \neq j$ and $= 1$ if $i = j$

ϵ ..... a small parameter

η ..... independent computational space variable

θ ..... azimuthal angle, arctan y/x

κ ..... k/ω

λ ..... wavelength or l/ω

$\lambda_1, \lambda_2, \lambda_3, \lambda_4$ ..... eigenvalues

μ ..... average operator

ν ..... reduced frequency, $\frac{\omega a}{2u_\infty}$

ν_4 ..... fourth order artificial viscosity coefficient

ν_6 ..... sixth order artificial viscosity coefficient

ξ ..... independent computational space variable or vorticity

ρ ..... density

σ ..... acoustic cross section

τ ..... thickness

ϕ ..... velocity potential or arctan $y\beta/x$

ω ..... frequency

Vector and Matrix Variables

SYMBOL ..... DEFINITION

$\mathbf{A}$ ..... coefficient matrix in x direction

$\mathbf{B}$ ..... coefficient matrix in y direction

$\mathbf{C_g}$ ..... group velocity

$\mathbf{d_1}, \mathbf{d_2}$ ..... computational diagonal vector

$\mathbf{F}$ ..... spatial flux vector in x or ξ direction

$\mathbf{G}$ ..... spatial flux vector in y or η direction

$\mathbf{i}$ ..... unit vector in x direction

$\mathbf{j}$ ..... unit vector in y direction

$\mathbf{n}$ ..... surface normal vector

$\mathbf{Q}$ ..... vector of dependent conservative variables

$\mathbf{r}$ ..... position vector

$\mathbf{S}$ ..... source term vector (Equation 2.28)

$\mathbf{U}$ ..... total velocity

$\mathbf{u}$ ..... mean or perturbation velocity

$\mathbf{u^L}$ ..... left eigenvector

$\mathbf{v^L}$ ..... left eigenvector, $\mathbf{v^L} = \mathbf{u^L A}$

$\mathbf{v^R}$ ..... right eigenvector

Superscripts and Subscripts

SYMBOL	DEFINITION
$(\ )'$	perturbation quantity
$(\ )''$	values in local x'' and y'' domain
$(\ )'''$	values in local x''' and y''' domain
$\widetilde{(\ )}$	complex perturbation quantity
$\hat{(\ )}$	Fourier mode
$\bar{(\ )}$	time averaged quantity
$(\ )_a$	acoustic quantity
$(\ )_i$	incident quantity
$(\ )_n$	dimensioned quantity
$(\ )_0$	*local* mean value
$(\ )_s$	scattered quantity
$(\ )_\infty$	values at infinity

Chapter 1

Introduction

1.1 Motivation for Current Study

Sound is a perception of pressure disturbances passing through the atmosphere, and acoustics is the science of propagation and production of sound. Aeroacoustics is a branch of acoustics which combines the classical acoustics, scattering and diffraction of sound by bodies in still media, with the acoustics of moving flow, the scattering and generation of sound by flow field inhomogeneities. It is not surprising that given the wealth of knowledge available to solve the wave equation, the initial theories of aeroacoustics were also based on the wave equation. Lighthill [44] found that by a formal manipulation of the Navier–Stokes equation an 'analogy' to the classical acoustic equation could be found. The acoustic analogy equation is,

$$\frac{\partial^2 \rho'}{\partial t^2} - c^2 \bigtriangledown^2 \rho' = \frac{\partial^2 T_{ij}}{\partial x_i \partial x_j} \tag{1.1}$$

where

$$T_{ij} = \rho v_i v_j + p_{ij} - \delta_{ij} c^2 \rho' \tag{1.2}$$

c is the local speed of sound, δ_{ij} is the Kronecker δ, and $'$ denotes a fluctuating acoustic quantity. p_{ij} is the total stress tensor containing both pressure and viscous terms and for an inviscid flow $p_{ij} = p\delta_{ij}$. Note that the left hand side is just the standard wave operator, and hence if the source term T_{ij} is known the exact solution can be found by usual

Green's function methods. T_{ij} contains all the sources of aerodynamically generated sound, i.e. sound sources due to unsteady injection of mass, momentum or energy; but in addition, T_{ij} also contains viscous diffusion and all the acoustic diffraction effects due to a varying velocity field. T_{ij}, therefore, embodies acoustic phenomena which are both energy-conserving (diffraction) and energy-transferring (sound creation/attenuation).

The basis of Lighthill's theory is that if we know T_{ij} the problem of sound generation and propagation is reduced to that of solving a problem of conventional acoustics. However, for realistic aeronautical cases (say $Re = 10^6$ and $M_0 = 0.7$) the flow is compressible, and the boundary layer may be turbulent. In such situations the $\rho v_i v_j$ term in Equation 1.2 is not only nonlinear but also third order, and the specification of T_{ij} is usually quite difficult for practical situations. The most profound value of Lighthill theory, perhaps, is that it can reveal many dominant features of the sound field in terms of easily estimated parameters of the flow; the theory is capable of correctly predicting dimensional trends and scaling laws. The much heralded 'U^8'–law for acoustic energy of cold jets is one example of the usefulness and power of the Lighthill analogy. Past efforts [17, 19, 27] seem to indicate that such analysis, if sufficient care is taken, can reveal sound field values within a factor of 10 of actual values.

If, however, one is interested in a detailed study of aeroacoustics, T_{ij} must be specified accurately, and a rigorous specification of T_{ij} requires the resolution of the unsteady Kolmogorov microscale; we need the complete unsteady time history of the turbulent compressible boundary layer. It is exceedingly difficult to accurately specify T_{ij} for realistic problems, even with the current class of computer resources. Consider a turbulent boundary layer over a square flat plate of 1×1, and assume that the boundary layer thickness grows as $Re_x^{-1/5}$ [66], where Re_x is the Reynolds number based on the position along the plate. Also assume that the nondimensional Kolmogorov length scales as $Re^{-7/8}$. Then for a three dimensional case, we would require a grid of,

$$Re^{7/8} \times Re^{7/8} \times Re^{7/8} \times Re^{-1/5} \sim 10^{14} \text{ nodes}$$

in the normal directions to have about 1 node point per micro vortex width. This is computationally impractical for steady problems, and even less so for unsteady cases, because we would need the complete solution at each time step.

In the CFD community the turbulence resolution requirements are bypassed by employing a 'model' to emulate the subgrid scales. But we require an *unsteady* model and such a model does not seem to exist. Therefore, given that full computational resolution of turbulence is not possible and given also that there does not exist a simplified model of turbulence, we need to restrict our research to those cases in which the turbulent quadrupole sources of sound are not the dominant sources. We are eliminating all nonlinear sources of sound, such as those due to vortex pairing and those due to turbulent microscales.

A full linearization and the isentropy/inviscid assumption of the Lighthill source term T_{ij} leads to the convective form of the wave equation in sound pressure p',

$$\frac{\partial^2 p'}{\partial t^2} - c_0^2 \bigtriangledown^2 p' = -2u_0 \frac{\partial^2 p'}{\partial x \partial t} + u_0^2 \frac{\partial^2 p'}{\partial x^2} \tag{1.3}$$

when the mean flow is in the $+x$ direction. The above equation is the basis of most aeroacoustic effort of laminar unsteady flow to date. It has been used to model sound radiation from a flat plate as a response from a vortical gust [3, 6, 7, 13, 27] and it has also been used to model the scattering of sound by a flat plate [35, 62]. An important question is: how realistic is the linear flat plate model with respect to a thick cambered airfoil at an angle? Undoubtedly the answer will depend on the various length and time scales involved. In fact one of the thrusts of current thesis is to quantify the parametric dependence. But even without a detailed computational analysis, an observer can expect Equation 1.3 to eventually produce faulty results simply because Equation 1.3 assumes a uniform mean flow.

A fundamental and perhaps an obvious method of including the effects of flow nonuniformity on sound propagation would be to directly integrate the full set of laminar Navier–Stokes equations using CFD techniques.

The past 20 years have seen a large increase in both CFD and computer capabilities. Many researchers currently use Navier–Stokes methods to accurately compute lift and drag profiles for a variety of two and three dimensional bodies in a wide range of Mach and Reynolds number flows. Many issues, particularly turbulence, remain unresolved, but for engineering purposes CFD has gained wide acceptance.

The question is then: What Is the most efficient method of adapting current CFD capabilities to compute the acoustic values?

Ignore viscous effects and let us consider an illustrative example. Suppose we need to compute a propagation of a single frequency plane acoustic wave through an arbitrary domain. One method of solution would be to spatially discretize the wave and explicitly integrate in time to 'track' the moving wave. But if the domain is large and if there are reflections at the boundaries, this approach can be quite expensive and inefficient. The maximum time step allowed in the integration would be of the smallest cell in the domain for all the cells, and thus, the time evolution process can be quite slow if there are variations in grid densities. A more efficient approach would be to Fourier transform the equations and solve for the resulting complex coefficients in the domain. Here the time derivative simply becomes a simple algebraic factor and all the convergence acceleration schemes for *steady* flows such as local time stepping and multigrid methods can be directly applied. Furthermore, when the complete time history is desired, the explicit 'tracking' approach would require considerably more memory, because the entire solution for at least one complete period would have to be stored. In contrast, the complex domain approach requires only one (real and imaginary) solution to be saved.

This is the approach that the current thesis applies. The acoustic values are considered an unsteady linear perturbation of the steady, mean, inviscid flow, and the full set of Fourier transformed linearized Euler equations are integrated to yield complex sound amplitudes in the domain. Such an approach is equivalent to retaining all the diffraction effects but discarding the nonlinear sources of sound in the inviscid Lighthill source term T_{ij}. The implications of the linear assumption are that we must now limit

the applications to those cases where the unsteadiness is not very large, or equivalently, we must limit the application to those cases in which the nonlinear sources of sound are not the dominant sources of sound.

1.2 A Brief Survey

Linear perturbation methods for unsteady aerodynamic analysis have been extensively used in the past. For a two dimensional, inviscid, incompressible parallel flow the governing equation is the Rayleigh equation. Its solution has been used to predict the stability of a fluid subjected to an infinitesimal disturbance [20, 41]. A two dimensional, compressible parallel flow cannot be reduced to a single linear equation, and a system of coupled equations must be solved. The solution processes for the eigenvalue problem are in References [46, 48]. A general two dimensional compressible case has, however, not been analyzed.

In the aeroacoustic community, the most commonly used computational methods are of acoustic analogy type. Infinitely many choices of acoustic analogy are possible. The Lighthill's version is the most popular, although the analogy versions by Ffowcs Williams–Hawking [9, 27], Phillips & Lilley [27, 45], Ribner [60], and Powell [59] have also been used. They all share the characteristic that the aeroacoustic problem reduces to a forced wave equation of the form,

$$(\frac{1}{c_0^2}\frac{\partial^2}{\partial t^2} - \nabla^2)h = q \tag{1.4}$$

where c_0 is the sound speed in the quiescent field and h is the variable which in the far field is the acoustic pressure. The choices for h and q are arbitrary, but they must be consistent with the equations of mass, momentum, and energy conservation, and furthermore, all the choices should lead to the same sound field if the flow variables are known. The advantage of one choice over another is dependent on the details of the particular problem [18].

The acoustic analogy is directly applicable when the mean Mach number is very low. The source terms are approximated from the incompressible flow solution; for instance, when the flow is inviscid/isentropic and the mean Mach number is $\ll 1$ the source term for the Lighthill's version of the analogy is,

$$q = \frac{\partial^2 T_{ij}}{\partial x_i \partial_j}$$

where

$$T_{ij} \approx \rho_0 v_i v_j.$$

The source terms are assumed to be independent of the acoustic values, and the solution is obtained via a Green's function integral. Applications of such approach for rotors maybe found in References [55], for cold jets References [60], and for turbulent flow Reference [17, 18, 31].

Another commonly used method has been of Kirchoff type. In the Kirchoff approach the solution is an integral solution to the wave equation external to some real or imaginary surface on which the relevant acoustic data is known. The acoustic surface values are often a near field solution to the acoustic analogy [6]. The Kirchoff method is used later to compute the far field values.

Linear perturbation potential methods have also been applied to aeroacoustics [6, 7, 62]. Generally a quiescent or uniform flow is assumed, and thus the potential methods are similar to the acoustic analogy equations except that the dependent variable in the wave/convective–wave operator is the perturbation velocity potential. A wake allows a finite discontinuity in the velocity potential but not in pressure, and therefore the potential methods allow problems which include unsteady lift. Note that the potential methods, as applied, do not allow production or convection of vorticity except as a specified boundary condition of a 'jump' in the potential. The methods are therefore generally not applicable for cases in which the vorticity location is not known a priori or when the free convection of vorticity is important.

Perturbation Euler techniques which naturally allow vorticity and entropy production/convection have recently received attention from both the acoustic community and also the unsteady fluids community at large. Khan et al. [40] solved the perturbation Euler equations to analyze the acoustic radiation from a monopole in uniform flows, and Hariharan et al. [32, 33] computed the acoustic radiation in cylindrical ducts by using the linearized Euler equations in a quiescent field.

The linearized Euler equations can be cast as a set of steady equations in frequency domain by using the single frequency assumption. No generality is lost in the assumption since in linear problems the complete solution can be reconstructed as a sum of multiple frequencies using the Fourier synthesis. The frequency domain Euler approach was pioneered by Ni [54] and Hall [30] who applied the method to study unsteady flows in turbomachinery. Ni used the isentropic form of the linearized Euler equations to validate the concept with the linear flat plate cascade analysis, and Hall investigated transonic duct flows and cascades using a combination of both the linear perturbation and full Euler equations. The current thesis extends the works of Ni and Hall to aeroacoustics of external flows.

It should also be noted that recently there has been some effort in direct numerical simulations of acoustics using the full set of Navier–Stokes equations. Ridder & Beddini [61] integrated the full set of axisymmetric Navier–Stokes equations for acoustic radiation of sound from resonance tubes, and Colonius et al. [15] have integrated the full set of Navier–Stokes equations for the problem of plane wave scattering by a compressible vortex. Ridder & Beddini's solution correctly predicted the general trend of pressure oscillation but suffered from noticeable dissipative errors due to insufficient grid resolution. Colonius et al. used high amplitude ($\sim 10^{-5}$) sound waves with a fourth order accurate spatial discretization in an orthogonal rectangular domain. The numerical domain guaranteed a minimum resolution of 60 points per shortest wavelength, and the computed solution was "within a few percent" of the solution predicted by the acoustic analogy. The two examples not withstanding, a direct Navier–Stokes acoustic

calculation for a realistic flow geometry has not yet been computed. A high grid resolution requirement, a lack of an effective far field boundary condition, and an accurate unsteady turbulence model are believed to be the primary obstacles [31].

1.3 Synopsis of the Thesis

A numerical method to determine acoustic values is presented. The governing equations are derived from the Euler equations with an assumption that an acoustic value is a small unsteady pressure perturbation about a steady mean quantity. The small perturbation assumption allows the use of linearization and the single frequency supposition.

Much of the numerical method is based upon previously used CFD techniques and is completely general geometrically. The application will also allow arbitrary mean steady flows, although there is some limitation in the free stream Mach number so that nonlinearities such as wave-steepening and shock oscillations do not dominate the flow field.

In the following chapter we discuss the derivation of the governing equations, and we determine the range of parameters within which the derived equations are valid.

In chapter 3 the unsteady wall boundary conditions and the nonreflecting far field boundary conditions are presented.

Chapter 4 analyzes the numerical approach with particular emphasis on the truncation error, pseudo–time stability, and convergence acceleration schemes.

In chapter 5 we apply the numerical method to simulate the sound radiation process from a vortical gust–airfoil interaction. The first set of computations are benchmarked with known analytic solutions to assure accuracy and consistency. Later we investigate the effects of thickness, Mach number, angle of attack, and the reduced frequency on the generated sound field.

Chapter 6 presents computational models of sound generation from an oscillating airfoil. We present a set of 6 cases which highlights the effect of thickness and angle of

attack on radiated sound field from an isolated airfoil in high subsonic flow.

Chapter 7 presents acoustic scattering results from incident pressure waves. We discuss diffractive effects of nonuniform mean flows, and we measure sound attenuation/amplification in lifting and nonlifting situations. We also measure changes in scattering patterns from varying the mean Mach number and the angle of attack.

In chapter 8 we put all the above into perspective and make suggestions for future research.

Chapter 2

Governing Equations

An accurate determination of acoustic signatures resulting from an unsteady flow in or around aircraft components is important to efforts in noise suppression and in the design of advanced aircraft. In this work, we analyze some aspects of changes in flow parameters (Mach number, angle of attack, etc.) on the generation and propagation of sound. We are concerned primarily with the gross features of aeroacoustics; the effects of flow variations which scale with the dominant length scale upon audible wavelengths of sound.

The Reynolds number of the mean flow is to be of typical transport aircraft range ($\sim 10^6$), and hence the viscous effects are confined to thin boundary layers and wakes. We will not consider extremely high frequencies of sound which have wavelengths of the same scale as the viscous layers, and furthermore, the acoustic boundary layer is assumed to remain attached. Thus for current purposes, the flow is inviscid, and compressible, but may be rotational and nonisentropic. The governing equations for the present aeroacoustic field are, therefore, derived from the unsteady Euler equations.

We begin with the derivation of the Euler equations in the integral form.

2.1 Integral form of the Conservation Laws

Consider an adiabatic, inviscid, compressible fluid in two dimensions passing through a region D enclosed by a surface S which is fixed in space as shown in Figure 2-1. The quantities to be conserved are mass, momentum, and energy. The statement of

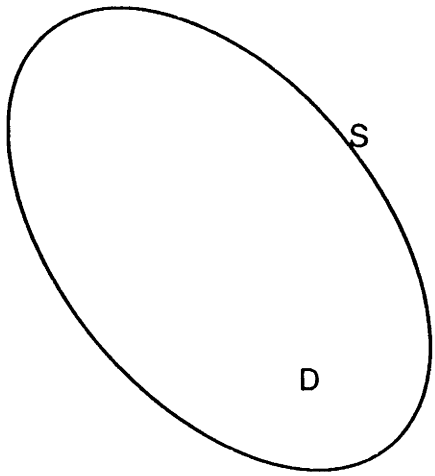

Figure 2-1: Control area used to derive the conservation equations.

conservation of mass is that the rate of change of mass within the control area is equal to the rate at which mass flows into or out of the region through the surface (the mass flux). In integral form,

$$\int_D \frac{\partial}{\partial t}\rho \, dD = -\int_s \rho \mathbf{U} \cdot \mathbf{n} \, dS \tag{2.1}$$

where ρ and $\mathbf{U}$ are the density and velocity of the fluid; t is the time and $\mathbf{n}$ is a unit normal vector pointing out of the region.

The statement of conservation of momentum can be expressed in a similar way. The rate of change of momentum within the control area is equal to the sum of the body forces acting on the fluid particles plus the integrated surface forces acting on the boundary. With no body forces,

$$\int_D \frac{\partial}{\partial t}\rho \mathbf{U} \, dD + \int_s \rho \mathbf{U}(\mathbf{U} \cdot \mathbf{n}) \, dS = -\int_s p\mathbf{n} \, dS \tag{2.2}$$

where p is the pressure. The first term in Equation 2.2 represents the time rate of change of momentum within the region D, and the second term represents the rate at which

momentum leaves the domain (the momentum flux). Together the two terms represent the rate of change of momentum of the fluid particles which pass through the surface S, and this then is equal to the sum of the forces acting on the boundary surface S.

Now consider the principle of the conservation of energy. The net rate of change of energy of a group of fluid particles in the control area is equal to the work done on them by external forces. Mathematically we have that,

$$\int_D \frac{\partial}{\partial t}\rho(e_i + \frac{U^2}{2})\,dD + \int_s \rho(e_i + \frac{U^2}{2})\mathbf{U}\cdot\mathbf{n}\,dS = -\int_s p\mathbf{U}\cdot\mathbf{n}\,dS \tag{2.3}$$

where ρe_i is the internal energy per unit volume of the fluid, and the term $\rho U^2/2$ is the kinetic energy per unit volume. For a perfect gas,

$$\rho e_i = \frac{p}{\gamma - 1}$$

where γ is the ratio of specific heats and is assumed to be 1.4. The rate of change of total energy of fluid particles within the control area is equal to the two terms on the left hand side of Equation 2.3, and this in turn is equal to the external work done by pressure acting on the surface S.

2.2 Differential form of the Conservation Laws

In the previous section the conservation laws were presented in the integral form; however, it is sometimes more useful to express the conservation equations in an equivalent differential form. By applying the divergence theorem the conservation laws can be recast as,

$$\int_D [\frac{\partial}{\partial t}\rho + \nabla\cdot(\rho\mathbf{U})]\,dD = 0 \tag{2.4}$$

$$\int_D [\frac{\partial}{\partial t}\rho\mathbf{U} + \nabla\cdot(\rho\mathbf{U}\mathbf{U}) + \nabla p]\,dD = 0 \tag{2.5}$$

$$\int_D \{\frac{\partial}{\partial t}\rho(e_i + \frac{U^2}{2}) + \nabla\cdot[\rho(e_i + \frac{U^2}{2})\mathbf{U} + p\mathbf{U}]\}\,dD = 0 \tag{2.6}$$

where the term $\nabla \cdot (\rho \mathbf{U}\mathbf{U})$ represents a divergence of a dyadic tensor and may be expressed as [39],

$$\nabla \cdot (\rho \mathbf{U}\mathbf{U}) = \rho \mathbf{U} \cdot \nabla \mathbf{U} + \mathbf{U} \nabla \cdot (\rho \mathbf{U}). \tag{2.7}$$

If the above equations are to hold for any arbitrary region of fluid, then all of the integrands must vanish identically everywhere within the fluid. The differential conservation laws (the Euler equations) in Cartesian form are therefore,

$$\frac{\partial}{\partial t}\mathbf{Q} + \frac{\partial}{\partial x}\mathbf{F} + \frac{\partial}{\partial y}\mathbf{G} = 0 \tag{2.8}$$

where,

$$\mathbf{Q} = \begin{pmatrix} \rho \\ \rho u \\ \rho v \\ \rho e \end{pmatrix} \tag{2.9}$$

$$\mathbf{F} = \begin{pmatrix} \rho u \\ \rho u^2 + p \\ \rho uv \\ \rho uh \end{pmatrix}, \quad \mathbf{G} = \begin{pmatrix} \rho v \\ \rho uv \\ \rho v^2 + p \\ \rho vh \end{pmatrix} \tag{2.10}$$

u and v are the x and y components of the velocity $\mathbf{U}$; e and h are the total energy and enthalpy of the fluid; for a perfect gas they are defined as,

$$e = e_i + \frac{1}{2}(u^2 + v^2)$$

$$h = e + \frac{p}{\rho}.$$

2.3 Linearized Euler Equations

As a sound wave travels it perturbs the fluid from its mean state. These disturbances are nearly always small. We will consider acoustic quantities to be small unsteady perturbations about a steady space varying mean value. We assume that,

$$u(x,y,t) = u_0(x,y) + u'(x,y,t), \quad v(x,y,t) = v_0(x,y) + v'(x,y,t) \tag{2.11}$$

$$\rho(x,y,t) = \rho_0(x,y) + \rho'(x,y,t), \quad p(x,y,t) = p_0(x,y) + p'(x,y,t) \tag{2.12}$$

where the subscript $_0$ refers to the steady mean quantity, and the superscript $'$ refers to the time varying acoustic quantity. The ratio $|p'/p_0|$ is in most acoustic cases very much less than unity. Even at the threshold of pain $|p'/p_0|$ is $\sim 10^{-3}$, and at the threshold of hearing $|p'/p_0|$ is only $\sim 10^{-10}$. The flow perturbations involved in acoustic waves are very small, and all products of the perturbed quantities can usually be neglected. This is equivalent to stating that the response of the acoustic field is typically linear.

The governing aeroacoustic equations are derived by substituting the perturbation relations (Equations 2.11 and 2.12) into the Euler Equations 2.8. Collecting terms of equal order and neglecting terms of second order produces the equation for the steady mean flow and the equation for the first order unsteady perturbation quantities. The steady mean flow equations are,

$$\frac{\partial}{\partial x}\mathbf{F_0} + \frac{\partial}{\partial y}\mathbf{G_0} = 0 \tag{2.13}$$

where,

$$\mathbf{F_0} = \begin{pmatrix} \rho_0 u_0 \\ \rho_0 u_0^2 + p_0 \\ \rho_0 u_0 v_0 \\ \rho_0 u_0 h_0 \end{pmatrix}, \quad \mathbf{G_0} = \begin{pmatrix} \rho_0 v_0 \\ \rho_0 u_0 v_0 \\ \rho_0 v_0^2 + p_0 \\ \rho_0 v_0 h_0 \end{pmatrix} \tag{2.14}$$

which is identical to the original equations with the time derivative terms set to zero.

Note that the mean flow is represented by a set of coupled nonlinear equations.

The first order perturbation equations are given by,

$$\frac{\partial}{\partial t}\mathbf{Q} + \frac{\partial}{\partial x}\mathbf{F} + \frac{\partial}{\partial y}\mathbf{G} = 0 \tag{2.15}$$

where,

$$\mathbf{Q} = \begin{pmatrix} \rho' \\ (\rho u)^* \\ (\rho v)^* \\ (\rho e)^* \end{pmatrix} \tag{2.16}$$

$$\mathbf{F} = \begin{pmatrix} (\rho u)^* \\ u_0[2(\rho u)^* - u_0\rho'] + p' \\ v_0[(\rho u)^* - u_0\rho'] + (\rho v)^* u_0 \\ u_0[(\rho h)^* - h_0\rho'] + (\rho u)^* h_0 \end{pmatrix}, \quad \mathbf{G} = \begin{pmatrix} (\rho v)^* \\ u_0[(\rho v)^* - v_0\rho'] + (\rho u)^* v_0 \\ v_0[2(\rho v)^* - v_0\rho'] + p' \\ v_0[(\rho h)^* - h_0\rho'] + (\rho v)^* h_0 \end{pmatrix}. \tag{2.17}$$

The state equation is given as,

$$p' = (\gamma - 1)\{(\rho e)^* - \frac{1}{2}[u_0(2(\rho u)^* - u_0\rho') + v_0(2(\rho v)^* - v_0\rho')]\} \tag{2.18}$$

and the * quantities are defined as,

$$(\rho u)^* = \rho u - \rho_0 u_0 = \rho_0 u' + \rho' u_0 \tag{2.19}$$

$$(\rho v)^* = \rho v - \rho_0 v_0 = \rho_0 v' + \rho' v_0$$

$$(\rho e)^* = \rho e - \rho_0 e_0 = \frac{p'}{\gamma - 1} + \rho_0 u_0 u' + \rho_0 v_0 v' + \frac{1}{2}\rho'(u_0^2 + v_0^2)$$

$$(\rho h)^* = \rho h - \rho_0 h_0 = (\rho e)^* + p'.$$

These equations are linear in the perturbation variables; the mean flow values are known from the solution of Equation 2.13.

2.3.1 Single Frequency Approach

The governing perturbation Euler Equation 2.15 is also homogeneous, therefore any unsteadiness must arise from the applied boundary conditions such as those due to upstream and/or downstream pressure disturbances. Suppose that these external excitations are harmonic in time with a frequency ω, then since the given equations are linear, the time dependent solution will also be harmonic with frequency ω. Thus the completely unsteady Euler equations can be recast as a set of steady complex equations by the use of the single frequency assumption,

$$u' = \Re(\tilde{u}(x,y)e^{-i\omega t}), \quad v' = \Re(\tilde{v}(x,y)e^{-i\omega t})$$

$$p' = \Re(\tilde{p}(x,y)e^{-i\omega t}), \quad \rho' = \Re(\tilde{\rho}(x,y)e^{-i\omega t})$$

where the superscript $\tilde{}$ denotes a complex quantity and $\Re$ refers to the real part.

The governing equations then become,

$$-i\omega\mathbf{Q} + \frac{\partial}{\partial x}\mathbf{F} + \frac{\partial}{\partial y}\mathbf{G} = 0 \tag{2.20}$$

$$\mathbf{Q} = \begin{pmatrix} \tilde{\rho} \\ \widetilde{(\rho u)} \\ \widetilde{(\rho v)} \\ \widetilde{(\rho e)} \end{pmatrix} \tag{2.21}$$

$$\mathbf{F} = \begin{pmatrix} \widetilde{(\rho u)} \\ u_0[2\widetilde{(\rho u)} - u_0\tilde{\rho}] + \tilde{p} \\ v_0[\widetilde{(\rho u)} - u_0\tilde{\rho}] + \widetilde{(\rho v)}u_0 \\ u_0[\widetilde{(\rho h)} - h_0\tilde{\rho}] + \widetilde{(\rho u)}h_0 \end{pmatrix}, \quad \mathbf{G} = \begin{pmatrix} \widetilde{(\rho v)} \\ u_0[\widetilde{(\rho v)} - v_0\tilde{\rho}] + \widetilde{(\rho u)}v_0 \\ v_0[2\widetilde{(\rho v)} - v_0\tilde{\rho}] + \tilde{p} \\ v_0[\widetilde{(\rho h)} - h_0\tilde{\rho}] + \widetilde{(\rho v)}h_0 \end{pmatrix} \tag{2.22}$$

and the state equation of the form,

$$\tilde{p} = (\gamma - 1)\{\widetilde{(\rho e)} - \frac{1}{2}[u_0(2\widetilde{(\rho u)} - u_0\tilde{\rho}) + v_0(2\widetilde{(\rho v)} - v_0\tilde{\rho})]\}. \tag{2.23}$$

The variables $\widetilde{(\rho u)}$, $\widetilde{(\rho v)}$, $\widetilde{(\rho e)}$, $\widetilde{(\rho h)}$ are defined similarly as in Equation 2.19,

$$\widetilde{(\rho u)} = \rho_0\tilde{u} + \tilde{\rho}u_0 \tag{2.24}$$

$$\widetilde{(\rho v)} = \rho_0\tilde{v} + \tilde{\rho}v_0$$

$$\widetilde{(\rho e)} = \frac{\tilde{p}}{\gamma - 1} + \rho_0 u_0\tilde{u} + \rho_0 v_0\tilde{v} + \frac{1}{2}\tilde{\rho}(u_0^2 + v_0^2)$$

$$\widetilde{(\rho h)} = \widetilde{(\rho e)} + \tilde{p}.$$

It should be noted that no generality has been lost due to the single frequency assumption. Since the governing equations are linear, a general case of n number of frequencies can be solved as a superposition of n number of single frequencies by applying the Fourier theorem. That is to say, a total solution can be thought of as composed of an infinite number of discrete frequencies such that,

$$\rho' = \Re(\sum_{\omega=-\infty}^{\infty} \tilde{\rho}(\omega)e^{-i\omega t}), \quad p' = \Re(\sum_{\omega=-\infty}^{\infty} \tilde{p}(\omega)e^{-i\omega t}) \tag{2.25}$$

$$u' = \Re(\sum_{\omega=-\infty}^{\infty} \tilde{u}(\omega)e^{-i\omega t}), \quad v' = \Re(\sum_{\omega=-\infty}^{\infty} \tilde{v}(\omega)e^{-i\omega t}). \tag{2.26}$$

Except in situations where the sound is very 'broad banded' and contains many discrete frequencies, it is usually more efficient to solve the governing equations a single Fourier component at a time. This is because we can tailor a numerical grid to that specific wavelength rather than to the shortest wavelength amongst a group of frequencies, and thus each frequency is solved using the coarsest most efficient grid possible.

Moreover, one of the goals of the current thesis is to investigate the effects of mean flow variations on a range of wavelengths. For research purposes, a time domain ap-

proach would unduly complicate the analysis.

2.3.2 Scattered Form

The linearized complex Euler Equation 2.20 can now be solved using an appropriate numerical method. Sometimes, however, it is more efficient to recast the equations in the 'scattered' form. Consider, for instance, a scattering problem in which a disturbance wave travels from infinity and is diffracted by an object at $x = 0$. Assume that the object is 'thin' with respect to the wavelength of the disturbance so that the 'scattered' portion of the solution decays as $|x|$ becomes large (typically as $|x|^{-1/2}$). In such scattering problems, the governing equations can be more efficiently solved by 'splitting' the dependent variables into a known 'incident' quantity and a 'scattered' quantity [24]. This is because the scattered form requires less grid resolution in the far field where the scattered quantities are expected to be small, but where the incident quantities are not. The total perturbation quantity is formed as a sum of the incident quantity and the scattered quantity,

$$\tilde{p} = \tilde{p}_i + \tilde{p}_s, \quad \tilde{\rho} = \tilde{\rho}_i + \tilde{\rho}_s$$

$$\tilde{u} = \tilde{u}_i + \tilde{u}_s, \quad \tilde{v} = \tilde{v}_i + \tilde{v}_s$$

where the subscripts $_i$ and $_s$ denote the incident and scattered parts, respectively. The governing Equations 2.20 in scattered form is then,

$$-i\omega \mathbf{Q}_s + \frac{\partial}{\partial x}\mathbf{F}_s + \frac{\partial}{\partial y}\mathbf{G}_s = \mathbf{S} \tag{2.27}$$

where,

$$\mathbf{S} = i\omega \mathbf{Q}_i - \frac{\partial}{\partial x}\mathbf{F}_i - \frac{\partial}{\partial y}\mathbf{G}_i. \tag{2.28}$$

Note that the 'splitting' is strictly a mathematical definition; the incident quantity does not correspond exactly to the physical incident wave everywhere. By definition the mathematically defined incident wave is equivalent to the physical incident wave only

at infinity, i.e. where the mean flow is uniform. Thus $\mathbf{S}$ contains all the incident wave–mean flow diffraction terms and $\mathbf{S} \to 0$ as $r \to \infty$, and also $\mathbf{S} \equiv 0$ when there is no mean flow.

Given a 'nonscattering' problem in which sound is generated by a defined unsteady motion of a body within the domain, Equation 2.27 is still valid except here $S \equiv 0$ and $\mathbf{Q_s}$ is the complete perturbation quantity.

2.3.3 Pseudo–Time

There are multiple methods to solve the Equation 2.27. We can solve it by directly inverting the space varying coefficient matrix as in Hall [30], or we can introduce a pseudo–time variable and solve them in a time marching iterative fashion as in Ni [54]. We use the latter approach, because the use of a pseudo–time variable makes it possible to adopt the convergence acceleration methods developed in CFD such as local time stepping and multigrid methods. The modified form of the perturbation equations is,

$$\frac{\partial}{\partial t^*}\mathbf{Q_s} + \frac{\partial}{\partial x}\mathbf{F_s} + \frac{\partial}{\partial y}\mathbf{G_s} - i\omega\mathbf{Q_s} = \mathbf{S} \tag{2.29}$$

where t^* is the pseudo–time variable. We can also introduce the pseudo–time variable to the mean flow equations to obtain,

$$\frac{\partial}{\partial t^*}\mathbf{Q_0} + \frac{\partial}{\partial x}\mathbf{F_0} + \frac{\partial}{\partial y}\mathbf{G_0} = 0 \tag{2.30}$$

where

$$\mathbf{Q_0} = \begin{pmatrix} \rho_0 \\ \rho_0 u_0 \\ \rho_0 v_0 \\ \rho_0 e_0 \end{pmatrix}.$$

In the asymptotic limit $\frac{\partial}{\partial t^*} \to 0$, Equation 2.29 is equivalent to Equation 2.27, and Equation 2.30 is equivalent to Equation 2.13; the consistency of the methods are pre-

served.

2.3.4 Nondimensionalization

The independent length and frequency variables are nondimensionalized as,

$$(x, y) = \frac{(x_n, y_n)}{a} \tag{2.31}$$

$$\omega = \frac{\omega_n a}{\sqrt{p_\infty / \rho_\infty}}. \tag{2.32}$$

The various flow variables are nondimensionalized as follows,

$$\rho_0 = \frac{\rho_{0n}}{\rho_\infty}, \quad p_0 = \frac{p_{0n}}{p_\infty} \tag{2.33}$$

$$(u_0, v_0) = \frac{(u_{0n}, v_{0n})}{\sqrt{p_\infty / \rho_\infty}} \tag{2.34}$$

for the mean flow variables and,

$$\tilde{\rho} = \frac{\tilde{\rho}_n}{\rho_\infty}, \quad \tilde{p} = \frac{\tilde{p}_n}{p_\infty} \tag{2.35}$$

$$(\tilde{u}, \tilde{v}) = \frac{(\tilde{u}_n, \tilde{v}_n)}{\sqrt{p_\infty / \rho_\infty}} \tag{2.36}$$

for the perturbation aeroacoustic variables. The subscript $_n$ refers to a dimensional quantity and a to some reference length quantity.

2.4 Energy Corollary

The set of governing equations is complemented by an energy corollary relation. The corollary is derived by algebraic manipulations of the governing equations. It is not an independent equation, and the equation need not be integrated. The utility of the relation is that it expresses a second order balance of energy which involves only first order perturbation quantities.

The second order energy balance may be expressed as a time variation of the total energy density E_a [51, 52, 53],

$$\frac{\partial E_a}{\partial t} + \nabla \cdot \mathbf{I}_a = D_a \tag{2.37}$$

where

$$E_a = \frac{p'^2}{2\rho_0 c_0^2} + \frac{\rho_0(u'^2 + v'^2)}{2} + \rho' \mathbf{u}_0 \cdot \mathbf{u}' + \frac{\rho_0 T_0 s'^2}{2c_p}$$

$$\mathbf{I}_a = (\frac{p'}{\rho_0} + \mathbf{u}_0 \cdot \mathbf{u}')(\rho_0 \mathbf{u}' + \rho' \mathbf{u}_0) + \rho_0 \mathbf{u}_0 T' s'$$

$$D_a = \rho_0 \mathbf{u}_0 \cdot (\xi' \times \mathbf{u}') + \rho' \mathbf{u}' \cdot (\xi_0 \times \mathbf{u}_0) + s' \rho_0 \mathbf{u}_0 \cdot \nabla T' - s'(\rho_0 \mathbf{u}' + \rho' \mathbf{u}_0) \cdot \nabla T_0$$

and T is the temperature, s is the entropy and $\xi = \nabla \times \mathbf{u}$ the vorticity. $\mathbf{I}_a$ represents the flux of energy transported by both the mean and the perturbation flow and is referred to as the intensity. The source term D_a represents the production of energy associated with interactions between the mean vorticity and the perturbation velocity and between the mean velocity and the perturbation vorticity as well as the production arising from the presence of entropy fluctuations.

Given a rotational but isentropic flow, E_a, $\mathbf{I}_a$, and D_a reduce to simpler forms,

$$E_a = \frac{p'^2}{2\rho_0 c_0^2} + \frac{\rho_0(u'^2 + v'^2)}{2} + \rho' \mathbf{u}_0 \cdot \mathbf{u}' \tag{2.38}$$

$$\mathbf{I}_a = (\frac{p'}{\rho_0} + \mathbf{u}_0 \cdot \mathbf{u}')(\rho_0 \mathbf{u}' + \rho' \mathbf{u}_0) \tag{2.39}$$

$$D_a = \rho_0 \mathbf{u}_0 \cdot (\xi' \times \mathbf{u}') + \rho' \mathbf{u}' \cdot (\xi_0 \times \mathbf{u}_0). \tag{2.40}$$

An equivalent form of energy conservation is obtained by taking the time average then integrating the differential equation (2.37) over an area A bounded by a closed loop σ. The conservation equation becomes,

$$W \equiv \oint_\sigma \bar{\mathbf{I}}_a \cdot \mathbf{n} \, d\sigma = \iint_A \bar{D}_a dA \tag{2.41}$$

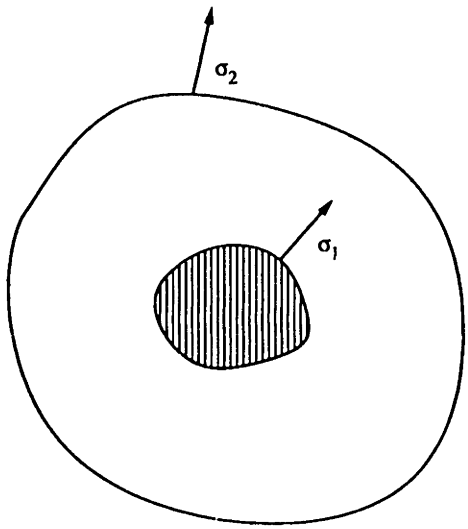

Figure 2-2: Acoustic Power from Two Surfaces σ_1 and σ_2

where $^-$ corresponds to a time averaged variable, $\mathbf{n}$ is the unit normal vector to the surface $d\sigma$, and we define W as the power. The time derivative term disappeared because of the averaging, and we have used the divergence theorem to convert the second integral over an area to that of a closed loop. The usefulness of power is in its continuity property: if σ_1 and σ_2 are two surfaces enclosing the same sources of sound (Figure 2-2), the same value of W is found for both surfaces.

Given an isentropic, irrotational flow the source term D_a becomes zero, and if there are no sources within the area A, the conservation law simply becomes,

$$W \equiv \oint_{\sigma} \bar{\mathbf{I}}_a \cdot \mathbf{n} d\sigma = 0. \tag{2.42}$$

When there are no sound sources and in an irrotational, isentropic flow the sound power crossing any closed surface σ is zero.

Since the energy corollary is algebraically derived from the governing equations it is not unique, and indeed other forms have been proposed. In fact the acoustic energy cannot, in general, be found from a solution of the linear equation, since the energy relation

is by definition second order in fluctuating quantities. The equations of motion formally need to be solved to second order. This difficulty is pointed out in References [5, 49]. The choice of energy definition is, therefore, somewhat arbitrary, and we have chosen a definition with an implicit understanding that other investigators will generate results with at least a *qualitative* agreement. Otherwise, the current form was chosen because it has a wide range of conditions under which the continuity property of Equation 2.41 is valid. The wider the range of conditions, the more general is the continuity property and the more useful the definition. For example, the energy definition provided in Reference [65] defines the intensity $\mathbf{I}_a$ for an isentropic flow as,

$$\mathbf{I}_a = p'\mathbf{u}' + \mathbf{u}_0[\frac{p'^2}{2\rho_0 c_0^2} + \frac{\rho_0 \mathbf{u}' \cdot \mathbf{u}'}{2}] \tag{2.43}$$

which has a certain intuitive appeal; if the first term is interpreted as the flux of energy relative to the fluid, then the second term appears to represent the convected acoustic energy (potential + kinetic) [51].

The difficulty with this type of definition is the production term in the energy balance, D_a. Included in the energy production rate are terms like,

$$\rho_0 \frac{\partial u_0}{\partial y} u'v'$$

which vanish only where the mean velocity is uniform. The acoustic source term of Equation 2.37, on the other hand, leads to an energy production rate that vanishes wherever the flow is irrotational and isentropic. The definition of Equation 2.37, therefore, extends the continuity property to a wider class of mean flows and is generally more useful.

Finally, the current form also has the property that when there is no mean flow and no entropy gradient the energy relation (2.37) reduces to the classical acoustic energy balance,

$$\frac{\partial}{\partial t}[\frac{p'^2}{2\rho_0 c_0^2} + \frac{\rho_0(u'^2 + v'^2)}{2}] + \nabla \cdot (p'\mathbf{u}') = 0.$$

2.5 Limitations of Linear Analysis

The current thesis is based on the assumption that the fluid flow can be linearized about some nominal steady flow. For small perturbations in the flow, this is a reasonable assumption. But for flows with finite perturbations the linear perturbation method may not be valid.

The linearized Euler equations ignore terms of order two and higher in the perturbation analysis, and therefore do not describe the acoustic process exactly. They are an approximation which will provide an accurate description in many cases, but will provide only adequate or perhaps even completely wrong description in other situations. An important question is then: In which situations is the current approach valid? We will investigate the validity of our method using a Fourier series analysis as shown by Hall [30].

Consider the continuity equation in one dimension,

$$\frac{\partial \rho}{\partial t} + \frac{\partial}{\partial x}\rho u = 0 \tag{2.44}$$

and assume a periodic boundary condition. The continuity equation, like the momentum and energy equations, is nonlinear in the primitive dependent variables. Now expand the dependent variables in a complex Fourier series in ω, where ω is the frequency of a dominant excitation [34],

$$\rho(x,t) = \sum_{n=-\infty}^{\infty} \rho_n(x) e^{i\omega n t} \tag{2.45}$$

$$u(x,t) = \sum_{n=-\infty}^{\infty} u_n(x) e^{i\omega n t} \tag{2.46}$$

where ρ_n and u_n are complex functions of x only. The Fourier coefficients are defined by,

$$\rho_0(x) = \frac{1}{T}\int_0^T \rho(x,t)\,dt$$

$$\rho_n(x) = \frac{1}{T}\int_0^T \rho(x,t) e^{-i\omega n t}\,dt$$

and T is the period, $T = 2\pi/\omega$.

Substitute the Fourier coefficients in Equations 2.45 and 2.46 into the continuity Equation 2.44 such that,

$$in\omega \sum_{n=-\infty}^{\infty} \rho_n(x)e^{i\omega nt} + \frac{\partial}{\partial x}[(\sum_{n=-\infty}^{\infty} \rho_n(x)e^{i\omega nt})(\sum_{n=-\infty}^{\infty} u_n(x)e^{i\omega nt})] = 0. \tag{2.47}$$

Now wherever products of dependent variables occur, the multiplication of the Fourier series is carried out term by term, and the resulting series is arranged in like powers of $\exp(i\omega t)$,

$$\frac{\partial}{\partial x}(\cdots + \rho_{-2}u_2 + \rho_{-1}u_1 + \rho_0 u_0 + \rho_1 u_{-1} + \rho_2 u_{-2} + \cdots) = 0 \tag{2.48}$$

$$i\omega\rho_1 + \frac{\partial}{\partial x}(\cdots + \rho_{-2}u_3 + \rho_{-1}u_2 + \rho_0 u_1 + \rho_1 u_0 + \rho_2 u_{-1} + \cdots) = 0 \tag{2.49}$$

$$-i\omega\rho_{-1} + \frac{\partial}{\partial x}(\cdots + \rho_{-2}u_1 + \rho_{-1}u_0 + \rho_0 u_{-1} + \rho_1 u_{-2} + \rho_2 u_{-3} + \cdots) = 0 \tag{2.50}$$

$$2i\omega\rho_2 + \frac{\partial}{\partial x}(\cdots + \rho_{-1}u_3 + \rho_0 u_2 + \rho_1 u_1 + \rho_2 u_0 + \rho_3 u_{-1} + \cdots) = 0 \tag{2.51}$$

$$-2i\omega\rho_{-2} + \frac{\partial}{\partial x}(\cdots + \rho_{-3}u_1 + \rho_{-2}u_0 + \rho_{-1}u_{-1} + \rho_0 u_{-2} + \rho_1 u_{-3} + \cdots) = 0 \tag{2.52}$$

and so forth.

In principle, the complete solution to the continuity Equation 2.44 can be obtained by solving the above set of nonlinear simultaneous differential equations. This, however, is impossible since the above set involves an infinite number of variables in an infinite number of nonlinear equations. Nevertheless, some insight into the effects of nonlinearities can be analyzed by assuming an asymptotic behavior of the variables,

$$\rho_0 \gg \rho_{\pm 1} \gg \rho_{\pm 2} \gg \cdots$$

$$u_0 \gg u_{\pm 1} \gg u_{\pm 2} \gg \cdots$$

Then to leading order, the Fourier coefficients are given by,

$$\frac{\partial}{\partial x}\rho_0 u_0 = 0 \tag{2.53}$$

$$i\omega\rho_1 + \frac{\partial}{\partial x}(\rho_0 u_1 + \rho_1 u_0) = 0 \tag{2.54}$$

and

$$2i\omega\rho_2 + \frac{\partial}{\partial x}(\rho_1 u_1 + \rho_0 u_2 + \rho_2 u_0) = 0. \tag{2.55}$$

The first equation above is the steady mean equation, and the second equation is the first order equation in which the current thesis is based upon. The last equation is the leading order behavior of the second harmonic (nonlinear) component in the flow. Note that the second harmonic component is excited by a product of first order components $\rho_1 u_1$. The component of the nonlinearity present will be approximately proportional to the square of the linear components, and thus to leading order, the linearized Euler equations give the correct results.

Next consider the higher order corrections to the mean and the fundamental frequency equations. Keeping only the next highest order terms in the equations gives,

$$\frac{\partial}{\partial x}(\rho_0 u_0 + \rho_1 u_1^* + \rho_1^* u_1) = 0 \tag{2.56}$$

for the mean equation and,

$$i\omega\rho_1 + \frac{\partial}{\partial x}(\rho_0 u_1 + \rho_1 u_0 + \rho_2 u_1^* + \rho_1^* u_2) = 0 \tag{2.57}$$

for the fundamental frequency equation where we have used the definition,

$$\rho_{-n} = \rho_n^*, \quad u_{-n} = u_n^*$$

and * denotes the conjugate operator. The first equation indicates that the mean flow is affected by the presence of unsteadiness. These nonlinear terms in the continuity

equation (and similar terms in the momentum and the energy equations) show that the mean of an unsteady flow is not the same as the steady flow when the unsteadiness is large. Fortunately, this effect is second order and therefore very small in acoustics.

The higher order corrections to the first order equation are a product of the second harmonic component and the fundamental component, i.e. they are third order. The linearized Euler equations are, therefore, valid so long as the square of the unsteadiness is not significant, and the corresponding error between the results of the linearized Euler analysis and an exact solution will also be of the order of the square of the unsteadiness. Note that the Fourier expansion was performed only in time, and since the mean flow solver is completely nonlinear, the current method is valid so long as the square unsteadiness is not very large even for highly nonlinear cases such as transonic flows.

Hall [30] showed that for a subsonic flow, even when $|p_1|/p_0$ was as high as 0.02 there was little difference between the complete Euler and the linearized Euler solutions. Therefore, the Fourier analysis shows that the linearized Euler equations are valid for most acoustical processes which involve realistic sound pressure levels ($|p_1|/p_0$ no greater than 10^{-3}).

2.6 Summary

In this chapter, the governing set of linearized Euler equations was derived. The linearized equations were cast in the frequency domain by utilizing the single frequency assumption; the equations were further modified by casting them in the scattered form.

The concept of acoustic energy and intensity were also introduced. Their definitions in differential and integral forms were derived.

The limitations of the current approach was also discussed. The method was shown to be inadequate when the square of the unsteadiness was large.

Chapter 3

Boundary Conditions

3.1 Surface Conditions

A rigid wall type of boundary condition was used for all calculations. For an inviscid wall the correct boundary condition is that there is no normal flow relative to the surface, or that the flow velocity normal to the surface is equal to the surface normal velocity.

$$\mathbf{U} \cdot \mathbf{n} = \frac{\partial \mathbf{r}}{\partial t} \cdot \mathbf{n} \tag{3.1}$$

where $\mathbf{U}$ is the flow velocity, $\mathbf{n}$ is the unit normal vector to the surface, and $\mathbf{r}$ is the surface position vector. Since in general the normal vector is a function of position, $\mathbf{n} = \mathbf{n}(\mathbf{r})$ and the boundary condition in Equation 3.1 is nonlinear.

Ideally, the above boundary condition should be applied at the instantaneous location of the surface. If the surface moves, the location at which the boundary condition is applied should correspondingly change also. It is, thus, more convenient to rederive the boundary condition so that it is enforced at the fixed, mean position. To do this, we linearize the variables about the mean and assume a small amplitude harmonic perturbations as in References [26, 30],

$$\mathbf{r} = \mathbf{r}_0 + \tilde{\mathbf{r}} e^{-i\omega t}$$

$$\mathbf{n} = \mathbf{n}_0 + \tilde{\mathbf{n}} e^{-i\omega t}$$

and

$$\mathbf{U} = \mathbf{u_0} + \tilde{\mathbf{u}} e^{-i\omega t}$$

where the subscript $_0$ refers to the steady mean quantity, and ˜ values denote the complex perturbation amplitudes.

Next we expand in Taylor series the velocity $\mathbf{U}$ for small excursions in the surface position,

$$\begin{aligned} \mathbf{U}(\mathbf{r}) &\approx \mathbf{U}(\mathbf{r_0}) + (\mathbf{r} - \mathbf{r_0}) \cdot \nabla \mathbf{U} \\ &\approx \mathbf{u_0}(\mathbf{r_0}) + \tilde{\mathbf{u}}(\mathbf{r_0}) e^{-i\omega t} + \tilde{\mathbf{r}} \cdot \nabla \mathbf{u_0} e^{-i\omega t}. \end{aligned} \tag{3.2}$$

If we substitute the above equations into the boundary condition in Equation 3.1, we obtain,

$$\mathbf{u_0} \cdot \mathbf{n_0} = 0 \tag{3.3}$$

for the mean steady boundary condition and,

$$\tilde{\mathbf{u}} \cdot \mathbf{n_0} = -\mathbf{u_0} \cdot \tilde{\mathbf{n}} - \tilde{\mathbf{r}} \cdot \nabla(\mathbf{u_0} \cdot \mathbf{n_0}) - i\omega \tilde{\mathbf{r}} \cdot \mathbf{n_0} \tag{3.4}$$

for the first order unsteady boundary condition. Since the motion of the body is prescribed, all the terms on the right hand side are known values.

Note that for a stationary surface $\tilde{\mathbf{r}} = \tilde{\mathbf{n}} = 0$, and the boundary condition simplifies to,

$$\tilde{\mathbf{u}} \cdot \mathbf{n_0} = 0 \tag{3.5}$$

or in terms of the scattered quantities,

$$\tilde{\mathbf{u}}_s \cdot \mathbf{n_0} = -\tilde{\mathbf{u}}_i \cdot \mathbf{n_0} \tag{3.6}$$

where $\tilde{\mathbf{u}}_i$ is a given incident complex velocity. In addition for no mean flow situations,

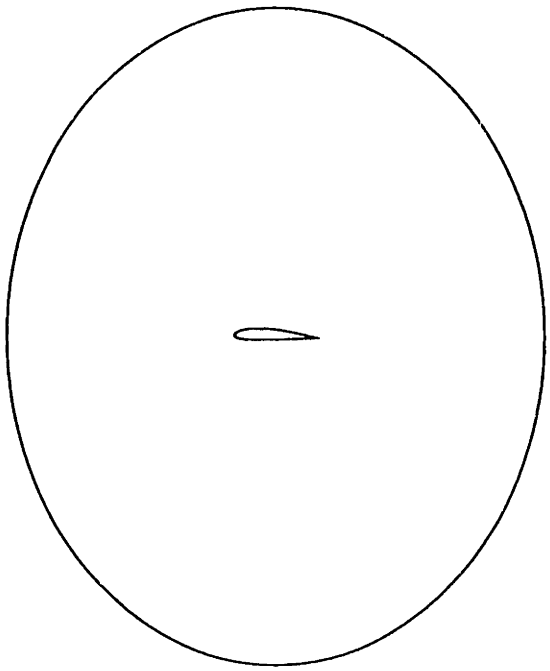

Figure 3-1: Isolated Airfoil Geometry

we obtain the classical boundary condition for moving walls,

$$\tilde{\mathbf{u}} \cdot \mathbf{n_0} = -i\omega\tilde{\mathbf{r}} \cdot \mathbf{n_0}. \tag{3.7}$$

3.2 Far Field Conditions

The implementation of far field boundary conditions is dependent on the geometry of the domain. Here we are primarily concerned with isolated airfoil type of problems as shown in Figure 3-1.

The analytic far field boundary conditions for the dependent variables $\tilde{Q}$ are that,

$$\tilde{Q} \to 0 \quad \text{as} \quad r \to \infty \tag{3.8}$$

and the variables must also satisfy the *causality* condition. That is the information about the current source activity should not be contained in past waves that anticipate

the present [19]. For simple no mean flow situations the causality condition is equivalent to the Sommerfeld radiation condition,

$$\lim_{r\to\infty} r(\frac{\partial p'}{\partial t} + c_0\frac{\partial p'}{\partial r}) = 0. \tag{3.9}$$

For aeronautical applications involving nonzero base mean flows, the causality condition is not equivalent to the Sommerfeld radiation condition, and in addition, for practical reasons we need to specify the boundary conditions on a finite domain.

There are many different methods to specify the far field boundary conditions. One common approach is to map the convective wave equation in pressure to the standard wave equation using Prandtl-Glauert methods, then the boundary conditions commonly used in no mean flow methods such as the Sommerfeld radiation condition or the Bayliss & Turkel radiation condition [10, 11] can be applied. These methods are usually simple and can often be quite effective for steady mean flow calculations [10, 11, 23]. But for unsteady perturbation analysis they have been found to be inadequate [36], primarily because the boundary conditions ignore the unsteady vortical wake, and also because they are one dimensional and ignore all variations in the azimuthal direction.

Another commonly used approach is to apply unsteady one dimensional characteristic conditions. The characteristic conditions are also quite simple to apply, and in fact, we have used such an approach as a first attempt and only later abandoned them because of their high errors in cases with large azimuthal variations.

The boundary conditions we currently use are an extension of the theory by Giles [25, 26] for isolated airfoil type geometries.

3.2.1 Perturbation Flow Far Field Boundary Conditions

In perturbation problems, any reflection is of the same order as the desired solution, and the effectiveness of the far field boundary conditions is critical to the overall accuracy of the scheme. Given a domain of about 10 chords and 10 wavelengths, one dimensional characteristic or radiation boundary conditions maybe insufficient for isolated airfoil

type of problems. The conditions are typically only effective when the outgoing waves are close to normal incidence with the boundary.

A correct mathematical model would extend the domain to infinity, and would require only outgoing wave modes (Radiation Condition) which vanish at infinity. This is impractical numerically, and a set of wellposed boundary conditions must be placed on a finite domain. Wellposedness is the requirement that a solution exists, is unique, and is bounded in some norm sense. All acoustic problems included in the current thesis arise from models of physical problems, and therefore, any far field boundary conditions which are used to truncate the domain must give a wellposed problem.

The far field conditions generally become more accurate as the boundary is placed further away from the source, but at the same time, the numerical efficiency is necessarily decreased as the numerical domain is increased. It is thus desirable to implement a set of conditions which would allow the smallest wellposed numerical domain without compromising accuracy or stability.

The current methodology uses a slightly modified version of the multi–dimensional nonreflecting boundary conditions by Giles. The boundary conditions are an extension of contributions made earlier by Engquist & Madja [21], Ferm [22], and Gustafson [29]; the complete details are found in References [25, 26]. They are repeated here for completeness.

The linear perturbation Equations 2.15 may be expressed in 'primitive' form as,

$$\frac{\partial \mathbf{U}}{\partial t} + \mathbf{A}\frac{\partial \mathbf{U}}{\partial x} + \mathbf{B}\frac{\partial \mathbf{U}}{\partial y} = 0, \tag{3.10}$$

where $\mathbf{U}$ is the column vector of perturbation variables

$$\mathbf{U} = \begin{pmatrix} \rho' \\ u' \\ v' \\ p' \end{pmatrix}, \tag{3.11}$$

and the coefficient matrices **A** and **B** are assumed constant matrices based on the steady mean variables,

$$\mathbf{A} = \begin{pmatrix} u & 1 & 0 & 0 \\ 0 & u & 0 & 1 \\ 0 & 0 & u & 0 \\ 0 & 1 & 0 & u \end{pmatrix}, \quad \mathbf{B} = \begin{pmatrix} v & 0 & 1 & 0 \\ 0 & v & 0 & 0 \\ 0 & 0 & v & 1 \\ 0 & 0 & 1 & v \end{pmatrix} \tag{3.12}$$

where the matrices **A** and **B** are nondimensionalized using the steady density and speed of sound. Consider wavelike solutions of the form,

$$\mathbf{U}(x, y, t) = \mathbf{u}e^{i(kx+ly-\omega t)}.$$

Substituting this into the differential equation gives,

$$(-\omega\mathbf{I} + k\mathbf{A} + l\mathbf{B})\mathbf{u} = 0. \tag{3.13}$$

For a nontrivial solution it must follow that,

$$\det(-\omega\mathbf{I} + k\mathbf{A} + l\mathbf{B}) = 0$$

or

$$(uk + vl - \omega)^2[(uk + vl - \omega)^2 - (k^2 + l^2)] = 0. \tag{3.14}$$

Equation 3.14 is called the dispersion relation, and is a polynomial equation of degree 4 in each of ω, k, and l.

Define right eigenvectors $\mathbf{v}^{\mathbf{R}}$ and left eigenvectors $\mathbf{u}^{\mathbf{L}}$ and $\mathbf{v}^{\mathbf{L}}$ such that,

$$(-\omega\mathbf{I} + k\mathbf{A} + l\mathbf{B})\mathbf{u}^{\mathbf{R}} = 0 \tag{3.15}$$

$$\mathbf{u}^{\mathbf{L}}(-\omega\mathbf{I} + k\mathbf{A} + l\mathbf{B}) = 0 \tag{3.16}$$

and,

$$\begin{aligned} \mathbf{v^L A^{-1}}(-\omega \mathbf{I} + k\mathbf{A} + l\mathbf{B}) &= \\ \mathbf{v^L}(-\omega \mathbf{A^{-1}} + k\mathbf{I} + l\mathbf{A^{-1}B}) &= 0. \end{aligned} \tag{3.17}$$

$\mathbf{u^L}$ are the left eigenvectors of $(k\mathbf{A} + l\mathbf{B})$ with eigenvalue ω, and $\mathbf{v^L}$ are the left eigenvectors of $(-\omega\mathbf{A^{-1}} + l\mathbf{A^{-1}B})$ with eigenvalue $-k$. $\mathbf{u^R}$ are the right eigenvectors of both $(k\mathbf{A} + l\mathbf{B})$ and $(-\omega\mathbf{A^{-1}} + l\mathbf{A^{-1}B})$ with eigenvalues ω and $-k$, respectively. In general, the left and right eigenvectors are orthogonal such that,

$$\mathbf{v_n^L u_m^R} = 0$$

if $m \neq n$, and also

$$\mathbf{v_n^L} = \mathbf{u_n^L A}.$$

Suppose that the differential Equation 3.10 is to be solved in some domain $x_0 < x < x_1$, $y_0 < y < y_1$ and one wants to construct nonreflecting boundary conditions at $x = x_1$ to minimize the reflection of outgoing waves. At the boundary $x = x_1$, $\mathbf{U}$ can be decomposed into a sum of Fourier modes in y and t and into a sum of its eigenmodes in x,

$$\mathbf{U}(x, y, t) = \sum_{\omega=-\infty}^{+\infty} \sum_{l=-\infty}^{+\infty} \sum_{n=1}^{4} a_n \mathbf{u_n^R} e^{i(k_n x + ly - \omega t)} \tag{3.18}$$

where k_n is the n^{th} root of the dispersion relation for the given values of ω and l, and $\mathbf{u_n^R}$ is the corresponding right eigenvector. Then for each value of ω and l, the ideal nonreflecting boundary conditions would be to specify that $a_n = 0$ for each n that corresponds to an incoming wave. Because of orthogonality,

$$\begin{aligned} \mathbf{v_n^L U}(x, y, t) &= \mathbf{v_n^L}(\sum_{m=1}^{4} a_m \mathbf{u_m^R} e^{ik_m x}) e^{i(ly - \omega t)} \\ &= a_n(\mathbf{v_n^L u_n^R} e^{ik_n x}) e^{i(ly - \omega t)} \end{aligned} \tag{3.19}$$

so that an equivalent specification of nonreflecting boundary conditions is,

$$\mathbf{v}_\mathbf{n}^\mathbf{L}\mathbf{U} = 0 \tag{3.20}$$

for each incoming mode n.

Given the system of Equations 3.10 the eigenvalues and the corresponding left eigenvectors are found to be,

$$k_1 = \tfrac{\omega - vl}{u} \quad , \mathbf{v}_1^\mathbf{L} = \begin{pmatrix} -1 & 0 & 0 & 1 \end{pmatrix} \tag{3.21}$$

$$k_2 = \tfrac{\omega - vl}{u} \quad , \mathbf{v}_2^\mathbf{L} = \begin{pmatrix} 0 & -u\lambda & 1 - v\lambda & -\lambda \end{pmatrix} \tag{3.22}$$

$$k_3 = \tfrac{(\omega - vl)(S-u)}{(1-u^2)} \quad , \mathbf{v}_3^\mathbf{L} = \begin{pmatrix} 0 & (1 - v\lambda) & u\lambda & (1 - v\lambda)S \end{pmatrix} \tag{3.23}$$

$$k_4 = -\tfrac{(\omega - vl)(S+u)}{(1-u^2)} \quad , \mathbf{v}_4^\mathbf{L} = \begin{pmatrix} 0 & -(1 - v\lambda) & -u\lambda & (1 - v\lambda)S \end{pmatrix} \tag{3.24}$$

where $\lambda = \frac{l}{\omega}$ and,

$$S = \sqrt{1 - \frac{(1-u^2)\lambda^2}{(1-v\lambda)^2}}.$$

The direction of propagation is computed by analyzing the group velocity vector,

$$\mathbf{C_g} = \begin{pmatrix} \frac{\partial\omega}{\partial k_1} \\ \frac{\partial\omega}{\partial k_2} \\ \frac{\partial\omega}{\partial k_3} \\ \frac{\partial\omega}{\partial k_4} \end{pmatrix} = \begin{pmatrix} u \\ u \\ \frac{1-u^2}{-u+1/S} \\ \frac{1-u^2}{-u-1/S} \end{pmatrix}. \tag{3.25}$$

The first two eigenvalues, k_1 and k_2, correspond to entropy and vorticity waves, respectively, and convect at the local velocity u. Assuming that $|u| < 1$ and S is purely real, k_3 corresponds to a pressure wave which travels in the $+x$ direction, and k_4 corresponds to a pressure wave which travels in the $-x$ direction. The nonreflecting

boundary condition when $+x$ direction points out of the domain is thus,

$$\mathbf{v}_4^{\mathbf{L}}\mathbf{U} = 0 \tag{3.26}$$

when $u \geq 0$ (outflow conditions) and,

$$\begin{pmatrix} \mathbf{v}_1^{\mathbf{L}} \\ \mathbf{v}_2^{\mathbf{L}} \\ \mathbf{v}_4^{\mathbf{L}} \end{pmatrix} \mathbf{U} = 0 \tag{3.27}$$

when $u < 0$ (inflow conditions).

3.2.2 Local Implementation: (Nonzero Mean Flow Cases)

In principle the above exact boundary conditions can be implemented in a numerical scheme; however, because $\mathbf{v}_\mathbf{n}^{\mathbf{L}}$ depends on ω and l, the implementation would require a Fourier transform in y. This is computationally difficult for nonperiodic type geometries or when the outer boundary has both incoming and outgoing regions. The current method implements a local approximate form of the left eigenvector $\mathbf{v}_\mathbf{n}^{\mathbf{L}}$ when the free stream Mach number is nonzero.

For a local implementation, a space varying reference frame (x', y') which is defined for each point on the outer boundary and points directly out of the domain in the positive x' direction is needed (see Figure 3-2). In addition since the left eigenvectors $\mathbf{v}_\mathbf{n}^{\mathbf{L}}$ are functions of u, v and λ, some knowledge of the outward traveling waves is also required.

Suppose the direction of the acoustic wave propagation is known, say for example, that an airfoil appears as a simple source in uniform flow at the far field. Define the anticipated acoustic wave travel to be in the positive x'' direction in the reference frame (x'', y''), as shown in Figure 3-2.

The assumption of propagation is equivalent to specifying the wavenumbers k_0 and

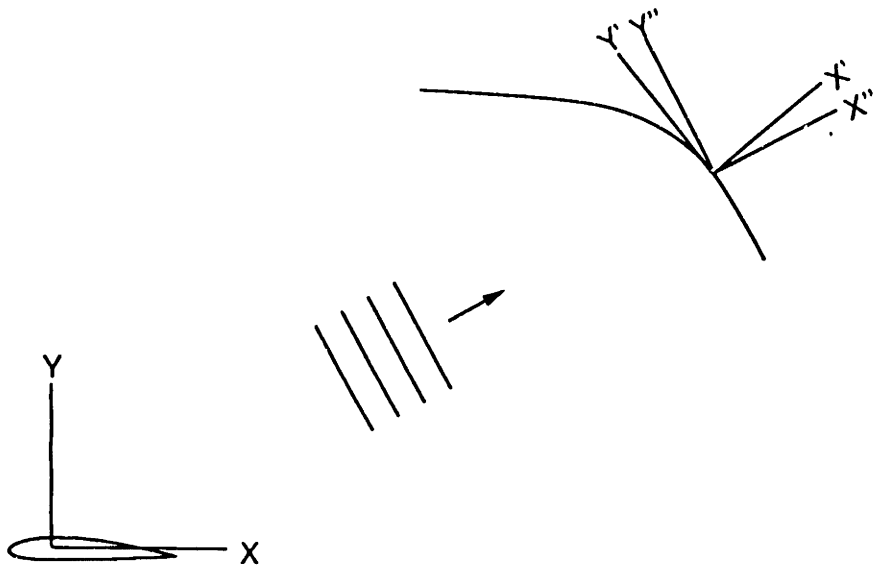

Figure 3-2: Global Reference Frame (x, y), and Local Reference Frames (x', y'), (x'', y'')

l_0 by using the dispersion relationship. The acoustic portion of the dispersion equation is,

$$(uk_0 + vl_0 - \omega)^2 - (k_0^2 + l_0^2) = 0. \tag{3.28}$$

The velocity of propagation of sound wave energy is equal to the group velocity obtained by differentiating the dispersion relation [25]. The group velocity is thus,

$$\mathbf{C_g} = \begin{pmatrix} \frac{\partial \omega}{\partial k_0} \\ \frac{\partial \omega}{\partial l_0} \end{pmatrix} = \begin{pmatrix} u \\ v \end{pmatrix} + \begin{pmatrix} \frac{k_0}{\omega - uk_0 - vl_0} \\ \frac{l_0}{\omega - uk_0 - vl_0} \end{pmatrix}. \tag{3.29}$$

When an acoustic wave travels purely in the positive x direction,

$$Cg_y = v + \frac{l_0}{\omega - uk_0 - vl_0} = 0. \tag{3.30}$$

Define κ_0 and λ_0 as,

$$\kappa_0 = \frac{k_0}{\omega}, \quad \lambda_0 = \frac{l_0}{\omega}.$$

The substitution of the above relation into Equation 3.30 gives,

$$\lambda_0 = \frac{v(u\kappa_0 - 1)}{1 - v^2} \tag{3.31}$$

and the dispersion relation gives,

$$\kappa_0 = \frac{-u \pm \sqrt{1 - v^2}}{1 - u^2 - v^2}. \tag{3.32}$$

The choice of the root depends whether the waves travel in the positive or negative x direction; the outgoing wave corresponds to the positive radical.

First Order Boundary Conditions

Once the two wave numbers k_0 and l_0 (or κ_0 and λ_0) are known, the boundary conditions in Equations 3.26 and 3.27 can be directly used since ω is a given parameter. This sort of boundary condition is first order accurate in l and is similar to the commonly found one dimensional characteristic conditions, such as in Reference [15].

The boundary conditions are,

$$\mathbf{v}_\mathbf{n}^\mathbf{L}\tilde{\mathbf{U}} = 0 \tag{3.33}$$

for each incoming mode n and where $\mathbf{U} = \tilde{\mathbf{U}}e^{-i\omega t}$. When $u < 0$, apply inflow boundary conditions,

$$\begin{pmatrix} \mathbf{v}_\mathbf{1}^\mathbf{L} \\ \mathbf{v}_\mathbf{2}^\mathbf{L} \\ \mathbf{v}_\mathbf{4}^\mathbf{L} \end{pmatrix} \tilde{\mathbf{U}} = 0$$

or

$$\begin{pmatrix} -1 & 0 & 0 & 1 \\ 0 & -u\lambda_0 & 1-v\lambda_0 & -\lambda_0 \\ 0 & -(1-v\lambda_0) & u\lambda_0 & (1-v\lambda_0)S_0 \end{pmatrix} \begin{pmatrix} \tilde{\rho} \\ \tilde{u} \\ \tilde{v} \\ \tilde{p} \end{pmatrix} = 0 \tag{3.34}$$

and when $u > 0$, apply outflow boundary conditions,

$$\mathbf{v}_4^{\mathbf{L}}\tilde{\mathbf{U}} = 0$$

or

$$\begin{pmatrix} 0 & -(1-v\lambda_0) & u\lambda_0 & (1-v\lambda_0)S_0 \end{pmatrix} \begin{pmatrix} \tilde{\rho} \\ \tilde{u} \\ \tilde{v} \\ \tilde{p} \end{pmatrix} = 0. \tag{3.35}$$

In practice the boundary conditions are more easily applied using characteristic variables. The equivalent boundary conditions in characteristic variables is,

$$\begin{pmatrix} \tilde{c}_1 \\ \tilde{c}_2 \\ \tilde{c}_4 \end{pmatrix} = \frac{1}{(1+S_0)(1-\lambda_0 v)^2 - \lambda_0^2 u(1-u)} \begin{pmatrix} 0 \\ \lambda_0(1+S_0 u)(1-\lambda_0 v)\tilde{c}_3 \\ (1-S_0)(1-\lambda_0 v)^2 + \lambda_0^2 u(1+u)\tilde{c}_3 \end{pmatrix} \tag{3.36}$$

for the inflow $u < 0$ condition, where $\tilde{c}_3$ is the outgoing characteristic. The boundary condition at the outflow $u > 0$ is,

$$\tilde{c}_4 = \frac{2u\lambda_0}{(1-v\lambda_0)(1+S_0)}\tilde{c}_2 + \frac{1-S_0}{1+S_0}\tilde{c}_3 \tag{3.37}$$

where $\tilde{c}_1$, $\tilde{c}_2$, and $\tilde{c}_3$ are the outgoing characteristics. The transformation to and from the characteristic variables is performed by simple matrix multiplications,

$$\tilde{\mathbf{C}} = \mathbf{D}\tilde{\mathbf{U}} \tag{3.38}$$

$$\begin{pmatrix} \tilde{c}_1 \\ \tilde{c}_2 \\ \tilde{c}_3 \\ \tilde{c}_4 \end{pmatrix} = \begin{pmatrix} -1 & 0 & 0 & 1 \\ 0 & 0 & 1 & 0 \\ 0 & 1 & 0 & 1 \\ 0 & -1 & 0 & 1 \end{pmatrix} \begin{pmatrix} \tilde{\rho} \\ \tilde{u} \\ \tilde{v} \\ \tilde{p} \end{pmatrix} \tag{3.39}$$

$$\tilde{\mathbf{U}} = \mathbf{D}^{-1}\tilde{\mathbf{C}} \tag{3.40}$$

$$\begin{pmatrix} \tilde{\rho} \\ \tilde{u} \\ \tilde{v} \\ \tilde{p} \end{pmatrix} = \begin{pmatrix} -1 & 0 & \frac{1}{2} & \frac{1}{2} \\ 0 & 0 & \frac{1}{2} & -\frac{1}{2} \\ 0 & 1 & 0 & 0 \\ 0 & 0 & \frac{1}{2} & \frac{1}{2} \end{pmatrix} \begin{pmatrix} \tilde{c}_1 \\ \tilde{c}_2 \\ \tilde{c}_3 \\ \tilde{c}_4 \end{pmatrix}. \tag{3.41}$$

The assumed direction of sound wave travel, i.e. the local reference frame (x'', y''), is defined as a sum of a vector whose direction is normal to the lines of constant pressure phase and whose magnitude is the local speed of sound plus the local velocity vector. The phase of pressure is computed such that at the far field the body is assumed to be a simple source in uniform flow. The amplitude of acoustic pressure then scales as,

$$\tilde{p}(d, \phi) \sim \frac{1}{\sqrt{\pi d}} H_1^{(1)}(\frac{\omega d}{c_0}) \sin\phi \tag{3.42}$$

for a dipole and,

$$\tilde{p}(d, \phi) \sim \frac{1}{\sqrt{\pi d}} H_0^{(1)}(\frac{\omega d}{c_0}) \tag{3.43}$$

for a monopole. d and ϕ are defined in Prandtl-Glauert coordinates such that,

$$d^2 = (x/\beta)^2 + y^2$$

$$\phi = \arctan \frac{y\beta}{x}$$

and $\beta = \sqrt{1 - M_0^2}$. The asymptotic approximation for a large argument of $H_j^{(1)}$ in Reference [1] is used to derive the normal to constant phase lines for both simple poles

for $\frac{\omega d}{c_0} \rightarrow \infty$ as,

$$\tan[\tan(\frac{\omega d}{c_0} - M_0\frac{\omega x}{c_0\beta^2} - \frac{\pi}{4})] = \text{constant}. \tag{3.44}$$

The boundary conditions are applied at each of the outer boundary points. Its implementation is as follows:

1. Renormalize variables with respect to the free stream density, pressure, and speed of sound.

2. Define the coordinate frame (x'', y''). When the mean flow is along the positive x axis and given a simple source, (u'', v'') is defined at the far field as,

$$\begin{pmatrix} u'' \\ v'' \end{pmatrix} = \begin{pmatrix} \cos\phi & \sin\phi \\ -\sin\phi & \cos\phi \end{pmatrix} \begin{pmatrix} u \\ v \end{pmatrix} \tag{3.45}$$

where

$$\cos\phi = \sqrt{1-(M_0\sin\theta)^2}\cos\theta - M_0\sin^2\theta$$

$$\sin\phi = \sqrt{1-(M_0\sin\theta)^2}\sin\theta + M_0\cos\theta\sin\theta$$

and M_0 is the free stream Mach number and $\tan\theta = \frac{y}{x}$.

3. Compute κ_0'' for an outgoing wave using Equation 3.32 and λ_0'' using Equation 3.31.

4. Transform velocities in (x, y) frame to (x', y') reference frame.

$$\begin{pmatrix} u' \\ v' \end{pmatrix} = \begin{pmatrix} \cos\beta & \sin\beta \\ -\sin\beta & \cos\beta \end{pmatrix} \begin{pmatrix} u \\ v \end{pmatrix} \tag{3.46}$$

where β is a function of the outer boundary shape. For a circular outer boundary,

$$\tan\beta = \frac{y}{x}.$$

5. Transform λ_0'' to λ_0' and compute S_0'.

$$\lambda_0' = -\sin(\beta - \phi)\kappa_0'' + \cos(\beta - \phi)\lambda_0'' \tag{3.47}$$

S_0' follows as,

$$S_0' = \sqrt{1 - \frac{(1 - u'^2)\lambda_0'^2}{(1 - v'\lambda_0')^2}}. \tag{3.48}$$

6. Apply boundary conditions on the (x', y') domain. When $u' < 0$ compute the outgoing characteristic $\tilde{c}_3'$ using Equation 3.38, then apply the inflow boundary conditions in Equation 3.36. When $u' > 0$ compute the outgoing characteristics $\tilde{c}_1'$, $\tilde{c}_2'$, and $\tilde{c}_3'$ using Equation 3.38, then apply the outflow boundary conditions in Equation 3.37.

7. Convert the characteristic variables to the perturbation variables using Equation 3.40.

8. Retransform velocities in (x', y') to (x, y),

$$\begin{pmatrix} u \\ v \end{pmatrix} = \begin{pmatrix} \cos\beta & -\sin\beta \\ \sin\beta & \cos\beta \end{pmatrix} \begin{pmatrix} u' \\ v' \end{pmatrix}. \tag{3.49}$$

Reference [26] shows that the current first order boundary conditions are wellposed, and that the error scales as,

$$\text{Error} = O(\frac{l_{exact} - l_{estimate}}{\omega})$$

where l_{exact} and $l_{estimate}$ are the exact and the assumed wavenumbers, respectively. The boundary conditions are exact if the outgoing waves are planar and if the estimated direction of propagation is the same as the actual direction of travel.

Fourth Order Inflow, Fourth/First Order Outflow Boundary Conditions

A higher order boundary condition is derived by expanding S about the assumed wave number l_0 (or λ_0),

$$S(\lambda_0 + \epsilon) \approx S_0 + \frac{\partial S}{\partial \lambda}\epsilon + \cdots \tag{3.50}$$

where the subscript $_0$ refers to the assumed values and again $\lambda = \frac{l}{\omega}$. Unfortunately a straight forward Taylor series expansion of this type often leads to an illposed set of boundary conditions. Giles [26] showed how a higher order, yet wellposed, set of boundary condition is derived by combining different order approximations of multiple eigenvectors. The boundary conditions are constructed by adding to the second order approximation of the third left eigenvector the first order approximation of the second eigenvector, multiplied by factor $a\epsilon$, and the first order approximation of the third eigenvector, multiplied by factor $b\epsilon$. The formal proof of the error scale and the wellposedness are in Reference [26].

The modified boundary conditions are of the form,

$$-i\omega \mathbf{B_1}\tilde{\mathbf{U}}' + (\mathbf{B_2} + v'\mathbf{B_1})\frac{\partial \tilde{\mathbf{U}}'}{\partial y'} = 0 \tag{3.51}$$

where the $'$ notation again refers to variables in the local normal and outward pointing coordinate frame (x', y'). In terms of the previously defined characteristic variables, the equivalent boundary condition is,

$$-i\omega \mathbf{B_1}\mathbf{D}^{-1}\tilde{\mathbf{C}}' + (\mathbf{B_2} + v'\mathbf{B_1})\mathbf{D}^{-1}\frac{\partial \tilde{\mathbf{C}}'}{\partial y'} = 0. \tag{3.52}$$

The matrix $\mathbf{D}$ is defined in Equation 3.38 and again $\mathbf{U}' = \Re(\tilde{\mathbf{U}}' e^{-i\omega t})$. The matrices

$\mathbf{B_1}$ and $\mathbf{B_2}$ are different for inflow and outflow regions,

$$\mathbf{B_1} = \begin{pmatrix} -1 & 0 & 0 & 1 \\ 0 & 0 & 1 & 0 \\ 0 & -1 + b\lambda_0' + au'\lambda_0'^2 & -u'b\lambda_0'^2 - a\lambda_0' & S_0'(1 - b\lambda_0') + (\frac{1-u'^2}{S_0'} + a)\lambda_0'^2 \end{pmatrix} \tag{3.53}$$

$$\mathbf{B_2} = \begin{pmatrix} 0 & 0 & 0 & 0 \\ 0 & -u' & 0 & -1 \\ 0 & -b - au'\lambda_0' & -u' - u'b\lambda_0' + a & S_0'b - (\frac{1-u'^2}{S_0'} + a)\lambda_0' \end{pmatrix} \tag{3.54}$$

when $u' < 0$ (inflow condition) and,

$$\mathbf{B_1} = \begin{pmatrix} 0 & -1 + b\lambda_0' + au'\lambda_0'^2 & -u'b\lambda_0'^2 - a\lambda_0' & S_0'(1 - b\lambda_0') + (\frac{1-u'^2}{S_0'} + a)\lambda_0'^2 \end{pmatrix} \tag{3.55}$$

$$\mathbf{B_2} = \begin{pmatrix} 0 & -b - au'\lambda_0' & -u' - u'b\lambda_0' + a & S_0'b - (\frac{1-u'^2}{S_0'} + a)\lambda_0' \end{pmatrix} \tag{3.56}$$

when $u' \geq 0$ (outflow condition). The constants a and b are defined to be,

$$a = -\frac{(1 - u'^2)(1 - (2 - u'^2)\lambda_0'^2)}{2S_0'^3(1 + u'S_0')} \tag{3.57}$$

$$b = -\frac{(1 - u'^2)\lambda_0'}{S_0'^2(1 + u'S_0')} \tag{3.58}$$

The above relations are for the case $v = 0$, and hence an additional coordinate transformation is required at the far field. Define a (x''', y''') coordinate system which is identical to the (x', y') frame (normal and outward pointing to the boundary) except that it has a relative velocity $(0, v')$ such that the fluid velocity component v''' is zero.

The boundary conditions are tailored at each outer boundary point. The implementation is as follows:

1. Renormalize variables with respect to free stream density, pressure, and speed of sound.

2. Define the anticipated direction of propagation (x'', y'') and compute (u'', v'')as in the first order case.

3. Compute κ_0'' for an outgoing wave using Equation 3.32 and λ_0'' using Equation 3.31.

4. Transform λ_0'' to λ_0''' and compute S_0'''.

$$\lambda_0' = -\sin(\beta - \phi)\kappa_0'' + \cos(\beta - \phi)\lambda_0'' \tag{3.59}$$

and because of the Doppler shift in frequency for the moving reference frame,

$$\lambda_0''' = \frac{\lambda_0'}{1 - v'\lambda_0'}. \tag{3.60}$$

S_0''' follows as,

$$S_0''' = \sqrt{1 - (1 - u'^2)\lambda_0'''^2} \tag{3.61}$$

5. Substitute S_0''' for S_0' and λ_0''' for λ_0' in Equations 3.53 - 3.58. Apply boundary conditions in Equation 3.52.

6. Retransform velocities in (x', y') to global reference frame (x, y) as in the first order case.

The inflow boundary conditions are of $O(\epsilon^4)$ in accuracy; the outflow boundary conditions are of $O(\epsilon)$ in accuracy for the vorticity wave and of $O(\epsilon^4)$ in accuracy for the acoustic pressure wave. The boundary conditions are again exact if the outgoing waves are planar and if the estimated direction of travel is exact, i.e. when $\epsilon = 0$.

3.2.3 Global Implementation: (No Mean Flow Cases)

When there is no mean flow and given a periodic grid, the Giles boundary conditions can be improved by implementing the global boundary conditions described in Section 3.2. The vorticity and entropy waves do not exist, and at each of the outer boundary points there are only one incoming and one outgoing pressure waves. Thus

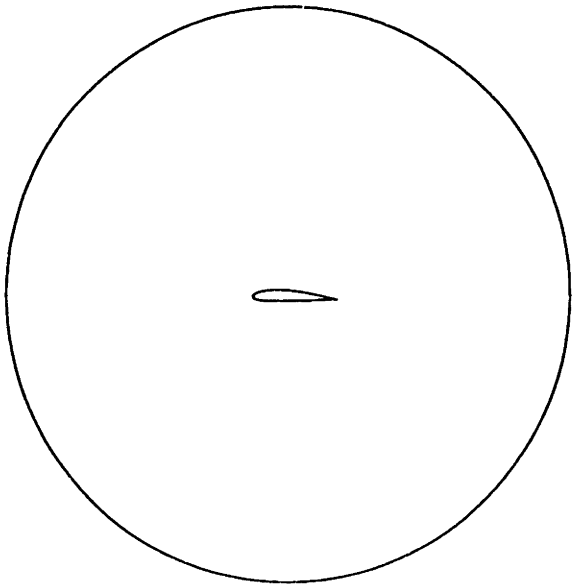

Figure 3-3: Circular Domain for Classical Acoustics

there are no separate inflow and outflow regions, and we can construct a highly accurate boundary conditions for cases which involve no mean flow.

Suppose we need to construct a nonreflecting boundary condition for a no mean flow case on a circular domain as shown in Figure 3-3. The most appropriate form of the equations for a circular outer boundary is the polar form of the perturbation equations,

$$\frac{\partial \mathbf{U}}{\partial t} + \mathbf{A}\frac{\partial \mathbf{U}}{\partial r} + \mathbf{B}\frac{\partial \mathbf{U}}{\partial s} + \mathbf{C}\frac{\mathbf{U}}{r} = 0 \tag{3.62}$$

where $\mathbf{U}$ is the column vector of perturbation variables

$$\mathbf{U} = \begin{pmatrix} p' \\ u' \\ v' \end{pmatrix} \tag{3.63}$$

and we have assumed an isentropic relation $p' = c_0^2 \rho'$ where c_0 is the speed of sound. The coefficient matrices $\mathbf{A}$, $\mathbf{B}$, and $\mathbf{C}$ are again normalized with respect to the free

stream pressure, density, and speed of sound and are defined as,

$$\mathbf{A} = \begin{pmatrix} 0 & 1 & 0 \\ 1 & 0 & 0 \\ 0 & 0 & 0 \end{pmatrix}, \quad \mathbf{B} = \begin{pmatrix} 0 & 0 & 1 \\ 0 & 0 & 0 \\ 1 & 0 & 0 \end{pmatrix}, \quad \mathbf{C} = \begin{pmatrix} 0 & 1 & 0 \\ 0 & 0 & 0 \\ 0 & 0 & 0 \end{pmatrix} \tag{3.64}$$

where the reference coordinates in (r, s) are related to the values in (x, y) by,

$$r = \sqrt{x^2 + y^2}$$

$$\tan\theta = \frac{y}{x}$$

and

$$s = r\theta.$$

In addition, u is the component of velocity in the r direction, and v is the component in the s direction. We seek wavelike solutions of the form,

$$\mathbf{U}(r, s, t) = \mathbf{u}e^{i(kr+ls-\omega t)}. \tag{3.65}$$

The substitution of the above equation into Equation 3.62 gives the dispersion relation,

$$\omega^3 - \omega[l^2 + k(k - \frac{i}{r})] = 0. \tag{3.66}$$

The first root is a degenerate root $\omega = 0$, and the two remaining roots are,

$$k_{1,2} = \pm\omega\sqrt{1 - \frac{1}{\omega r}(r^2l^2 + \frac{1}{4})} + \frac{i}{2r}. \tag{3.67}$$

k_1 and k_2 here are complex, and the wave modes are not purely nondissipative. The imaginary portion $i/2r$ corresponds to an exponentially decaying factor of $e^{-1/2}$.

For complex k we define incoming waves as those modes which have a negative group velocity or those which have $\Im(k) < 0$. The latter condition refers to exponentially

growing modes.

The group velocities are,

$$\mathbf{Cg}_{1,2} = \frac{\partial \omega}{\partial k}_{1,2} = \pm\sqrt{1 - (\frac{1}{\omega r})^2(r^2 l^2 + \frac{1}{4})}. \tag{3.68}$$

When $\mathbf{C_g}$ is purely real, k_1 and k_2 are an outward traveling and an inward traveling sound waves, respectively. Conversely when $\mathbf{C_g}$ is imaginary, both modes are simply exponential. The degenerate root $\omega = 0$ is the stationary 'vorticity' wave.

The boundary conditions require the derivation of the left eigenvectors $\mathbf{v_n^L}$, and they are computed using the methods described in Section 3.2,

$$\begin{pmatrix} \mathbf{v_1^L} \\ \mathbf{v_2^L} \end{pmatrix} = \frac{1}{2S_0} \begin{pmatrix} S - \frac{i}{2r\omega} & 1 & 0 \\ S + \frac{i}{2r\omega} & -1 & 0 \end{pmatrix} \tag{3.69}$$

where

$$S = \sqrt{1 - (\frac{1}{\omega r})^2(r^2 l^2 + \frac{1}{4})}$$

and

$$S_0 = \sqrt{1 - (\frac{1}{2\omega r})^2}.$$

There are only 2 left eigenvectors because the third 'vorticity' wave does not exist here.

The enforcement of the nonreflecting boundary condition is,

$$\mathbf{v_n^L}\tilde{\mathbf{U}} = 0 \tag{3.70}$$

where again

$$\mathbf{U}' = \tilde{\mathbf{U}}e^{-i\omega t}$$

for each n which corresponds to an incoming mode.

The implementation is as follows:

1. Renormalize the variables with respect to the free stream density, pressure, and

speed of sound.

2. Define polar coordinates (r, s) and recast the velocities.

3. Fourier transform the dependent variables $\tilde{p}, \tilde{u}, \tilde{v}$ in s at the outer boundary.

4. For each Fourier mode l determine if it is an incoming or an outgoing mode. If $\mathbf{C_g}$ is purely real then k_2 is the incoming mode, and the boundary condition is implemented as,

$$\mathbf{v_2^L}\tilde{\mathbf{U}} = \frac{1}{2S_0}\begin{pmatrix} S + \frac{i}{2r\omega} & -1 & 0 \end{pmatrix}\begin{pmatrix} \tilde{p} \\ \tilde{u} \\ \tilde{v} \end{pmatrix} = 0. \tag{3.71}$$

The equivalent boundary condition in the characteristic form is,

$$\tilde{c}_2 = \frac{S_0 - S}{S_0 + S}\tilde{c}_1 \tag{3.72}$$

where $\tilde{c}_1$ is the outgoing sound wave, and the characteristic variables are defined as,

$$\begin{pmatrix} \tilde{c}_1 \\ \tilde{c}_2 \end{pmatrix} = \frac{1}{2S_0}\begin{pmatrix} S_0 - \frac{i}{2r\omega} & 1 & 0 \\ S_0 + \frac{i}{2r\omega} & -1 & 0 \end{pmatrix}\begin{pmatrix} \tilde{p} \\ \tilde{u} \\ \tilde{v} \end{pmatrix} \tag{3.73}$$

and

$$\begin{pmatrix} \tilde{p} \\ \tilde{u} \\ \tilde{v} \end{pmatrix} = \begin{pmatrix} 1 & 1 \\ S_0 + \frac{i}{2r\omega} & -S_0 + \frac{i}{2r\omega} \\ 0 & 0 \end{pmatrix}\begin{pmatrix} \tilde{c}_1 \\ \tilde{c}_2 \end{pmatrix} \tag{3.74}$$

If $\mathbf{C_g}$ is imaginary then k_1 is outgoing and k_2 is incoming if $\Im(k_2) < 0$.

5. Compute $\tilde{v}$ by enforcing the irrotationality condition,

$$\frac{\partial}{\partial r}(r\tilde{v}) = \frac{\partial}{\partial \theta}\tilde{u}. \tag{3.75}$$

6. Inverse Fourier transform to obtain the original dependent variables.

7. Reconvert the velocities in the global Cartesian coordinates.

The boundary condition is performed for each Fourier component l and no local expansions of the left eigenvectors are performed, the boundary condition is therefore exact in the wavenumber l. However, the exponential wave assumption of Equation 3.65 is only strictly valid at infinity, and the reflections may be large when the boundary is close to the surface.

A typical physical solution scales algebraically for a large r,

$$\tilde{p} \sim \frac{1}{\sqrt{r}} \exp(\frac{i\omega r}{c_0})$$

whereas the current exponential expansion shows that for $r \gg 1$,

$$\tilde{p} \sim \exp(\frac{i\omega r}{c_0} + \frac{ic_0}{8\omega r}).$$

But as r tends infinity the variations of $1/\sqrt{r}$ is locally negligible and the two above relations become equivalent. In such situations the current boundary conditions are nearly exact and fully two dimensional.

3.2.4 Mean Flow Far Field Boundary Conditions

Nonreflecting far field boundary conditions for the steady mean flow equations are presented. The mean flow solver uses a combination of radiation boundary conditions by Bayliss & Turkel [10, 11] and a slightly modified form of one dimensional characteristic conditions discussed in previous sections.

In general steady flow problems, acoustic waves are transient perturbations on the desired nonfluctuating fluid variables. A one dimensional characteristic or radiation boundary conditions as in References [10, 11, 64, 68] are usually sufficient to guarantee a correct solution to within 5–10 % in lift given a domain which is about 10 chords in

radius.

The one dimensional characteristic equations are derived by assuming all cross derivative ($\frac{\partial}{\partial y'}$) terms to be small. Then following linearization and diagonalization, the governing mean flow Equations 2.13 can be cast as a set of uncoupled scalar equations of the form,

$$\frac{\partial c_i}{\partial t} + \lambda_i \frac{\partial c_i}{\partial x'} = 0 \tag{3.76}$$

where $'$ denotes variables in the local outward pointing reference frame (x', y') shown in Figure 3-2. The characteristics c_i are defined as,

$$\begin{pmatrix} c_1 \\ c_2 \\ c_3 \\ c_4 \end{pmatrix} = \begin{pmatrix} -c_\infty^2 & 0 & 0 & 1 \\ 0 & 0 & \rho_\infty c_\infty & 0 \\ 0 & \rho_\infty c_\infty & 0 & 1 \\ 0 & -\rho_\infty c_\infty & 0 & 1 \end{pmatrix} \begin{pmatrix} \delta\rho \\ \delta u' \\ \delta v' \\ \delta p \end{pmatrix} \tag{3.77}$$

$$\begin{pmatrix} \delta\rho \\ \delta u' \\ \delta v' \\ \delta p \end{pmatrix} = \begin{pmatrix} -\frac{1}{c_\infty^2} & 0 & \frac{1}{2c_\infty^2} & \frac{1}{2c_\infty^2} \\ 0 & 0 & \frac{1}{2c_\infty^2} & -\frac{1}{2c_\infty^2} \\ 0 & \frac{1}{\rho_\infty c_\infty} & 0 & 0 \\ 0 & 0 & \frac{1}{2} & \frac{1}{2} \end{pmatrix} \begin{pmatrix} c_1 \\ c_2 \\ c_3 \\ c_4 \end{pmatrix} \tag{3.78}$$

and the associated eigenvalues λ_i are,

$$\begin{pmatrix} \lambda_1 \\ \lambda_2 \\ \lambda_3 \\ \lambda_4 \end{pmatrix} = \begin{pmatrix} u'_\infty \\ u'_\infty \\ u'_\infty + c_\infty \\ u'_\infty - c_\infty \end{pmatrix} \tag{3.79}$$

where $_\infty$ quantities are the free stream values and are taken from the solution at the preceding time step. δ quantities denote the differences from the free stream variables,

$$\delta\rho = \rho_0 - \rho_\infty \tag{3.80}$$

$$\delta p = p_0 - p_\infty$$

$$\delta u' = u'_0 - v'_\infty$$

$$\delta v' = v'_0 - v'_\infty.$$

The diagonalized Equation 3.76 allows each c_i to be computed independently using the method of characteristics,

$$c_i = \text{constant.} \tag{3.81}$$

The characteristic c_i remains constant along the curve C_i in the $x't$ plane defined by $\frac{dx'}{dt} = \lambda_i$. A consistent boundary condition is then to set all incoming c_i's to 0.

In a typical steady subsonic two dimensional flow, the entropy and vorticity gradients in the fluid field are small at the far field. The pressure perturbations, however, may be large if the far field is brought in close to the surface. Thus in terms of the characteristic variables, c_1 and c_2 will be small while c_3 and c_4 may be large.

Bayliss & Turkel [10, 11] have constructed a family of radiation boundary conditions which are based on an asymptotic expansion of the solution of the wave equation. The condition asymptotically simulates outgoing pressure waves and at a sufficient distance from the source, prevents the generation of incoming pressure waves. The current scheme uses the Bayliss & Turkel operator to annihilate the incoming c_3 or c_4; c_1 and c_2 are computed using the appropriate characteristic condition. They are presented here without proof.

The Bayliss & Turkel operator used here is the first in the family and may be expressed as,

$$a\frac{\partial p}{\partial t} - \rho_\infty c_\infty^2 a^2 \frac{x}{d}\frac{\partial u}{\partial t} - \rho_\infty \frac{y}{d}\frac{\partial v}{\partial t} + \frac{\delta p}{2d} = 0 \tag{3.82}$$

where a and d are defined as,

$$a = \frac{1}{c_\infty \sqrt{1 - M_\infty^2}}$$

$$d = \sqrt{\xi^2 + y^2}$$

$$\xi = \frac{x}{\sqrt{1 - M_\infty^2}}.$$

The implementation is as follows:

1. Transform velocities in (x, y) reference frame to the local normal (x', y') reference frame as in the previous sections.

2. If $u'_\infty < 0$ then apply the inflow boundary conditions,

$$c_1 = c_2 = 0 \tag{3.83}$$

   and if $u'_\infty > 0$ then apply the outflow boundary conditions by computing c_1 and c_2 from Equation 3.78.

3. Compute pressure by applying the Bayliss & Turkel operator

4. Compute c_3 and c_4.

5. Compute δ variables by applying Equation 3.77 and compute the current dependent variables from Equation 3.80.

6. Retransform velocities to the global reference frame (x, y).

3.3 Kutta Condition

Continuous solutions for subsonic inviscid flow around a body with sharp edges are singular at those edges, the velocity there becoming infinite as some inverse fractional power of distance, r, the power depending on the wedge angle [8]. The situation is somewhat different for acoustics, given a flat plate for example, the pressure jump Δp across the plate will vanish like $r^{\frac{1}{2}}$ when there is no mean flow, but will become infinite like $r^{-\frac{1}{2}}$ in the presence of a mean flow [18]. Thus when there is a mean flow, one either has to accept a continuous solution which has a singularity at a sharp edge or must enforce an arbitrary condition which requires a finite pressure at the edge. The current method uses the latter approach, better known as the Kutta condition.

Euler solvers in use today automatically enforce the Kutta condition; that is to say, a numerical model of an inviscid flow does not allow infinite velocity gradients in the domain. It is thought that numerical diffusion (through artificial viscosity and grid stretching) is the dominant mechanism in which viscosity, however small, will not allow a finite pressure jump across a sharp edge. The current scheme behaves in a similar fashion and no explicit finiteness condition is enforced at a sharp edge.

3.4 Summary

A set of boundary conditions for rigid walls was presented. The boundary conditions were shown to be valid for both stationary and moving walls and were derived by linearizing the nonlinear boundary conditions about a steady mean state.

A set of nonreflecting far field boundary conditions for a finite numerical domain was also discussed. The boundary conditions for the perturbation equations using first and fourth order accurate local conditions in nonzero mean flow cases were derived. Global conditions valid for quiescent cases were also derived, and a simplified one dimensional characteristic/radiation condition for the mean flow equations was presented.

For all numerical computations, the fourth order perturbation far field boundary conditions of Section 3.2.2 were applied when the mean flow was nonzero, and the global boundary conditions of Section 3.2.3 were applied when there was no mean flow.

Finally, a numerical imposition of the Kutta condition in an inviscid model was discussed. The numerical viscosity enforces a pressure continuity condition at a sharp edge.

Chapter 4

Numerical Method

The governing mean steady and the unsteady aeroacoustic equations were derived in Chapter 2. The aeroacoustic quantities were defined to be linear perturbations about some nominal steady flow. The steady base flow is, thus, an input to the acoustic field and must be solved before any analysis on the perturbation values can be performed. In this chapter we discuss the numerical approximation methods to both the steady mean and the acoustic perturbation flows.

4.1 Grid

We are modelling a continuous solution in space and time by discrete approximations. The space domain is divided into distinct cells by a coordinate grid system, and while we could use a simple cartesian type orthogonal coordinates, they are usually not the most convenient or efficient for numerical computations about general two dimensional bodies. We have instead used a body–fitted coordinate system which offers the advantages of geometric generality and ease of boundary condition implementation.

'O–type' grids were used for all calculations, and a typical grid section about an arbitrary body is shown in Figure 4-1. Each of the nodes on the grid is referenced by two subscripts (i, j) denoting the node number in the azimuthal direction and in the normal direction, respectively. In the azimuthal direction, the nodes are numbered from 1 to I in the clockwise sense, and in the normal direction, the nodes are numbered from 1 to J in the outward sense. There are a total of $(I \cdot J)$ nodes.

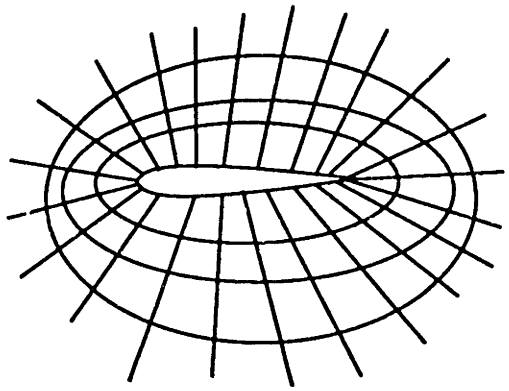

Figure 4-1: O–grid About a Body

4.2 Spatial Discretization

The conservation mean flow and the perturbation aeroacoustic equations are numerically solved using finite–volume, node–based schemes. The mean flow equations are discretized by a modified form of the Jameson method [37] and are of $O(h^2)$ in accuracy for a smooth grid, where h is a typical grid mesh length. The perturbation flow equations are discretized using a combination of the Jameson scheme and the Padé scheme and are of $O(h^2)$ accuracy in the normal direction and of $O(h^4)$ accuracy in the azimuthal direction. The Padé scheme is described in, among others, Anderson et al. [4], Orszag [56], Verhoff [69], and Lele [43].

We begin with methods of approximating the spatial fluxes for the base mean flow.

4.2.1 Mean Flow

At each node, the mean flow equations are discretized using a finite volume operator similar to the one used by Jameson [37]. Consider the mean flow Equations 2.13 which are to be satisfied over a super cell formed of 4 individual cells as shown in Figure 4-2. Since the mean flow equations are satisfied everywhere within a conservation volume, it

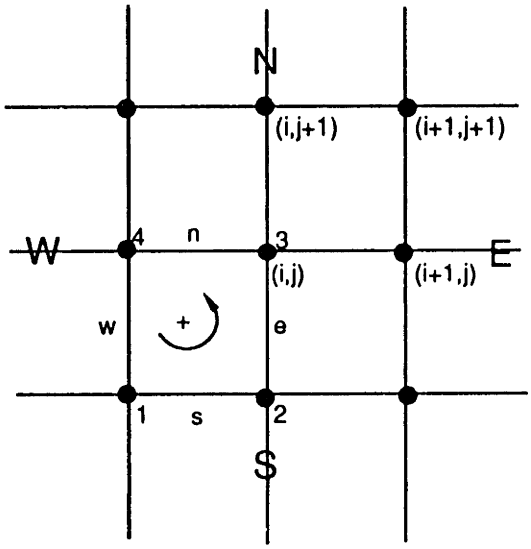

Figure 4-2: A Conservation Super Cell

must follow that,

$$\int\int(\frac{\partial \mathbf{Q_0}}{\partial t} + \frac{\partial \mathbf{F_0}}{\partial x} + \frac{\partial \mathbf{G_0}}{\partial y})dxdy = 0 \tag{4.1}$$

where the integral is satisfied over the super cell. The vectors $\mathbf{Q_0}$, $\mathbf{F_0}$, and $\mathbf{G_0}$ are again defined as,

$$\mathbf{Q_0} = \begin{pmatrix} \rho_0 \\ \rho_0 u_0 \\ \rho_0 v_0 \\ \rho_0 e_0 \end{pmatrix}, \quad \mathbf{F_0} = \begin{pmatrix} \rho_0 u_0 \\ \rho_0 u_0^2 + p_0 \\ \rho_0 u_0 v_0 \\ \rho_0 u_0 h_0 \end{pmatrix}, \quad \mathbf{G_0} = \begin{pmatrix} \rho_0 v_0 \\ \rho_0 u_0 v_0 \\ \rho_0 v_0^2 + p_0 \\ \rho_0 v_0 h_0 \end{pmatrix}.$$

Using the divergence theorem, the area integral is converted into a line integral of the form,

$$\int\int \frac{\partial \mathbf{Q_0}}{\partial t} dxdy + \oint (\mathbf{F_0}, \mathbf{G_0}) \cdot \mathbf{n} ds = 0 \tag{4.2}$$

which is equivalent to,

$$\int\int \frac{\partial \mathbf{Q_0}}{\partial t} dxdy + \oint \mathbf{F_0} dy - \oint \mathbf{G_0} dx = 0. \tag{4.3}$$

The grid is stationary in time, and so the integral Euler equations can be approximated as,

$$A_{i,j} \frac{d\mathbf{Q_0}}{dt} + \sum_{\text{sides}} (\mathbf{F_0} \Delta y - \mathbf{G_0} \Delta x) = 0 \tag{4.4}$$

where $A_{i,j}$ is the total area of the super cell, and Δx and Δy are positive in the counter-clockwise sense. The second term represents the total flux of mass, momentum, and energy through the sides of the super cell.

The area $A_{i,j}$ is computed as a sum of the 4 individual cell areas, and similarly, the total flux is computed as a sum of the 4 individual cell fluxes. So consider a single cell defined by the nodes (1234) in Figure 4-2. The area of the cell is,

$$\text{Area}_{(1234)} = \frac{1}{2} \mathbf{d_1} \times \mathbf{d_2} \tag{4.5}$$

where $\mathbf{d_1}$ is a vector from node 1 to node 3, and $\mathbf{d_2}$ is a vector from node 2 to node 4. This simplifies to,

$$\text{Area}_{(1234)} = \frac{1}{2}[(x_3 - x_1)(y_4 - y_2) - (y_3 - y_1)(x_4 - x_2)]. \tag{4.6}$$

The flux for the cell (1234) is computed at each of the cell faces using an average of the two ends. For example for the e face,

$$\text{Flux}_e = \frac{1}{2}[(\mathbf{F_3} + \mathbf{F_2})(y_3 - y_2) - (\mathbf{G_3} + \mathbf{G_2})(x_3 - x_2)] \tag{4.7}$$

and similarly for the n, w, and s faces, where the subscript number denotes values at that node position and the subscript $_0$ is implied. The total flux for the cell (1234) is

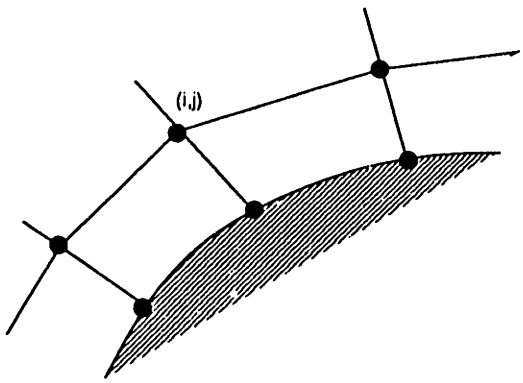

Figure 4-3: Conservation Volume at the Wall and at the Far–Field

then,

$$\text{Flux}_{(1234)} = \text{Flux}_n + \text{Flux}_s + \text{Flux}_e + \text{Flux}_w. \tag{4.8}$$

The areas and the fluxes for the remaining 3 cells of the super cell are computed in a like fashion.

Note that because of internal cancellation of fluxes, the total flux of the super cell in the azimuthal direction is,

$$\text{Total Azimuthal Flux} = \text{Flux}_E + \text{Flux}_W$$

and for the normal direction is,

$$\text{Total Normal Flux} = \text{Flux}_N + \text{Flux}_S$$

where N, S, E, and W faces comprise the two individual cell faces as shown in the Figure 4-2.

At a wall and at the far–field, a super cell is composed of only 2 individual cells as

shown in Figure 4-3, and the total area and the flux are obtained as a sum of the two contributing cells.

4.2.2 Perturbation Aeroacoustic Flow

A semi–discrete approximation to the perturbation Equations 2.29 is,

$$A_{i,j}\frac{d\mathbf{Q}}{dt} + \sum_{\text{sides}}(\mathbf{F}\Delta y - \mathbf{G}\Delta x) - i\omega A_{i,j}\mathbf{Q} = A_{i,j}\mathbf{S} \tag{4.9}$$

where again $A_{i,j}$ is the area and the second term represents the perturbation fluxes. The vectors $\mathbf{Q}$, $\mathbf{F}$, and $\mathbf{G}$ are defined in Section 2.3, and $\mathbf{S}$ is the source term defined in Section 2.3.2. Note that the above equation is similar to the mean Equation 4.4 in structure, and we can adopt the same discretization techniques as in the previous section.

Unlike typical steady mean flow calculations where only the region close to the surface is important, the perturbation acoustic calculation contains the body as well as its surrounding field as the domain of importance; we need to resolve the entire numerical domain. An O–type of grid has its typical mesh size h in the azimuthal direction which grows linearly with the distance from the body, and a grid which maintains a minimum number of node points per relevant length scale may become very large. We have, therefore, implemented here a higher order discretization method in the azimuthal direction which decreases the resolution requirement.

The perturbation Equations 2.29 are discretized using a finite volume operator similar to the one used for the mean flow equations. The flux calculations in the normal direction (the fluxes on the N and S faces for the super cell) are identical to the previous section. The discretization in the azimuthal direction, however, is based on the classical Padé scheme. The Padé scheme can be interpreted as an extrapolation technique of combining different multiples of adjacent fluxes to obtain a higher order approximation.

Define $\text{Flux}^{az}_{i,j}$ as the flux in the azimuthal direction for the super cell in Figure 4-2 obtained by the methods described in the previous section. We can then improve the

accuracy of the flux by summing them *implicitly* as,

$$\frac{1}{6}(\mathrm{Flux}'_{i-1,j} + 4\mathrm{Flux}'_{i,j} + \mathrm{Flux}'_{i+1,j}) = \mathrm{Flux}^{az}_{i,j} \tag{4.10}$$

where $\mathrm{Flux}'_{i,j}$ is the improved azimuthal flux evaluation at node (i,j). This leads to an aperiodic–tridiagonal system of equations in $\mathrm{Flux}'_{i,j}$,

$$\frac{1}{6}\begin{pmatrix} 4 & 1 & & & 1 \\ 1 & 4 & 1 & & \\ & & \ddots & & \\ & & 1 & 4 & 1 \\ 1 & & & 1 & 4 \end{pmatrix}\begin{pmatrix} \mathrm{Flux}'_{1,j} \\ \mathrm{Flux}'_{2,j} \\ \vdots \\ \mathrm{Flux}'_{I-1,j} \\ \mathrm{Flux}'_{I,j} \end{pmatrix} = \begin{pmatrix} \mathrm{Flux}^{az}_{1,j} \\ \mathrm{Flux}^{az}_{2,j} \\ \vdots \\ \mathrm{Flux}^{az}_{I-1,j} \\ \mathrm{Flux}^{az}_{I,j} \end{pmatrix}. \tag{4.11}$$

The inversion of the above matrix system gives the desired higher order flux evaluation.

The Padé scheme is *globally* conservative, and there is no net flux into or out of an azimuthal system of cells. However, the Padé scheme is not locally conservative, and a flux out of one cell is not necessarily the same flux into an adjacent cell; fortunately, conservativeness is not a critical issue here since the governing perturbation equations are linear.

Source Term Discretization

In Section 2.3.2 we discussed the utility of the scattered form of the equations for cases where the complete solution may be split into a known 'incident' and an unknown 'scattered' portions. The scattered form of the equations require less grid resolution at the far field where the scattered quantities are expected to be small, but where the incident quantities are not. By definition the mathematically defined incident wave is equivalent to the physical incident wave at infinity and therefore it must be that,

$$\mathrm{S} \to 0 \quad \text{as} \quad r \to \infty$$

where again,

$$\mathbf{S} = i\omega\mathbf{Q}_i - \frac{\partial}{\partial x}\mathbf{F}_i - \frac{\partial}{\partial y}\mathbf{G}_i. \tag{4.12}$$

We must be, however, careful in numerically determining the source term S so that near the far field S correctly approaches zero. A straightforward discretization of S will not necessarily guarantee the smooth vanishment of S at the far field, because the incident quantity is not small there. Define linear operators L and L_∞ which correspond to the spatial discretization of Equation 4.12 using the local and the far field mean flow values, respectively. Note that by definition,

$$L_\infty \mathbf{Q}_i \equiv 0.$$

A discretization of the source term using local mean flow values is,

$$\mathbf{S} = -L\mathbf{Q}_i.$$

But the above method requires a high grid resolution at the far field, because the operator L must discretize the incident term $\mathbf{Q}_i$ which is large and has gradients which may also be large.

The incident term $\mathbf{Q}_i$ may, however, be 'factored' out of the far field source term if we discretize S as,

$$\begin{aligned} \mathbf{S} &= -L\mathbf{Q}_i \\ &= (L_\infty - L)\mathbf{Q}_i. \end{aligned} \tag{4.13}$$

Here the source term S can be discretized using a grid tailored only for the scattered term, and we would require a correspondingly coarser grid at the far field. This is because $L_\infty \approx L$ at the far field where there are little mean flow variations, and S correctly approaches zero at the far field irregardless of the discretization used.

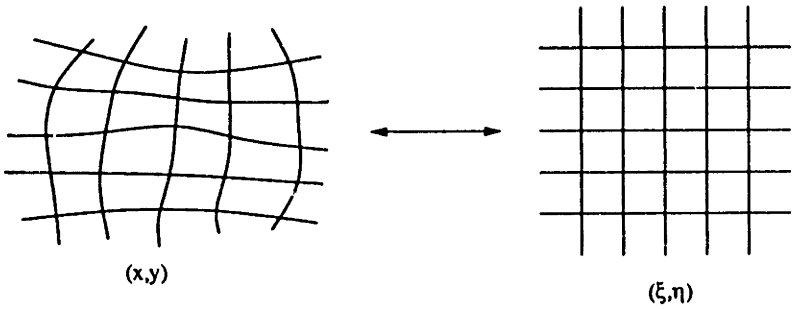

Figure 4-4: Grid Transformation

4.2.3 Numerical Operator Notation

The current spatial techniques are most conveniently expressed in numerical operator form. The physical domain in (x, y) is transformed to the computational domain (ξ, η) such that the computational domain is composed of simple rectangular regions with equal grid spacing, as shown in Figure 4-4 [2, 37].

Define the standard difference operator δ and the averaging operator μ such that,

$$\delta_\xi U_{i+\frac{1}{2},j} = U_{i+1,j} - U_{i,j}$$

$$\mu_\xi U_{i+\frac{1}{2},j} = \frac{1}{2}(U_{i+1,j} + U_{i,j})$$

$$\delta_\eta U_{i,j+\frac{1}{2}} = U_{i,j+1} - U_{i,j}$$

$$\mu_\eta U_{i,j+\frac{1}{2}} = \frac{1}{2}(U_{i,j+1} + U_{i,j}).$$

The semi-discrete form of the method can then be written as,

$$J\frac{d}{dt}\mathbf{Q}_{0ij} + \mu_\eta^2\mu_\xi\delta_\xi\mathbf{F}'_{0ij} + \mu_\xi^2\mu_\eta\delta_\eta\mathbf{G}'_{0ij} = 0 \tag{4.14}$$

for the mean flow solver and,

$$J\frac{d}{dt}\mathbf{Q}_{ij} + \frac{\mu_\eta^2\mu_\xi\delta_\xi}{1+\delta_\xi^2/6}\mathbf{F'}_{ij} + \mu_\xi^2\mu_\eta\delta_\eta\mathbf{G'}_{ij} - i\omega J\mathbf{Q}_{ij} = J\mathbf{S}_{ij} \tag{4.15}$$

for the perturbation aeroacoustic solver. $\Delta\xi$ and $\Delta\eta$ are set to 1, and hence have been omitted. For both equations the second and third terms represent the spatial fluxes in the azimuthal and normal directions of the super cell. The vectors $\mathbf{F'_0}$, $\mathbf{G'_0}$, $\mathbf{F'}$, and $\mathbf{G'}$ are defined as,

$$\mathbf{F'_0} = \mathbf{F}_0 y_\eta - \mathbf{G}_0 x_\eta$$

$$\mathbf{G'_0} = -\mathbf{F}_0 y_\xi + \mathbf{G}_0 x_\xi$$

and

$$\mathbf{F'} = \mathbf{F} y_\eta - \mathbf{G} x_\eta$$

$$\mathbf{G'} = -\mathbf{F} y_\xi + \mathbf{G} x_\xi.$$

J is the determinant of the Jacobian matrix in the coordinate transformation and is equivalent to the area of the super cell,

$$J = x_\xi y_\eta - x_\eta y_\xi.$$

4.3 Numerical Analysis of 1–D Model Equation

An analysis of the current method's consistency and stability is presented. A consistent discrete model of partial differential equations results in a finite amount of truncation error which decays as some power of the mesh size. In the limit the mesh size vanishes, the discrete model becomes equivalent to the continuous equation.

A stable numerical scheme is one for which errors from any source does not grow from one iteration to the next. The stability of our numerical model is important because we are 'pseudo–time marching' our discrete equations to convergence, i.e. until $\frac{\partial}{\partial t}$ term is

suitably small. A consistent numerical scheme is not necessarily stable, and we need to prove that our current scheme is both consistent and stable.

We begin the analysis by examining the truncation errors of the spatial discretizations using Taylor series expansions.

4.3.1 Taylor Series Truncation Error

For simplicity and clarity, consider a one dimensional scalar version of the governing equations,

$$\frac{\partial u}{\partial t} + a\frac{\partial u}{\partial x} - i\omega u = 0 \tag{4.16}$$

with periodic boundary conditions. The above equation is an appropriate model equation for both the mean and the perturbation flows; we merely set $\omega \equiv 0$ for the mean flow examples.

Let the domain be divided into equal Δx segments, the semi-discrete form of Equation 4.16 using Jameson's scheme is then identical to the one obtained using the standard central differencing,

$$\frac{du_j}{dt} + a\frac{\mu_\xi \delta_\xi}{\Delta x} u_j - i\omega u_j = 0 \tag{4.17}$$

and the semi-discrete form for the compact differencing (Padé scheme) is,

$$\frac{du_j}{dt} + \frac{a}{\Delta x}\frac{\mu_\xi \delta_\xi}{1 + \delta_\xi^2/6} u_j - i\omega u_j = 0. \tag{4.18}$$

Expand u in Taylor series about u_j such that,

$$u_{j+1} = u_j + \frac{\partial u}{\partial x_j}\Delta x + \frac{\partial^2 u}{\partial x_j^2}\frac{\Delta x^2}{2} + \cdots$$

$$u_{j-1} = u_j - \frac{\partial u}{\partial x_j}\Delta x + \frac{\partial^2 u}{\partial x_j^2}\frac{\Delta x^2}{2} + \cdots$$

The substitution of the above relations into Equations 4.17 and 4.18 gives,

$$\frac{\partial u_j}{\partial t} + a\frac{\partial u}{\partial x_j} - i\omega u_j = \frac{a\Delta x^2}{6}\frac{\partial^3 u}{\partial x_j^3} + \cdots \tag{4.19}$$

for central differencing and,

$$\frac{du_j}{dt} + a\frac{\partial u}{\partial x_j} - i\omega u_j = \frac{a\Delta x^4}{180}\frac{\partial^5 u}{\partial x_j^5} + \cdots \tag{4.20}$$

for compact differencing. Central differencing has its leading order truncation error which scales as $O(\Delta x^2)$, and compact differencing has its leading order truncation error which scales as $O(\Delta x^4)$. The truncation errors decay uniformly when Δx approaches zero, and thus both schemes are consistent.

If a, $\frac{1}{6}\frac{\partial^3 u}{\partial x^3}$, and $\frac{1}{180}\frac{\partial^5 u}{\partial x^5}$ are all order 1, then for a 1% local error Δx must be ≈ 0.1 for central differencing and Δx must be ≈ 0.3 for compact differencing. The associated resolution requirement is about 10 points per relevant wavelength for central but only about 3 points per relevant wavelength for compact differencing.

4.3.2 Fourier Analysis

The accuracy and stability characteristics of the current scheme have been analyzed by applying the discrete Fourier analysis. The present analysis follows somewhat closely to that of Lele's [43], who has previously conducted a thorough investigation of resolution properties of compact differencing.

Reconsider the model Equation 4.16 and let u be composed of discrete Fourier modes such that,

$$u_j(x,t) = \hat{u}(k,t)e^{ij\theta}$$

where $\theta = k\Delta x$. Substitution into semi-discrete central difference Equation 4.17 yields,

$$\frac{d\hat{u}}{dt} + i[\frac{a\sin\theta}{\Delta x} - \omega]\hat{u} = 0 \tag{4.21}$$

and the same substitution for the compact Equation 4.18 yields,

$$\frac{d\hat{u}}{dt} + i[\frac{a\sin\theta}{\Delta x(1-\frac{2}{3}\sin^2\frac{\theta}{2})} - \omega]\hat{u} = 0. \tag{4.22}$$

The above two equations can be integrated to give,

$$\hat{u}(k,t) = \hat{u}(k,0)\exp[-i(\frac{a\sin\theta}{\Delta x} - \omega)t] \tag{4.23}$$

for central differencing and,

$$\hat{u}(k,t) = \hat{u}(k,0)\exp[-i(\frac{a\sin\theta}{\Delta x(1-\frac{2}{3}\sin^2\frac{\theta}{2})} - \omega)t] \tag{4.24}$$

for compact differencing.

The dispersion relationships are then obtained as,

$$\Omega_{central} = \frac{a\sin\theta}{\Delta x} - \omega \tag{4.25}$$

$$\Omega_{compact} = \frac{a\sin\theta}{\Delta x(1-\frac{2}{3}\sin^2\frac{\theta}{2})} - \omega. \tag{4.26}$$

The analytic dispersion relationship is obtained by substituting the continuous form of Fourier transform in space,

$$u(x,t) = \hat{u}(k,0)e^{ikx}$$

which yields,

$$\frac{d\hat{u}}{dt} + i[ak - \omega]\hat{u} = 0. \tag{4.27}$$

The analytic dispersion relation follows as,

$$\Omega_{analytic} = ak - \omega. \tag{4.28}$$

The true analytic dispersion relationship is a real linear function of k. The discrete

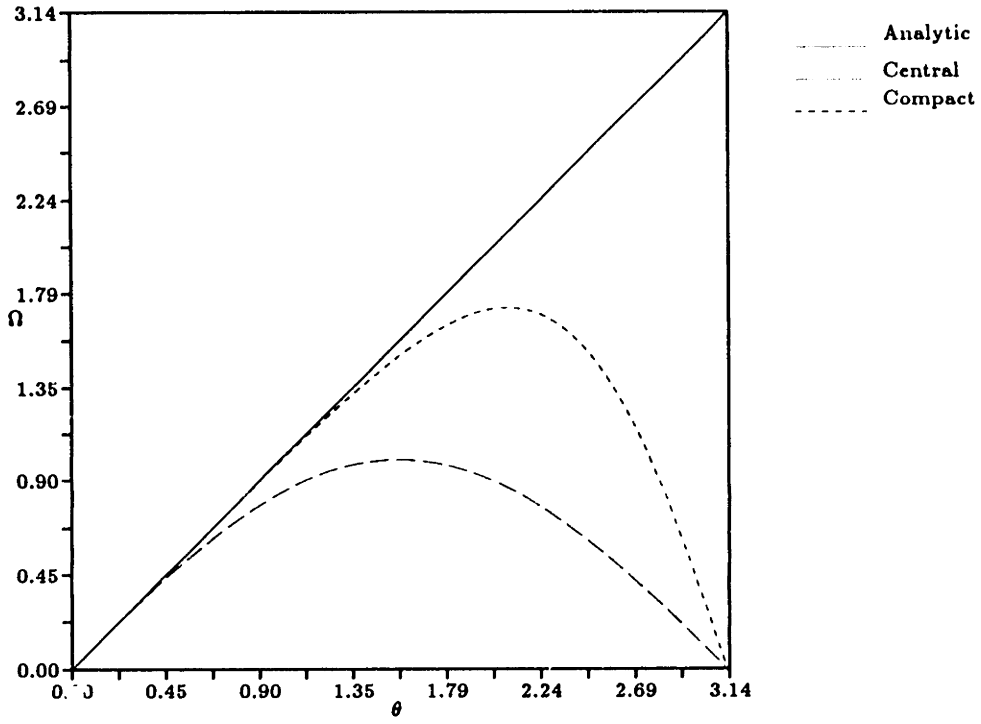

Figure 4-5: Input Wavenumber vs. Output Wavenumber

dispersion relationships are, however, real nonlinear functions of k, and, therefore, both discrete approximations are nondissipative but dispersive.

The exact group velocity is obtained by differentiating Equation 4.28 with respect to k,

$$\frac{\partial \Omega}{\partial k}_{analytic} = a. \tag{4.29}$$

Similarly the group velocities for central and compact differencing are,

$$\frac{\partial \Omega}{\partial k}_{central} = a \cos\theta \tag{4.30}$$

$$\frac{\partial \Omega}{\partial k}_{compact} = \frac{a}{1 - \frac{2}{3}\sin^2\frac{\theta}{2}}(\cos\theta + \frac{\frac{1}{3}\sin^2\theta}{1 - \frac{2}{3}\sin^2\frac{\theta}{2}}). \tag{4.31}$$

The errors in the group velocities make it clear that both finite approximations have introduced phase errors such that modes of varying wavenumbers travel at different

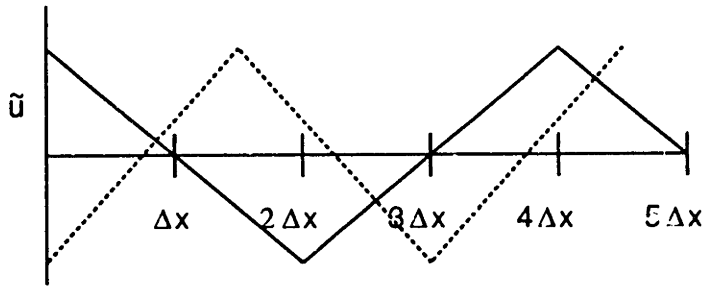

Figure 4-6: 'Saw–toothed' Modes

speeds rather than at the correct speed of a. But when k is fixed and $\Delta x \rightarrow 0$, it must follow that $\theta \rightarrow 0$, and so both $\frac{\partial \Omega}{\partial k}_{central} \rightarrow a$ and $\frac{\delta \Omega}{\partial k}_{compact} \rightarrow a$. As the mesh is refined, the dispersive errors decrease until in the limit the finite group velocities and the analytic group velocity become identical.

The magnitudes of the dispersive errors are illustrated graphically in Figure 4-5. The figure is a plot of Ω versus θ for the Equations 4.25 and 4.26 and Ω versus k for Equation 4.28 with $a = 1$ and $\omega = 0$. The straight line represents the true analytic solution. Notice that central differencing technique begins to exhibit noticeable phase errors at $\theta \approx 0.375$ and compact differencing at $\theta \approx 1.1$. Since $\theta = k\Delta x$ and for a wavelength of 1, $k = 2\pi$, an approximate resolution requirement for central differencing is 17 points and for compact differencing is 6 points per minimum relevant wavelength. This is a somewhat higher requirement than that obtained by Taylor series analysis.

4.3.3 Time Integration and Stability (Von Neumann Analysis)

The stability characteristics of the numerical schemes can be analyzed by examining the previously derived dispersion relationships in Equations 4.25 and 4.26. We require all Fourier modes to be stable, and hence we seek the most unstable modes. For central differencing, the most unstable mode is at $\theta = \frac{\pi}{2}$ which corresponds to $\Omega_{max} = 1$, and similarly for compact differencing, the most unstable mode is at $\theta = \frac{2\pi}{3}$ which

corresponds to $\Omega_{max} = \sqrt{3}$. Wave modes of $\theta = \frac{\pi}{2}$ and $\theta = \frac{2\pi}{3}$ are 'saw-toothed' modes of wavelength $4\Delta x$ and $3\Delta x$, respectively. This is illustrated in Figure 4-6.

The stability of the mean solver is derived from the model Equation 4.16 with $\omega \equiv 0$. The CFL condition states that the numerical domain of influence must be less than or equal to the analytic domain of influence,

$$\Delta t_{CFL} \leq \frac{\Delta x}{a}$$

where Δt is the time step. The mean flow solver uses central differencing, and since $\Omega_{max} = 1$, a necessary condition for stability using a fully explicit time-integration method must scale with the CFL condition,

$$\Delta t \leq \frac{\sigma_i \Delta x}{a} \tag{4.32}$$

where $[-i\sigma_i, i\sigma_i]$ is the portion of the imaginary axis in the stable region for the time integration method.

The stability of the perturbation solver is also similarly derived from the model Equation 4.16 but with $\omega \neq 0$. The perturbation solver uses both types of differencing, and since Ω_{max}'s are different amongst them, they have different time step limitations. For a fully explicit central differencing scheme the stability requirement is,

$$\Delta t \leq \frac{\sigma_i}{\frac{a}{\Delta x} + \omega} \tag{4.33}$$

and the time step limit for a fully explicit compact scheme is,

$$\Delta t \leq \frac{\sigma_i}{\frac{a\sqrt{3}}{\Delta x} + \omega}. \tag{4.34}$$

Notice that when ω is small, central differencing allows larger time steps to be used than compact differencing, but when ω is large the two schemes have similar time step values. The use of compact differencing is most efficient for the high frequency cases.

A fully discrete form of the above equation using a four stage explicit Runge–Kutta method then follows as,

$$\hat{u}^0 = \hat{u}^n \tag{4.35}$$

$$\hat{u}^k - \hat{u}^0 = -\alpha_k \Delta t \hat{R}^{k-1}, \quad k = 1, 4$$

$$\hat{u}^{n+1} = \hat{u}^4$$

where $\alpha_1 = 1/4$, $\alpha_2 = 1/3$, $\alpha_3 = 1/2$, $\alpha_4 = 1$,

$$\hat{R}^k = i(\gamma + \omega)\hat{u}^k.$$

Define now the amplification factor G,

$$G = \frac{\hat{u}^{n+1}}{\hat{u}^n} \tag{4.36}$$

and we require $|G| \leq 1$ for stability. For the explicit Runge–Kutta scheme G is,

$$G = 1 - \frac{1}{2}(D + \Gamma)^2 + \frac{1}{24}(D + \Gamma)^4 + i[\frac{1}{6}(D + \Gamma)^3 - (D + \Gamma)] \tag{4.37}$$

where

$$D = \omega \Delta t, \quad \Gamma = \gamma \Delta t.$$

A corresponding contour of $|G| \leq 1$ is shown in Figure 4-7.

We require all Fourier modes to be stable, and so we use the most unstable modes derived in the previous section to compute the time step constraints as,

$$\Delta t \leq \frac{2\sqrt{2}}{\frac{a}{\Delta x} + \omega} \tag{4.38}$$

for central differencing and,

$$\Delta t \leq \frac{2\sqrt{2}}{\frac{a\sqrt{3}}{\Delta x} + \omega} \tag{4.39}$$

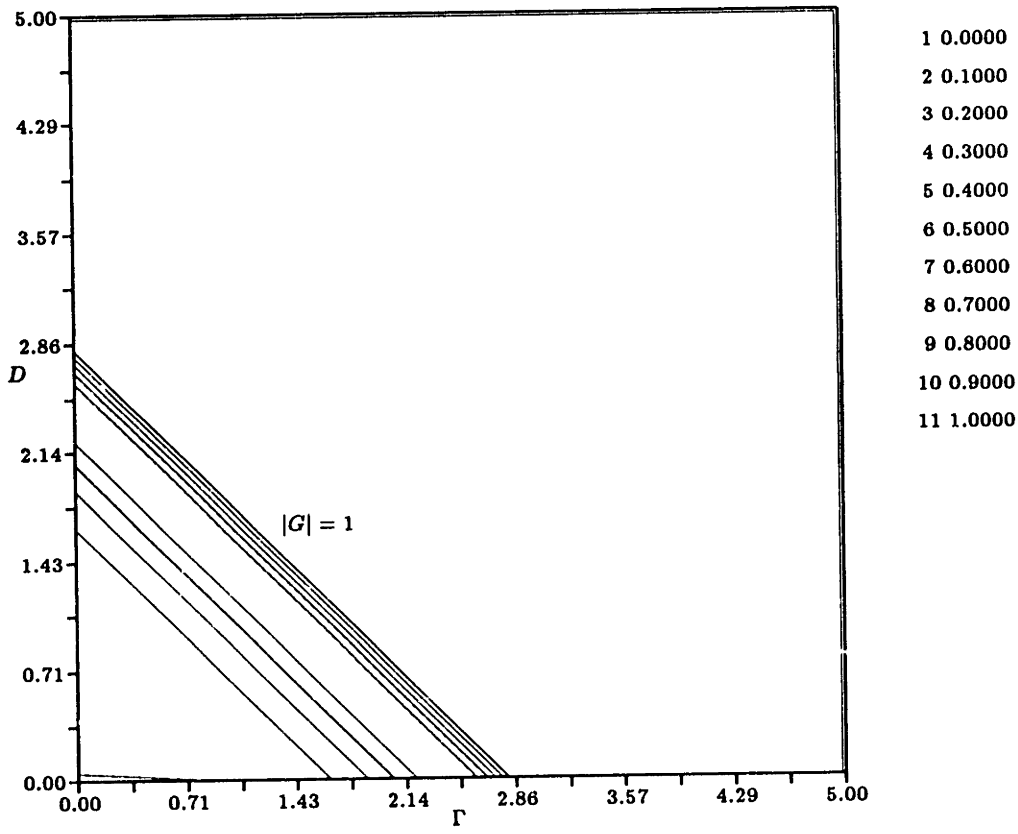

Figure 4-7: Contours of $|G| \leq 1$ for a Fully Explicit Runge–Kutta Scheme

for compact differencing. In the limit $\omega \to \infty$, the time step restriction becomes,

$$\Delta t \leq \frac{2\sqrt{2}}{\omega}$$

for both differencing techniques, and so the explicit Runge–Kutta scheme is stiff when ω is large.

The time step constraint for the mean flow solver is obtained by setting $\omega \equiv 0$ in the amplification Equation 4.37. The amplification factor then becomes,

$$G = 1 - \frac{1}{2}\Gamma^2 + \frac{1}{24}\Gamma^4 + i(\frac{1}{6}\Gamma^3 - \Gamma). \tag{4.40}$$

$|G|$ is ≤ 1 if $\Gamma \leq 2\sqrt{2}$ and so for central differencing,

$$\Delta t \leq \frac{2\sqrt{2}\Delta x}{a}. \tag{4.41}$$

4.4 Nonuniform Grid

The one dimensional uniform grid analysis has shown that the numerical method is consistent and stable when the time step is within the specified constraint. The analysis also showed that the numerical method is nondissipative, and given a resolution of about 6 points per wavelength for compact differencing and about 17 points per wavelength for central differencing, the numerical method is also nearly nondispersive.

We are using a body-fitted coordinate system, and the grid may be distorted and nonuniform near a body, but at least 2 or 3 chord lengths away from the body, the grid should be smooth and nearly uniform. In such regions the previous one dimensional analysis is directly applicable, and a grid which guarantees the just defined resolution requirement should be accurate in both amplitude and phase.

However, while the body-fitted coordinate system allows easy boundary condition implementation, it also implies that the grid near the body may be nonuniform. The accuracy of both central and compact differencing for a nonuniform mesh can be better understood by analyzing the Taylor series truncation error of $\frac{\partial u}{\partial x}$ on a variable grid. Let Δx and r_x be defined such that,

$$\Delta x = x_j - x_{j-1}$$

$$r_x = \frac{x_{j+1} - x_j}{x_j - x_{j-1}}.$$

Then it is shown in Reference [23] that for central differencing,

$$\frac{\partial u}{\partial x_j} = \mu_\xi \delta_\xi \left(\frac{u_j}{x_j}\right) + \text{TE} \tag{4.42}$$

where

$$\mathrm{TE} = -\frac{r_x - 1}{2}\Delta x \frac{\partial^2 u}{\partial x_j^2} - \frac{(1 + r_x)^2}{24}\Delta x^2 \frac{\partial^3 F}{\partial x_j^3} + \cdots$$

For compact differencing,

$$\frac{\partial u}{\partial x_j} = \frac{\mu_\xi \delta_\xi (u_j / x_j)}{1 + \delta_\xi^2 / 6} + \mathrm{TE} \tag{4.43}$$

where

$$\mathrm{TE} = -\frac{r_x - 1}{3}\Delta x \frac{\partial^2 u}{\partial x_j^2} - \frac{(r_x - 1)^2}{24}\Delta x^2 \frac{\partial^3 u}{\partial x_j^3} + \Theta[(r_x - 1)^3 \Delta x^3]\frac{\partial^4 u}{\partial x_j^4} + O(\Delta x^4) + \cdots$$

The accuracy of the schemes are functions of the grid uniformity, and both schemes are only of $O(\Delta x)$ given an arbitrary grid. The accuracy increases to $O(\Delta x^2)$ for both schemes when $r_x = 1 + O(\Delta x)$, and compact differencing reaches its peak accuracy of $O(\Delta x^4)$ when $r_x = 1 + O(\Delta x^3)$. Unfortunately, a grid near a typical body shape would only be approximately $r_x = 1 + O(\Delta x)$ or at best $r_x = 1 + O(\Delta x^2)$, which translates to a peak accuracy in the azimuthal direction of $O(\Delta x^3)$. When $r_x = 1 + O(\Delta x)$ the truncation error of compact differencing is approximately $\frac{2}{3}$ of that for central differencing.

Note that for an arbitrary grid the leading order error terms scale as $\frac{\partial^2 u}{\partial x^2}$, and therefore, both schemes are dissipative. Note also that the leading order dispersive term $\frac{\partial^3 u}{\partial x^3}$ will be larger for a stretched grid because the associated coefficients will be greater.

Actual amount of truncation error depends upon the grid size and higher order derivatives, but it is usually safe to assume that we need to increase the grid density near the surface of a highly contoured mesh. Fortunately, when the wavelength and chord length are about the same and given an O–type of mesh, a grid which has 6 points per wavelength at a far–field of 10 chords usually has more than 100 points per wavelength near the body. An $O(\Delta x)$ accurate scheme requires about 100 points per wavelength for 1% accuracy, and so such a grid should be able to resolve most of the physically relevant length scales everywhere in the flow field.

4.5 Filtering

The truncation error analysis has shown that the current method is dispersive, and that in regions which has high flow gradients (where $\frac{\partial^3 u}{\partial x^3}$ term is large) or in regions which has small length scales (where Δx is relatively large) the numerical method can generate unphysical wave modes. These unwanted wave modes are most typically created near a sharply contoured body where both the flow gradients and the relative grid sizes are large, but they may also be generated elsewhere by far field reflections or even by numerical round-off errors. The most dominant unstable modes are the 'saw-toothed' modes shown in Figure 4-6.

The one dimensional Fourier analysis has illustrated that the discrete forms of the dispersion relations from Equations 4.26 and 4.25 are purely real. This is, in general, a desirable quality of the spatial discretization since it implies that the traveling wave form preserves its amplitude, but it also implies that, once generated, the numerical scheme is incapable of eliminating the unwanted wave modes. Thus the current spatial discretization techniques admit oscillatory solutions which are not solutions of the true analytic equation. Some dissipation, therefore, must be present in the discretization to dampen the unwanted wave modes. The goal of the filtering scheme is thus to efficiently annihilate those modes which are not realizable by the discretization technique while undisturbing the physically relevant modes.

The mean flow finite volume scheme is augmented with explicit fourth order dissipation in both azimuthal ξ and normal η directions. The perturbation flow finite volume scheme uses explicit sixth order dissipation in the ξ direction and fourth order dissipation in the η direction. The fourth order differences are described in References [37, 63], and the sixth order differences are an extension of the fourth order differences.

The governing equations are then modified by added dissipative terms $\mathbf{D_0}$ and $\mathbf{D}$ such that,

$$J\frac{d}{dt}\mathbf{Q_0}_{ij} + \mu_\eta^2\mu_\xi\delta_\xi\mathbf{F'_0}_{ij} + \mu_\xi^2\mu_\eta\delta_\eta\mathbf{G'_0}_{ij} = \mathbf{D_0}_{ij} \tag{4.44}$$

for the mean flow and,

$$J\frac{d}{dt}\mathbf{Q}_{ij} + \frac{\mu_\eta^2 \mu_\xi \delta_\xi}{1+\delta_\xi^2/6}\mathbf{F'}_{ij} + \mu_\xi^2 \mu_\eta \delta_\eta \mathbf{G'}_{ij} - i\omega J\mathbf{Q}_{ij} = \mathbf{D}_{ij} + J\mathbf{S}_{ij} \tag{4.45}$$

for the perturbation flow. The dissipation terms $\mathbf{D_0}$ and $\mathbf{D}$ are defined as,

$$\mathbf{D}_{0ij} = -\nu_4 \delta_\xi (\frac{J}{\Delta \bar{t}} \delta_\xi^3)\mathbf{Q}_{0ij} - \nu_4 \delta_\eta (\frac{J}{\Delta \bar{t}} \delta_\eta^3)\mathbf{Q}_{0ij} \tag{4.46}$$

$$\mathbf{D}_{ij} = \nu_6 \delta_\xi (\frac{J}{\Delta \bar{t}} \delta_\xi^5)\mathbf{Q}_{ij} - \nu_4 \delta_\eta (\frac{J}{\Delta \bar{t}} \delta_\eta^3)\mathbf{Q}_{ij}. \tag{4.47}$$

In the above equations, ν_4 and ν_6 are the fourth and the sixth difference dissipation coefficients, J is again the cell area, and $\bar{t}$ is the time step when the CFL number is 1. The inclusion of the cell area J is necessary so that the amount of added dissipation does not scale with the area of the cell. Similarly, the scaling term $\bar{t}$ assures that the artificial viscosity is independent of the CFL number.

The fourth order dissipation terms in the mean flow solver and in the η direction of the perturbation solver scale as Δx^3, and the sixth order dissipation term in the ξ direction perturbation solver scales as Δx^5. Thus the second order accuracy is assured for the mean flow solver and η direction perturbation solver, and similarly, fourth order accuracy is formally preserved in ξ direction perturbation solver. The numerical schemes, nevertheless, may still be overly dissipative in coarse grid regions, and hence it is important to minimize the dissipation coefficients ν_4 and ν_6 to preserve the accuracy. It is also important to minimize the dissipation so that it does not affect the inviscid time step limits. For all numerical cases, ν_4 was between 0.008 and 0.01, and ν_6 was between 0.0008 and 0.001.

4.6 Time Integration

For the current two-dimensional system of equations with dissipation, the time integration is computed as follows,

$$\mathbf{Q}_{ij}^0 = \mathbf{Q}_{ij}^n \tag{4.48}$$

$$\mathbf{Q}_{ij}^1 - \mathbf{Q}_{ij}^0 = -\alpha_1 \frac{\Delta t_{ij}}{J}(\mathbf{R}_{ij}^0 - \mathbf{D}_{ij}^0)$$

$$\mathbf{Q}_{ij}^2 - \mathbf{Q}_{ij}^0 = -\alpha_2 \frac{\Delta t_{ij}}{J}(\mathbf{R}_{ij}^1 - \mathbf{D}_{ij}^0)$$

$$\mathbf{Q}_{ij}^3 - \mathbf{Q}_{ij}^0 = -\alpha_3 \frac{\Delta t_{ij}}{J}(\mathbf{R}_{ij}^2 - \mathbf{D}_{ij}^0)$$

$$\mathbf{Q}_{ij}^4 - \mathbf{Q}_{ij}^0 = -\alpha_4 \frac{\Delta t_{ij}}{J}(\mathbf{R}_{ij}^3 - \mathbf{D}_{ij}^0)$$

$$\mathbf{Q}_{ij}^{n+1} = \mathbf{Q}_{ij}^4$$

$$\alpha_1 = \frac{1}{4}, \quad \alpha_2 = \frac{1}{3}, \quad \alpha_3 = \frac{1}{2}, \quad \alpha_4 = 1$$

where for the mean flow solver,

$$\mathbf{R}_{ij}^k = \mu_\eta^2 \mu_\xi \delta_\xi \mathbf{F}'_{0ij} + \mu_\xi^2 \mu_\eta \delta_\eta \mathbf{G}'_{0ij}$$

and subscript $_0$ is implied. For the perturbation solver,

$$\mathbf{R}_{ij}^k = \frac{\mu_\eta^2 \mu_\xi \delta_\xi}{1 + \delta_\xi^2/6} \mathbf{F}'^k_{ij} + \mu_\xi^2 \mu_\eta \delta_\eta \mathbf{G}'^k_{ij} - i\omega J \mathbf{Q}_{ij}^k - J\mathbf{S}_{ij}^k.$$

A single evaluation of the dissipative terms is required at the initial stage of the temporal integration. This is to reduce the operation count for the scheme.

The time step limit for the current two-dimensional system of equations is computed by computing the spectral radii of the linearized coefficient matrices **A** and **B** shown in Section 3.2.1. For the current scheme a conservative estimate of the time step criterion

is computed as,

$$\Delta t_{ij} \leq \frac{\sigma_i J}{|q| + |r| + c_0 \chi_0} \tag{4.49}$$

for the mean flow solver and,

$$\Delta t_{ij} \leq \frac{\sigma_i J}{\sqrt{3}|q| + |r| + c_0 \chi + J\omega} \tag{4.50}$$

for the perturbation flow solver. The variables q, r, χ_0, and χ are defined as,

$$\chi_0 = \sqrt{x_\eta^2 + y_\eta^2 + x_\xi^2 + y_\xi^2 + 2|x_\eta x_\xi + y_\eta y_\xi|}$$

$$\chi = \sqrt{3x_\eta^2 + 3y_\eta^2 + x_\xi^2 + y_\xi^2 + 2\sqrt{3}|x_\eta x_\xi + y_\eta y_\xi|}$$

$$q = u_0 y_\eta - v_0 x_\eta$$

$$r = -u_0 y_\xi + v_0 x_\xi$$

and c_0 is the local speed of sound.

We seek here the steady state solution to the governing equations, and hence each node is integrated in time using the maximum time step allowed by the stability limit, i.e. at $\sigma_i = 2\sqrt{2}$. Each node is integrated with the same CFL number but with different time steps.

4.7 Summary

Numerical techniques for the steady base mean flow and the linear perturbation flow were presented.

The finite-volume, node-based schemes are based upon the integral form of the governing equations and are second order accurate for the mean flow solver and second/fourth order accurate for the perturbation solver.

The truncation error and the Fourier analysis has shown that the numerical methods are consistent and have leading order error terms which are dispersive but nondissipative

for an uniform grid.

The time–stability is assured when the time step limits are within the restriction of the Von Neumann amplification analysis.

A fourth/sixth order dissipation terms are added to the numerical methods to filter the artificially generated high wavenumber disturbances. The dissipation terms are computed such that the formal accuracy of the discretization schemes are maintained.

Chapter 5

Sound Radiation from Gust–Airfoil Interaction

When a body convects in a nonuniform flow sound is generated as a result of interactions between the unsteadiness in the flow and the body. This noise generation mechanism is common to many aerospace components such as wings and propellers and may be due to a variety of sources like atmospheric turbulence, inlet distortions, and rotor–stator interactions. Noise generated by such mechanisms often tend to be loud and are important sources of sound. In this chapter, we will investigate the sound generation properties from one such unsteady process.

Consider an airfoil in a steady flow which encounters an unsteady 'gust'. We model the gust as a velocity perturbation in the y direction. In a reference frame fixed to the airfoil such a gust is a transverse velocity defect which convects with the local mean flow, and although a gust can be of any arbitrary function in time and space, for simplicity we limit the scope of the research to an incoming sinusoidal gust only,

$$v' = e^{i(kx-\omega t)} \tag{5.1}$$

where

$$k = \frac{\omega}{u_0}$$

and u_0 is the free stream velocity. Note that within the framework of linearity, a general vortical disturbance can always be thought of composed as a sum of multiple Fourier modes and hence no generality is lost in the single frequency assumption.

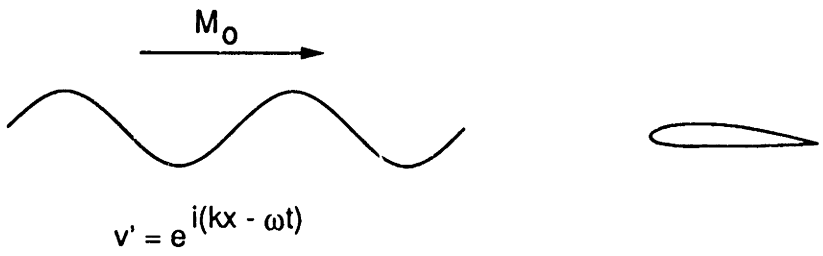

Figure 5-1: Incident Sinusoidal Gust on an Airfoil

The wall boundary conditions are that the total normal velocity on the airfoil is zero, and since the surface is stationary the boundary condition is as in Equation 3.6,

$$\tilde{\mathbf{u}}_s \cdot \mathbf{n_0} = -\tilde{\mathbf{u}}_i \cdot \mathbf{n_0} \tag{5.2}$$

where

$$\tilde{\mathbf{u}}_i = e^{ikx}\mathbf{j}$$

and $\mathbf{j}$ is the unit vector in the transverse y direction.

The boundary condition on the wall is such that it exactly cancels the incoming vortical disturbance, and the total normal velocity on the wall is zero. This condition is equivalent to the plate with camber oscillating, and so the current study is closely related to that of sound produced by a cambered airfoil in unsteady motion. Such unsteady airfoil undulations necessitate a continuous shedding of vorticity into a wake with the implementation of the Kutta condition at the trailing edge. The vorticity sheet, in turn, influences the velocity field on the body, and so the radiated sound is strongly affected by the trailing wake. For an accurate numerical solver it is important to resolve both the acoustic field as well as the vortical wake.

5.1 The Aerodynamic Problem

Before we embark on the numerical study, it is useful to first consider the mathematics for the flat plate problem which may illuminate some insights and identify some key parameters.

The linearized Euler equations in a uniform flow can be represented by an equivalent convective form of the wave equation in the perturbation velocity potential ϕ,

$$\phi_{tt} + 2u_0\phi_{xt} - (c_0^2 - u_0^2)\phi_{xx} - c_0^2\phi_{yy} = 0 \tag{5.3}$$

where $u' = \phi_x$ and $v' = \phi_y$.

Following the substitutions presented in References [6, 7], we introduce the succeeding transformations for both dependent and independent variables, $(x, y, t, \phi) \leftrightarrow (\xi, \eta, t, \Phi)$,

$$\xi = x, \ \eta = \beta y$$

$$\Phi(\xi, \eta, t) = \phi(x, y)e^{-i(\omega t + M_0 K x)}$$

where,

$$\beta = \sqrt{1 - M_0^2}$$

$$K = \frac{\nu M_0}{\beta^2}$$

and $\nu = \frac{\omega a}{2u_\infty}$ is the reduced frequency, where a is the characteristic length. We then arrive at,

$$(\tilde{\nabla}^2 + K^2)\Phi = 0 \tag{5.4}$$

with the boundary conditions,

$$\frac{\partial \Phi}{\partial \eta} = -\frac{1}{\beta}e^{-i\nu/\beta^2} \tag{5.5}$$

along the body, $-a/2 < \xi < a/2$ and,

$$\Delta\Phi = (\Delta\Phi)_{t.e.} e^{-i\nu/\beta^2} \tag{5.6}$$

along the wake, $\xi > a/2$. $\tilde{\nabla}$ is the Laplacian operator computed in the (ξ, η) domain, and $\Delta\Phi$ represents the jump of Φ across the wakeline. The latter boundary condition results from the continuity of pressure in the wake.

The Helmholtz Equation 5.4 can be solved using the Green's theorem,

$$\Phi(\xi,\eta) = \frac{1}{2\pi} \oint (\Phi \frac{\partial G}{\partial \eta'} - G \frac{\partial \Phi}{\partial \eta'}) d\xi'. \tag{5.7}$$

The integration is over both the body and the wake. The free space Green's function for Equation 5.4 is

$$G(r) = i\frac{\pi}{2} H_0^{(1)}(Kr) \tag{5.8}$$

where $r = \sqrt{(\xi - \xi')^2 + (\eta - \eta')^2}$ and $H_0^{(1)}$ is the Hankel function of the first kind zeroth order. An exact solution to Equation 5.7 requires the enforcement of boundary conditions, but even without such a statement, the nature of the general solution illustrates that the parameter K plays an important role. K is actually a nondimensional parameter based on the ratio of expected length scales. An acoustic length scale is based on the acoustic wavelength,

$$L_{acou} = \bar{\lambda} = \frac{2\pi c}{\omega} \tag{5.9}$$

where c is the speed of sound and $\bar{\lambda}$ is an average acoustic wavelength in the domain. The convection length scale is dependent on the geometry of the case, and for now, define it to be a,

$$L_{conv} = a. \tag{5.10}$$

K can then be cast as a simple multiple of the ratio $\frac{L_{conv}}{L_{acou}}$,

$$K = \frac{\nu M_0}{\beta^2} = \frac{\pi}{\beta^2} \frac{L_{conv}}{L_{acou}} = \frac{\pi}{\beta^2} \frac{a}{\bar{\lambda}}. \tag{5.11}$$

A flat plate in a gust has the second term in the integral Equation 5.7 equal to zero, and the flat plate can be thought of as a distribution of simple dipoles. At a given point, the sound heard from such collection of dipoles is a function of compressibility and the 'compactness' of the source.

In compressible flows with finite phase speeds, the concept of 'compactness' is an important issue. A compact source is one in which the acoustic length scale is much longer than the body such that an observer 'hears' the distribution of sources in phase, and there are little or no retarded time differences. The differences in 'firing' time $\Delta(t - r/c_0)$ are small such that all the sources can be thought to be grouped as a single dipole firing in phase.

In contrast, a noncompact source is one in which the acoustic length scale is much shorter than the body such that an observer 'hears' the distribution of sources out of phase; he 'hears' the sources closest to him first, and there are large retarded time differences between the sources. In such cases, instead of radiation from a simple dipole we expect a more complicated acoustic field due to a distribution of dipoles over the chord with large differences in phase.

K is a measure of the compactness of the acoustic source. When K is small, it must follow that $L_{conv} \ll L_{acou}$ and the body is essentially compact. Conversely when K is large, $L_{conv} \gg L_{acou}$ and the body is no longer compact.

Note that in an unsteady flow, the condition $M_0 \ll 1$ is not sufficient to guarantee an incompressible flow. We need to require that the acoustic length scale is much longer than the flow length scale, i.e. we need to assure that the source is compact, and so the correct parameterization is $M_0 \ll 1$ *and* $K \ll 1$.

5.2 Validation

We begin the numerical analysis by first considering a set of three numerical calculations for which there exists an analytic or an asymptotic expansion solution. For historical reasons we start the analysis with a flat plate in incompressible gust.

5.2.1 Incompressible Flow

Consider a flat plate in an incompressible flow which encounters a sinusoidal vorticity field of the form in Equation 5.1. We seek to compute the time-harmonic response of the plate and its surrounding fluid perturbed by the incoming vortical gust. The steady base mean flow was computed first, and the following parameters were used:

- Geometry: NACA0001
- Grid: 300×150
- M_0: 0.1
- α: 0.0
- Far Field Radius: 10 chords
- ν_4: 0.01
- Iterations: 500
- $L_2(\delta\rho)$: 1.3×10^{-4}

M_0 is the free stream Mach number, α is the angle of attack, and ν_4 is the dissipation coefficient for the fourth order artificial viscosity. $L_2(\delta\rho)$ is the L_2 norm of the difference in density and is equivalent to the root mean square of the density residual. The residual is normalized such that the first iteration difference is set to 1. The calculation required 500 iterations for 5 orders of magnitude convergence in density.

The Mach number was purposely chosen to be small so that the simulation would closely resemble an incompressible flow, and a NACA0001 airfoil section was used to model a flat plate.

The mean flow solution was used as an input to the perturbation solver on an identical grid with the same base Mach number. The run time perturbation parameters were as follows:

- ω: 0.01
- Iterations: 9000
- ν_4: 0.01
- ν_6: 0.001
- $L_2(\delta\tilde{\rho})$: 1.5×10^{-4}

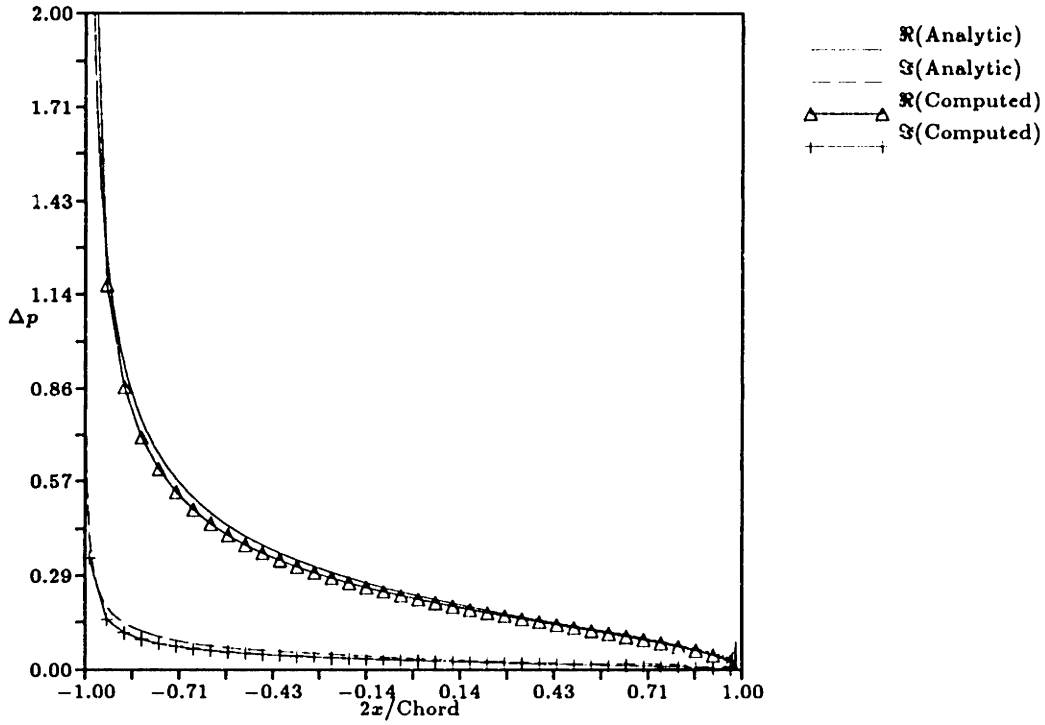

Figure 5-2: $\Delta\tilde{p}$ on the Flat Plate in Incompressible Flow

ν_6 is the dissipation coefficient for the sixth order artificial viscosity in the azimuthal direction. The computation required 9000 iterations for 4 orders of magnitude convergence in density amplitude.

$\omega = 0.01$ corresponds to a reduced frequency, $\nu = 0.0425$ and a wavelength of 743 chords. Within a domain of 10 chords the computed solution should correspond closely to that of an incompressible approximation. Figure 5-2 shows a plot of the difference in the upper and the lower surface pressures, $\Delta\tilde{p}$, along the flat plate. The lines represent the real and imaginary parts of exact $\Delta\tilde{p}$ which is given in Reference [13], and the symbols represent the corresponding computed solutions. The accuracy is good and uniform even at the leading edge where there is a singularity. In terms of the total lift, the analytic solution is $|\tilde{L}| = 0.3448$ and $\arg(\tilde{L}) = 7.3°$ and the computed solution is $|\tilde{L}| = 0.3496$ and $\arg(\tilde{L}) = 8.7°$. The error is approximately 1.4% in amplitude and approximately 1.4° in phase. It appears that the methodology is accurate in predicting

the unsteady pressure values and the vorticity shedding process.

The computation required 174 minutes of cpu time on a Cray X–MP for convergence. The time required was large but expected since the Mach number was so low. A low Mach number case is inefficient when integrated by a compressible solver, because the vorticity and acoustic waves travel at very different rates, and the solver must integrate in a CFL limit sense to accommodate the slower moving wave.

5.2.2 Compressible Compact Gust

We now consider a flat plate in compressible flow which encounters a compact gust of the form in Equation 5.1. The compactness is defined as per Amiet in Reference [3] such that when $K \leq 1$ the gust is assumed compact. For the current case $K = 0.5$. The base mean flow was computed first and the numerical parameters were as follows:

- Geometry: NACA0001
- Grid: 200×100
- M_0: 0.5
- α: 0.0
- Far Field Radius: approximately 4 wavelengths
- ν_4: 0.01
- Iterations: 400
- $L_2(\delta\rho)$: 1.8×10^{-4}

The calculation required 400 iterations for 4 orders of magnitude convergence.

The mean flow values were used as an input to the perturbation solver and the acoustic parameters were as follows:

- ω: 0.8875
- Iterations: 1500
- ν_4: 0.01
- ν_6: 0.001
- $L_2(\delta\tilde{\rho})$: 3.2×10^{-3}

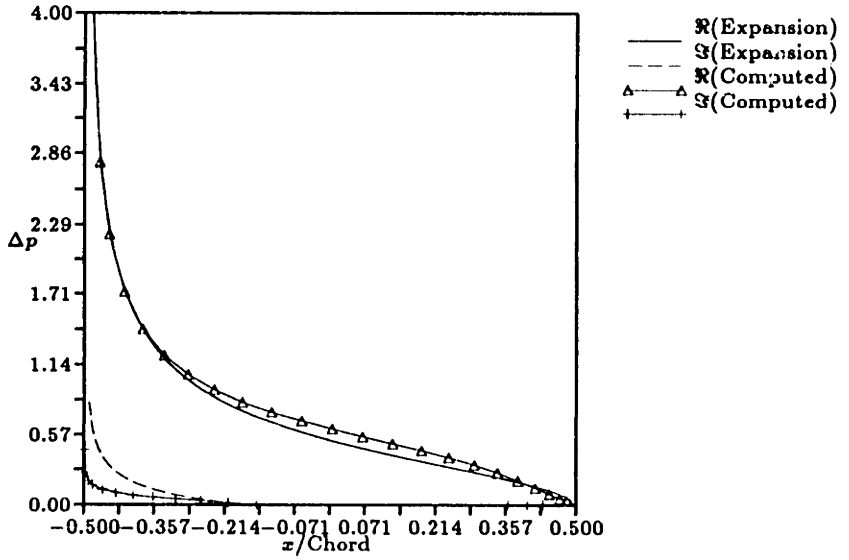

Figure 5-3: $\Delta\tilde{p}$ on the Flat Plate for a Compact Gust

The calculation required 1500 iterations for about 3 order of magnitude convergence.

Amiet [3] has provided an expansion solution for the compact case as an extension to the incompressible theory of Sears [67]. The pressure difference Δp along the flat plate is given as,

$$\Delta p = 2\frac{\rho_0}{\beta}U_0\sqrt{\frac{(a/2)-x}{(a/2)+x}}\,S(\nu^*)e^{-i\nu^* M_0^2 x}e^{-i\nu^* f(M_0)} \tag{5.12}$$

where

$$\nu^* = \nu/\beta^2$$

$$f(M_0) = (1-\beta)\ln M_0 + \beta\ln(1+\beta) - \ln 2 \tag{5.13}$$

and S is the Sears function defined in Reference [67],

$$S(\sigma) = \frac{1}{-i\sigma[K_0(-i\sigma) + K_1(-i\sigma)]}. \tag{5.14}$$

K_0 and K_1 are modified Bessel functions. The associated lift on the flat plate is [3],

$$\tilde{L}_e = -2\pi\frac{\rho_0}{\beta}\frac{U_0 a}{2}S(\nu^*)[J_0(M_0K) + iJ_1(M_0K)] \tag{5.15}$$

where J_0 and J_1 are Bessel functions of order 0 and 1, respectively.

Figure 5-3 compares the computed values of Δp versus the expansion of Amiet. The symbols represent the computed solution and the lines represent the Amiet's approximation. The agreement is quite close, except perhaps the imaginary portion of the solution at the leading edge. In terms of the lift the computed solution was $|\tilde{L}_c| = 0.84336$, $\arg\tilde{L}_c = 1.2698°$ and the Amiet solution is $|\tilde{L}_e| = 0.83899$, $\arg\tilde{L}_e = 2.3685°$. The difference is about 0.6% in amplitude and 1.1° in phase. It seems the numerical solution is accurate in the near field.

Once the pressure distribution on the flat plate is known then we can use the Green's theorem to compute for the pressure values everywhere else in the flow field,

$$\tilde{p}(x,y) = \frac{1}{2\pi}\int_{-a/2}^{a/2}\Delta p\frac{\partial G}{\partial y}dx \tag{5.16}$$

where the Green's function is defined in Equation 5.8. The above integral can be simplified by expanding it in inverse powers of r as shown in Reference [6],

$$\tilde{p}(x,y) = F(\alpha_0)\beta\sqrt{\frac{K}{8\pi}}\frac{e^{-i\pi/4}}{\sqrt{r}}\frac{\sin\theta}{(1-M_0^2\sin^2\theta)^{3/4}}e^{-ir[K(1-M_0^2\sin^2\theta)^{1/2}-M_0K\cos\theta]}+O(r^{-3/2}) \tag{5.17}$$

where

$$F(\alpha_0) = \int_{-a/2}^{a/2}\Delta p e^{-i\alpha_0 x}dx$$

and

$$\alpha_0 = K\frac{\cos\theta}{\sqrt{1-M_0^2\sin^2\theta}} - M_0K$$

$$\theta = \arctan\frac{y}{x}.$$

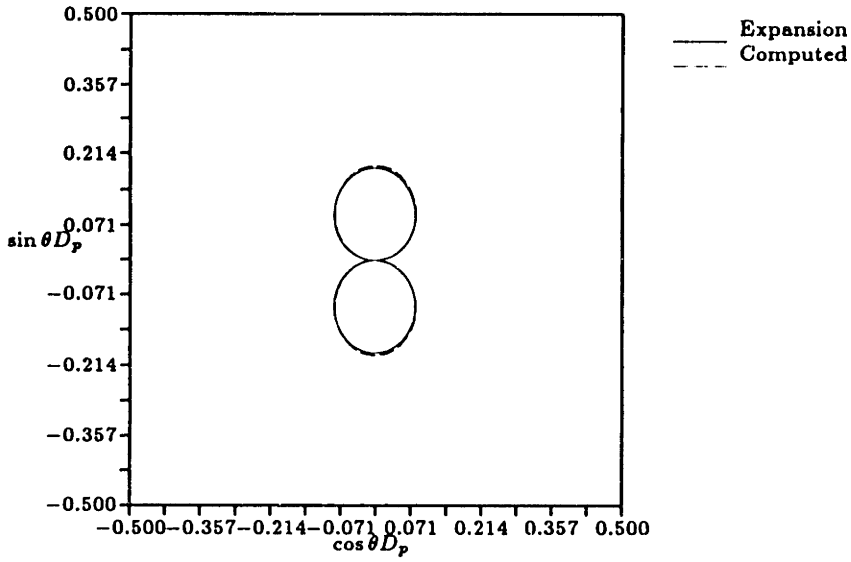

Figure 5-4: Polar Plot of D_p at the Far Field for a Compressible Compact Gust

We have compared the computed solution at the far field with the above asymptotic approximation to insure that the numerical method does not admit large reflections. Figure 5-4 shows the polar directivity D_p of the two methods. D_p is the amplitude of acoustic pressure scaled by $\sqrt{r}$,

$$D_p = \sqrt{r}|\tilde{p}|. \tag{5.18}$$

The continuous line is the expansion of Equation 5.17 and the broken line is the numerical approximation. The agreement is quite good in all directions, and it appears the current far field boundary condition is effective in preventing noticeable reflections.

Figure 5-5 shows the contour of amplitude of sound pressure in the domain. The figure '8' shape in the amplitude contours indicate that the flat plate appears as a single dipole at the far field, i.e. the flat plate is a compact source.

Note also that the amplitude of pressure is zero along the wake line. A symmetric airfoil under a purely transverse gust will have zero pressure along the wake line with the enforcement of the Kutta condition. As a proof, consider a flat plate in a vertical

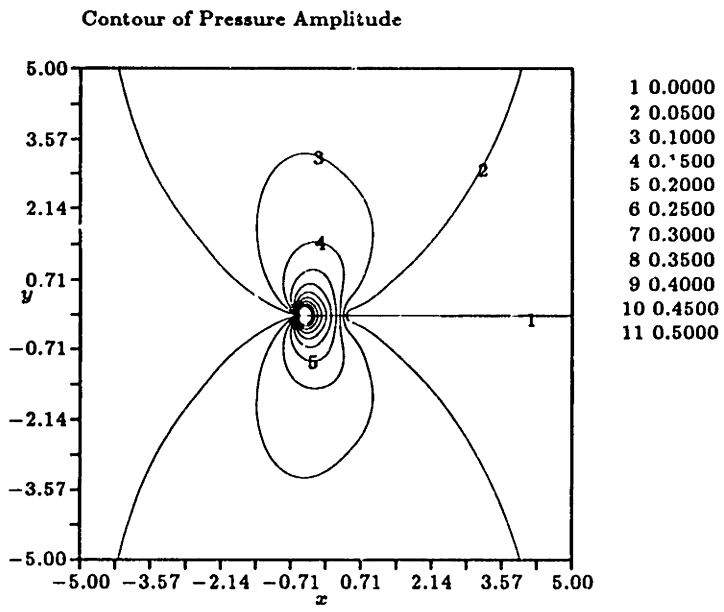

Figure 5-5: Amplitude Contour of Acoustic Pressure, $M_0 = 0.5$, $K = 0.5$

oscillation with velocity,

$$v = v_o e^{-i\omega t}$$

as shown in the upper portion of Figure 5-6. Then because of linearity there will be an associated pressure field which is also harmonic in time,

$$p(x, y) = \tilde{p}(x, y)e^{-i\omega t}.$$

Now consider the same oscillating flat plate in (x', y') domain where $y' = -y$ as shown in the lower portion of Figure 5-6. v' must be $-v$ for all time such that,

$$v' = v_o e^{-i\omega(\frac{\pi}{\omega}+t)}$$

and,

$$p(x', y') = \tilde{p}(x', y')e^{-i\omega(\frac{\pi}{\omega}+t)}.$$

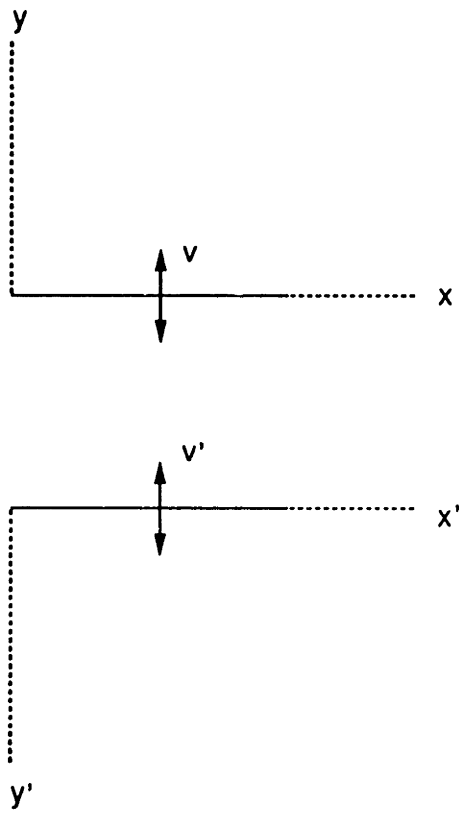

Figure 5-6: $\tilde{p} = 0$ Along the Wake Line for a Symmetric Airfoil

But p must be same in both domains so,

$$\tilde{p}(x, y) = -\tilde{p}(x', y')$$

and by enforcing the Kutta condition along the wake line we must have,

$$\Delta\tilde{p} = 0 \quad @\, y = y' = 0.$$

Which is equivalent to,

$$\tilde{p}(x, 0^+) = \tilde{p}(x, 0^-)$$

$$\tilde{p}(x', 0^+) = \tilde{p}(x', 0^-)$$

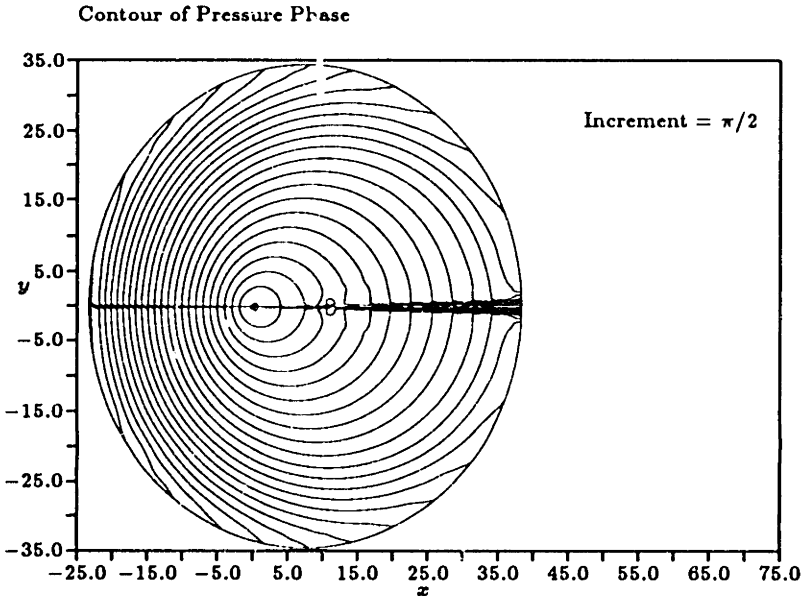

Figure 5-7: Phase Contour of Acoustic Pressure, $M_0 = 0.5$, $K = 0.5$

however since,

$$\tilde{p}(x, 0^-) = -\tilde{p}(x', 0^+)$$

it must follow that,

$$\tilde{p}(x, 0^+) = -\tilde{p}(x, 0^+)$$

which is only possible if $\tilde{p}(x, 0) = 0$ along $y = 0$ wake line. This is not true for a general asymmetric airfoil.

Figure 5-7 shows the contour of acoustic pressure phase. The phase plot indicates that the airfoil appears as a single source concentrated at a position near the quarter-chord point. Note that the contour lines are spaced further apart in the downstream direction than in the upstream direction due to the Doppler effect. The acoustic wavelengths are longer in the direction of the flow and shorter in upstream direction. In general the acoustic wavelength will vary in space as,

$$\lambda_a = \frac{2\pi(c_0 + U_0 \cos\theta)}{\omega} \tag{5.19}$$

where θ is the angle between the reference point and the positive x axis.

5.2.3 Compressible Noncompact Gust

Now consider a flat plate in a compressible flow which encounters a noncompact gust of the form in Equation 5.1. K for this validation case is 3.0. The base mean flow was computed first and the numerical parameters were as follows:

- Geometry: NACA0001
- Grid: 230×120
- M_0: 0.4
- α: 0.0
- Far Field Radius: approximately 4 wavelengths
- ν_4: 0.01
- Iterations: 500
- $L_2(\delta\rho)$: 2.5×10^{-4}

The calculation required 400 iterations for about 4 orders of magnitude convergence.

The mean flow values were used as an input to the perturbation solver and the acoustic parameters were as follows:

- ω: 5.964
- Iterations: 2000
- ν_4: 0.01
- ν_6: 0.001
- $L_2(\delta\tilde{\rho})$: 2.7×10^{-3}

The calculation required 2000 iterations for approximately 3 orders of magnitude convergence.

Landahl [42] has provided an iterative method of computing the surface pressure distribution for a gust of arbitrary wavelength. The solution process divides the flat plate problem into two distinct leading and trailing edge problems in which iterations are performed to match the two solutions. In the leading edge problem the chord is allowed to extend infinitely in the downstream direction which eliminates the Kutta

condition and the wake from the problem. A trailing edge problem is then solved in order to correct the leading edge solution in the wake. The sum of these two solutions satisfies the flow tangency on the airfoil and pressure continuity across the wake, but it violates the condition of $\phi = 0$ upstream. Additional iterations are computed to provide a more accurate solution.

In the short wavelength limit, however, the leading and the trailing edges become largely independent of each other. Furthermore, the fluctuating lift does not act through the quarter–chord point when the reduced frequency is large, but rather moves toward the leading edge as the frequency increase; the trailing edge region is relatively unimportant at the higher reduced frequencies [27]. Given noncompact sources the fluctuating lift can be computed using only Landahl's leading edge solution. The fluctuating pressure difference across a semi–infinite flat plate due to a gust of this type is given by,

$$\Delta p = -i2\rho_0 U_0 \frac{e^{-i\nu}}{\sqrt{\pi i \nu}(1+M_0)(1+2x/a)} e^{i[M_0\nu/(1+M_0)][(2x/a)+1]}. \tag{5.20}$$

The associated lift L_e is,

$$L_e = \pi \rho_0 U_0 a S(\nu, M_0) \tag{5.21}$$

where

$$S(\nu, M_0) = \frac{e^{-i\nu}}{\nu\pi}\sqrt{\frac{2i}{M_0}}\mathcal{F}\left(\sqrt{\frac{4\nu M_0}{\pi(1+M_0)}}\right) \tag{5.22}$$

is the high–frequency approximation to the compressible Sears function and

$$\mathcal{F}(x) = \int_0^x e^{i(\pi/2)\xi^2} d\xi \tag{5.23}$$

is the complex Fresnal integral. This formula is accurate to about 10% in lift when $K > 1$ according to Reference [27].

Figure 5-8 compares the computed values of Δp versus the expansion of Landahl [27]. The symbols represent the computed solution and the lines represent the expansion of Landahl. The agreement is quite close, except perhaps towards the trailing edge where

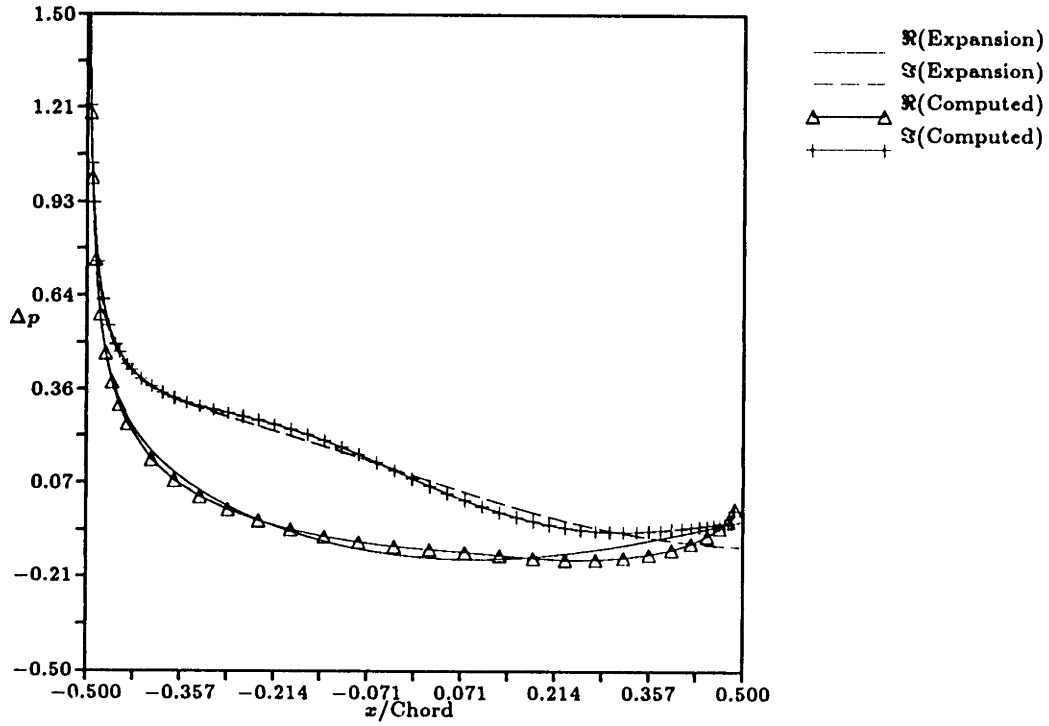

Figure 5-8: $\Delta\tilde{p}$ on the Flat Plate for a Noncompact Gust

the expansive solution violates the Kutta condition of zero pressure jump. In terms of the lift, the computed solution was $|\tilde{L}_c| = 0.1383$, $\arg\tilde{L}_c = -75.43°$ and the Landahl solution is $|\tilde{L}_e| = 0.1288$, $\arg\tilde{L}_e = -83.49°$, where we have also used the following asymptotic approximation for the Sears function,

$$S \sim \frac{1}{\pi\nu}\frac{e^{-i[\nu-(\pi/2)]}}{\sqrt{M_0}} \quad \text{as} \quad \nu \to \infty.$$

The difference is about 7.4% in amplitude and 8.06° in phase. It seems the numerical solution is also accurate for the noncompact case in the near field.

The far field values were checked for unwanted reflections using Green's theorem in Equation 5.16 and the asymptotic approximation in Equation 5.17. The comparison between the computed and the approximation D_p is shown in Figure 5-9. The computed solution is in good agreement with the approximation in all directions.

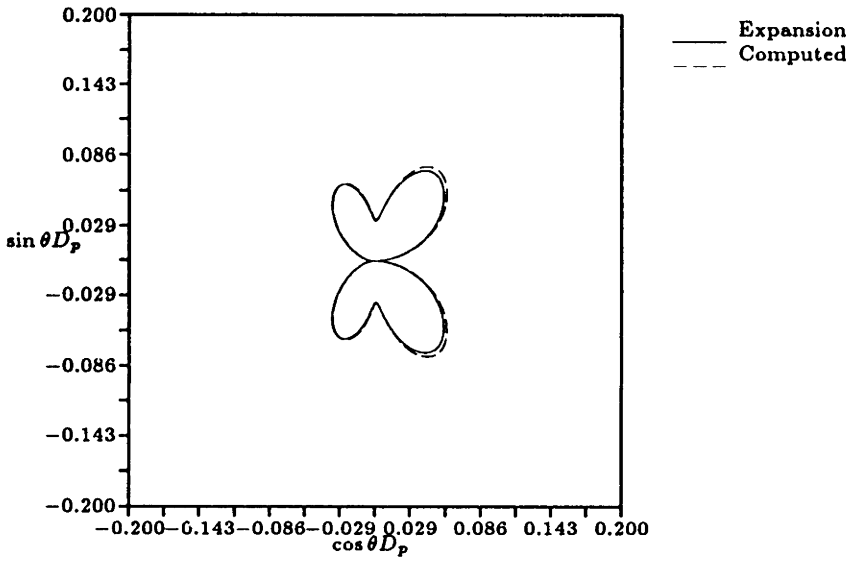

Figure 5-9: Polar Plot of D_p at the Far Field for a Compressible Noncompact Gust

Figure 5-10 shows the amplitude contours of acoustic pressure. Notice the amplitude contour shape is more complicated than a simple figure '8' shape. This is due to the noncompactness and the retarded time differences between the dipoles along the flat plate.

Figure 5-11 shows the phase contours of acoustic pressure. Close to the airfoil two distinct sources at the leading and the trailing edges are visible. At moderate distance from the airfoil the elliptical contour lines show higher eccentricity than the compact case in Figure 5-7, because the sources appear to be distributed along the entire length of the flat plate rather than concentrated at a single point. Still further away from the plate, the phase contour lines are similar to the compact case, because the reference distance is much farther than the average acoustic wavelength. It is important to note that at long distances the phase contours between the compact and the noncompact sources look similar, but because of the retarded time differences the radiation patterns as illustrated in Figures 5-4 and 5-9 are not.

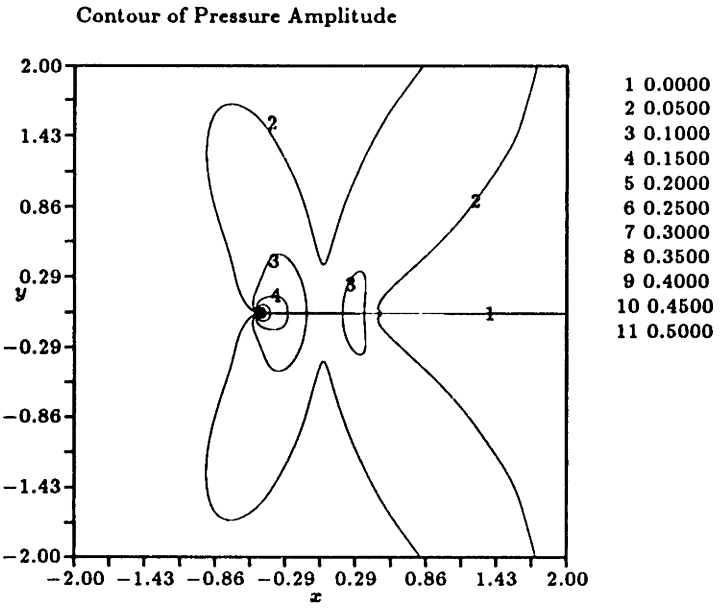

Figure 5-10: Amplitude Contour of Acoustic Pressure, $M_0 = 0.4$, $K = 3.0$

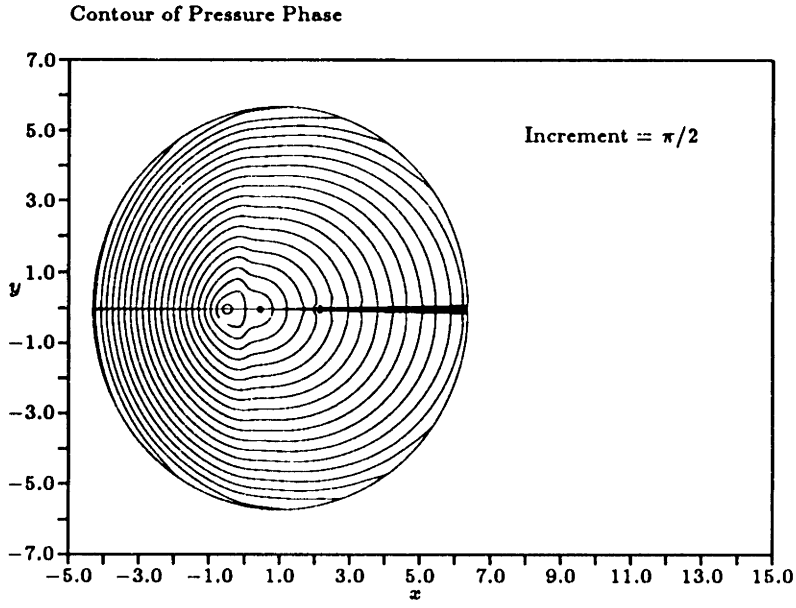

Figure 5-11: Phase Contour of Acoustic Pressure, $M_0 = 0.4$, $K = 3.0$

5.3 Parametric Studies

The previous section illustrated that the current numerical method is accurate and consistent throughout the domain. We now turn our attention to parametric studies to determine some gross effects of the mean flow Mach number, the mean loading, the airfoil thickness, and the upstream gust parameter on the radiated sound field.

The existing linear theory by Sears [67] and others [3, 27, 42] has been presented in Sections 5.1 and 5.2. It is directly applicable for airfoils with small excursions from a flat plate in low Mach number flows.

Consider a thin airfoil with its edge defined by the equation $g(x) = 0$, and let ϵ be a small parameter such that the $y = \epsilon f(x)$ determines the mean position of the surface of the airfoil, and $\epsilon\sqrt{g}$ determines its thickness distribution.

The velocity in the domain can be represented as,

$$\mathbf{U} = u_0\mathbf{i} + \mathbf{u}'_i + \mathbf{u}'_s \tag{5.24}$$

where u_0 is the free stream velocity, $\mathbf{u}'_i$ is the imposed gust perturbation, and $\mathbf{u}'_s$ is the 'scattered' perturbation velocity such that,

$$\mathbf{u}'_s \to 0 \quad \text{as} \quad r \to \infty.$$

Then for an inviscid body the linearized boundary condition can be expressed as in Reference [27],

$$-\epsilon\left(\frac{\partial f}{\partial x} \pm \frac{1}{2\sqrt{g}}\frac{\partial g}{\partial x}\right)u_0 + v'_i = -v'_s \tag{5.25}$$

on $y = \pm 0$ and $g > 0$ and where the $\pm$ refers to the upper and lower surface of the airfoil, respectively. The first term on the left side of the equation contains the effects of thickness, camber and angle of attack and is independent of time while the second term which depends on time, is uninfluenced by these geometric effects. In the linearized approximation the effects of geometry, therefore, contribute only to the steady mean

solution and make no contributions to the unsteady perturbation component.

Reference [42] also shows that the convective wave Equation 5.3 itself is invalid when the free stream Mach number approaches unity. So we see that the linearization is constrained by both the geometry and the free stream Mach number (and also possibly by the compactness).

We will now conduct a systematic study to see if and when the linear theory is valid, and in situations where it is not valid, we will attempt to identify and discuss parameters which govern the nonlinearity.

5.3.1 Similarity Parameter K

We have seen that K is an important parameter in the solution of the radiated sound field, and that when K is small a flat plate emits sound as a compact source. We now prove this by performing 3 different calculations at different Mach numbers and frequencies but with an identical K.

In each of the runs we used a grid of 200x100 about a NACA0001 airfoil, and the far field was placed such that there was approximately 4 wavelengths in all directions within the domain. The mean flow was computed first, and a convergence of at least 4 orders in magnitude for the RMS residual of density was assured. Key parameters in the 3 calculations are tabulated below:

	M_0	ν	K
Case 1	0.4	2.100	1.0
Case 2	0.6	1.067	1.0
Case 3	0.7	0.729	1.0

Table 5.1: Parameters for Compact Source $K = 1.0$ Cases

The amplitudes of acoustic pressure $|\tilde{p}|$ are shown in Figures 5-12, 5-13, 5-14. Notice the similarity in the directivity patterns between the three cases. The amplitudes increase with the free stream Mach number, but the radiation patterns remain the same. Also note that the amplitude of sound is zero along the wake. The radiation patterns at the far field are illustrated in Figure 5-15. The figure is a polar plot of the quantity

D_p for the three cases. It indicates that as the incoming Mach number increases the amplitude of sound pressure increases correspondingly, but the directivity remains the same. Note also that the directivity pattern is symmetric about the horizontal axis but is not about the vertical axis; there is a slight tilt towards the downstream direction.

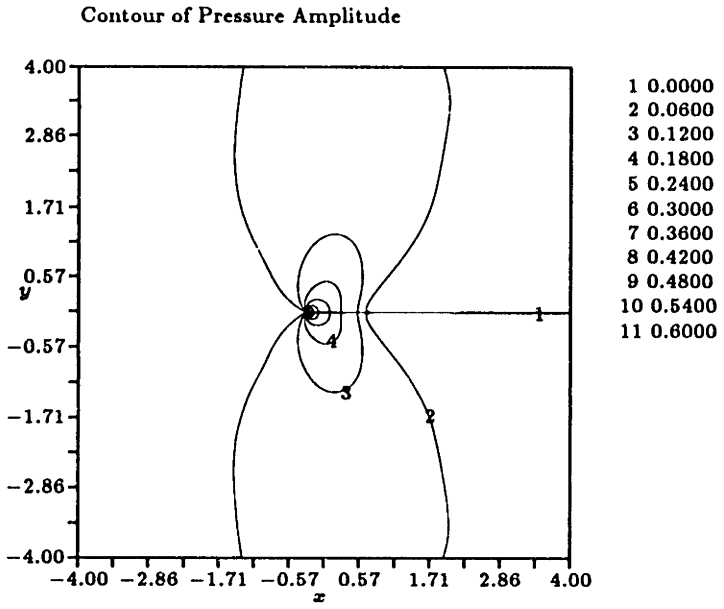

Figure 5-12: Amplitude Contour of Acoustic Pressure, $M_0 = 0.4$, $\nu = 2.10$, $K = 1.0$

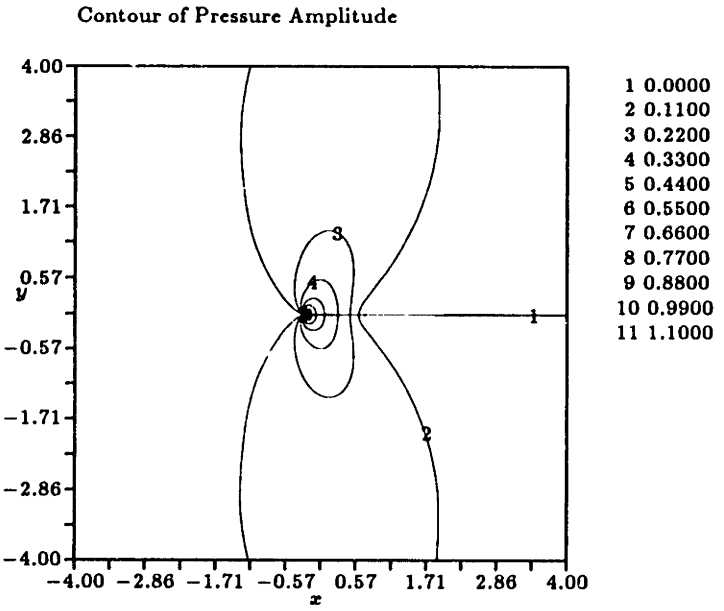

Figure 5-13: Amplitude Contour of Acoustic Pressure, $M_0 = 0.6$, $\nu = 1.067$, $K = 1.0$

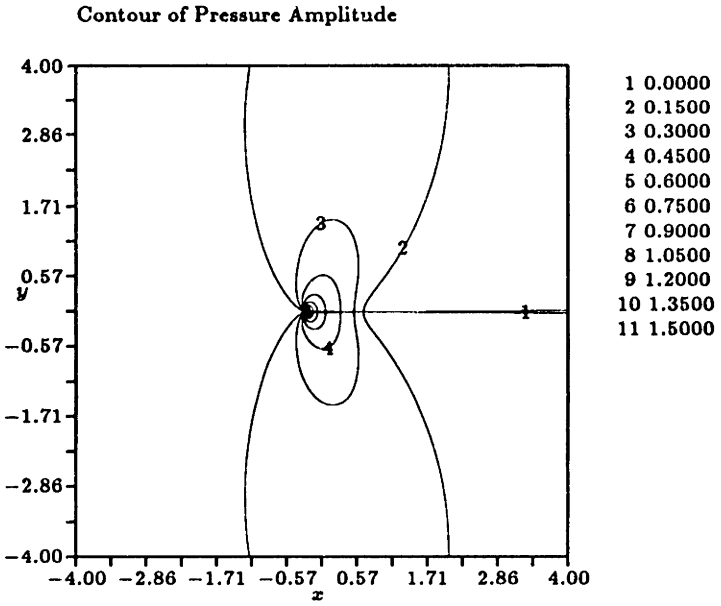

Figure 5-14: Amplitude Contour of Acoustic Pressure, $M_0 = 0.7$, $\nu = 0.729$, $K = 1.0$

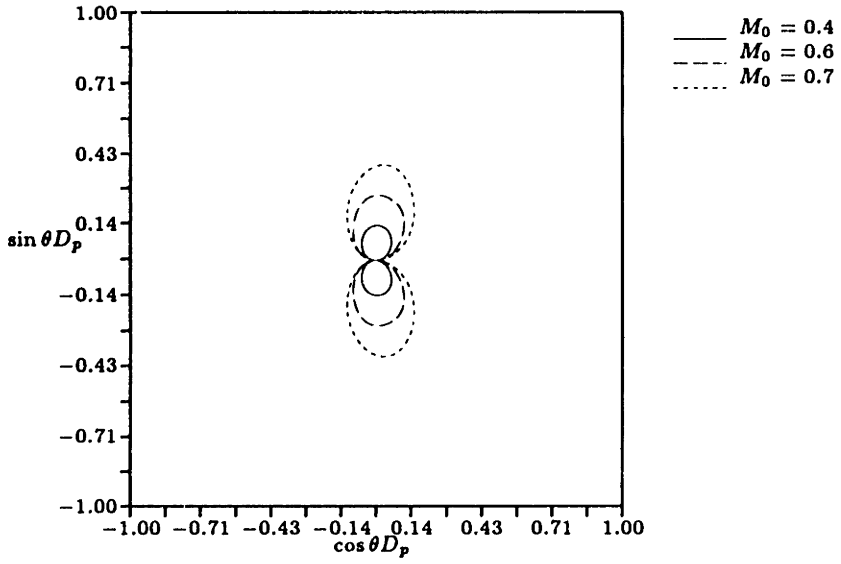

Figure 5-15: Polar Plot of D_p at the Far Field, $K = 1.0$

Now consider a noncompact case at 3 different Mach numbers and frequencies but with an identical K.

In each of the runs we used a grid of 230x120 about a NACA0001 airfoil, and the far field was placed such that there was approximately 4 wavelengths in all directions within the domain. As before the mean flow was computed first, and a convergence of at least 4 orders in magnitude for the RMS residual of density was assured. Key parameters in the 3 calculations are tabulated below:

	M_0	ν	K
Case 1	0.4	6.300	3.0
Case 2	0.6	3.201	3.0
Case 3	0.7	2.186	3.0

Table 5.2: Parameters for Noncompact Source $K = 3.0$ Cases

Amplitudes of acoustic pressure $|\tilde{p}|$ are shown in Figure 5-10 on page 115 and in Figures 5-16, 5-17 on the following pages. Again the figures indicate that the amplitude increases as the Mach number increases but the directivity remains the same. This is also illustrated in the polar plot of far field D_p in Figure 5-18.

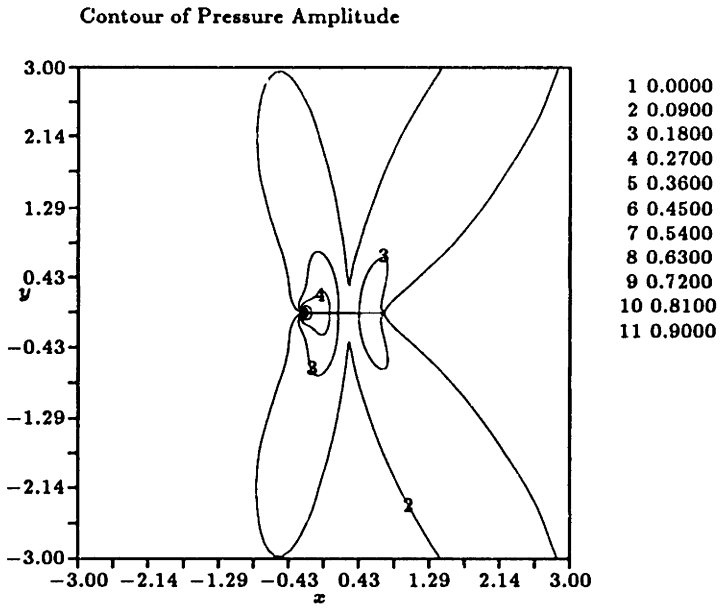

Figure 5-16: Amplitude Contour of Acoustic Pressure, $M_0 = 0.6$, $\nu = 3.201$, $K = 3.0$

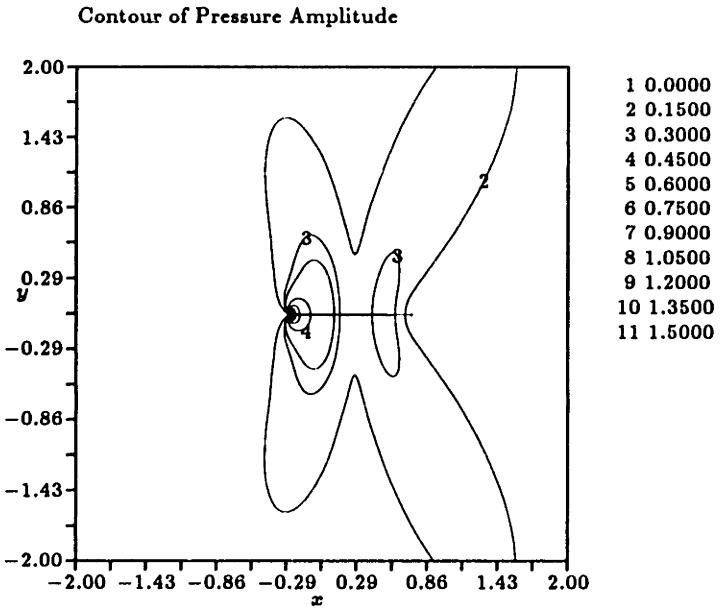

Figure 5-17: Amplitude Contour of Acoustic Pressure, $M_0 = 0.7$, $\nu = 2.186$, $K = 3.0$

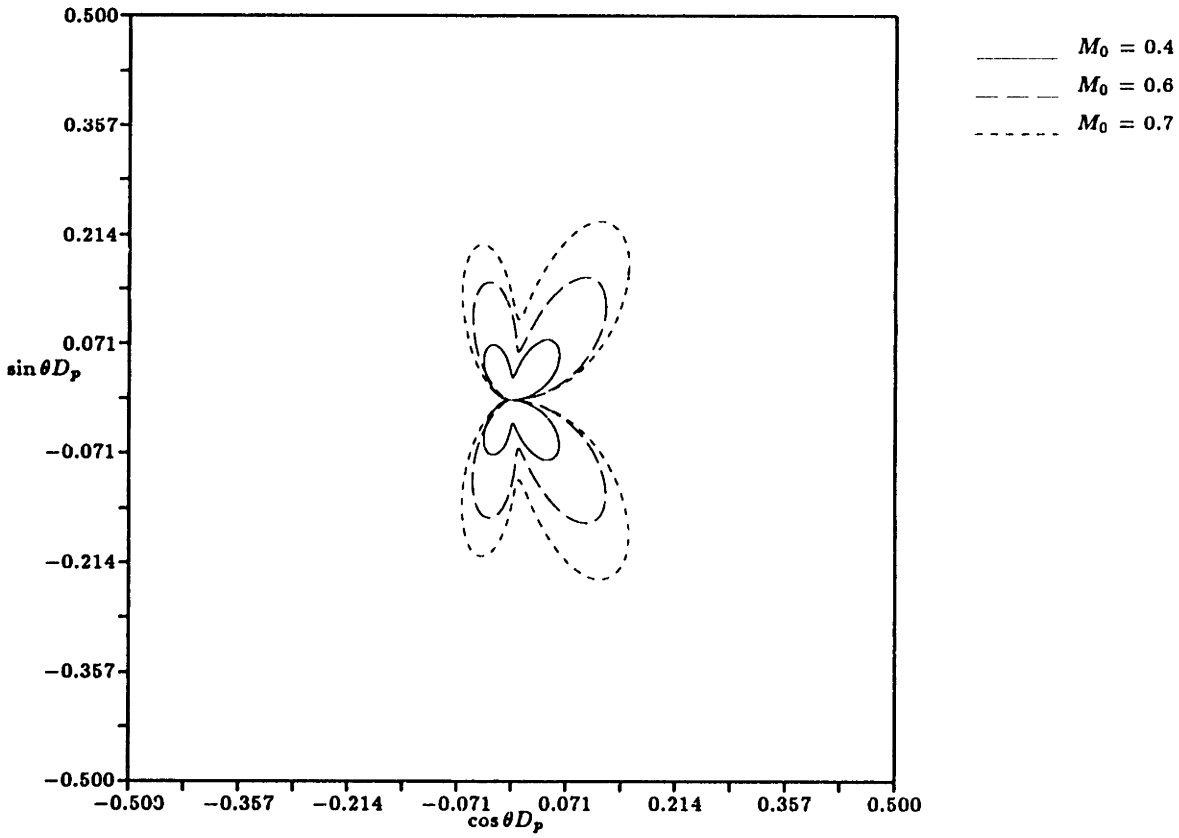

Figure 5-18: Polar Plot of D_p at the Far Field, $K = 3.0$

5.3.2 Thickness

We have seen that K is a similarity parameter such that disturbances of the same K have the same directivity patterns. We now turn our attention to the effects changes in the thickness of the airfoil have on the radiated sound field. Note again that according to the linear theory, the thickness does not have any effect on the unsteady solution. However, as we increase the thickness we expect the linear theory to eventually breakdown because there must necessarily be diffraction of sound from flow and surface gradients.

Accustic diffraction occurs in a region which has a solid body of interference or in a region which allows some part of the wave front to propagate faster than another.

In a homogeneous media, i.e. in a uniform flow, diffraction occurs near a solid surface as wave fronts are necessarily distorted when the traveling waves 'bend' in order to accommodate the surface. Diffraction can also occur in an inhomogeneous media when the group velocity varies as a function space. The wave fronts 'bend' as different parts of the wave front propagate at different rates. Reconsider the acoustic portion of the dispersion Equation 3.14 derived earlier in Section 3.2,

$$(u_0 k + v_0 l - \omega)^2 - c_0^2(k^2 + l^2) = 0 \tag{5.26}$$

where again k and l are the spatial wavenumbers and ω is the temporal frequency. The above equation can be differentiated with respect to k and l to obtain the acoustic group velocity,

$$\mathbf{C_g} = \begin{pmatrix} \frac{\partial \omega}{\partial k} \\ \frac{\partial \omega}{\partial l} \end{pmatrix} = \begin{pmatrix} u_0 \\ v_0 \end{pmatrix} + c_0^2 \begin{pmatrix} \frac{k}{\omega - u_0 k - v_0 l} \\ \frac{l}{\omega - u_0 k - v_0 l} \end{pmatrix}. \tag{5.27}$$

The group velocity can be interpreted as a vector sum of the local convection velocity plus a vector whose magnitude is equal to the local speed of sound and whose direction is normal to the wavecrest defined by [26],

$$kx + ly = \text{constant}.$$

Thus when c_0 or (u_0, v_0) is a function of space, $\mathbf{C_g}$ must also be a corresponding function of space. Diffraction can occur by spatial changes in the local speed of sound and/or by spatial changes in the local convection velocity.

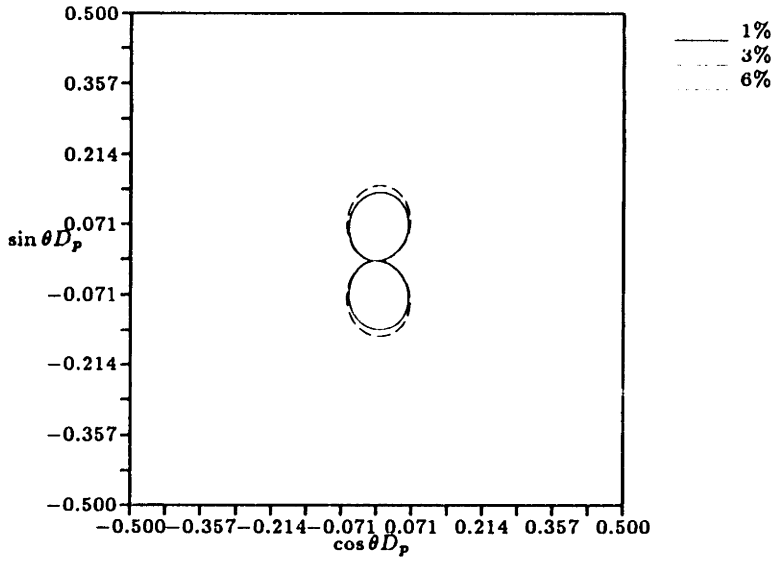

Figure 5-19: Polar Plot of D_p at the Far Field, $M_0 = 0.4$, $K = 1.0$

Compact Cases

We present first a set of compact cases in which the maximum thickness τ is varied from 1% to 6% while we keep the compactness ratio K and the free stream Mach number M_0 constant at 1 and 0.4, respectively. We used a grid of 200x100 about NACA00 sections, and the far field was chosen such that the domain contained approximately 4 wavelengths in all directions. The key parameters for this set are in Table 5.3 where $|\tilde{L}|$ is the amplitude of complex lift.

The lift is slightly higher for the two thicker cases and this results in a small increase in the far field amplitude as shown in Figure 5-19. The effect of thickness is quite small in this set, and a simple dipole model with its strength set by the unsteady lift would provide an accurate solution.

	M_0	ν	K	τ	$\|\tilde{L}\|$
Case 1	0.4	2.100	1.0	1%	0.46
Case 2	0.4	2.100	1.0	3%	0.49
Case 3	0.4	2.100	1.0	6%	0.49

Table 5.3: Parameters for $M_0 = 0.4$, $K = 1.0$ Varying Thickness Cases

We now present a set of compact cases in which the maximum thickness τ is varied from 1% to 13% while we keep the compactness ratio K and the free stream Mach number M_0 constant at 1 and 0.7, respectively. We used a grid of 200x100 about NACA00 sections, and the far field was chosen such that the domain contained approximately 4 wavelengths in all directions. The key parameters for this set are tabulated below:

	M_0	M_{max}	ν	K	τ	$\|\tilde{L}\|$
Case 1	0.7	0.71	0.729	1.0	1%	1.21
Case 2	0.7	0.75	0.729	1.0	3%	1.19
Case 3	0.7	0.82	0.729	1.0	6%	1.18
Case 4	0.7	0.98	0.729	1.0	13%	1.16

Table 5.4: Parameters for $M_0 = 0.7$, $K = 1.0$ Varying Thickness Cases

M_{max} is the peak Mach number in the domain. In this set there is a small ($< 5\%$) decrease in the lift as the thickness increases, and thus the dipole strength should be roughly equivalent between the four cases. The contours of constant acoustic pressure for the 13% airfoil are shown in Figure 5-20. Compare this plot with the 1% airfoil result of Figure 5-14 on page 120. Near the airfoil where the flow gradients are high, the 13% airfoil indicates large gradients of acoustic pressure, and away from the surface, there is a 'tilt' of acoustic directivity towards the upstream direction.

The far field sound directivity is illustrated in Figure 5-21. Figure 5-21 is a polar plot of far field D_p for all four airfoils. The thickness does not seem to affect the far field sound pressure in a noticeable way when the thickness is 6% or less, but there is a distinct tilt of the lobes towards the upstream direction for the 13% case.

Reference [42] shows that the linear assumption is valid and that the convective

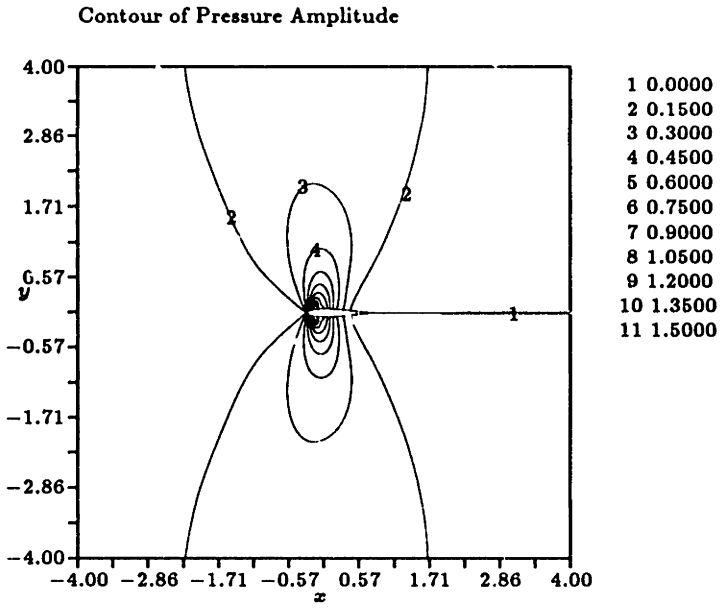

Figure 5-20: Amplitude Contour of Acoustic Pressure, $M_0 = 0.7$, $K = 1$, $\tau = 13\%$

wave equation of the type in Equation 5.3 can be used when,

$$|1 - M_0| \gg \tau^{2/3}. \tag{5.28}$$

For $M_0 = 0.4$ and $1\% < \tau < 6\%$ above constraint is clearly satisfied, and the convective wave equation produces correct results. For the $M_0 = 0.7$ case the above criteria may or may not be satisfied when $\tau = 6\%$ ($\tau^{2/3} \approx 0.15$) and is clearly not valid when $\tau = 13\%$. The solution obtained indicates that the directivity does not change noticeably from that of a simple dipole when $\tau \leq 6\%$, but when $\tau = 13\%$ the sound radiation pattern departs significantly from the linear theory in both the near and far field regions. It seems that as long as the sources are compact the linear theory is accurate for a moderately thick airfoil in low Mach number flows; however, when the airfoil is thick enough such that the peak Mach number approaches unity the existing theory is inadequate.

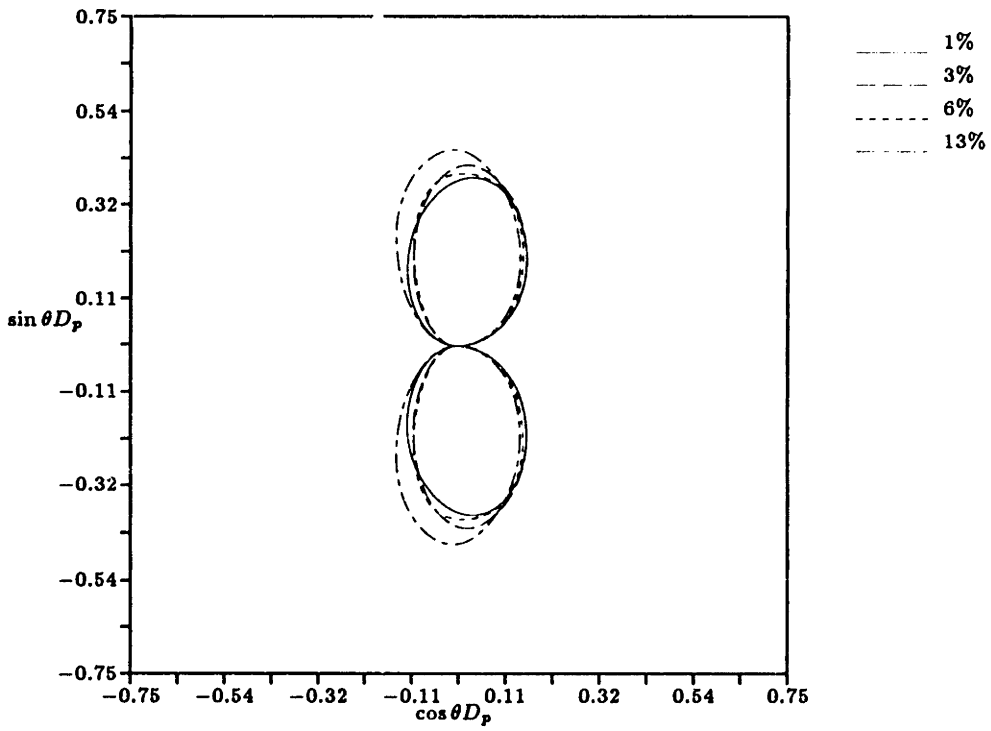

Figure 5-21: Polar Plot of D_p at the Far Field, $M_0 = 0.7$, $K = 1.0$

Noncompact Cases

We now consider noncompact cases at a low Mach number of $M_0 = 0.4$. The maximum thickness τ is varied from 1% to 6% while we keep the compactness ratio K and the free stream Mach number M_0 constant at 3 and 0.4, respectively. We used a grid of 230x120 about NACA00 sections, and the far field was chosen such that the domain contained approximately 4 wavelengths in all directions. The key parameters for this set are tabulated below:

	M_0	ν	K	τ	$\lvert\check{L}\rvert$
Case 1	0.4	6.300	3.0	1%	0.17
Case 2	0.4	6.300	3.0	3%	0.18
Case 3	0.4	6.300	3.0	6%	0.18

Table 5.5: Parameters for $M_0 = 0.4$, $K = 3.0$ Varying Thickness Cases

All three thickness cases have virtually the same amount of lift so, in an integral sense, each has an equivalent total dipole distribution along the airfoil. However, as shown in Figure 5-22 the far field directivity varies considerably from one airfoil to the next. The thickness has enhanced sound amplitude in the forward direction and, to a lesser degree, in the downward direction, while it has reduced the sound amplitude in the normal direction. Apparently the varying mean flow has diffracted sound away from the center region towards the up and downstream directions. This is more evident in the phase contour plots in Figures 5-23 and 5-24. Compare these two plots with the flat plate (1%) phase plot Figure 5-11 on page 115. The mean flow has diffracted sound such that the leading and trailing edge regions appear as two distinct radiators of sound.

The two thicker solutions differ significantly from that of the flat plate result, and the previously described linear method would not be sufficiently accurate for the $\tau \geq 3\%$ cases. The effect of mean flow diffraction is too great to be ignored for the current noncompact case. Evidently the constraint,

$$|1 - M_0| \gg \tau^{2/3} \tag{5.29}$$

is not necessarily sufficient when the reduced frequency is large, even when the Mach number and τ are small.

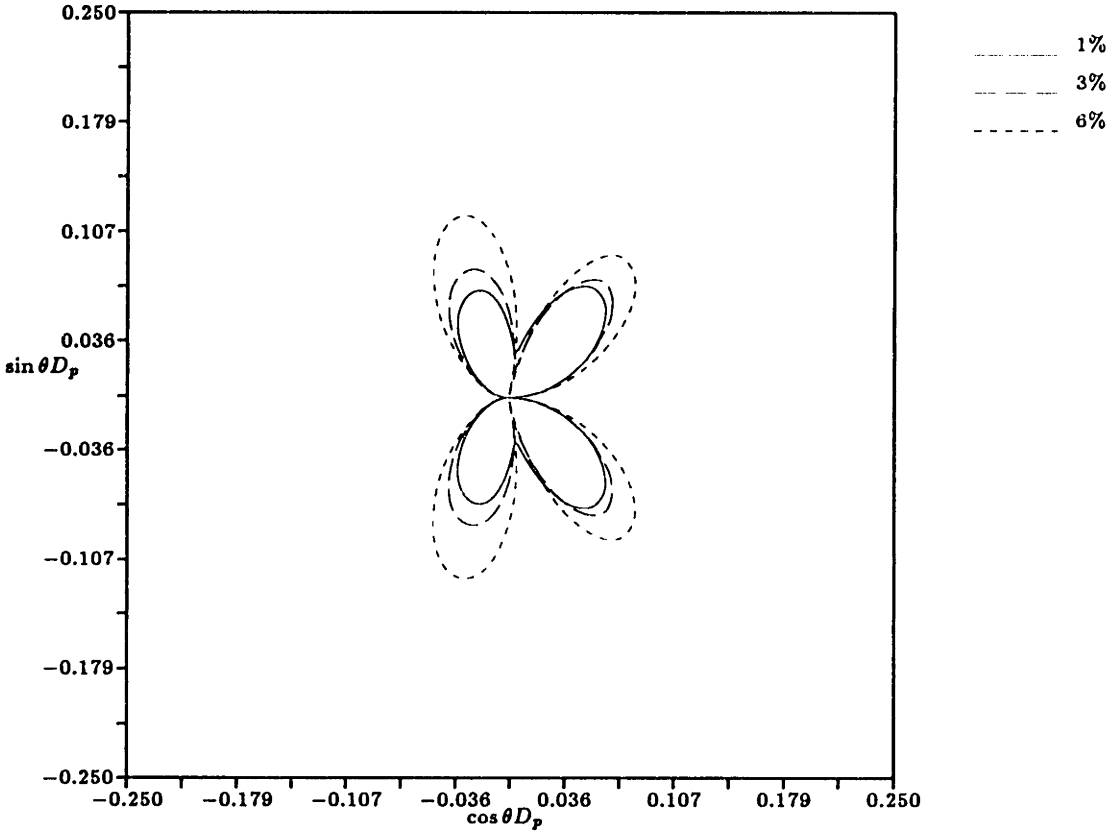

Figure 5-22: Polar Plot of D_p at the Far Field, $M_0 = 0.4$, $K = 3.0$

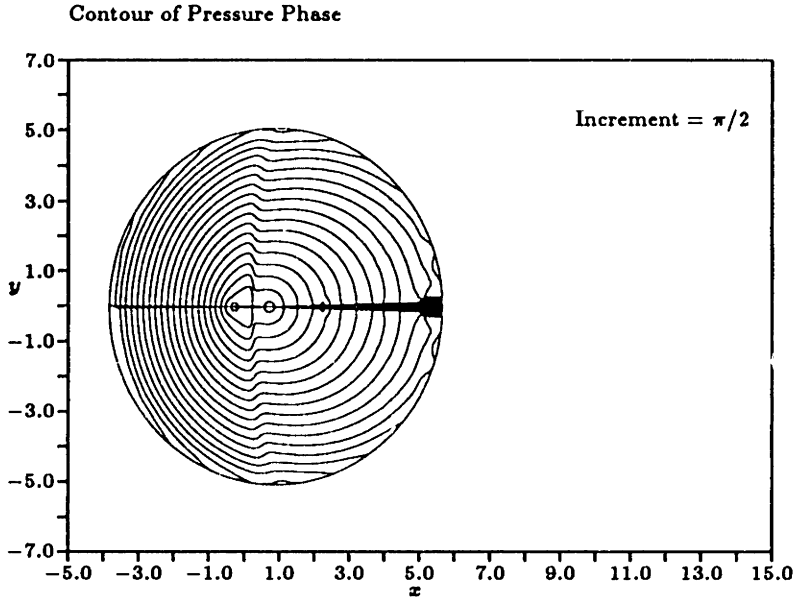

Figure 5-23: Phase Contour of Acoustic Pressure, $M_0 = 0.4$, $K = 3.0$, $\tau = 3\%$

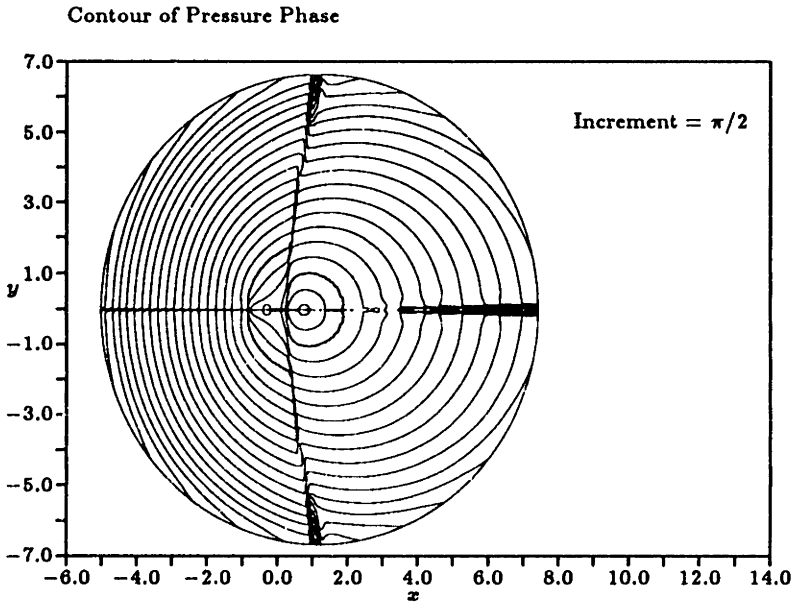

Figure 5-24: Phase Contour of Acoustic Pressure, $M_0 = 0.4$, $K = 3.0$, $\tau = 6\%$

Consider a noncompact set in free stream of Mach number 0.7. The maximum thickness τ is varied from 1% to 13% while we keep the compactness ratio K and the free stream Mach number M_0 constant at 3 and 0.7, respectively. We used a grid of 270x120 about NACA00 sections, and the far field was chosen such that the domain contained approximately 4.5 wavelengths in all directions. The key parameters for this set are tabulated below:

	M_0	M_{max}	ν	K	τ	$\lvert\tilde{L}\rvert$
Case 1	0.7	0.71	2.186	3.0	1%	0.62
Case 2	0.7	0.75	2.186	3.0	3%	0.64
Case 3	0.7	0.82	2.186	3.0	6%	0.63
Case 4	0.7	0.98	2.186	3.0	13%	0.65

Table 5.6: Parameters for $M_0 = 0.7$, $K = 3.0$ Varying Thickness Cases

All four thickness cases have virtually the same amount of lift and total dipole distribution along the airfoil. The directivity patterns of the 4 airfoils are shown in Figure 5-25. For the 3% airfoil case, the thickness has enhanced sound amplitude in the forward and downward directions, while it has reduced the sound amplitude in the normal direction. The varying mean flow has diffracted sound from the center region towards the up and downstream directions. For the 6% airfoil case, there is an amplification of sound in the downstream direction and an increase in the peak sound pressure in the upstream direction. However, the angle of peak sound radiation is different in this case than in the flat plate case. Evidently the mean flow has affected the sound propagation direction such that in the 6% case the forward directivity pattern is altered. This diffractive effect is even more dramatic for the 13% case. There are large increases in sound amplitude of the 4 lobes, and there exists 2 new lobes in the upstream direction.

The effect of thickness on the acoustic near field is illustrated in the constant pressure contour plot for the 13% airfoil in Figure 5-26. Compare the plot with the 1% result of Figure 5-17 on page 122. There are large gradients of pressure through out the domain but particularly near the thick leading edge region.

The diffraction of sound from the varying mean flow is also illustrated in the pressure phase contour plots of Figures 5-27, 5-28, 5-29, and 5-30. The 3% case shows a separation of leading and trailing edge regions. The 6% and 13% cases also increase the separation of sound radiation, but they also illustrate a complicated phase behavior directly ahead of the airfoil indicating that the forward upstream direction is a region of high diffraction. This is to be expected since the acoustic wavelength is significantly shorter in the upstream direction and is, therefore, more sensitive to small changes in flow gradients.

Conclusions

In this section we have investigated the effects of thickness on the radiated sound field. When the gust is compact and the free stream Mach number is sufficiently small such that the constraint in Equation 5.28 is satisfied, thickness has little effect on the radiated sound field. The linear dipole model would suffice in these cases. However, when the thickness is sufficiently large, the effect of thickness on a compact gust is to tilt the acoustic radiation towards upstream direction.

When the gust is noncompact and the free stream Mach number is small, the mean flow diffracts sound away from the center region towards the up and downstream directions. At a higher Mach number the separation of source regions also occur, but in addition, there exists a more complicated diffraction in the forward upstream direction. The linear method is not effective for noncompact gusts even when given a moderately thick airfoil and the constraint 5.28 is satisfied.

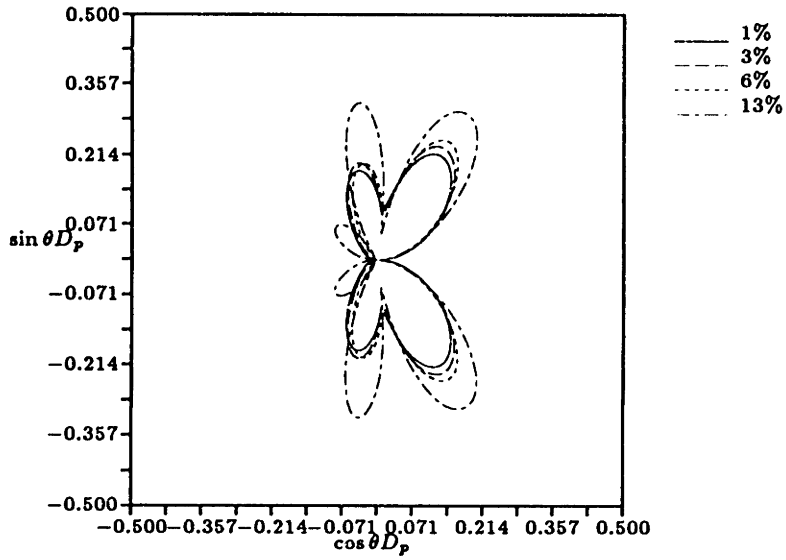

Figure 5-25: Polar Plot of D_p at the Far Field, $M_0 = 0.7$, $K = 3.0$

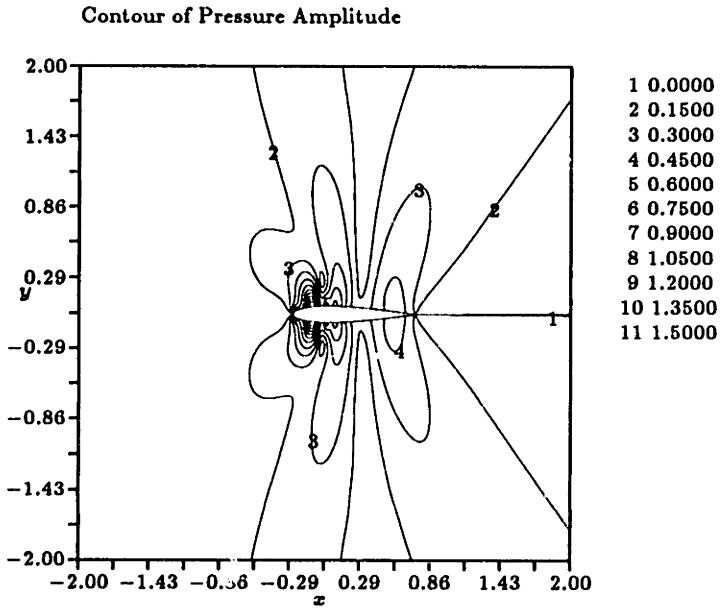

Figure 5-26: Amplitude Contour of Acoustic Pressure, $M_0 = 0.7$, $K = 3$, $\tau = 13\%$

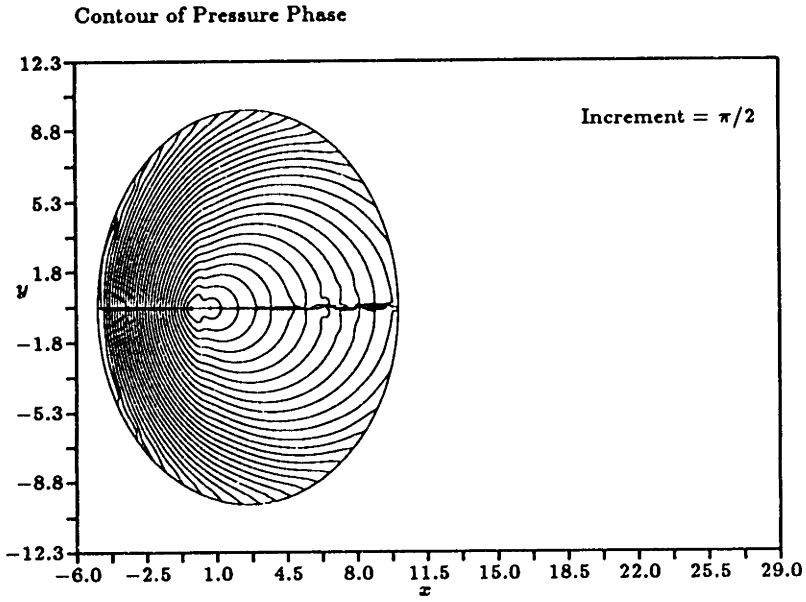

Figure 5-27: Phase Contour of Acoustic Pressure, $M_0 = 0.7$, $K = 3.0$, $\tau = 1\%$

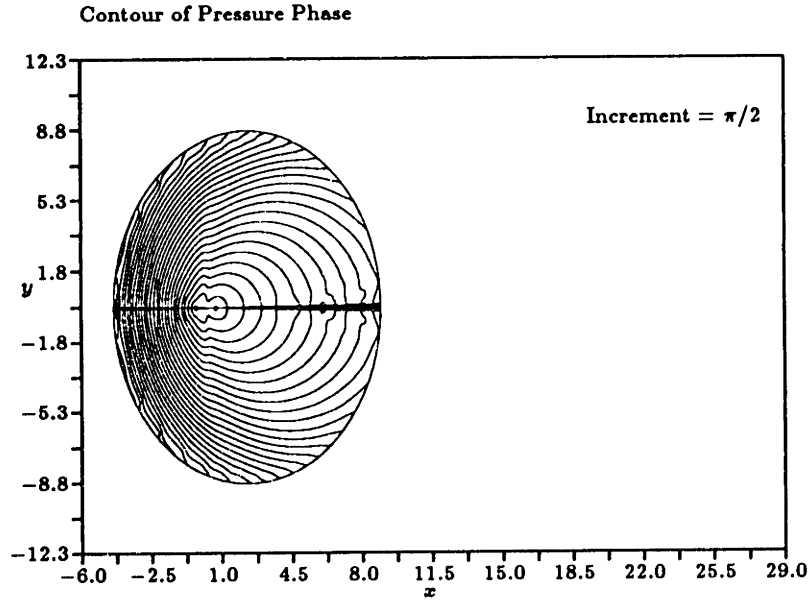

Figure 5-28: Phase Contour of Acoustic Pressure, $M_0 = 0.7$, $K = 3.0$, $\tau = 3\%$

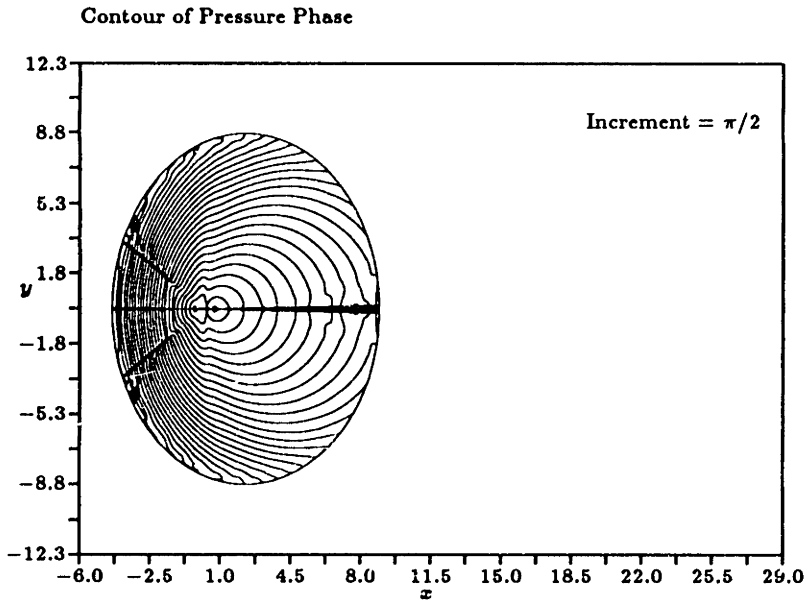

Figure 5-29: Phase Contour of Acoustic Pressure, $M_0 = 0.7$, $K = 3.0$, $\tau = 6\%$

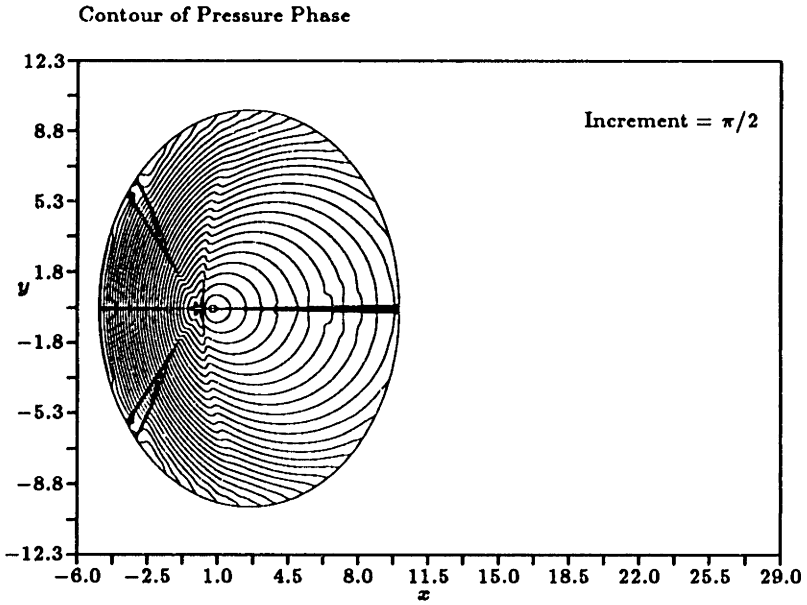

Figure 5-30: Phase Contour of Acoustic Pressure, $M_0 = 0.7$, $K = 3.0$, $\tau = 13\%$

5.3.3 Angle of Attack

We now investigate the effects of small changes in the angle of attack on the radiated sound field of an airfoil subject to a vortical gust. In linear theory, the airfoil at an angle of attack is projected as an equivalent flat plate with zero incidence. Angle of attack, therefore, decreases the actual chord length and its associated unsteady lift amplitude.

Compact Cases

A NACA0012 airfoil is at $M_0 = 0.5$ and at 3 different angles of attack. A compact transverse gust of reduced frequency $\nu = 1.0$ and a compactness ratio of $K = 2/3$ impinges on the airfoil. The important parameters for the 3 angles are tabulated below:

	M_0	M_{max}	ν	K	α	$\lvert\tilde{L}\rvert$	W_a
Case 1	0.5	0.62	1.0	2/3	0	0.624	0.0300
Case 2	0.5	0.75	1.0	2/3	3°	0.616	0.0297
Case 3	0.5	0.95	1.0	2/3	5°	0.651	0.0330

Table 5.7: Parameters for $M_0 = 0.5$, $\nu = 1.0$ Varying Angle of Attack Cases

W_a is the radiated sound power and is computed by numerically integrating the acoustic intensity around a closed loop. The acoustic power has been previously defined in page 38 and is repeated here,

$$W \equiv \oint_\sigma \bar{\mathbf{I}}_a \cdot \mathbf{n}\, d\sigma \tag{5.30}$$

where the overbar $\bar{}$ denotes a time-averaged quantity, and the acoustic intensity $\mathbf{I}_a$ is defined as,

$$\mathbf{I}_a = (\frac{p'}{\rho_0} + \mathbf{u}_0 \cdot \mathbf{u}')(\rho_0 \mathbf{u}' + \rho' \mathbf{u}_0) \tag{5.31}$$

and we have assumed an isentropic flow.

The perturbation velocity $\mathbf{u}'$ is, in general, composed of both vortical and acoustic parts, and we must include just the acoustic portion in the integral of Equation 5.30 for

sound power. The decomposition can be accomplished using the Helmholtz method as described in Reference [57], but this usually entails a solution to the Poisson equation over the numerical domain. We have chosen a less accurate, but a simpler splitting method, one which becomes exact as $r \rightarrow \infty$.

Recall from the earlier group velocity analysis in Section 5.3.2 that the direction of energy propagation (and of acoustic velocity) is determined by the group velocity. Recall also that as $r \rightarrow \infty$ the acoustic waves locally appear planar. The acoustic portion of velocity is thus computed such that the amplitude and phase is determined as,

$$\tilde{u}_a = \frac{\tilde{p}}{\rho_0 c_0}$$

and its direction is chosen to coincide with the group velocity vector. The approximation is strictly valid only at $r = \infty$, but in practice the planar assumption is accurate at much smaller values of r. Figure 5-31 is a plot of radiated acoustic power versus distance along the positive x-axis for the three angles. Note that the O-grid is not circular so that the values on the horizontal axis do not coincide with actual radial distance. The airfoil is the only sound source so we expect the plot to indicate a constant acoustic power for all r. The figure shows that close to the surface the approximation is inaccurate, but by $r = 1.5$ (only 1.5 chords away from the quarter-chord position) the power values are essentially at the correct asymptotic values. The simple splitting method seems adequate as long as the circuit integral is not performed too close to the surface.

Table 5.7 indicates that at 3° angle of attack there is a small decrease in the unsteady lift amplitude and sound energy. This is as expected from the linear theory. However, for the 5° angle of attack case, there is an *increase* in both the lift amplitude (+4 %) and the associated sound energy (+10 %). This could only occur if there was an extraction of energy from the mean flow to the acoustic perturbation.

Recall that energy can be transferred from the steady mean flow to the perturbation flow through interactions between the mean velocity and the perturbation vorticity. The

perturbation energy source term D_a is repeated here,

$$D_a = \rho_0 \mathbf{u}_0 \cdot (\xi' \times \mathbf{u}') + \rho' \mathbf{u}' \cdot (\xi_0 \times \mathbf{u}_0) \tag{5.32}$$

where ξ is the vorticity vector. The second term above is zero in an inviscid 2–D flow, but the first term may not be when the unsteady lift is nonzero and there maybe transfer of energy through the wake into the vortical mode. Normally the acoustic and vortical modes convect as if the other were not present, but they can easily be coupled by any surface which bounds the flow [27]. A sharp trailing edge of the airfoil provides just such a rigid body, and through the imposition of the Kutta condition there can be a net increase in the acoustic energy when the vortical mode gains energy from the mean flow.

Figure 5-32 shows the directivity patterns for the 3 angles. The azimuthal angle θ here is rotated by $-\alpha$ such that the reference angle is with respect to the chord line of the airfoil. As the angle of attack is increased, the sound radiation becomes amplified in the zone $90° < \theta - \alpha < 180°$ and is attenuated in the zone $0° > \theta - \alpha > -90°$. Notice that the directivity patterns for both the 3° and 5° cases are the same in the zone $0° > \theta - \alpha > -180°$, but the 5° case has significantly higher amplitude in the zone $0° < \theta - \alpha < 180°$ than the 3° case. The 5° case must, therefore, have higher energy content than the 3° case.

The effects of angle of attack is more clearly shown in the 3 amplitude contour Figures 5-33, 5-34, and 5-35. The contour plots clearly indicate that as the angle of attack is increased, the sound is amplified on the suction upstream area and is attenuated in the lower downstream zone.

The effect of angle of attack on the phase of pressure is illustrated in Figure 5-36. There is a rotation of phase in the counterclockwise direction. Notice also that there is no jump in phase across the wake line. The acoustic pressure is non–zero along the wake line, because the numerical case is no longer symmetric.

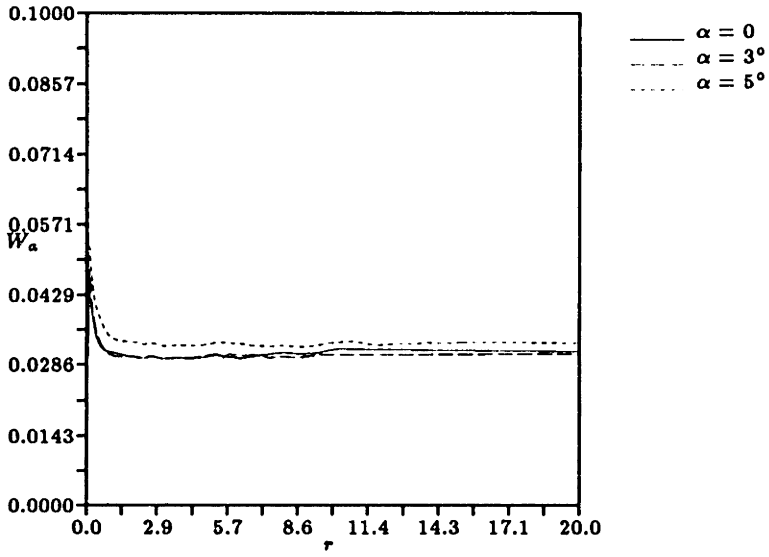

Figure 5-31: Acoustic Power versus Distance Along $+x$-Axis

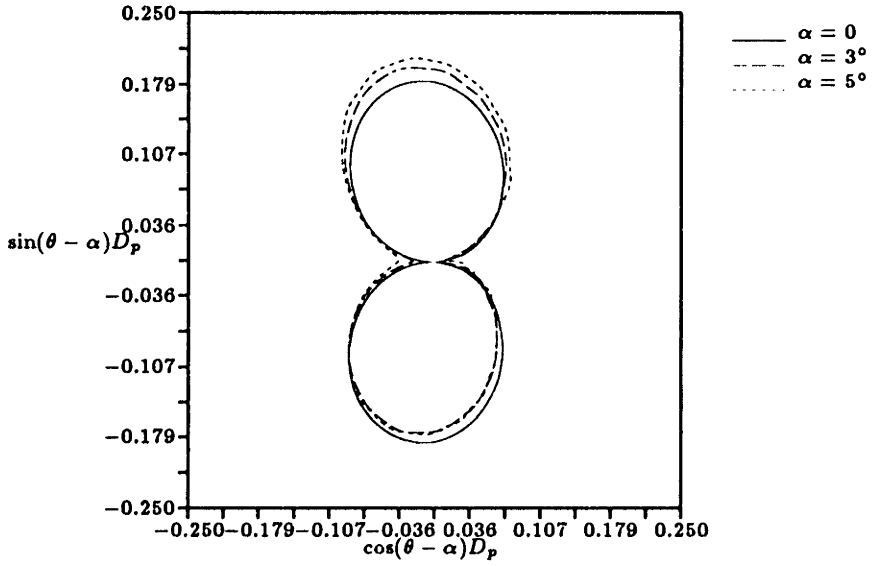

Figure 5-32: Polar Plot of D_p at the Far Field, $M_0 = 0.5$, $K = 2/3$

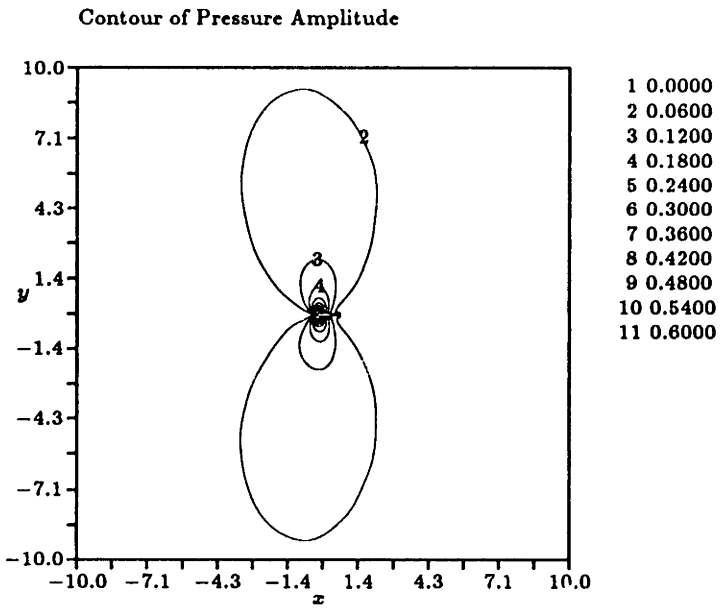

Figure 5-33: Amplitude Contour of Acoustic Pressure, $M_0 = 0.5$, $K = 2/3$, $\alpha = 0°$

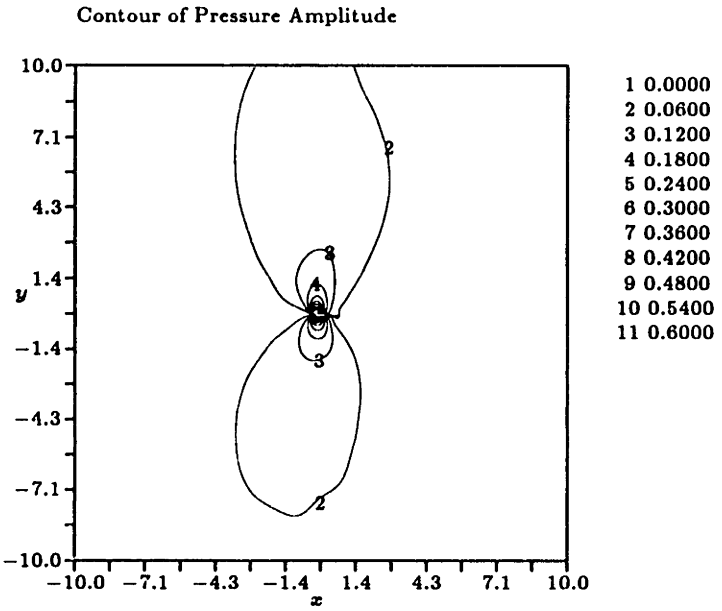

Figure 5-34: Amplitude Contour of Acoustic Pressure, $M_0 = 0.5$, $K = 2/3$, $\alpha = 3°$

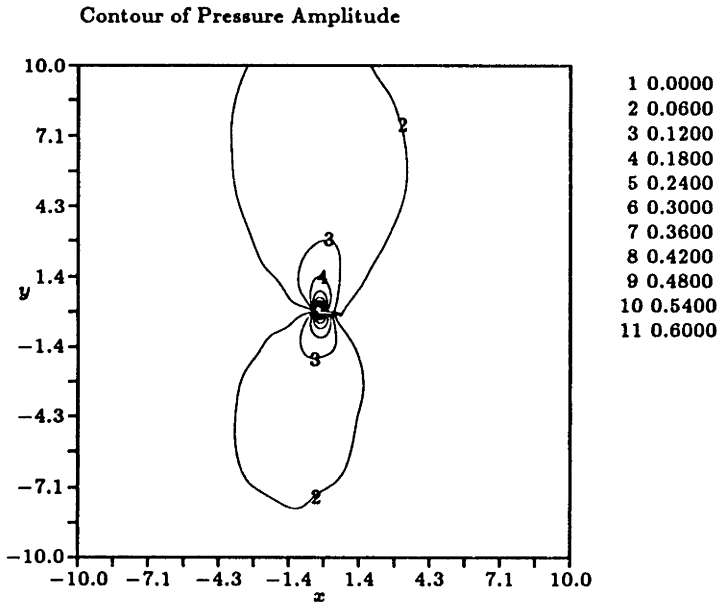

Figure 5-35: Amplitude Contour of Acoustic Pressure, $M_0 = 0.5$, $K = 2/3$, $\alpha = 5°$

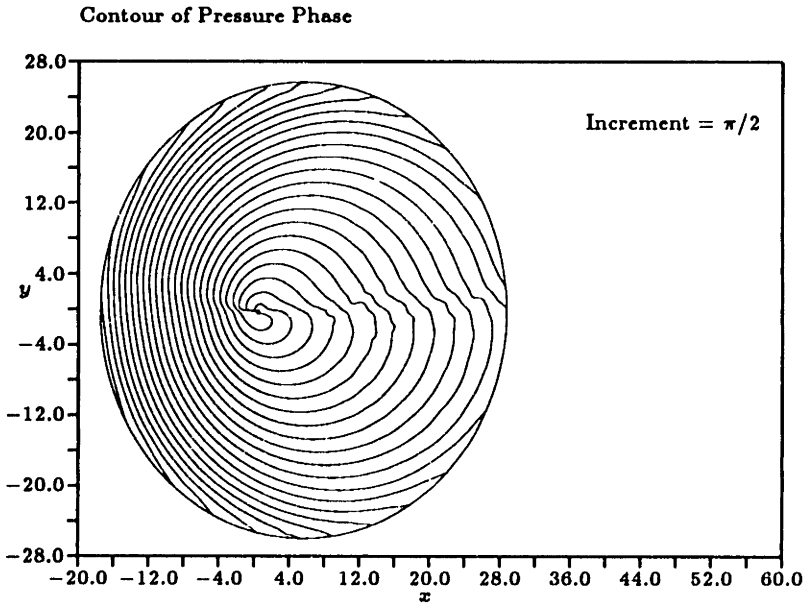

Figure 5-36: Phase Contour of Acoustic Pressure, $M_0 = 0.5$, $K = 2/3$, $\alpha = 5°$

Noncompact

Consider now 3 angle of attack cases for a NACA0012 airfoil subject to a noncompact gust of $K = 1.73$. The important parameters are tabulated below:

	M_0	M_{max}	ν	K	α	$\lvert\tilde{L}\rvert$	W_a
Case 1	0.5	0.62	3.0	1.73	0	0.404	0.026
Case 2	0.5	0.75	3.0	1.73	3°	0.388	0.025
Case 3	0.5	0.95	3.0	1.73	5°	0.427	0.029

Table 5.8: Parameters for $M_0 = 0.5$, $\nu = 3.0$ Varying Angle of Attack Cases

At 3° angle of attack there is a small decrease in the lift amplitude and sound energy. But at 5° angle of attack, there is again an increase in both the lift amplitude (+6 %) and the sound energy (+11 %). Apparently there was a transfer of energy from the mean flow to the acoustic mode via the wake.

Figure 5-38 shows the far field directivity patterns for the 3 angles, and the Figures 5-39, 5-40, and 5-41 show the contours of sound pressure in the domain. For the 3° case, the angle of attack has amplified the sound pressure on the upper front lobe while it has decreased both lobes on the lower side of the airfoil. This is similar to the events of the compact case. For the 5° case, however, there is an increase in sound pressure for *both* upper lobes of the airfoil and only the front lower lobe shows any decrease in sound amplitude. There seems to be an overall increase in sound energy for the 5° case.

Figures 5-42 and 5-43 show the acoustic pressure phase contours for $\alpha = 0$ and $\alpha = 5°$ cases, respectively. In the $\alpha = 5°$ case the phase lines appear to be rotated in the *clockwise* direction. This is in direct contrast to the compact case which, at an angle of attack, rotated the phase lines in the counterclockwise fashion.

The leading edge suction effect, which assures that in an inviscid flow the total force vector is purely in the lift direction, tends to rotate the phase in the counterclockwise fashion. This is what we observed in Figure 5-36. Further away from the airfoil, however, the mean bound vorticity on the airfoil rotates the pressure phase in the clockwise direction. Figure 5-37 illustrates that, at an angle of attack, the bound mean vorticity

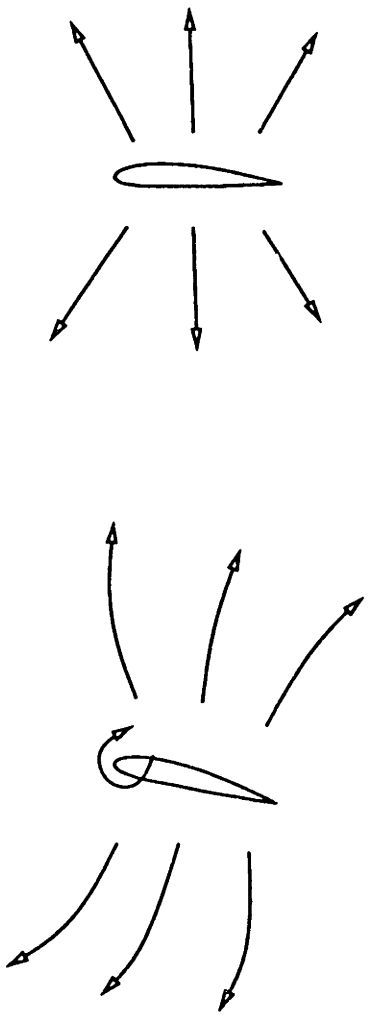

Figure 5-37: Diffraction of Sound by a Bound Vortex

diffracts sound propagation in the clockwise fashion. Thus there are two competing effects, one rotates the directivity in the counterclockwise direction and is dominant close to the airfoil, and the other rotates the directivity in the clockwise direction and is dominant further away from the airfoil. At a particular point in the domain either effect may be dominant depending on the distance from the airfoil and the compactness of the disturbance. The compact case has a much longer wavelength than the noncompact case, and the leading edge suction effect is more dominant than the bound vortex effect for the compact case at a fixed chord length from the airfoil.

Note also that there is considerably more 'warping' of the phase lines for the 5° case than for the no angle of attack case. There must be a higher level of diffraction in the 5° case. The phase lines are also closer together on the upper side of the airfoil for the 5° case, because the flow has a higher velocity on that side and the acoustic wavelength must be correspondingly shorter there.

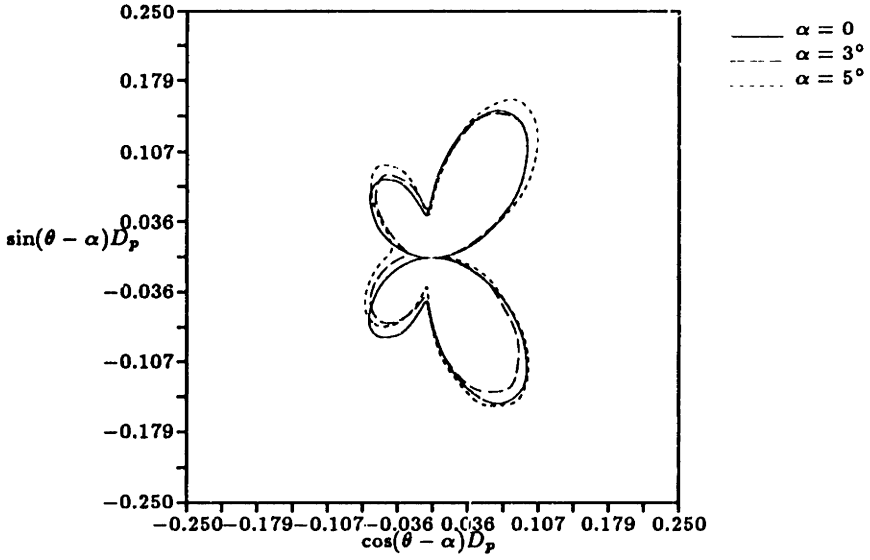

Figure 5-38: Polar Plot of D_p at the Far Field, $M_0 = 0.5$, $K = 1.7$

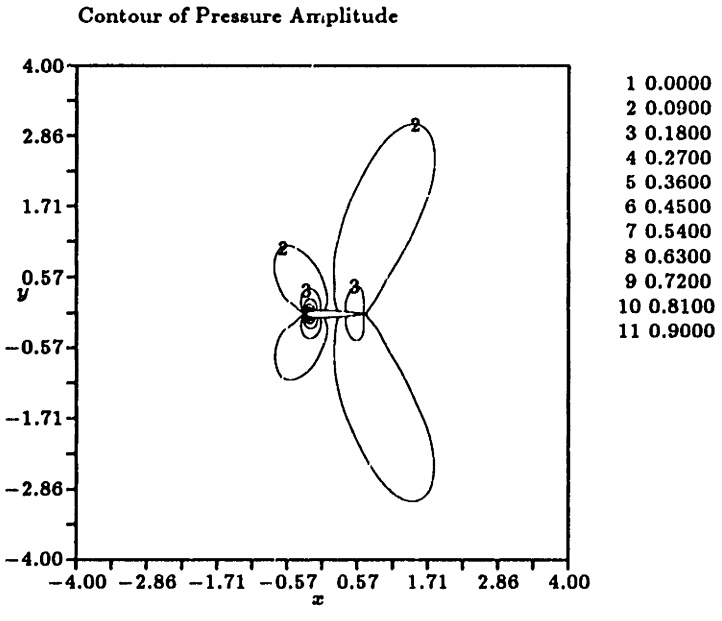

Figure 5-39: Amplitude Contour of Acoustic Pressure, $M_0 = 0.5$, $K = 1.7$, $\alpha = 0°$

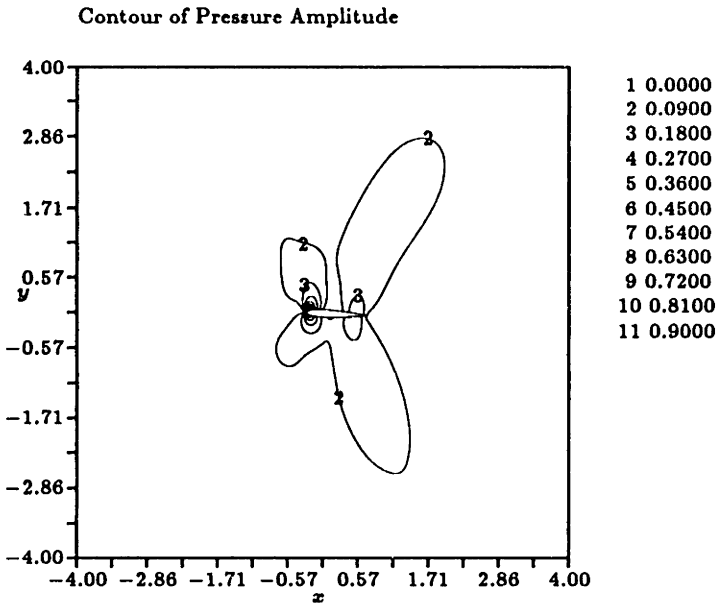

Figure 5-40: Amplitude Contour of Acoustic Pressure, $M_0 = 0.5$, $K = 1.7$, $\alpha = 3°$

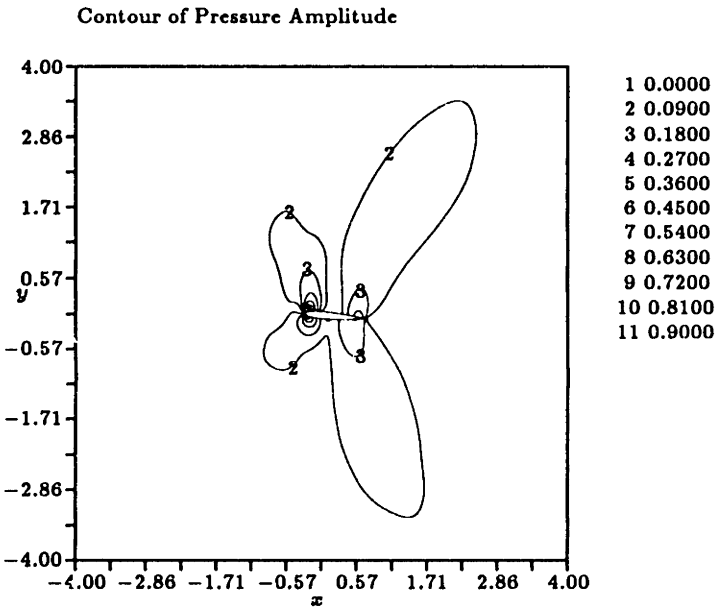

Figure 5-41: Amplitude Contour of Acoustic Pressure, $M_0 = 0.5$, $K = 1.7$, $\alpha = 5°$

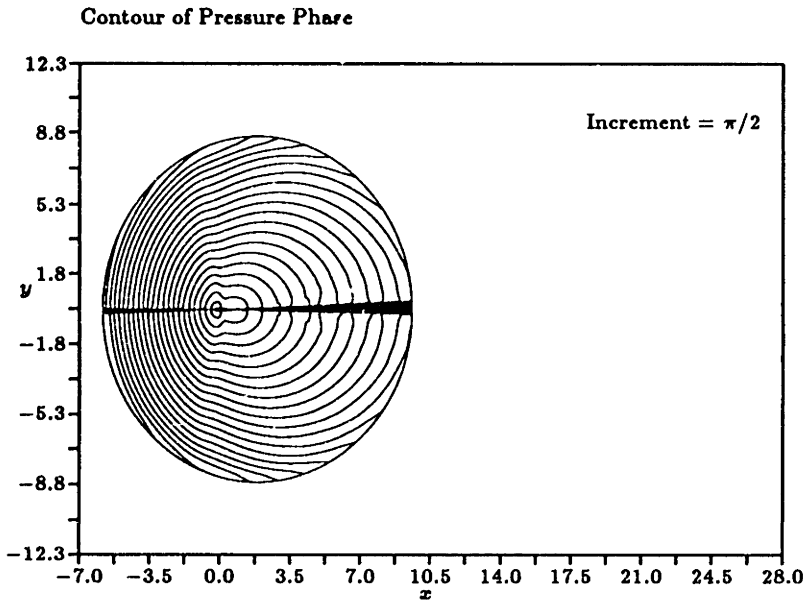

Figure 5-42: Phase Contour of Acoustic Pressure, $M_0 = 0.5$, $K = 1.7$, $\alpha = 0°$

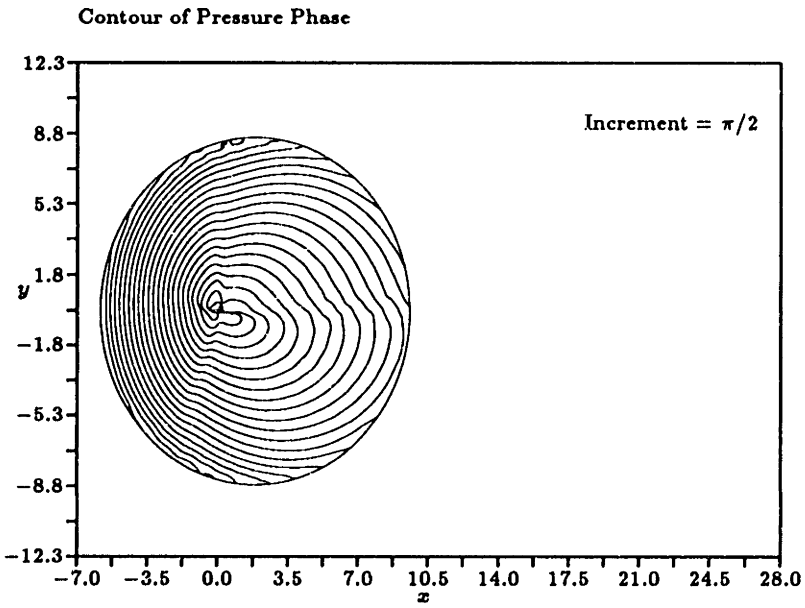

Figure 5-43: Phase Contour of Acoustic Pressure, $M_0 = 0.5$, $K = 1.7$, $\alpha = 5°$

Conclusions

We have seen that the effects of angle of attack on both the radiated sound directivity and phase can be large, even for moderate angles and compact gusts.

For compact gusts the effect of small angles of attack is to rotate the directivity in the counterclockwise fashion, while the overall sound energy decreases slightly. The linear theory would also predict the slight reduction in sound energy levels, but it would not account for the rotation of directivity. At larger angles of attack there is also a rotation of directivity, but in addition there is an increase in overall sound pressure and energy levels. The effect of angle of attack on a noncompact gust is similar to the compact case except that at the far field the bound vortex rotates the directivity in the clockwise fashion.

Evidently, the presently available linear theory would be applicable for an airfoil at an angle of attack only if the angle is very small ($<< 3°$).

5.3.4 Thick Airfoils at an Angle of Attack

The previous two sections have demonstrated that the effects of thickness and angle of attack on a vortical gust are to alter both the directivity and the overall noise levels in the flow field. We have attempted to highlight these effects by examining the thickness and lift problems as separate and distinct problems. However, in contrast with the case of linearized steady flow, the effects of thickness and angle of attack cannot simply be superposed. This is because the varying steady mean flow creates variations in the wavelength of the incident vorticity wave while also causing variations in both the amplitude and phase of its associated velocity field [28]. Such distortions of the incoming gust impart a nonlinear character to the problem.

We thus suspect that given a very thick airfoil at moderate angle of attack, the effects of thickness and angle of attack will be different from a simple summation of the previously described results.

Consider a NACA0024 airfoil at 5.5° angle of attack. We have computed two separate

cases, each of which corresponds with the compact and noncompact examples in the previous section. The pertinent parameters are tabulated below:

	M_0	M_{max}	ν	K	α	$\lvert\tilde{L}\rvert$	W_a
Case 1	0.5	1.0	1.0	2/3	5.5°	0.700	0.040
Case 2	0.5	1.0	3.0	1.73	5.5°	0.430	0.030

Table 5.9: Parameters for $M_0 = 0.5$, NACA0024 Airfoil Varying Reduced Frequency Cases

For case 1 there is an increase in both lift amplitude (+11%) and in radiated acoustic power (+33%) when compared with the zero incidence results. This is a much larger increase than the 5° NACA0012 case. Case 2 has a small incremental increase in lift amplitude (+6.4%) and in sound power (+15%) as compared to the zero angle results. Evidently the energy transfer process is a function of both the angle of attack and the reduced frequency of disturbance.

Figure 5-44 shows the far field polar directivity for the first compact case. The directivity of the previous compact angles have also been superimposed to allow a direct comparison. The radiated sound is greater in almost all directions, and there is a larger amplitude increase of the lower lobe than in the upper lobe. This is an unexpected result and is in direct contrast to the 3° and 5° NACA0012 case which indicated larger increases to the *upper* lobe. Because of the 'leading edge suction' effect, the pressure amplitude is higher over the upper surface of the airfoil than the lower surface; which in turn, usually creates a far field amplification and tilting of the upper lobe at the expense of the lower lobe. This is what we see in the 3° and 5° cases, but not in the latest 5.5° case.

Figure 5-45 is a contour plot of constant acoustic pressure amplitude. Notice that close to the airfoil we indeed have greater sound amplitude over the upper region than the lower region, but also notice that further away from the airfoil, the lower upstream region has higher sound amplitude than the comparable upper region. Apparently the diffractive effect of the bound vortex is dominant at the far field even for a compact disturbance when the airfoil is very thick.

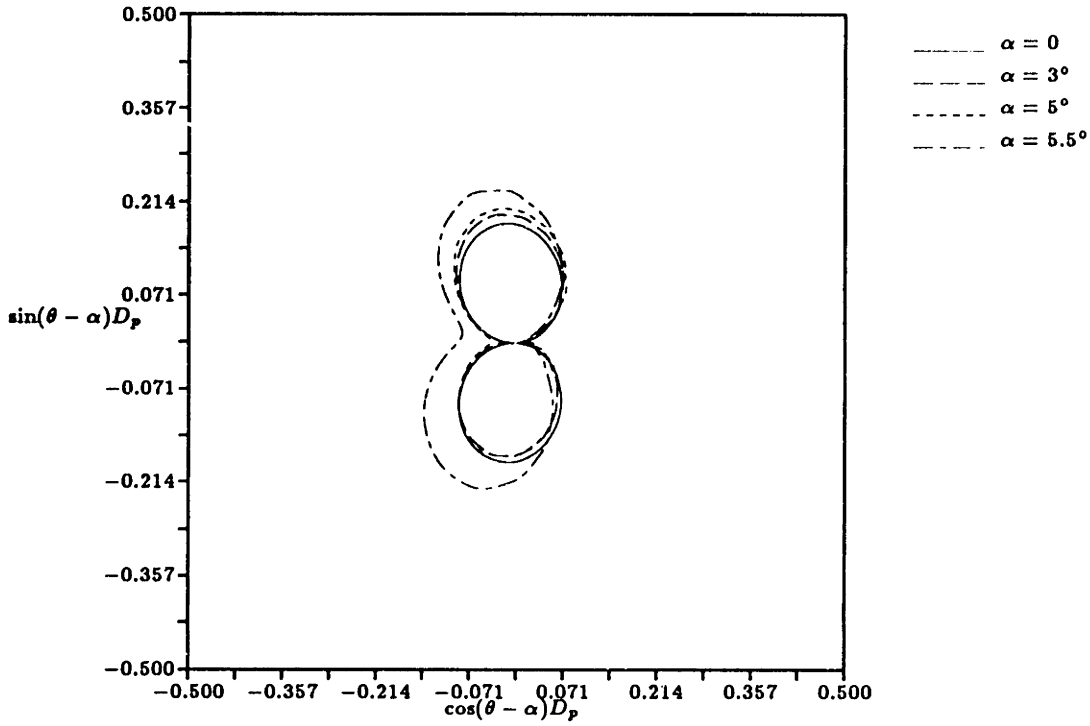

Figure 5-44: Polar Plot of D_p at the Far Field, $M_0 = 0.5$, $K = 2/3$

The constant pressure phase contours in Figure 5-46 indicate the similar near field phase rotation as in Figure 5-36 on page 142, but the thicker airfoil indicates opposite direction of rotation at the far field. Evidently the thicker airfoil has stronger bound vortex influence. Note also that close to the surface, the latest result has a more complicated phase structure due to complex mean flow–acoustic interactions created by the thicker airfoil.

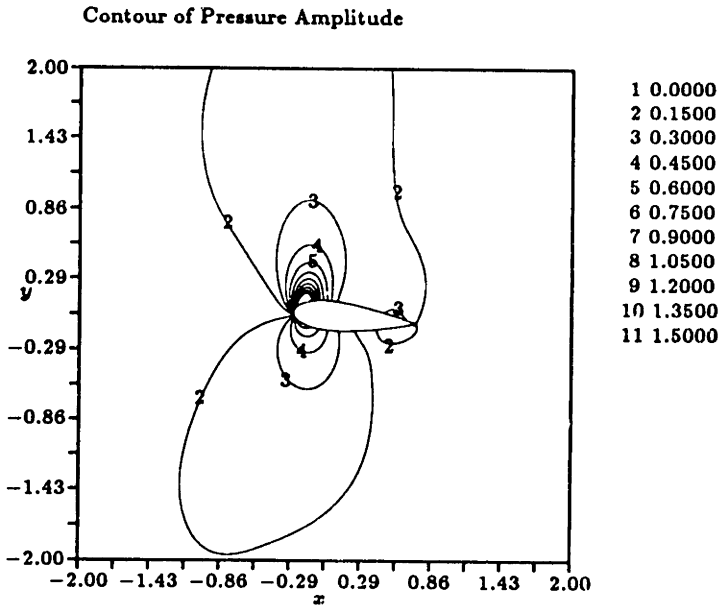

Figure 5-45: Amplitude Contour of Acoustic Pressure, $M_0 = 0.5$, NACA0024 Airfoil, $K = 2/3$, $\alpha = 5.5°$

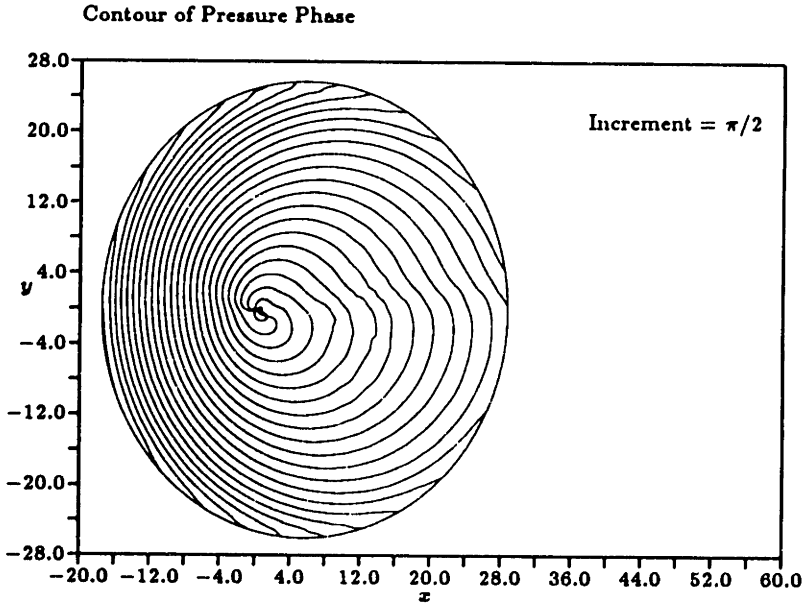

Figure 5-46: Phase Contour of Acoustic Pressure, $M_0 = 0.5$, NACA0024 Airfoil, $K = 2/3$, $\alpha = 5.5°$

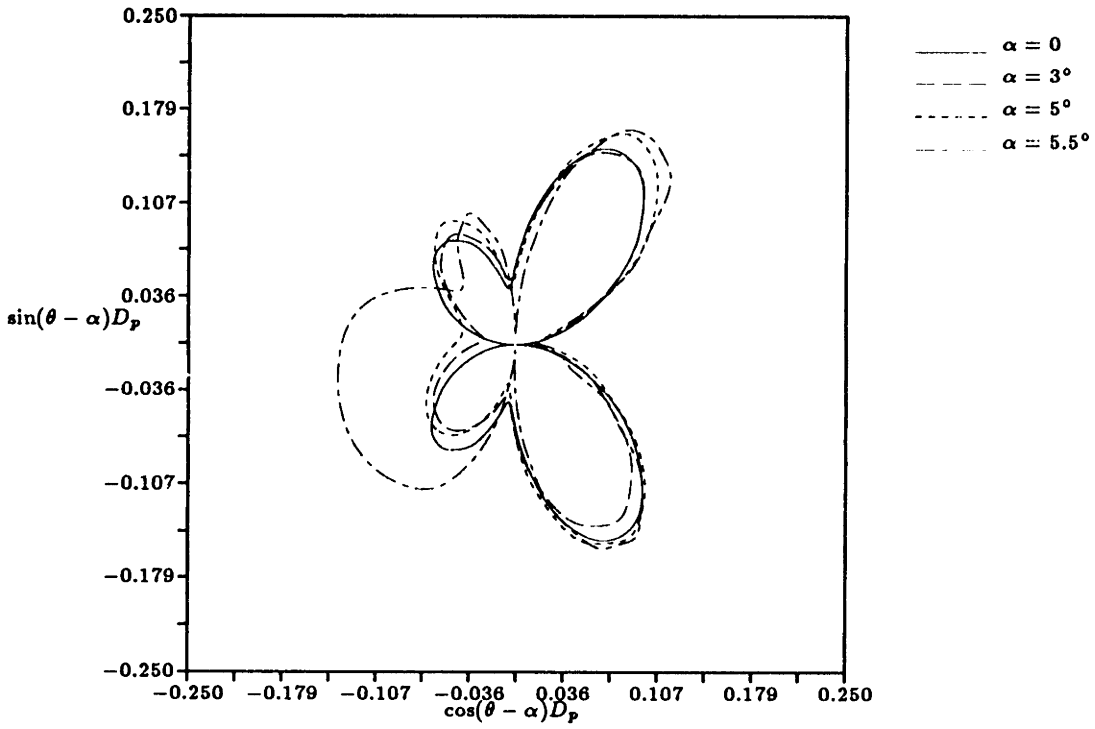

Figure 5-47: Polar Plot of D_p at the Far Field, $M_0 = 0.5$, $K = 1.7$

Figure 5-47 is the far field polar directivity for the noncompact 5.5° case. The previous noncompact results have again been superimposed to allow a direct comparison. The plot illustrates a large increase in sound in the forward upstream direction and a smaller increase in the down stream direction. There is also an attenuation in the normal direction. The mean flow has diffracted sound away from the center region towards the up and down stream directions. This is similar to the result obtained from the noncompact thickness study. But there is also a rotation of directivity which is unexpectedly larger than the 5° case, and the result is different from what one would expect from a superposition of thickness and angle of attack studies.

Figure 5-48 shows the amplitude contour of acoustic pressure. Compare this figure with Figure 5-41 on page 147. The pressure contours are considerably more complicated in the thicker case, especially near the surface; there must be a higher level of diffraction for the thicker airfoil. Notice also the increase in sound pressure in the lower region upstream of the airfoil.

The phase of acoustic pressure is shown in Figure 5-49. Compared to Figure 5-43, there is more 'warping' of the constant phase lines in the 5.5° case. This too is an indication of higher level of diffraction.

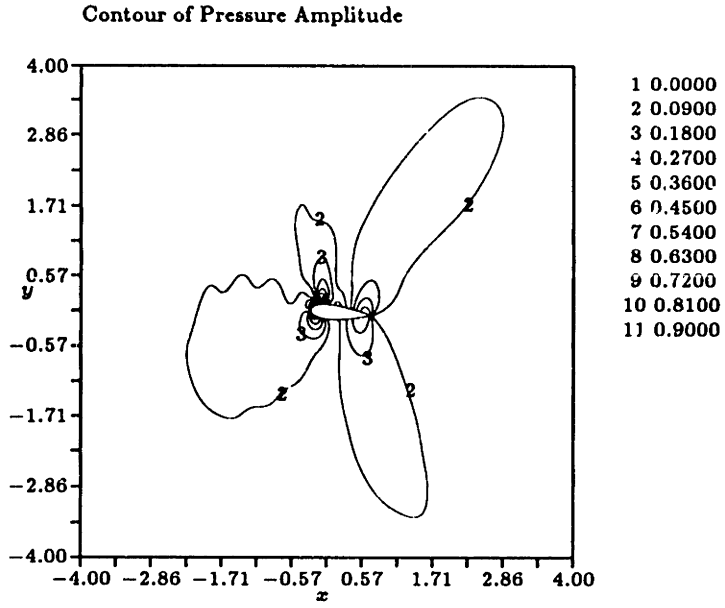

Figure 5-48: Amplitude Contour of Acoustic Pressure, $M_0 = 0.5$, NACA0024 Airfoil, $K = 1.7$, $\alpha = 5.5°$

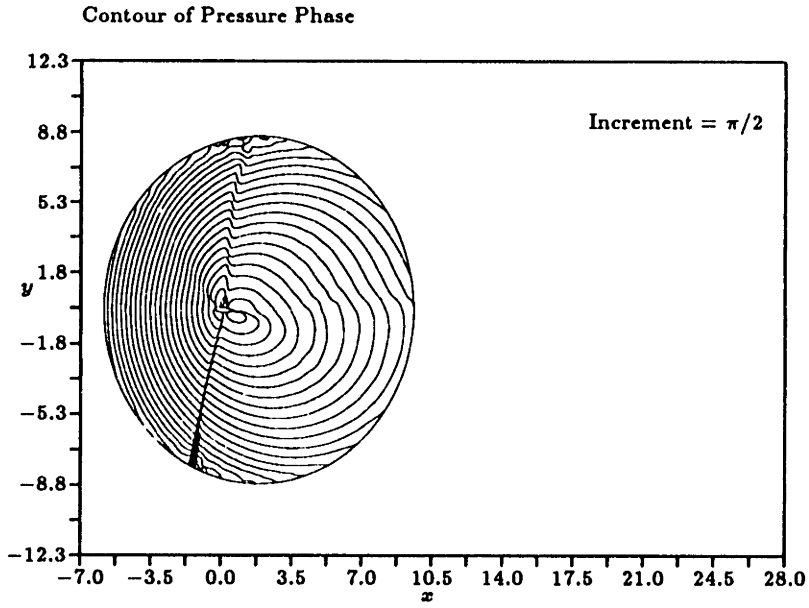

Figure 5-49: Phase Contour of Acoustic Pressure, $M_0 = 0.5$, NACA0024 Airfoil, $K = 1.7$, $\alpha = 5.5°$

5.4 Summary

In the past chapter we have investigated the effects of Mach number, airfoil thickness and angle of attack, and upstream compactness on the radiated sound of an airfoil impressed with a vortical gust.

A compact source appears as a single dipole radiating in phase, and at a constant Mach number, an increase in compactness ratio increases the retarded time differences which appear as additional lobes in directivity.

Changes in thickness do not alter the amplitude of unsteady lift or the radiated sound energy, but they do affect the directivity of sound when the compactness ratio is large. Given a moderate Mach number, the effect of thickness on a compact gust is small in terms of both the directivity and phase. For a noncompact gust, however, thick airfoils direct sound away from the center region towards the up and downstream directions. At a higher Mach number there also appears complex diffractive effects in the upstream direction directly ahead of the airfoil. The presently available linear theory is adequate for compact gusts only if the thickness is not very large (i.e. within the constraint of Equation 5.28), and is inadequate for noncompact cases.

For a compact source at small angles of attack, the directivity is rotated in the counterclockwise direction, and the amplitude of lift and the radiated sound energy decreases. At higher angles, the directivity is also similarly rotated, but in addition, there is also an extraction of energy from the mean flow which creates higher sound pressure levels at the far field. The effect of angle of attack on a noncompact source is similar except that the rotation of directivity at the far field is in the clockwise direction. It is believed that the mean bound vortex and its associated clockwise rotational flow alter the sound propagation direction in the clockwise sense. The linear theory is applicable only if the angle of attack is very small.

Unlike linear steady flow analysis, an airfoil at an angle of attack cannot be decomposed into a separate thickness and an angle of attack problem. Thus given a thick airfoil at a critical angle of attack, the noise level can easily be far higher than the

angle of attack alone would predict, and there may exist an unexpectedly complicated directivity structure.

Chapter 6

Sound Radiation from Oscillating Bodies

An oscillating body will generate propagating pressure disturbances, and if the frequency of oscillation is within the audible range, we perceive such disturbances as sound. This, in fact, is the basis of classical acoustics – sound generation from unsteady motion of bodies in still media.

In aeronautical applications an airfoil in unsteady motion, say flutter, can also create a similar sound radiation. However, if the airfoil is also convecting the propagating pressure wave can interact with the underlying mean flow, and such interactions may create unexpectedly complicated sound fields.

6.1 Oscillating Circular Cylinder

We begin the study of sound radiation from oscillating bodies by first considering an example from classical acoustics. Consider a circular cylinder in a quiescent field which oscillates in the x direction with an amplitude of 1 and a frequency of ω as shown in Figure 6-1.

The surface boundary conditions are that the local normal fluid velocity and the cylinder velocity are the same. In mathematical terms the boundary condition can be expressed as,

$$\tilde{\mathbf{u}} \cdot \mathbf{n}_0 = -i\omega\tilde{\mathbf{r}} \cdot \mathbf{n}_0 \tag{6.1}$$

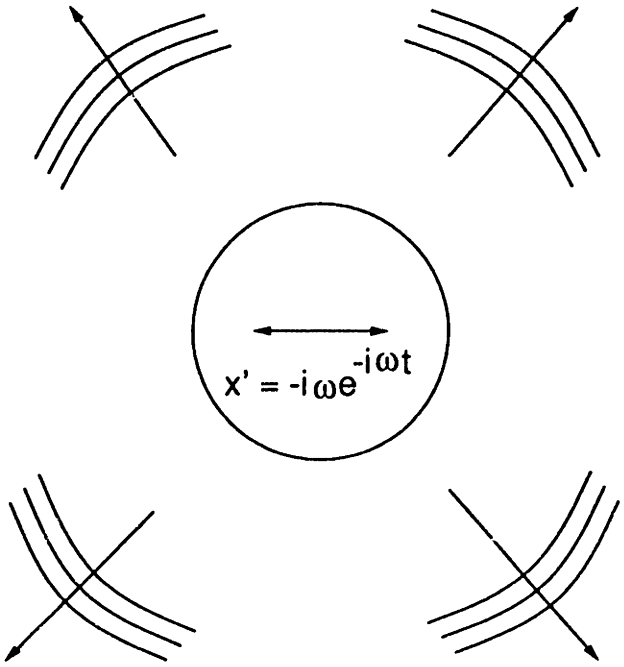

Figure 6-1: Oscillating Circular Cylinder

where,

$$\tilde{\mathbf{r}} = \mathbf{i}$$

$\mathbf{n_0}$ and $\mathbf{i}$ are the surface unit normal vector and the unit vector in the $+x$ direction, respectively.

At the far field we have implemented the specialized no-flow version of the Giles' boundary condition as described in Section 3.2.3 on page 62.

The runtime parameters were as follows:

- Grid: 129×100
- ω: 7.434 ($\lambda = 1$)
- ν_4: 0.01
- ν_6: 0.001
- Far-field: 1
- Iters: 800
- $L_2(\delta\tilde{\rho})$: 4.3×10^{-4}

$\omega = 7.434$ corresponds to an acoustic wavelength of 1 and so the domain contains exactly 1 wavelength in all directions. The computation required 800 iterations for almost 4 orders of magnitude convergence.

The exact analytic solution is provided in Reference [19] and it is,

$$\tilde{p} = \frac{\omega c_0 \cos\theta}{H_0^{(1)''}(\frac{\omega}{2c_0})} H_0^{(1)'}(\frac{\omega r}{c_0}) \tag{6.2}$$

where $r = \sqrt{x^2 + y^2}$ and θ is measured counterclockwise sense from the $+x$ axis.

Figures 6-2 and 6-4 show the amplitude and phase of the computed acoustic pressure, and Figures 6-3 and 6-5 show the amplitude and phase of the exact acoustic pressure. High accuracy in both the amplitude and the phase is evident in the entire domain. Figures 6-6 and 6-7 show the absolute error of the $\Re(\tilde{p})$ and the $\Im(\tilde{p})$. The largest absolute errors of approximately 0.03 for the real part and of approximately 0.04 for the imaginary part are at the far field. The average $L_2(\Delta|\tilde{p}|)$ was 1.2714×10^{-5}, the average $L_2(\Delta\Re(\tilde{p}))$ was 1.0638×10^{-5}, and the average $L_2(\Delta\Im(\tilde{p}))$ was 1.9656×10^{-5}.

In no flow situations, the combination of current numerical scheme and the specialized far field boundary conditions produce highly accurate results.

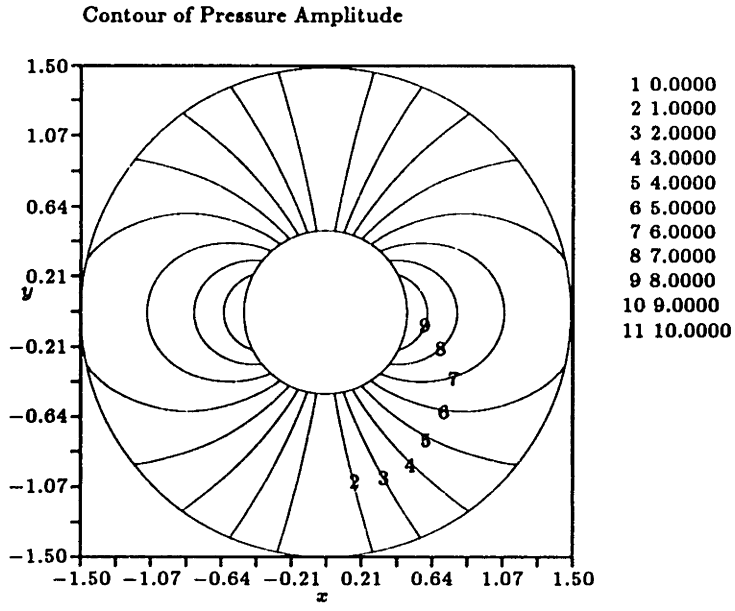

Figure 6-2: Amplitude of Computed Acoustic Pressure

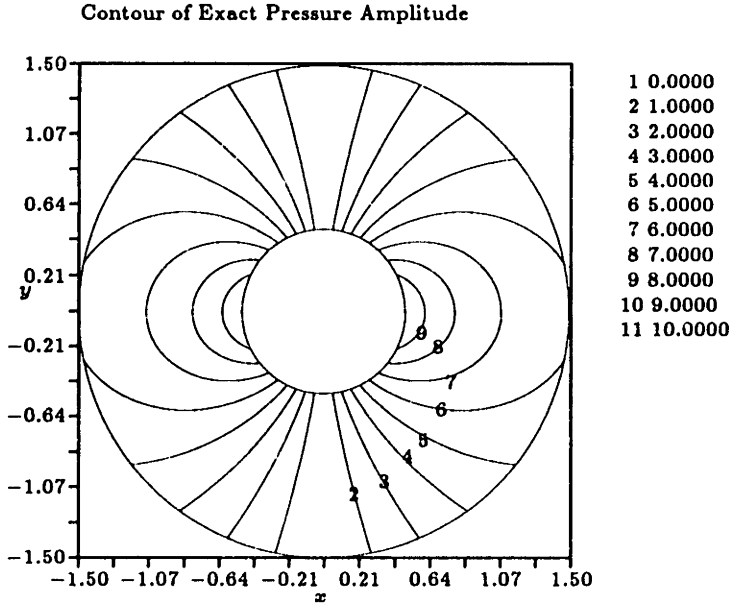

Figure 6-3: Amplitude of Exact Acoustic Pressure

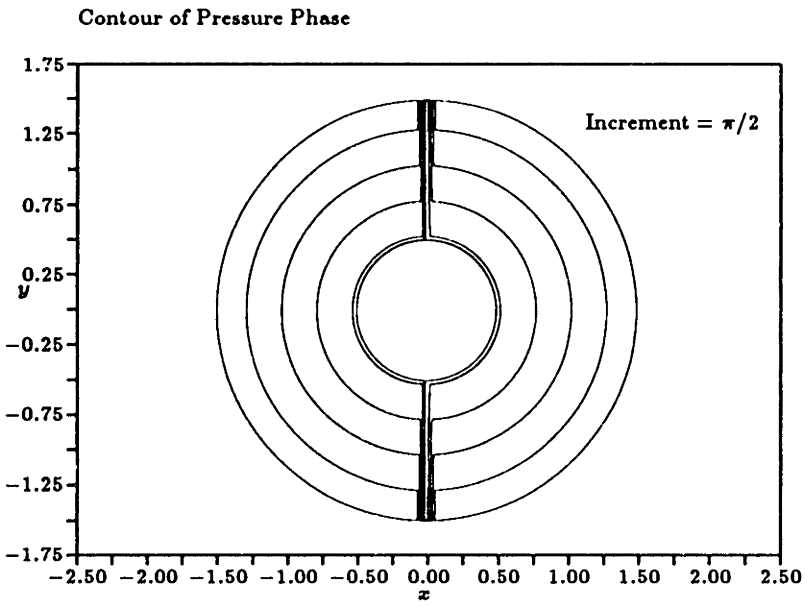

Figure 6-4: Phase of Computed Acoustic Pressure

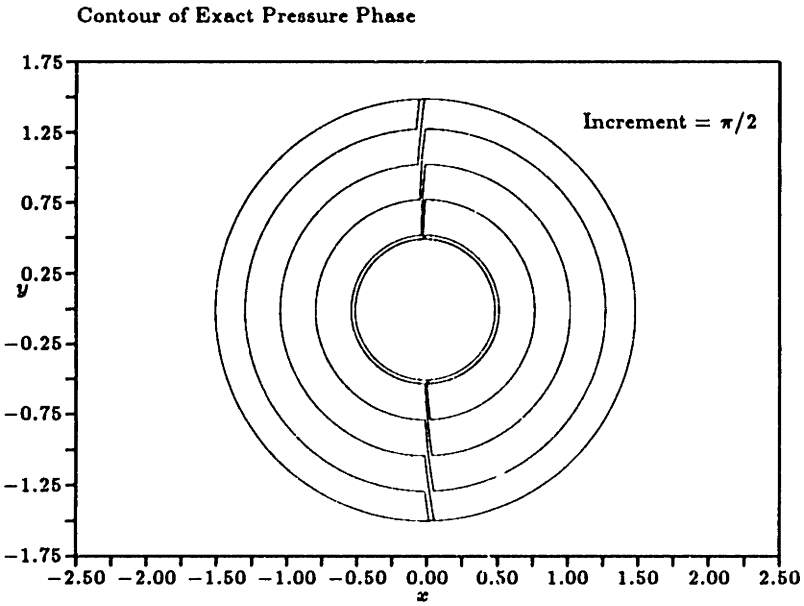

Figure 6-5: Phase of Exact Acoustic Pressure

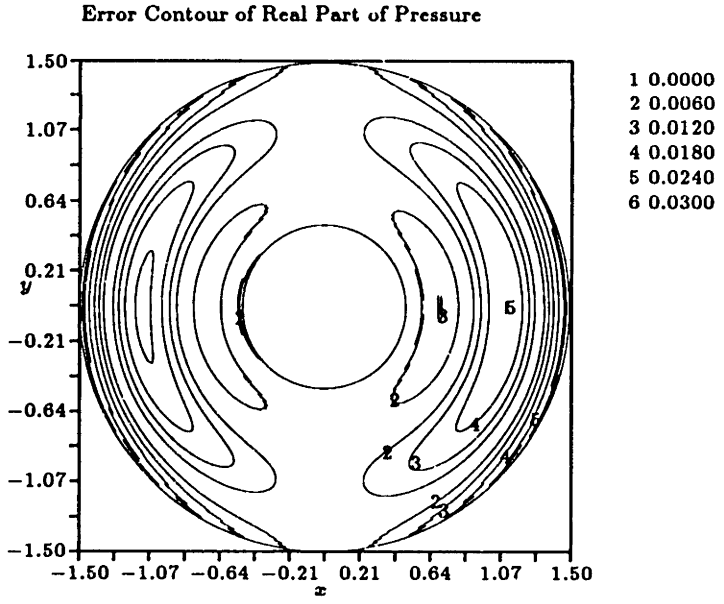

Figure 6-6: Absolute Value of Error of Real Part of Acoustic Pressure

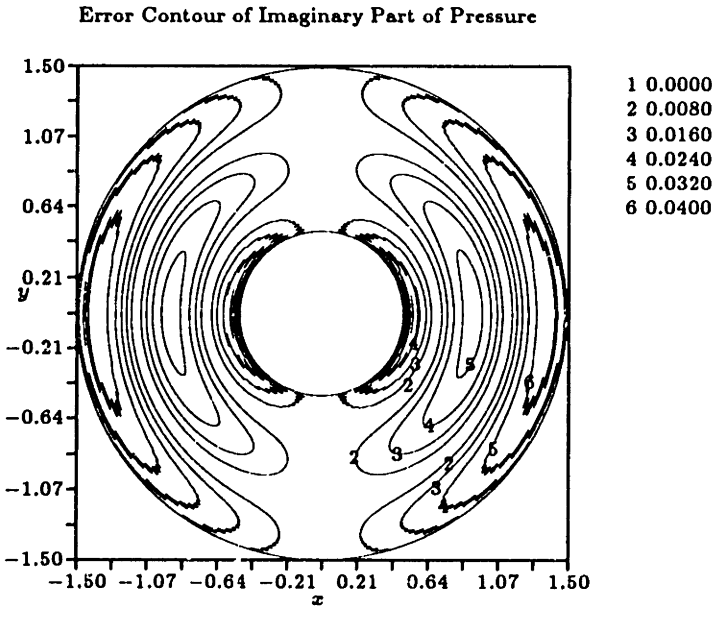

Figure 6-7: Absolute Value of Error of Imaginary Part of Acoustic Pressure

6.2 Oscillating Airfoil in a Steady Flow

We will now investigate the sound generation and propagation from an isolated, oscillating airfoil in a variety of mean flows. We seek to understand the influence of Mach number, angle of attack, thickness, and the frequency of oscillation on the radiated sound field.

Consider an oscillating airfoil in otherwise a steady flow of M_0 as shown in Figure 6.2. We assume that the oscillation is purely in the transverse y direction, and that the

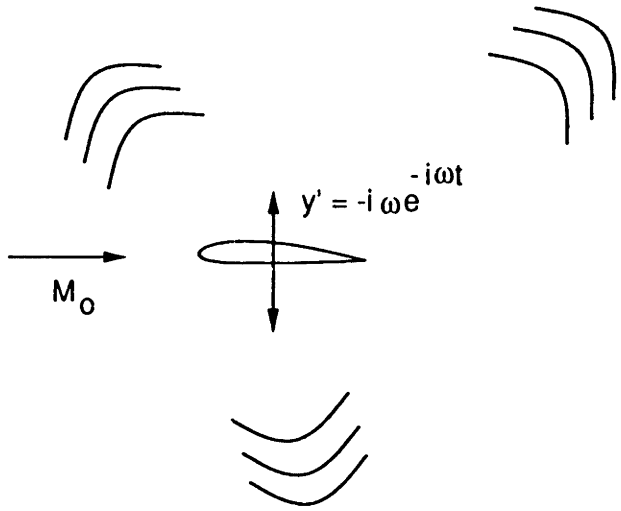

Figure 6-8: Sound Radiation from an Oscillating Airfoil

amplitude of oscillation is sufficiently small such that the complete flow can be thought of as a superposition of linear unsteady perturbation upon a steady mean flow. Then without any loss of generality, we can also assume that the airfoil oscillates with a single frequency ω.

The wall boundary conditions are that the total normal velocity with respect to the airfoil is zero, and since the surface is moving, the boundary condition is as in Equation 3.4,

$$\tilde{\mathbf{u}} \cdot \mathbf{n_0} = -\mathbf{u_0} \cdot \tilde{\mathbf{n}} - \tilde{\mathbf{r}} \cdot \nabla(\mathbf{u_0} \cdot \mathbf{n_0}) - i\omega\tilde{\mathbf{r}} \cdot \mathbf{n_0} \tag{6.3}$$

where,

$$\tilde{\mathbf{r}} = \mathbf{j}$$

and $\tilde{\mathbf{n}} = 0$ since the airfoil does not rotate. All the terms on the right hand side are functions of the steady mean solution and are known quantities. However, the second term involves the gradient of the normal mean velocity and must be computed numerically. At the wall the differencing must be of first order backward type in the normal direction, and it is thus important to maintain high grid densities near the surface so that the numerical solver remains second order accurate in the normal direction. This is particularly critical at the leading and trailing edges where the velocity gradients may be large.

A transversely oscillating airfoil is similar to an airfoil subject to a sinusoidal 'gust' of the previous chapter. In fact for a flat plate and $k \to \infty$, i.e. infinite wavelength, the two problems become identical. Thus we can use the incompressible gust validation case of the previous chapter as a check to ensure that the current surface boundary conditions are correctly enforced. The parameters for an oscillating flat plate (NACA0001 airfoil) in incompressible ($M_0 = 0.1$) are tabulated below. Notice that the parameters are identical to the incompressible gust case of Chapter 5 except that here all the values need to be scaled by the factor $-i\omega$.

- ω: 0.01
- Iterations: 8500
- ν_4: 0.01
- ν_6: 0.001
- $L_2(\delta\tilde{\rho})$: 3.8×10^{-4}

The computed total lift is $|\tilde{L}| = 3.455 \times 10^{-3}$ and $\arg(\tilde{L}) = -88.0°$, and the analytic solution is $|\tilde{L}| = 3.448 \times 10^{-3}$ and $\arg(\tilde{L}) = -82.7°$. There is approximately 0.2% error in amplitude and 5.3° error in phase. It appears that the surface boundary condition is correctly enforced.

In Chapter 5 we conducted several rigorous validation cases to ensure that the numerical scheme is accurate and consistent throughout the domain. We therefore are

confident that since the surface boundary condition seems to be accurately specified, the numerical scheme must be accurate and consistent throughout the domain for the current oscillating airfoil study as well.

6.2.1 Thickness

Consider now the effects of thickness on an oscillating airfoil. The currently available linear theory is again based upon the convective wave equation, and the aerodynamic analysis is as presented in Section 5.1 on page 99. The thickness does not have any effect on the unsteady solution, and, furthermore, we expect the radiation pattern to be a function of the compactness ratio K, where again K is defined as,

$$K = \frac{\nu M_0}{\beta^2}$$

and ν is the reduced frequency based on 1/2 chord length.

Compact Case

Let us first consider a compact case in which K is 1.0. We have computed 2 comparison studies for a NACA0001 and a NACA0013 airfoils in which the angle of attack is zero, and we have used a grid of 200x100 node points for both computations. Other pertinent parameters are as tabulated below:

	M_0	M_{max}	ν	K	τ	$\|\tilde{L}\|$	W_a
Case 1	0.7	0.71	0.729	1.0	1%	2.18	0.46
Case 2	0.7	0.98	0.729	1.0	13%	5.68	4.50

Table 6.1: Parameters for $M_0 = 0.7$, NACA0001 and NACA0013 airfoils in compact oscillation

In the previous chapter, we showed that the radiated acoustic energy from an airfoil subject to a vortical gust was only a weak function of the thickness of the airfoil. The thickness merely modified the direction of travel and had little effect on the overall integrated noise level.

The sound radiation due to an oscillating airfoil is, however, a direct function of the thickness. The 13% airfoil has significantly higher total lift ($\times 2.6$) and the radiated sound power ($\times 9.8$). The increased sound energy is graphically illustrated in the polar plot of far field directivity D_p shown in Figure 6-9. The sound amplitude is much higher for the 13% case in all directions, and, in addition, the sound pressure lobes indicate a direct 'tilt' towards the upstream direction for the 13% case.

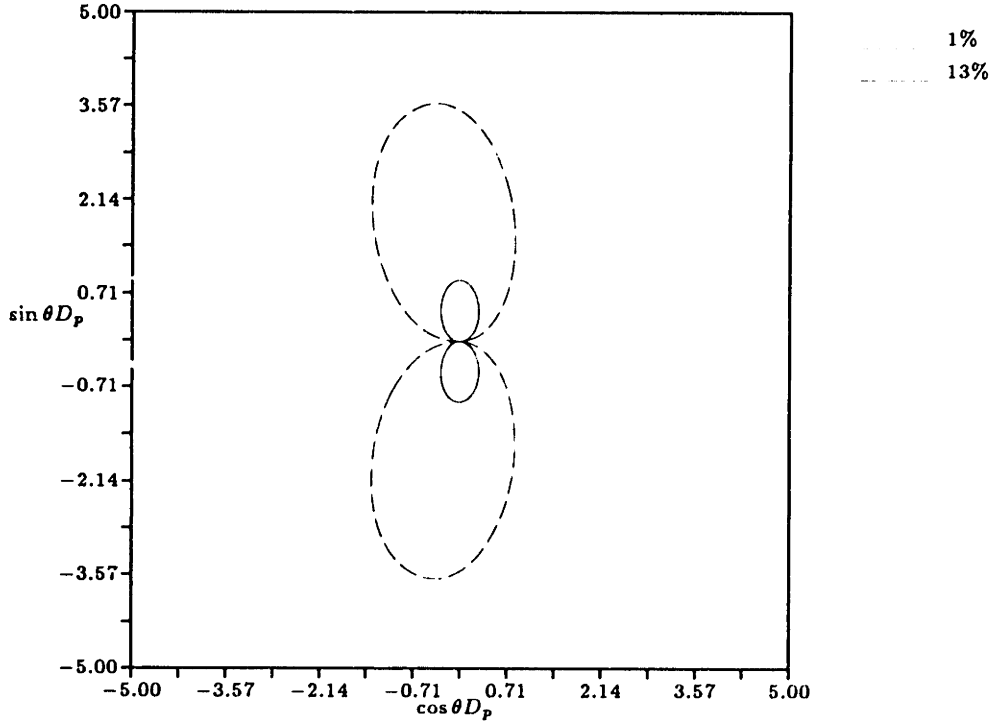

Figure 6-9: Polar Plot of D_p at the Far Field, $M_0 = 0.7$, $K = 1.0$

Recall that the surface boundary conditions for the gust problem is strictly a function of the incident vortical gust and is independent of the mean flow or the thickness. Thus the radiated sound energy is only weakly dependent on the thickness. The radiated sound energy in the oscillating airfoil case, however, is a strong function of the thickness, because the source distribution is a function of the mean flow gradient. Consider the surface boundary conditions of Equation 6.3. A large mean velocity gradient in the normal direction at a point translates directly to a large source strength at that point.

Thus a thick airfoil which has large mean flow gradients has strong source strengths along the airfoil.

Figures 6-10 and 6-11 show the contours of acoustic pressure amplitude in the domain. The 13% airfoil shows increased sound amplitude and a forward tilt in the directivity. Figures 6-12 and 6-13 show the contours of acoustic pressure phase in the domain. The constant phase contour lines for the two plots are virtually identical. Evidently the current long wavelength oscillation does not exhibit much diffraction for either thickness cases.

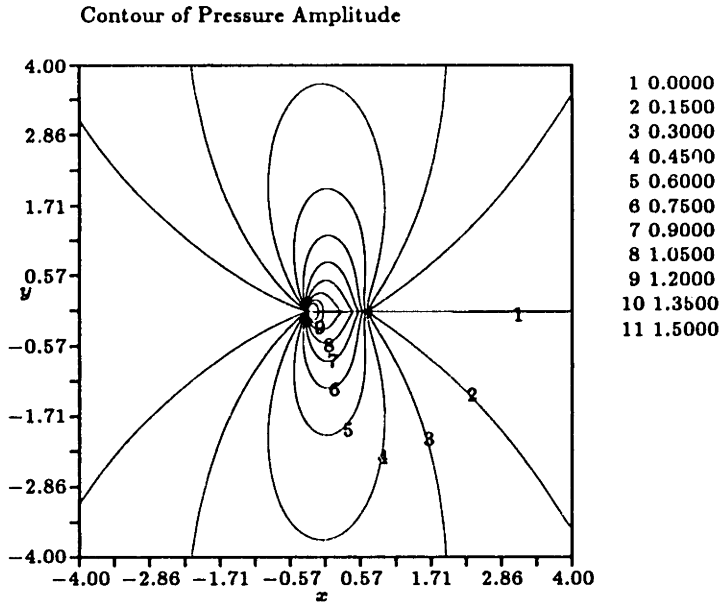

Figure 6-10: Amplitude of Acoustic Pressure, $M_0 = 0.7$, $K = 1.0$, $\tau = 1\%$

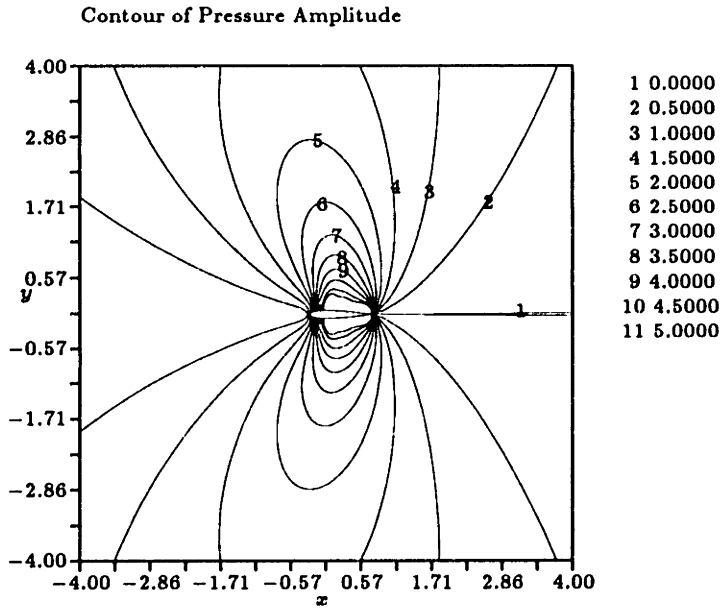

Figure 6-11: Amplitude of Acoustic Pressure, $M_0 = 0.7$, $K = 1.0$, $\tau = 13\%$

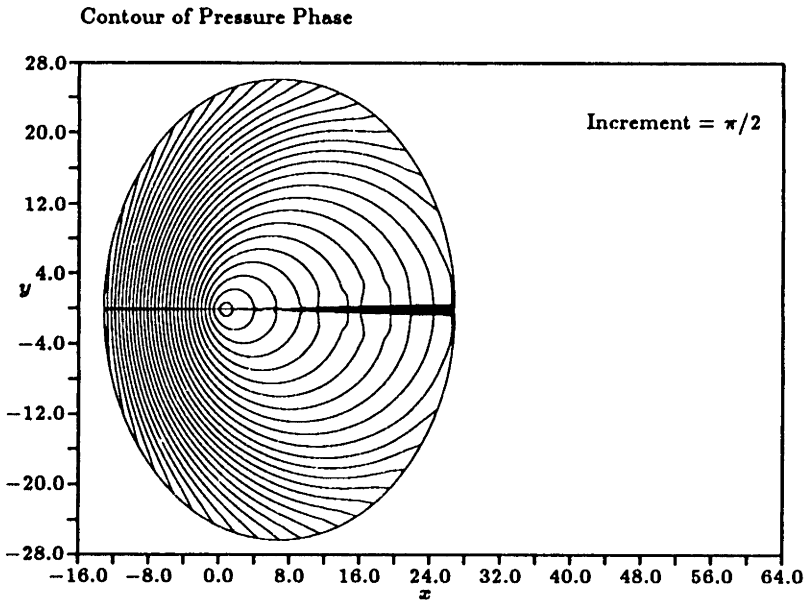

Figure 6-12: Phase of Acoustic Pressure, $M_0 = 0.7$, $K = 1.0$, $\tau = 1\%$

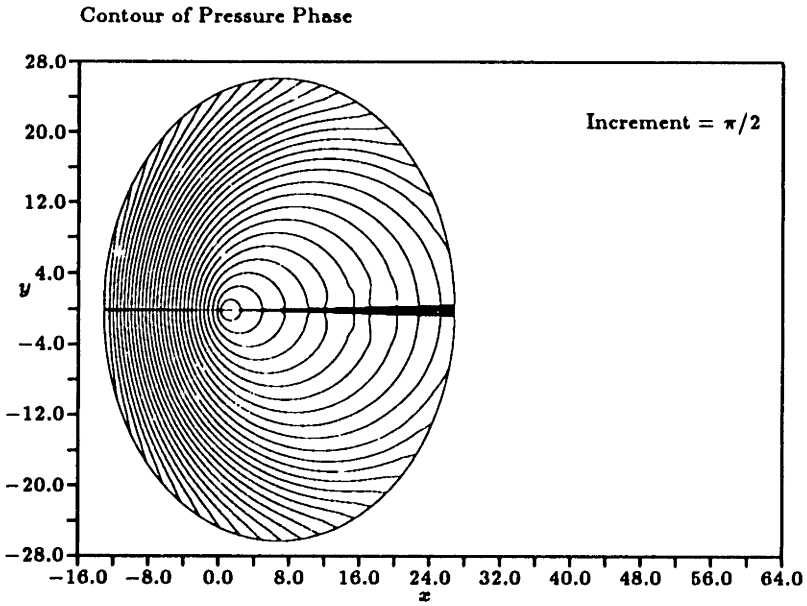

Figure 6-13: Phase of Acoustic Pressure, $M_0 = 0.7$, $K = 1.0$, $\tau = 13\%$

Noncompact Case

A 1% and a 13% NACA00 airfoils are oscillating such that the compactness ratio K is 3. A grid of 270x120 was used for both airfoils and the far field was chosen such that the domain contained approximately 4.5 wavelengths in all directions. The key parameters are tabulated below:

	M_0	M_{max}	ν	K	τ	$\|\tilde{L}\|$	W_a
Case 1	0.7	0.71	2.186	3.0	1%	7.88	11.9
Case 2	0.7	0.98	2.186	3.0	13%	9.16	18.0

Table 6.2: Parameters for $M_0 = 0.7$, NACA0001 and NACA0013 airfoils in noncompact oscillation

The 13% airfoil again has a higher lift (+16%) and sound power (+51%) than the 1% airfoil. The large mean flow gradient has increased the surface source strength.

Figure 6-14 is the polar plot of far field directivity. The sound pressure level is generally higher in all directions for the 13% airfoil, but it is particularly higher in the up and downstream directions. There also appears two additional lobes in the forward upstream direction. Compare the figure with the similar polar plot from the gust case in Figure 5-22 on page 130. The directivity patterns of the two figures are very similar since the mean flows are the same in the two cases.

Figures 6-15 and 6-16 show the constant acoustic pressure contours for the two thickness cases. The 13% case exhibits large pressure gradients through out the domain, particularly near the thick leading edge region. This is as expected since the mean flow gradients are also the greatest in the leading edge region.

The diffraction of sound from the varying mean flow is also illustrated in the pressure phase contour plots of Figures 6-17 and 6-18. Both airfoils exhibit some warping of the contour lines which shows that the airfoils are composed of sources 'firing' out of phase. The 13% airfoil also illustrates a complicated phase behavior directly ahead of the airfoil indicating that the forward upstream direction is a region of high diffraction. The acoustic wavelength is much shorter in the upstream direction and is, therefore,

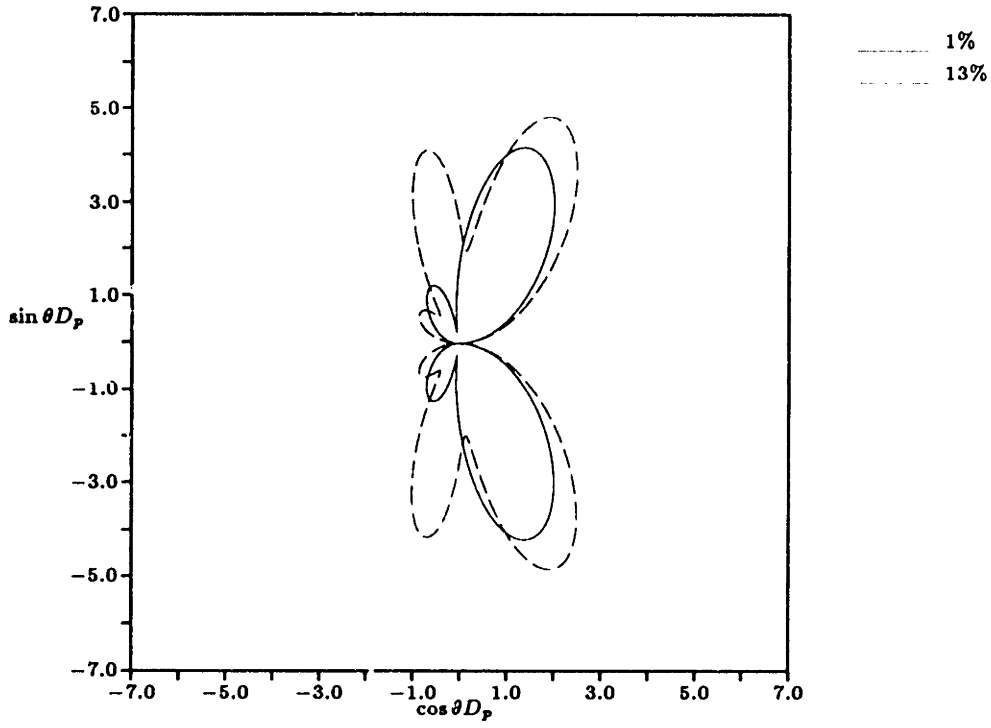

Figure 6-14: Polar Plot of D_p at the Far Field, $M_0 = 0.7$, $K = 3.0$

more sensitive to small changes in the flow gradients.

Conclusions

In the current section we have investigated the effects of thickness on the radiated sound field from an oscillating airfoil. When the oscillating frequency is sufficiently low such that the associated compactness ratio K is 1 or less, the thickness increases the integrated radiated sound energy. This amplification of sound is believed to be the result of an increase in the source specification along the airfoil caused by the gradients in the flow field. The directivity is also slightly altered such that the sound field has a slight tilt towards the upstream direction.

When the oscillating frequency is high and the airfoil is no longer a compact source of sound, the thickness still increases the integrated radiated sound energy, but, in addition, the diffractive effect of the varying mean flow amplifies sound in the upstream and

downstream directions and generally increases the complexity of the sound propagation patterns in the forward direction.

The currently available linear theory is unable to incorporate the diffractive effect of the varying mean flow or the increase in the overall sound pressure levels from the thickness. Consequently the linear method would only be applicable if both the thickness of the airfoil and the frequency of oscillation are quite small. We suspect that the constraint of Equation 5.28 is probably sufficient for the compact case, as was in the gust problem, but because of the diffractive effect of the mean flow, the constraint is probably insufficient in the noncompact case.

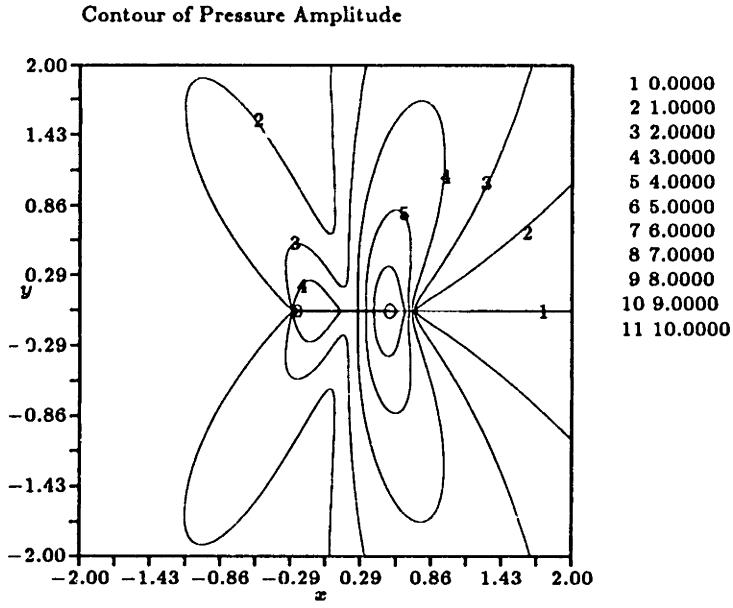

Figure 6-15: Amplitude of Acoustic Pressure, $M_0 = 0.7$, $K = 3.0$, $\tau = 1\%$

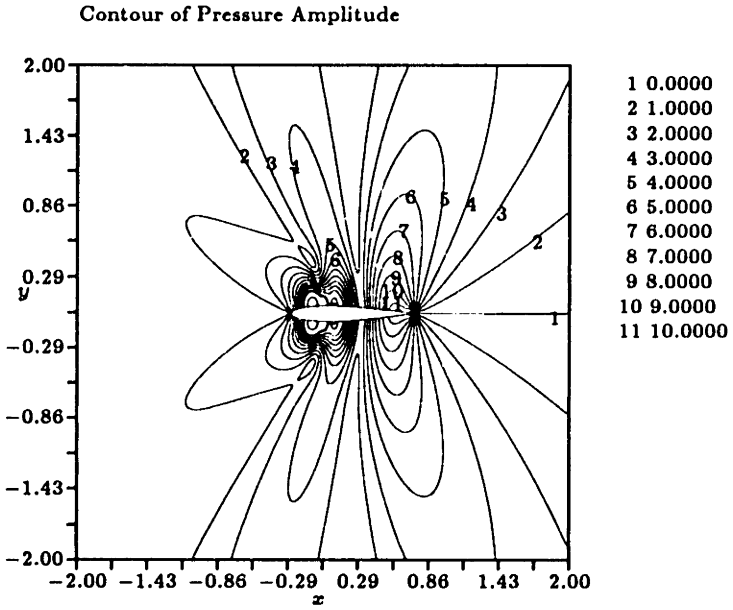

Figure 6-16: Amplitude of Acoustic Pressure, $M_0 = 0.7$, $K = 3.0$, $\tau = 13\%$

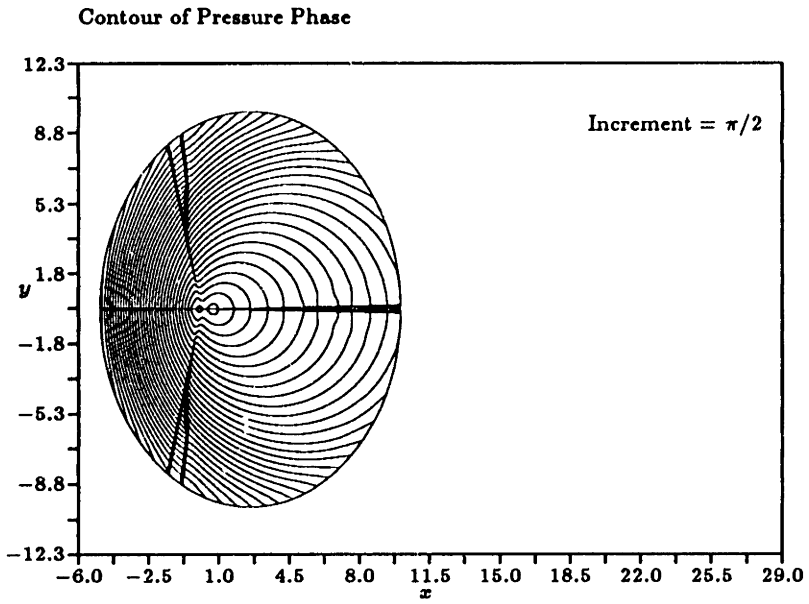

Figure 6-17: Phase of Acoustic Pressure, $M_0 = 0.7$, $K = 3.0$, $\tau = 1\%$

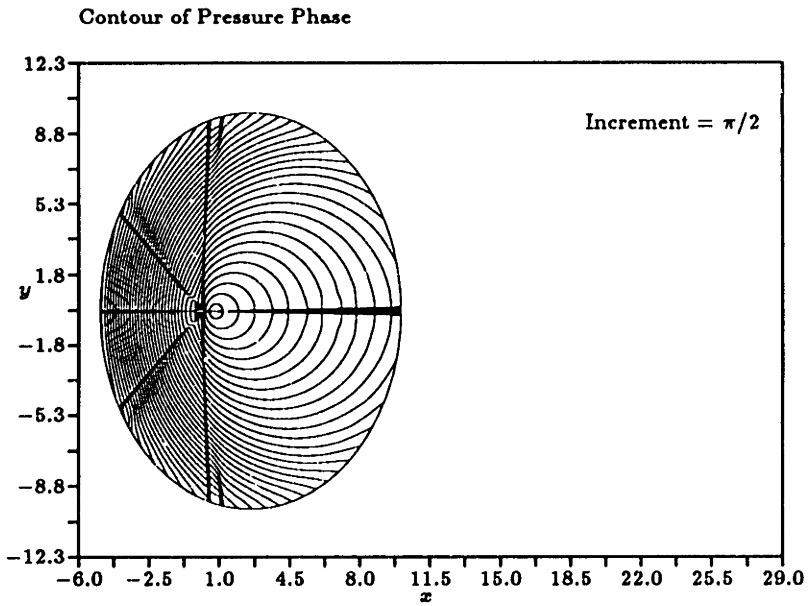

Figure 6-18: Phase of Acoustic Pressure, $M_0 = 0.7$, $K = 3.0$, $\tau = 13\%$

6.2.2 Angle of Attack

The effect of angle of attack on the radiated sound of an oscillating airfoil will now be studied. The linear theory based on the convective wave equation considers an airfoil at an angle of attack as an equivalent projected airfoil at zero incidence. Thus according to the linear theory, angle of attack should slightly decrease the amplitude of unsteady lift and the associated acoustic energy.

Compact Case

A thick NACA0024 airfoil is oscillating at a reduced frequency of $\nu = 1$ at 0 and 5.5° angles of attack. The computational domain contains 200x100 node points and the far field is approximately at 4 wavelengths away in all directions. The pertinent parameters are tabulated below:

	M_0	M_{max}	ν	K	α	$\lvert\tilde{L}\rvert$	W_a
Case 1	0.5	0.74	1.0	2/3	0	4.53	1.71
Case 2	0.5	1.00	1.0	2/3	5.5°	4.58	1.78

Table 6.3: Parameters for $M_0 = 0.5$, NACA0024 airfoils at $\alpha = 0$ and $\alpha = 5.5°$ in compact oscillation

There is a small increase in both the amplitude of lift (+1%) and the radiated sound power (+4%) for the $\alpha = 5.5°$ case. Evidently the radiated sound energy is only weakly dependent on the angle of attack for the current case.

Figures 6-20 and 6-21 show the contours of acoustic pressure amplitude in the domain. Near the airfoil the $\alpha = 5.5°$ case indicates higher sound pressure levels in the upper region than the lower region, but away from the airfoil the lower region has significantly higher sound amplitudes. Close to the airfoil the leading edge suction effect creates higher sound amplitudes for the upper region. Further away, however, the mean bound vorticity tends to direct sound towards the leading edge in the lower zone and towards the trailing edge in the upper zone, and thus sound amplitude levels are higher in the lower than in the upper region at the far field. Figure 6-19 clearly illustrates this

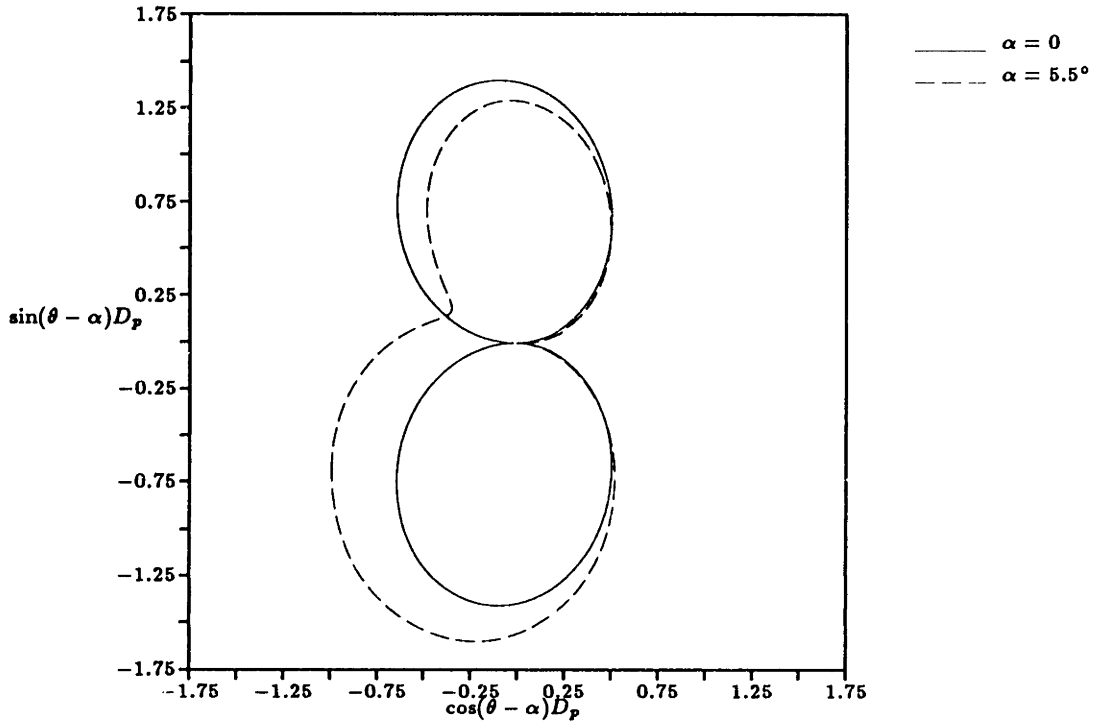

Figure 6-19: Polar Plot of D_p at the Far Field, NACA0024 airfoil, $M_0 = 0.5$, $K = 2/3$

mean flow diffraction effect. The lower lobe is amplified at the expense of the upper lobe for the 5.5° angle of attack airfoil.

Figures 6-22 and 6-23 show the contours of acoustic pressure phase for the two angles of attack cases. Note the rotation of phase lines in the clockwise direction for the 5.5° case; this is an indication of diffraction of sound towards the lower leading edge and the upper trailing edge regions.

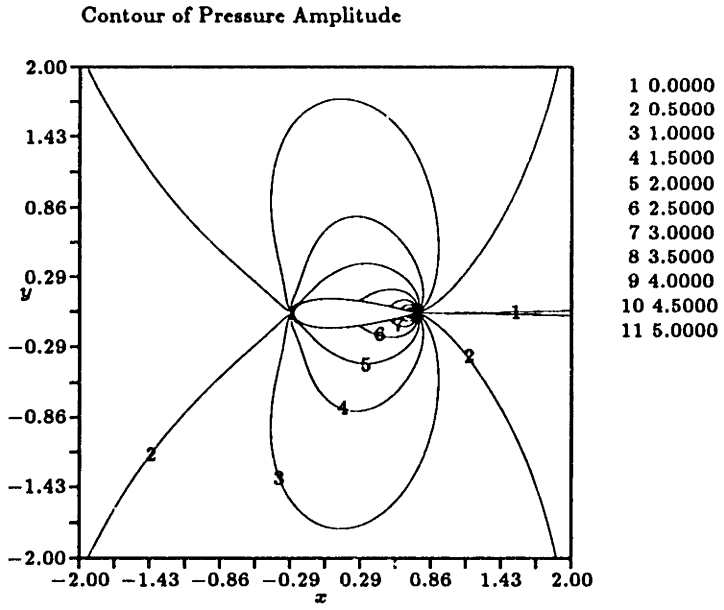

Figure 6-20: Amplitude of Acoustic Pressure NACA0024 airfoil, $M_0 = 0.5$, $K = 2/3$, $\alpha = 0$

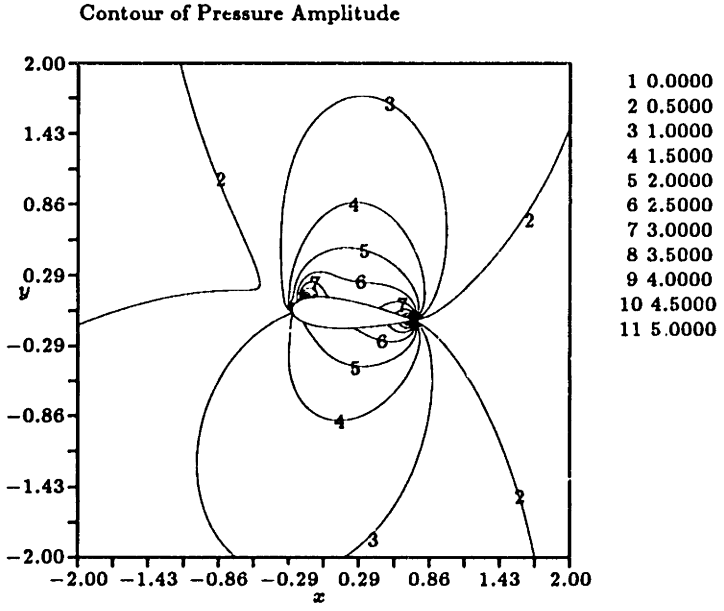

Figure 6-21: Amplitude of Acoustic Pressure NACA0024 airfoil, $M_0 = 0.5$, $K = 2/3$, $\alpha = 5.5^{\circ}$

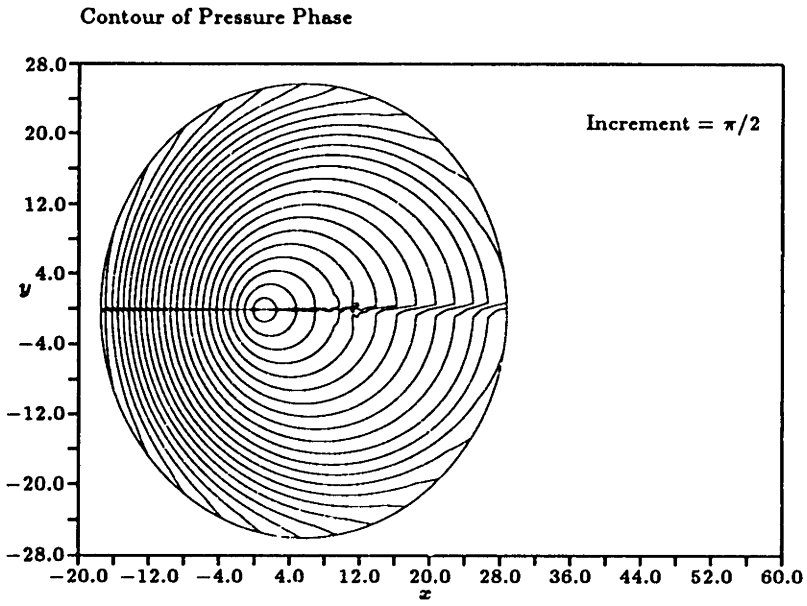

Figure 6-22: Phase of Acoustic Pressure NACA0024 airfoil, $M_0 = 0.5$, $K = 2/3$, $\alpha = 0$

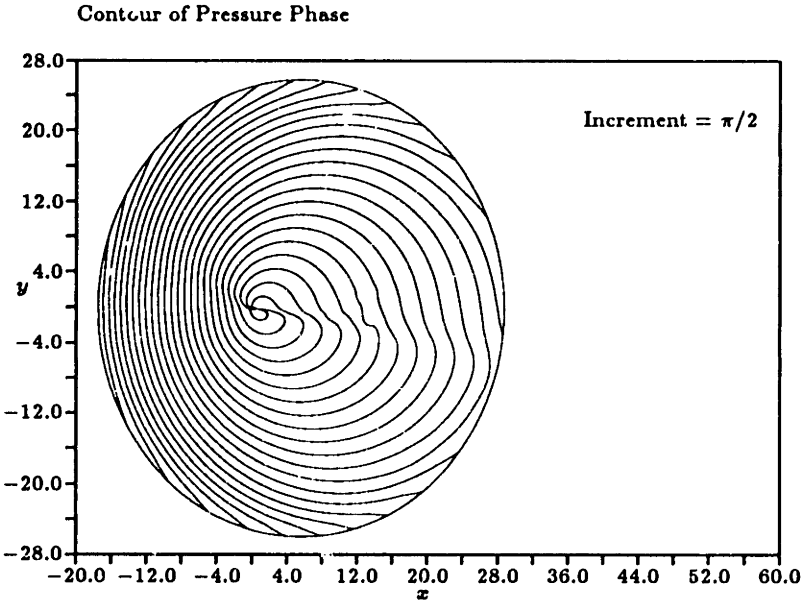

Figure 6-23: Phase of Acoustic Pressure NACA0024 airfoil, $M_0 = 0.5$, $K = 2/3$, $\alpha = 5.5°$

Noncompact Case

Consider an oscillating NACA0024 airfoil in a free stream of $M_0 = 0.5$ with angles of attack of $\alpha = 0$ and $\alpha = 5.5°$. The numerical domain contains 270x120 node points and approximately 4 wavelengths in all directions. The pertinent parameters are tabulated below:

	M_0	M_{max}	ν	K	α	$\|\check{L}\|$	W_a
Case 1	0.5	0.74	3.0	1.73	0	7.02	11.1
Case 2	0.5	1.00	3.0	1.73	5.5°	7.64	12.6

Table 6.4: Parameters for $M_0 = 0.5$, NACA0024 airfoils at $\alpha = 0$ and $\alpha = 5.5°$ in noncompact oscillation

There is a larger increase in both the amplitude of lift (+8.8%) and the radiated acoustic power (+13.5%) as compared to the compact case. Apparently there is a larger amount of transferred radiated sound energy from the mean flow when the compactness ratio is higher.

Figures 6-25 and 6-26 show the contours of acoustic pressure amplitude in the domain. Near the airfoil the $\alpha = 5.5°$ case has higher pressure levels on the upper surface than the lower surface; this is an indication of the leading edge suction effect. Further away from the airfoil the sound amplitude is higher in the lower region than the upper region, and this is an indication of diffraction by the mean bound vortex.

The diffractive effect of the bound vortex is also evident in the far field polar directivity plot of Figure 6-24. At 5.5° angle of attack there is a significant increase in the lower lobe, and there also appears an additional lobe towards the upstream direction.

Figures 6-27 and 6-28 show the contours of acoustic pressure for the two angles of attack cases. Away from the airfoil, the 5.5° case indicates a rotation of phase lines in the clockwise direction. In addition there are many regions of warped phase lines for both figures but particularly for the nonzero angle case; the warping of the phase lines is an indication of gradients in propagation direction, i.e. diffraction.

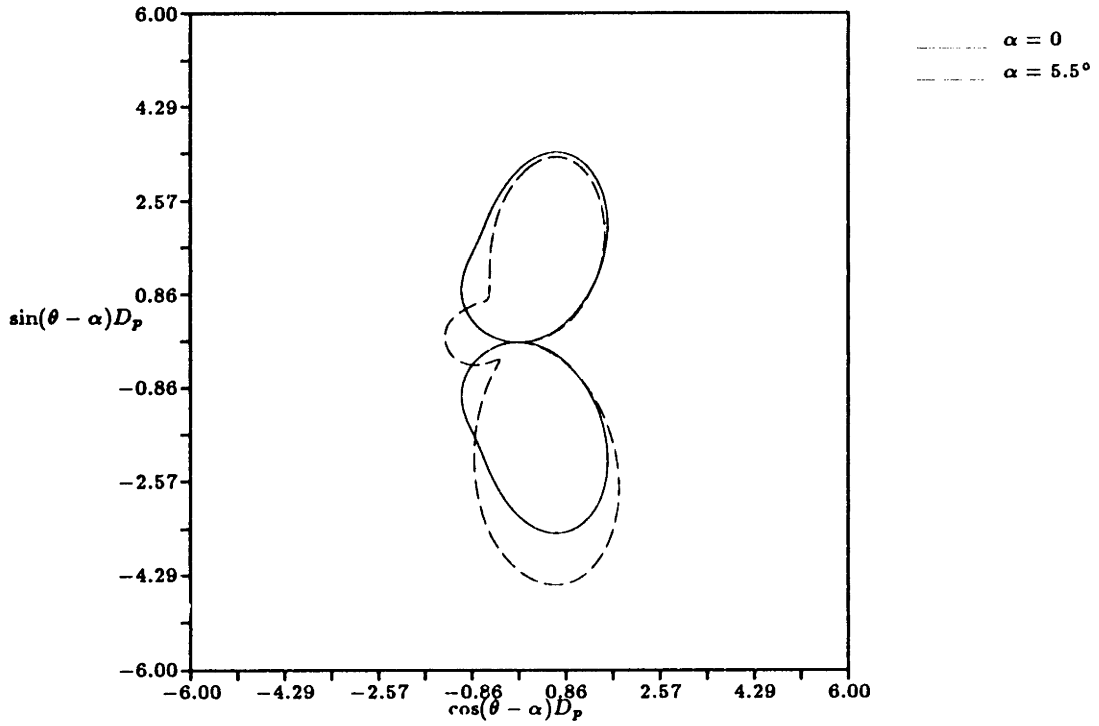

Figure 6-24: Polar Plot of D_p at the Far Field, NACA0024 airfoil, $M_0 = 0.5$, $K = 1.7$

Conclusions

In the current section we have investigated the effects of angle of attack on the radiated sound field of an oscillating airfoil.

When the frequency of disturbance is compact, the angle of attack modifies the sound propagation direction such that near the airfoil the leading edge on the upper 'suction' side of the airfoil is amplified, while in the far field the upstream lower 'pressure' side of the airfoil is amplified. The effects are purely diffractive, and the total radiated sound energy does not seem to be strongly influenced by the angle of attack.

Given a noncompact source of disturbance, the angle of attack similarly changes sound directivity in both the near and the far field, but in addition, there appears a new upstream directed sound lobe at the far field. The total radiated sound energy increases moderately when there is a mean lift.

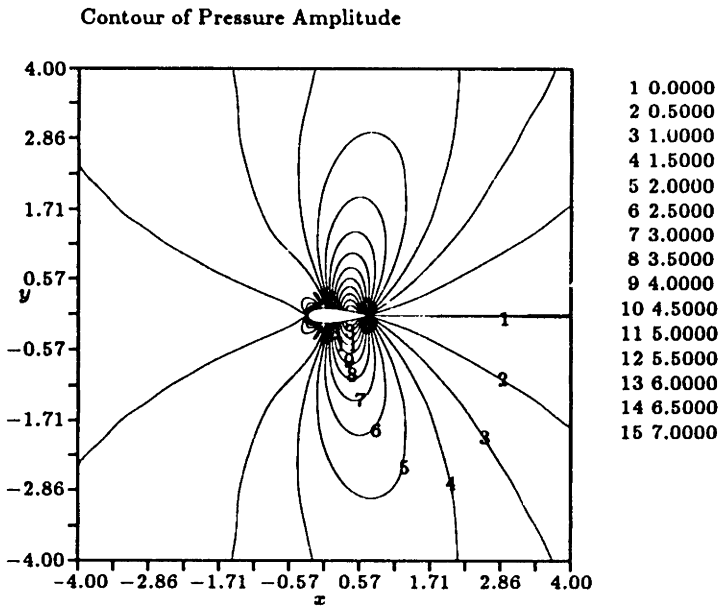

Figure 6-25: Amplitude of Acoustic Pressure NACA0024 airfoil, $M_0 = 0.5$, $K = 1.7$, $\alpha = 0$

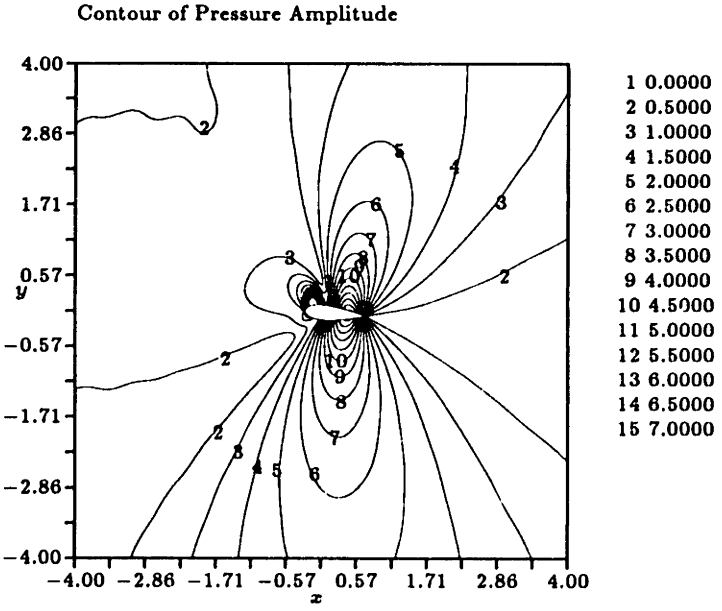

Figure 6-26: Amplitude of Acoustic Pressure NACA0024 airfoil, $M_0 = 0.5$, $K = 1.7$, $\alpha = 5.5°$

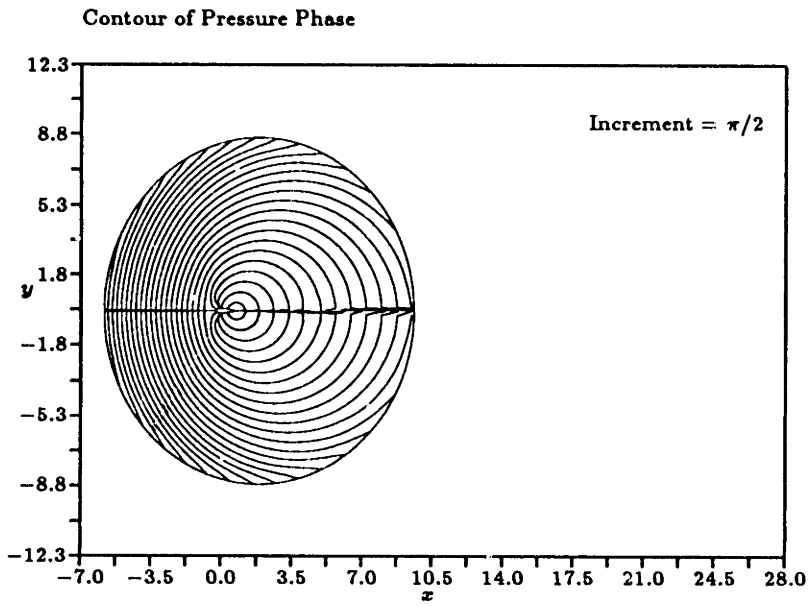

Figure 6-27: Phase of Acoustic Pressure NACA0024 airfoil, $M_0 = 0.5$, $K = 1.7$, $\alpha = 0$

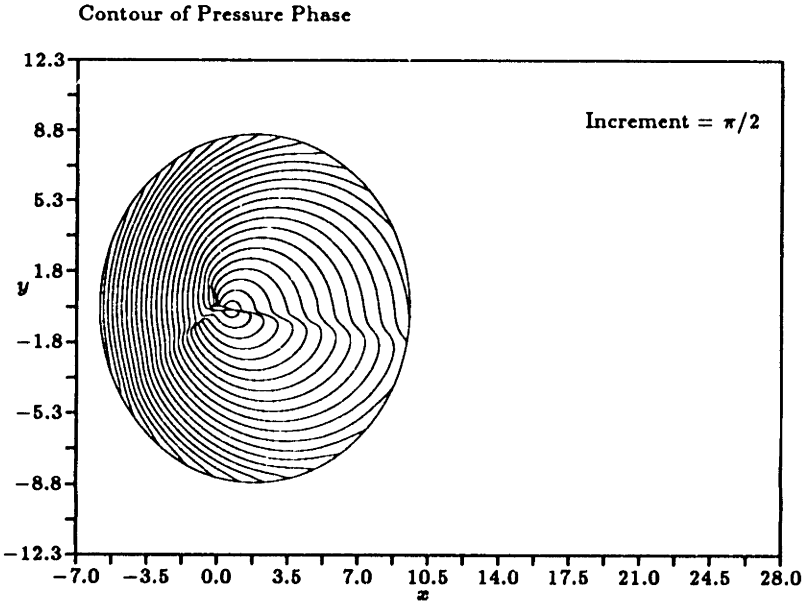

Figure 6-28: Phase of Acoustic Pressure NACA0024 airfoil, $M_0 = 0.5$, $K = 1.7$, $\alpha = 5.5°$

6.3 Summary

A preliminary study on the effects of the thickness and the angle of attack on an oscillating airfoil has been conducted. While we have not conducted enough case studies to conclude general trends, some early indications of the geometric influences have been formulated.

A thick symmetric airfoil at a zero incidence angle in a compact oscillation ($K < 1$) has a significantly higher acoustic energy level than a flat plate case. The symmetry of the problem precludes the mean flow energy transfer through the wake, and instead, the energy cascade is direct and immediate from the mean flow to the acoustic mode via interactions of the mean flow gradients and the oscillating airfoil. A large mean flow variations in the surface normal direction corresponds to large surface source strengths. The diffractive effect from the thickness is small for the long wavelength case, but there is a distinct upstream tilting of the directivity lobes due to the thick leading edge.

The same airfoil in a noncompact oscillation ($K > 1$) also has higher energy levels than a flat plate though to a lesser degree. The diffraction of sound due to the thickness is much more pronounced for the short wavelength case such that there is an amplification of sound in the zone $90° < \theta < 270°$, and moreover, in the directivity plot additional lobes appear in the forward upstream direction.

The linear theory based upon the convective wave equation does not incorporate the diffractive effect of the varying mean flow or the increase in the overall sound energy levels from the thickness. Thus the linear method would only be applicable if both the thickness of the airfoil and the frequency of the oscillation are small. As was in the previous chapter's gust case, the constraint of Equation 5.28 is expected to be sufficient for the compact case, but because of the diffractive effect of the mean flow, the constraint is probably insufficient in the noncompact case.

A thick symmetric airfoil at an angle of attack in a compact oscillation has only slightly higher energy levels when compared to the same airfoil at zero incidence. Apparently the energy transfer from the vortical wake is insignificant when compared to

the direct energy transfer through the thickness contributions. The diffraction of sound from the leading edge suction and the bound vortex effects create a sound field at the far field which has amplified sound pressure levels in the lower $180° < \theta < 270°$ zone.

The same airfoil in a noncompact oscillation has moderately higher energy levels than the same airfoil at zero incidence. The diffraction of sound from the mean bound vortex dominates at the far field, and there appears amplified pressure levels in the upstream direction.

The linear theory based upon the convective wave equation is unable to predict the diffraction of sound from both the leading edge suction and the bound vortex contributions, and therefore, is ineffective for thick airfoils at an angle of attack.

Chapter 7

Scattering of Sound

A traveling sound wave which encounters a solid body will be scattered by that object, and the scattered sound could, in turn, interact with the incident wave to create a complicated sound field composed of 'shadow' and 'illuminated' zones. In aeronautical applications, the scattering could be further complicated by the influence of the varying mean flow and the imposition of the Kutta condition. Past studies [35, 62] have suggested that the integrated scattered sound energy is strongly influenced by the unsteady lift, and that the overall noise level heard at the far field is a function the Mach number, the frequency, and the angle of the incident wave.

In this chapter, we will discuss some important aspects of the scattering phenomena, particularly as it pertains to external aerodynamic situations. We seek to understand the effects of flow and wave parameters such as the the Mach number, the angle of attack, and the frequency of the incident wave on the scattered sound field.

We will begin the analysis with a validation test case from classical acoustics.

7.1 Scattering Sound by a Circular Cylinder

Scattering of plane waves by a circular cylinder was computed as a good test case since there exists an analytic solution to the problem [50]. The incident plane waves were of the form,

$$p_i' = e^{i(kx-\omega t)} \tag{7.1}$$

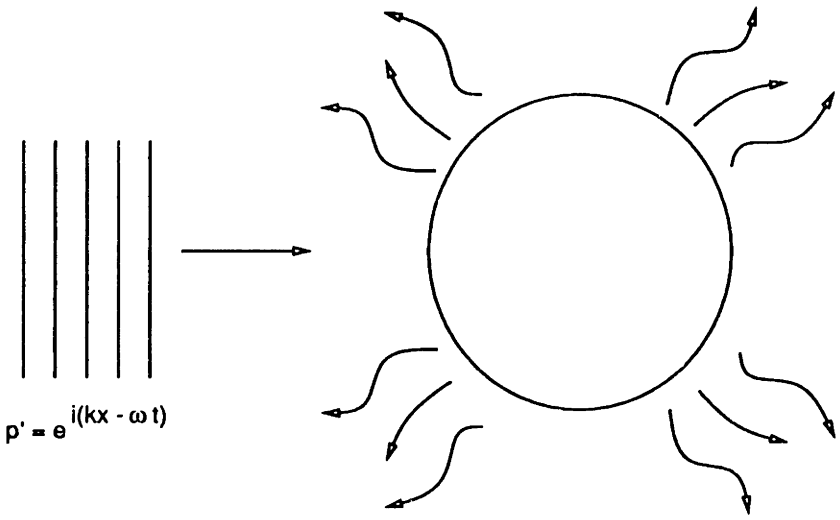

Figure 7-1: Plane Sound Wave Scattering by a Circular Cylinder

The wall boundary conditions are that the total normal velocity on the airfoil is zero, and since the surface is stationary the boundary condition is as in Equation 3.6,

$$\tilde{\mathbf{u}}_s \cdot \mathbf{n}_0 = -\tilde{\mathbf{u}}_i \cdot \mathbf{n}_0 \tag{7.2}$$

where $\tilde{\mathbf{u}}_i$ is the given incident perturbation velocity and can be computed as,

$$\tilde{\mathbf{u}}_i = \frac{\tilde{p}_i k}{\rho_0 \omega} \mathbf{i}$$

and $\mathbf{i}$ is the unit vector in the streamwise $+x$ direction.

The run time parameters were as follows:

- Grid: 256×90
- ω: 22.302 ($\lambda = \frac{1}{3}$)
- ν_4: 0.01
- ν_6: 0.001
- Far field: $\frac{1}{3}$
- Iters: 500
- $L_2(\delta\tilde{\rho})$: 2.0×10^{-5}

$\omega = 22.302$ corresponds to a wavelength of 1/3 diameter, and the domain contains 1 wavelength in all directions.

Figures 7-2 and 7-4 show the amplitude and phase of the computed scattered pressure, and Figures 7-3 and 7-5 show the amplitude and phase of the exact scattered pressure. Each set of figures shows contours which are very close to one another, and the computed solution is quite accurate.

Figures 7-6 and 7-7 show the absolute error in the real and imaginary parts of the scattered pressure, respectively. The largest absolute error of approximately 0.04 is found at the far field for both parts. The average $L_2(\Delta|\tilde{p}_s|)$ was 3.822×10^{-5}, the average $L_2(\Delta\Re(\tilde{p}_s))$ was 5.182×10^{-5}, and the average $L_2(\Delta\Im(\tilde{p}_s))$ was 5.752×10^{-5}. As was in the oscillating cylinder case, the present numerical scheme is quite accurate when there is no flow. The run required 24.2 minutes of cpu time on a Convex C1.

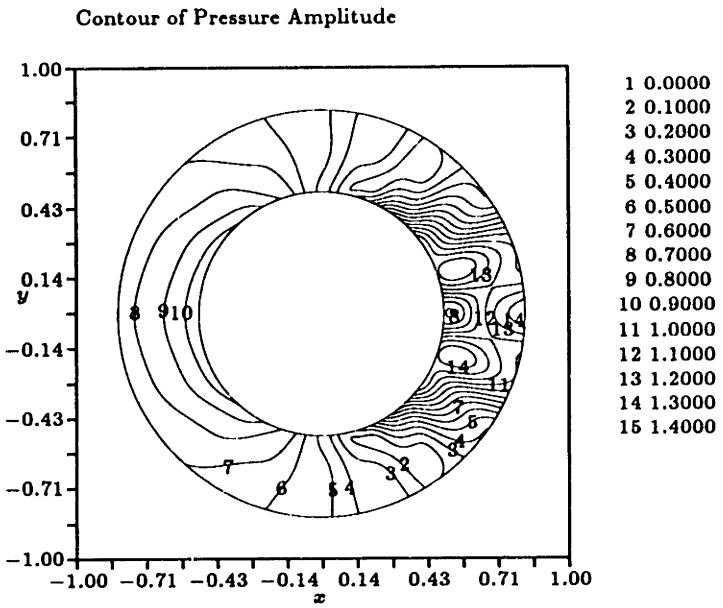

Figure 7-2: Amplitude of Scattered Pressure

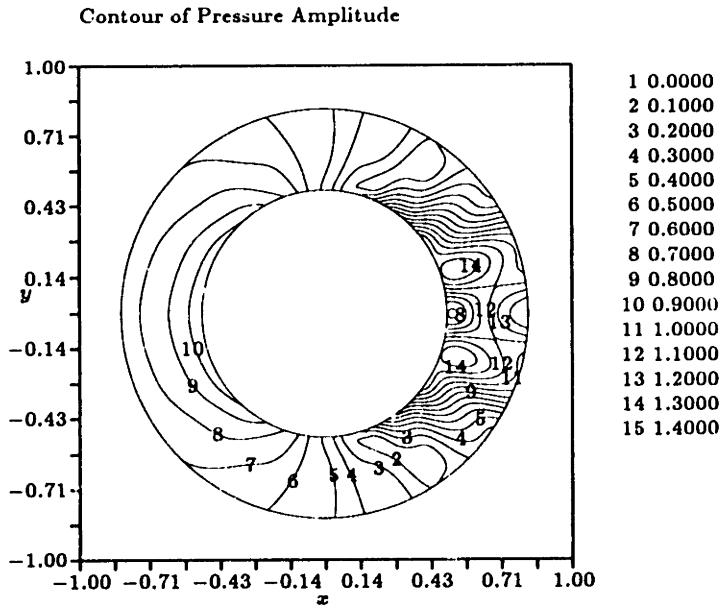

Figure 7-3: Amplitude of Exact Scattered Pressure

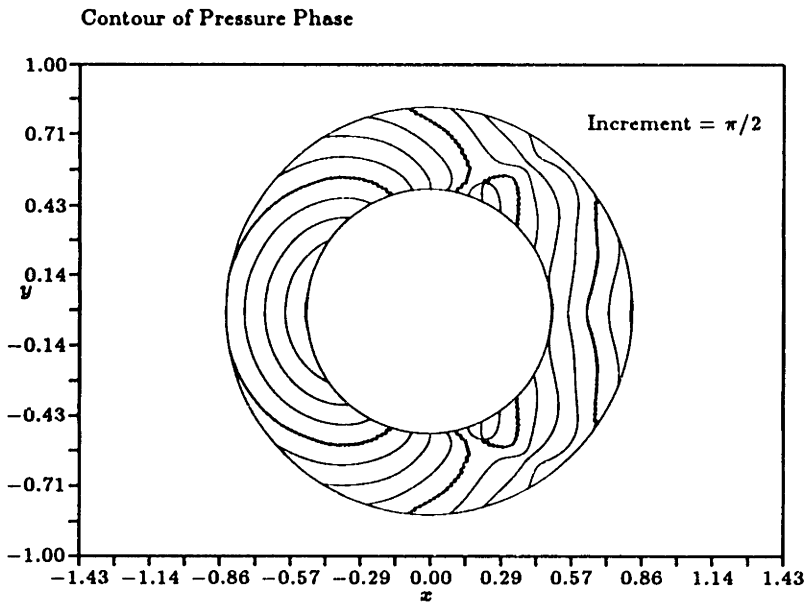

Figure 7-4: Phase of Scattered Pressure

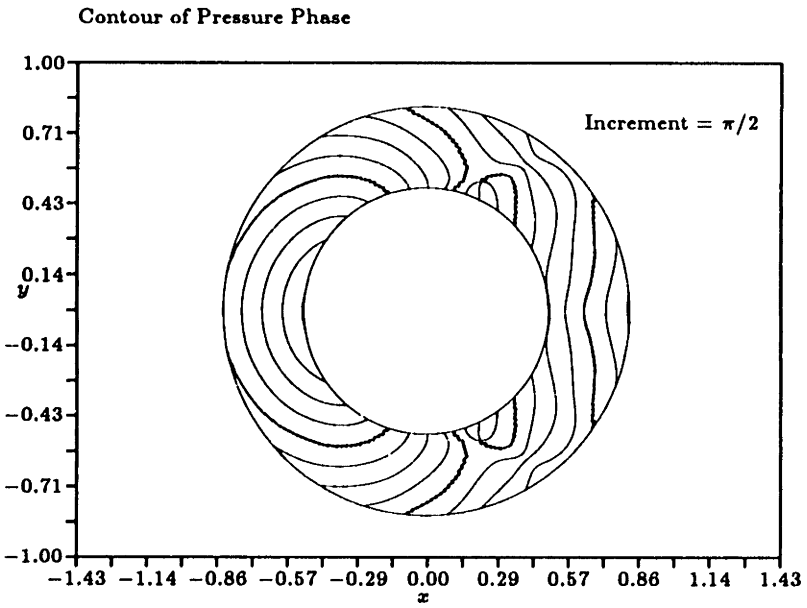

Figure 7-5: Phase of Exact Scattered Pressure

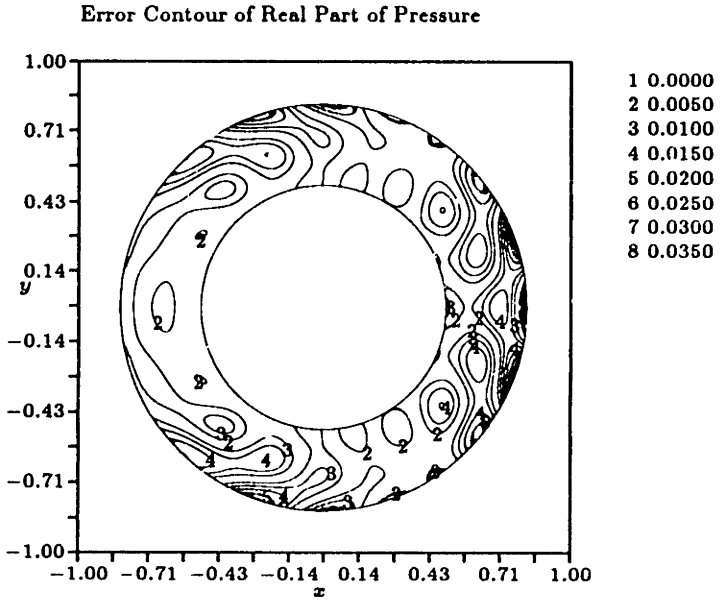

Figure 7-6: Error of the Real Part of $\tilde{p}_s$

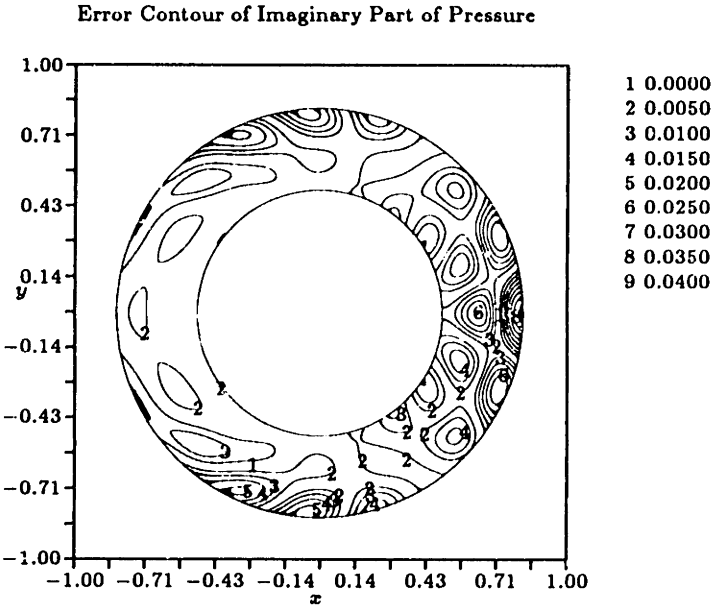

Figure 7-7: Error of the Imaginary Part of $\tilde{p}_s$

7.2 Scattering of Sound by an Airfoil in a Steady Flow

With an assurance that the surface boundary conditions are correctly enforced we now proceed with the aeronautical application at hand. Consider an airfoil at an angle of attack α in a steady mean flow of M_0 which encounters a plane sound wave of the form,

$$p_i' = e^{i(kx-\omega t)} \tag{7.3}$$

where,

$$k = \frac{\omega}{c_0(1+M_0)}.$$

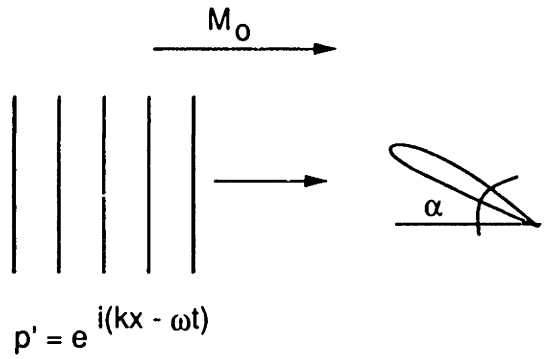

Figure 7-8: Scattering of Sound by an Airfoil in a Steady Flow

The wall boundary conditions are identical to the circular cylinder test case, except that the incident perturbation velocity now has a longer wavelength due to the Doppler effect,

$$\tilde{u}_i = \frac{\tilde{p}_i k}{\rho_0(\omega - u_0 k)}\mathbf{i}.$$

7.2.1 Effects of Mach Number

We seek to understand the effects of changes in Mach number on the scattering of plane sound waves. We have computed the scattered field for two identical airfoils at zero angles of attack in uniform flows of $M_0 = 0.3$ and $M_0 = 0.7$. The frequencies of

the disturbance waves were such that the compactness K remained the same in the two computations. It is important that K, and not the reduced frequency ν, remain constant so that in the transformed Prandtl-Glauert space the two cases would have an identical Helmholtz number and thus the same scattering patterns.

The key parameters for the two Mach number cases are tabulated below:

	M_0	M_{max}	ν	K	τ	$\lvert\tilde{L}\rvert$
Case 1	0.3	0.36	3.665	1.2	12%	0.0
Case 2	0.7	0.92	0.870	1.2	12%	0.0

Table 7.1: Parameters for $K = 1.2$ Varying Mach Number Case

The angles of attack for both cases were zero, and there is no unsteady lift. This is a thickness problem only, and the airfoil can be represented as a distribution of monopoles.

The two reduced frequencies ν translate to a compactness K of 1.2 and so the present cases are slightly noncompact. The maximum wavelengths in the downstream direction are 3.7 for the $M_0 = 0.3$ case and 8.7 for the $M_0 = 0.7$ case.

For both cases the numerical domains were chosen so as to guarantee a circular domain in the transformed Prandtl-Glauert space, and there were approximately 10 chord lengths along the up and downstream directions.

Since the thickness of the airfoil was only 3% and 1% of the incident wavelengths, the scattering effects were expected to be small. Figures 7-10 and 7-11 show the amplitudes of the scattered pressure $\tilde{p}_s$. The figures indicate that the leading edge was responsible for most of the scattered sound, which is as expected since the incident wave is traveling strictly in the $+x$ direction. When compared to the $M_0 = 0.3$ case, the $M_0 = 0.7$ case has a significantly higher scattered amplitude even though the leading edge radius is a smaller fraction of the incident wavelength.

Figure 7-12 is a polar plot of scattered directivity D_p at the far field. Notice that for both Mach numbers, the scattered field is almost completely in the forward direction, and also notice that the $M_0 = 0.7$ case has a much higher noise level than the $M_0 = 0.3$ case. In the $M_0 = 0.3$ case the leading edge emulates a compact scattered radiating

sound equally in all directions, but in the $M_0 = 0.7$ case there appears four new lobes in the upstream direction. This is an indication that the higher Mach number case is more sensitive to the noncompactness and the thickness. Evidently as the Mach number increases the overall noise level increases, and at the same time, the scattered field becomes more sensitive to the compactness ratio of the disturbance.

Figure 7-13 shows the phase of the scattered pressure for the $M_0 = 0.3$ case. The contours are spaced closer together in the upwind direction than in the downwind direction indicating a shorter wavelength upwind. The complexity of the phase structure close to the airfoil illustrates the diffractive effect of the accelerating fluid. The 'bends' in the contour lines at about $\pm 45°$ illustrate that at moderate distances the airfoil behaves as two monopoles located at each of the leading and trailing edges. Evidently the airfoil is not very compact with respect to the incoming wavelength.

Figures 7-14 and 7-15 show the amplitude contours of the scattered acoustic pressure plus the incident acoustic pressure, i.e. the complete acoustic pressure, for both Mach number cases. Note that the incident pressure amplitude is 1. In the $M_0 = 0.3$ case, there appears in the region directly ahead of the airfoil interference fringes from the interaction of the incident wave with the scattered wave; still because of the low scattered amplitudes, the pressure field is composed almost entirely of the incident field except at the leading edge region. In the $M_0 = 0.7$ case, there also appears interference fringes in the upstream region, but here the magnitudes of the fringes are much higher. For both Mach numbers, the downstream region is composed almost exclusively of the incident wave only. This is as expected since there was little scattered sound in the downstream direction.

Comparison cases of $M_0 = 0$ were computed for both Mach numbers to illustrate the diffractive effects of a varying flow field. The two previous chapters illustrated that local velocity gradients change the propagation direction of sound, and the same diffractive phenomena must be true here as well. The parameters for the comparison cases were chosen so that the computed values would transform to uniform flow values using simple

mapping functions.

In a uniform flow the pressure perturbation $p'(x, y, t)$ is represented by a convective form of the wave equation,

$$p'_{tt} + 2u_0 p'_{xt} - (c_0^2 - u_0^2)p'_{xx} - c_0^2 p'_{yy} = 0 \tag{7.4}$$

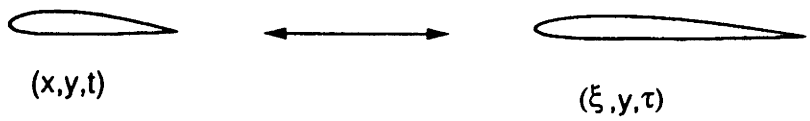

Figure 7-9: Unsteady Prandtl-Glauert Mapping

The above equation can be transformed into the standard wave equation by using the following 'unsteady Prandtl-Glauert' mapping variables [11],

$$\xi = \frac{x}{\beta},\ \tau = \beta t + \frac{M_0 x}{c_0 \beta}$$

where $\beta = \sqrt{1 - M_0^2}$. In (ξ, y, τ) space the equation for p' becomes,

$$p'_{\tau\tau} - c_0^2(p'_{\xi\xi} + p'_{yy}) = 0. \tag{7.5}$$

and in the frequency domain,

$$K^2 \tilde{p} + \tilde{p}_{\xi\xi} + \tilde{p}_{yy} = 0 \tag{7.6}$$

where $p'(\xi, y, \tau) = \Re(\tilde{p}(\xi, y)e^{-i\Omega\tau})$.

The complex amplitude $\tilde{p}(\xi, y)$ is related to $\tilde{p}(x, y)$ by the relation,

$$\tilde{p}(\xi, y) = \tilde{p}(x, y)\exp(\frac{iM_0\omega x}{c_0\beta^2}) = \tilde{p}(x, y)\exp(i\frac{1}{2}M_0 K x).$$

The comparison $M_0 = 0$ cases were computed in appropriate (ξ, y) spaces. The

pressure values were then mapped to (x, y) spaces of uniform $M_0 = 0.3$ and $M_0 = 0.7$ flows (Figure 7-9). The transformed values were, in turn, subtracted from the original $M_0 = 0.3$ and $M_0 = 0.7$ computed solutions. The differences, $\Delta\tilde{p}$, are a measure of the diffraction in a varying flow field. In regions where there are no flow gradients $\Delta\tilde{p}$ will be small, and thus a large $\Delta\tilde{p}$ indicates high diffraction. Figures 7-16 and 7-17 show the amplitude contours of $\Delta\tilde{p}$.

For the $M = 0.3$ case, the difference is small everywhere except in the vicinity of the leading edge of the airfoil. The leading edge region close to the airfoil is a region of high mean velocity gradients and of high diffraction. In the absence of mean flow the characteristic wavelength of the scattered wave at the leading edge will scale with the radius of curvature of the leading edge. The mean flow gradients will also scale with the radius of curvature, and hence a complex interaction between the scattered wave, the incident wave and the mean flow can occur at the leading edge.

For the $M_0 = 0.7$ case, the diffraction region is not limited to the immediate vicinity of the leading edge but encompasses almost the entire upstream region. In fact, the $\Delta\tilde{p}$ plot of Figure 7-17 is nearly identical to the scattered pressure amplitude plot of Figure 7-11. The transformed solution and the computed solutions have identical incident waves; but the scattered amplitude for the $M_0 = 0.7$ case is substantially higher, and the difference plot essentially indicates only the $M_0 = 0.7$ scattered pressure. Evidently the scattered amplitude is a strong function of the Mach number such that as the Mach number increases the scattered amplitude increases.

Section 5.3.2 on page 124 showed that the linear assumption is valid and that the convective wave equation can be used when,

$$|1 - M_0| \gg \tau^{2/3}.$$

In the $M_0 = 0.3$ case, the NACA0012 airfoil subject to a $K = 1.2$ pressure wave is sufficiently thin such that, in the far field, the sound pressure levels are nearly as expected by the linear theory. In the $M_0 = 0.7$ case, however, the airfoil does not satisfy

the above criteria and the computed solution differs from the linear theory throughout most of the domain.

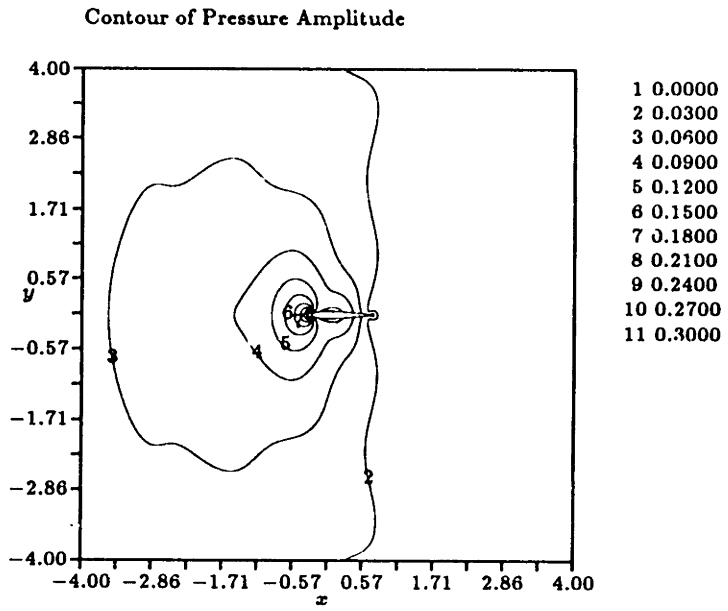

Figure 7-10: Amplitude of Scattered Pressure, $M_0 = 0.3$, $K = 1.2$

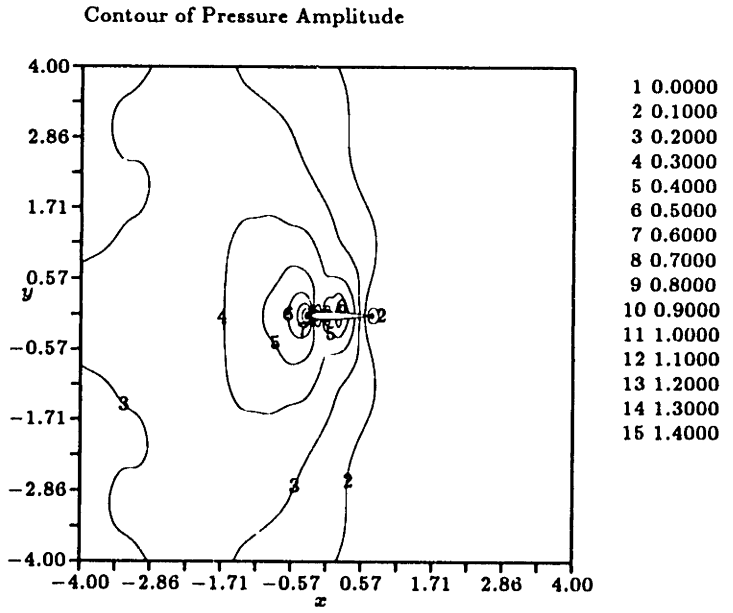

Figure 7-11: Amplitude of Scattered Pressure, $M_0 = 0.7$, $K = 1.2$

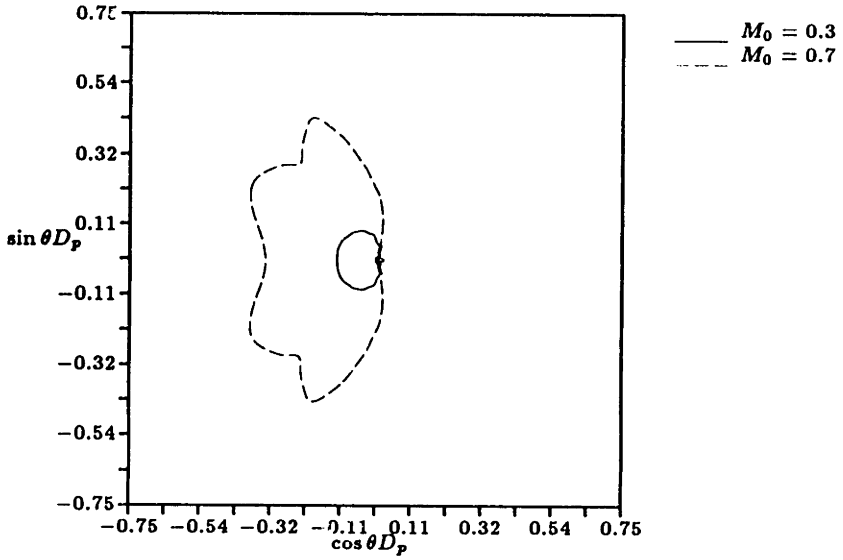

Figure 7-12: Polar Plot of Scattered Directivity for $M_0 = 0.3$ and $M_0 = 0.7$

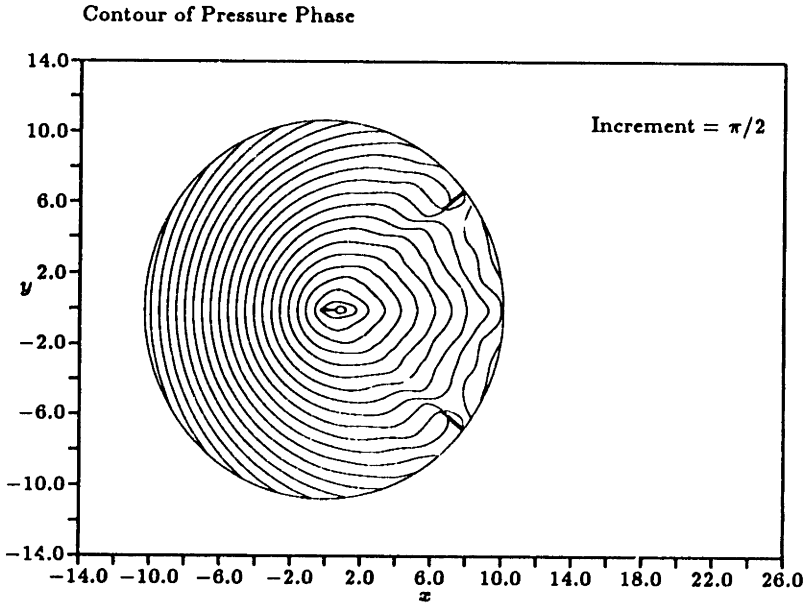

Figure 7-13: Phase of Scattered Pressure, $M_0 = 0.3$, $K = 1.2$

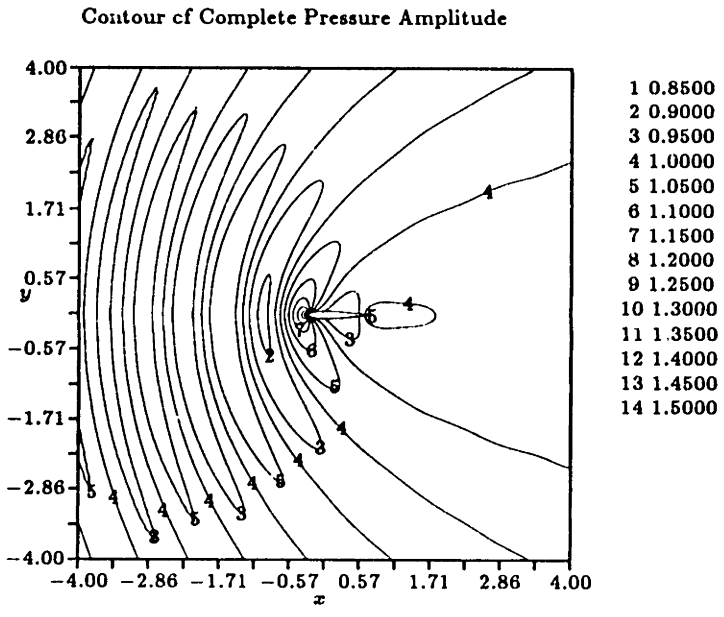

Figure 7-14: Amplitude of Combined Acoustic Pressure, $M_0 = 0.3$, $K = 1.2$

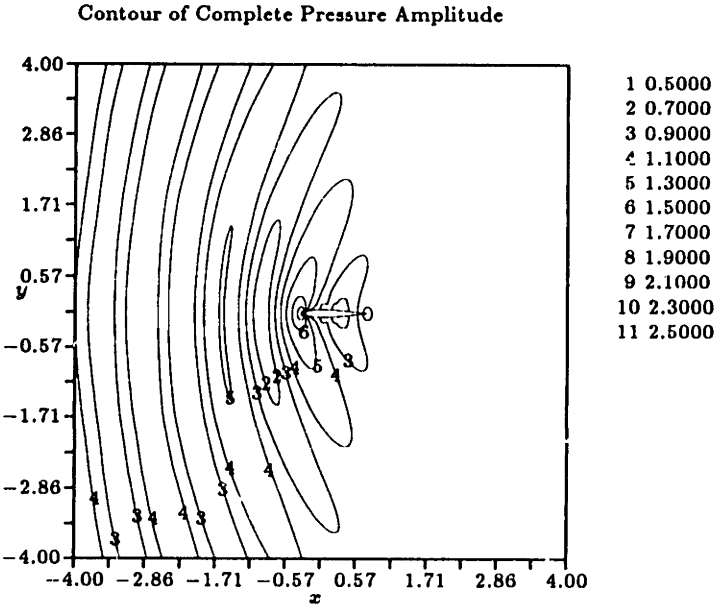

Figure 7-15: Amplitude of Combined Acoustic Pressure, $M_0 = 0.7$, $K = 1.2$

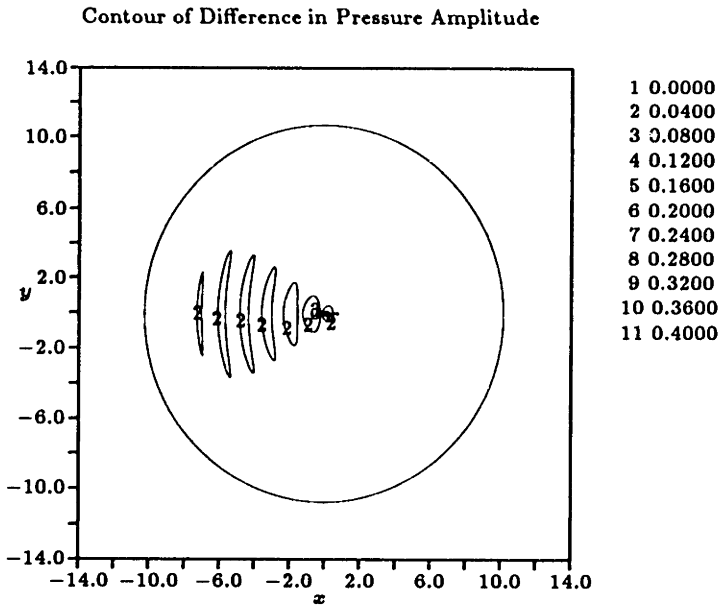

Figure 7-16: Amplitude Contour of $\Delta\tilde{p}$, $M_0 = 0.3$, $K = 1.2$

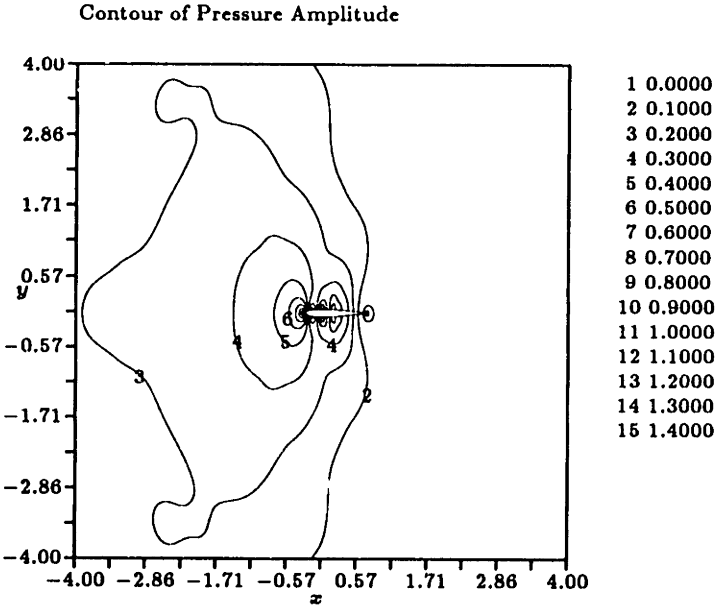

Figure 7-17: Amplitude Contour of $\Delta\tilde{p}$, $M_0 = 0.7$, $K = 1.2$

7.2.2 Effects of Angle of Attack

The diffraction and energy characteristics of plane acoustic waves scattered by an airfoil at an angle of attack have been studied. The enforcement of the Kutta condition creates an unsteady circulation about the airfoil and a vorticity sheet downstream of the trailing edge.

A NACA0012 airfoil is in a steady $M_0 = 0.3$ flow at angles of attack of 2° and 11°. A plane acoustic wave of the form,

$$p_i' = e^{i(kx-\omega t)} \tag{7.7}$$

impinges on the airfoil. The key parameters for the two cases are tabulated below:

	M_0	M_{max}	ν	K	α	$\lvert\tilde{L}\rvert$	W_s
Case 1	0.3	0.40	3.7	1.2	2°	0.0945	0.018
Case 2	0.3	1.00	3.7	1.2	11°	0.5103	0.240

Table 7.2: Parameters for $M_0 = 0.3$, $K = 1.2$ Varying Angle of Attack Cases

The two computed solutions have finite lift amplitudes, and the source distributions along the airfoil contain both monopoles and dipoles. W_s in Table 7.2 is the radiated acoustic power for the scattered portion of the solution only. The $\alpha = 11°$ case has substantially higher scattered acoustic lift ($\times 5.4$) and scattered acoustic power ($\times 13.3$).

The domains and the grids are unchanged from the previous case except for the rotation of the airfoil, and thus we expect similar resolution characteristics.

Figures 7-18 and 7-19 show the computed amplitudes of the scattered pressure $\tilde{p}_s$. Note the differences between the current cases and the corresponding values from the previous no lift set. In the $\alpha = 2°$ case, the scattered values have higher amplitudes since at an angle of attack, the airfoil has a higher effective cross-section imposing on the incoming acoustic wave, and the directivity pattern is asymmetric due to the acceleration of the fluid on the suction surface. In the $\alpha = 11°$ case, the scattered amplitudes are even higher, and the scattered directivity show strong diffraction effects

from the mean velocity gradients.

The effects of a varying mean flow on the scattered directivity of sound is illustrated in the polar plot of directivity in Figure 7-20. The figure includes the directivity of the two angles plus the previous zero incidence result for comparison. The zero incidence and the $\alpha = 2°$ results indicate a compact scattering pattern in the upstream direction, and the $\alpha = 2°$ case has a noncompact scattering in the downstream direction. The latter multi-lobe scattering pattern is due to the sharp trailing edge, and in fact, Reference [50] shows that when a plane sound wave is diffracted by a sharp edge, the scattered sound will have terms which vary in the azimuthal direction as,

$$e^{ikr\cos\theta}$$

where $k = \omega/c_0$. The trailing edge scattering is even more apparent in the $\alpha = 11°$ solution. Here the directivity pattern is noncompact even in the upstream direction, and the sound amplitudes in the downstream direction are significantly higher than in the upstream direction. It seems that for the 11° case the scattered field is dominated by the features due to the sharp trailing edge. This is in direct contrast to the zero incidence and 2° cases which have scattering patterns mostly influenced by the thick leading edge. The rotation of sound directivity in the counterclockwise direction due to the leading edge suction is also illustrated in the $\alpha = 11°$ solution.

Figures 7-22 and 7-23 show the computed phase of the scattered pressure. The $\alpha = 2°$ case indicates a complex phase structure near the airfoil and the shorter wavelength in the upwind direction. In addition, in the region $-90° < \theta < 90°$ there is much 'warping' of the phase lines, which indicates that the sound scattered by the trailing edge is noncompact and is sensitive to diffraction by mean flow gradients. The warping is even more evident in the $\alpha = 11°$ case. The diffraction of sound is clearly implied in all directions including in the *upstream* sense.

Figures 7-24 and 7-25 show the amplitude contours of the scattered plus the incident pressure. Compare the figures with the corresponding figure on page 200. The $\alpha = 2°$

figure is similar to the zero incidence case. The region ahead of the airfoil still exhibits the interference fringes from the interaction of the incident wave with the scattered wave, but in the $\alpha = 2°$ solution the fringes are of higher amplitude and are asymmetric. Also note the contour of 1.0 along the wake; the wake is acoustically silent. The $\alpha = 11°$ case is substantially different from the zero lift solution. The interference effects are much more complicated, particularly near the airfoil. Note also that the interference fringes also exist in the *downstream* direction due to sound scattering by the trailing edge.

When there is no scattering object, a traveling plane sound wave has zero acoustic power as defined in Section 2.4. There is an equal amount of energy flux into as well as out of a closed loop. Similarly for a zero lift scattering case, the acoustic power is also zero. The scattered sound combined with the incident sound creates local zones of 'illuminated' (amplified) and 'shadow' (attenuated) regions such that there is an equal amount of energy flux into and out of a given closed loop.

An airfoil at an angle of attack subject to an incident pressure wave has an unsteady lift and a wake associated with it. Then it must follow that the energy from the incoming acoustic wave is converted into hydrodynamic energy of the vorticies, and if the total amount of energy is constant there should be a net decrease in acoustic energy. To compare the energy levels of each let us define the quantity acoustic cross section σ as in Reference [58],

$$\sigma \equiv \lim_{r \to \infty} \oint_l \frac{\bar{p_s'^2}}{\rho_0 c_0} dl. \tag{7.8}$$

There is an infinite amount of energy associated with a plane wave and thus p_s' corresponds to the scattered portion of sound only.

In the previous section's nonlifting case where $\alpha = 0$, the ratio σ_{xy}/σ_{upg} should be $\equiv 1$ since there was no energy conversion. σ_{xy} is the computed acoustic cross section in the real plane (x, y) and σ_{upg} is the computed acoustic cross section in (ξ, y) space via the unsteady Prandtl-Glauert transformation. Without viscosity or the Kutta condition, an incident acoustic wave conserves energy. The actual ratio of σ_{xy}/σ_{upg} was 0.999.

A comparison of σ between the computed nonzero angles of attack solutions and the

no lift solution from the previous section have been made to determine the amount of energy transferred from the acoustic to the vortical mode. The presence of an unsteady wake implies that there must be energy conversion at the trailing edge, and therefore, the ratios σ_α/σ_0 for both angles should be < 1. σ_α is the acoustic cross section for the unsteady lift case and σ_0 is the acoustic cross section for the previous section's no lift computation. The ratio for the $\alpha = 2°$ was 0.995 and for the $\alpha = 11°$ case was 0.920. Evidently approximately 0.5% and 8% of the acoustic energy was converted into the vortical energy, respectively.

This suggests that if vorticity is produced by the interaction of sound with a solid surface, there could be an attenuation of sound (as proposed by References [17, 62]). Figure 7-21 shows the polar directivity of the complete acoustic pressure (scattered + incident) at the far field. The sound levels heard are roughly equivalent between $\alpha = 0$ and $\alpha = 2°$ cases; however, the sound heard in the $\alpha = 11°$ case is substantially *less* in all directions. The vortical mode has gained energy at the expense of the acoustic mode, and this is reflected in the reduced sound levels heard at the far field.

An airfoil at an angle of attack subject to a pressure wave can be modeled by the linear convective wave equation only when the angle is quite small ($\alpha \leq 2°$). At a small angle, the scattered sound is rotated slightly in the counterclockwise direction, and the sharp trailing edge creates noncompact scattering patterns in the downstream direction. But the sound pressure levels at the far field do not differ noticeably from that of the no lift case. At a higher angle, the rotation is more pronounced and the noncompact lobes appear in the entire domain. In addition, the vortical wake reduces the acoustic energy content such that there is a substantial attenuation of sound throughout the sound field.

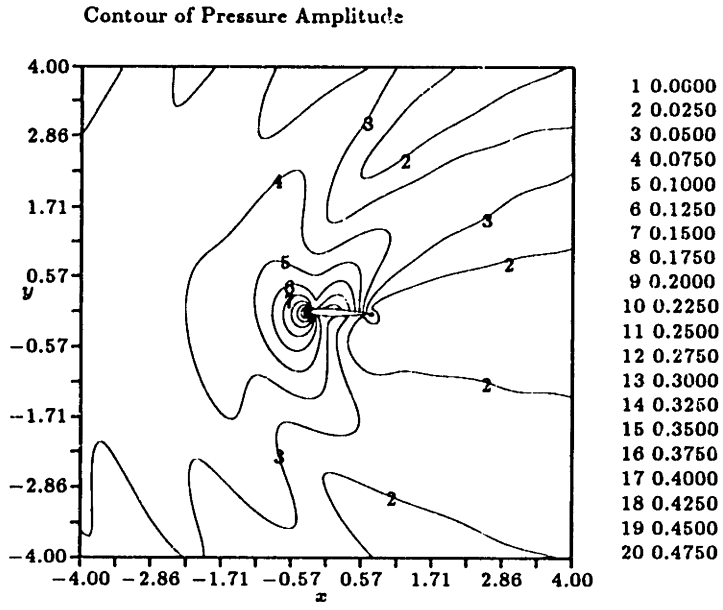

Figure 7-18: Amplitude of Scattered Pressure, $M_0 = 0.3$, $\alpha = 2°$

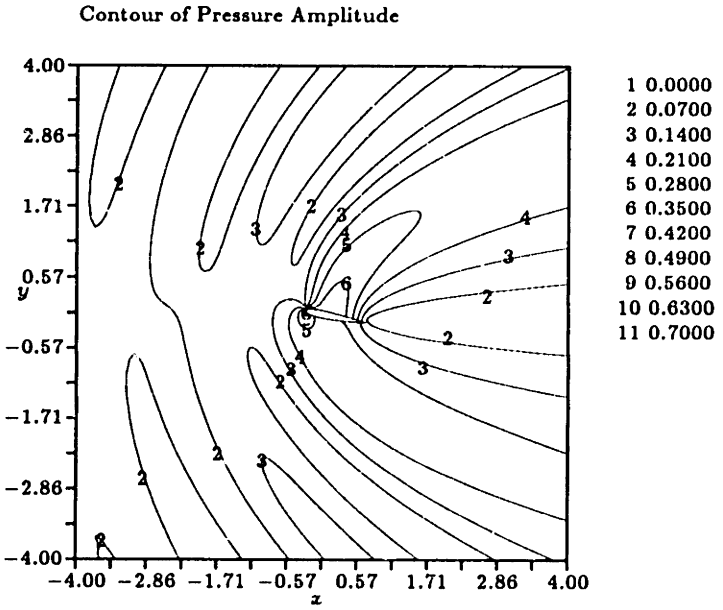

Figure 7-19: Amplitude of Scattered Pressure, $M_0 = 0.3$, $\alpha = 11°$

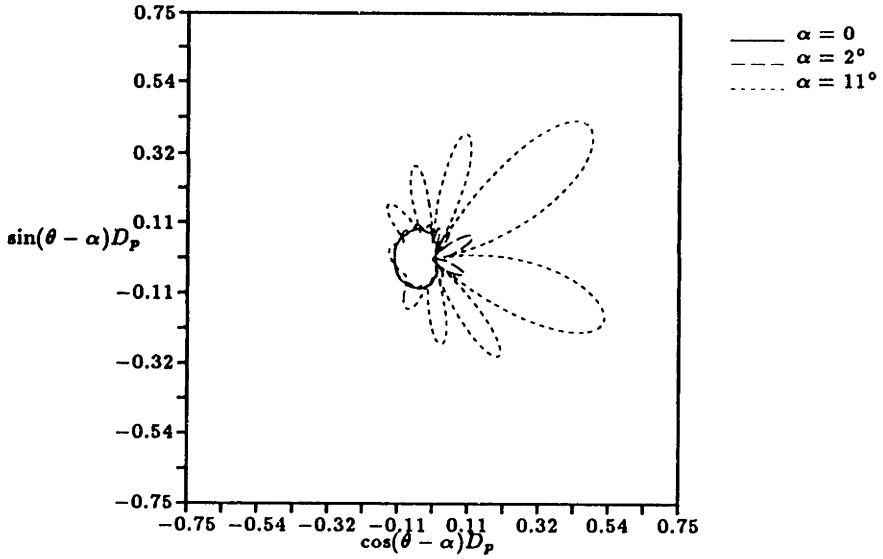

Figure 7-20: Polar Plot of Scattered Directivity, $M_0 = 0.3$, $K = 1.2$

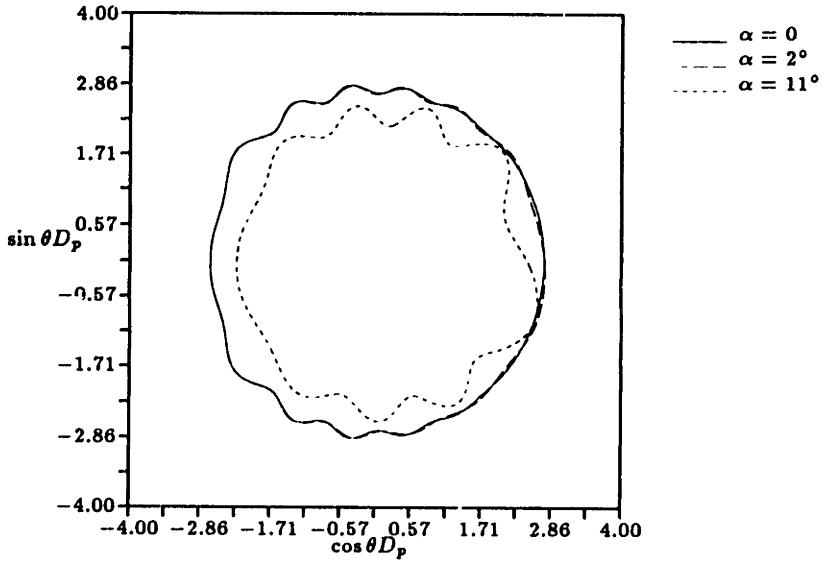

Figure 7-21: Polar Plot of Complete Directivity, $M_0 = 0.3$, $K = 1.2$

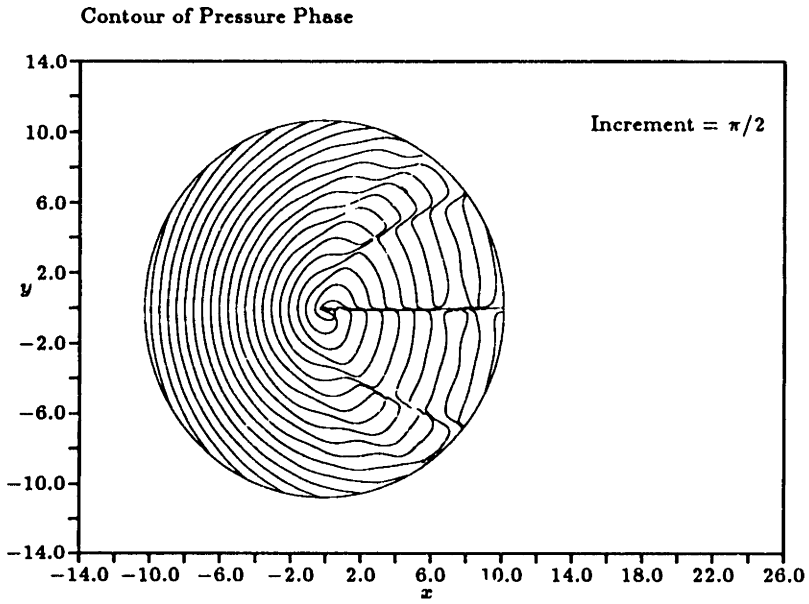

Figure 7-22: Phase of Scattered Pressure, $M_0 = 0.3$, $\alpha = 2°$

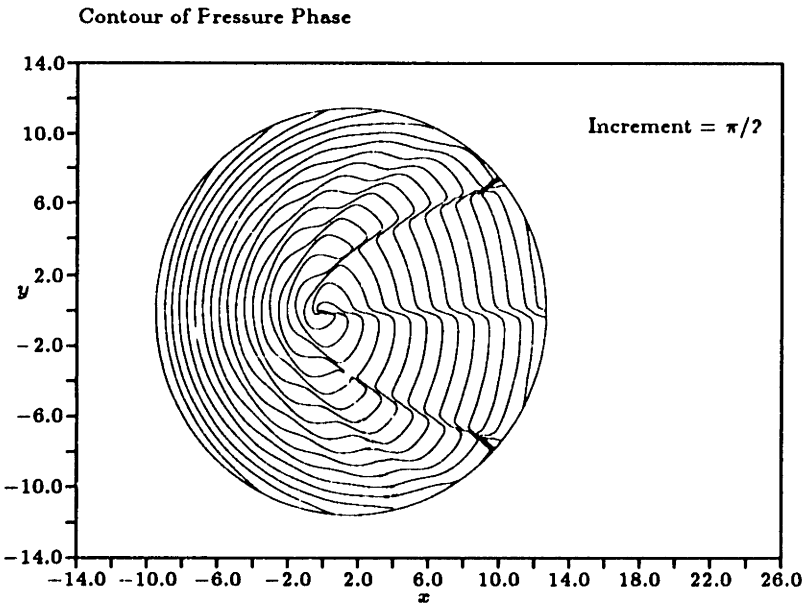

Figure 7-23: Phase of Scattered Pressure, $M_0 = 0.3$, $\alpha = 11°$

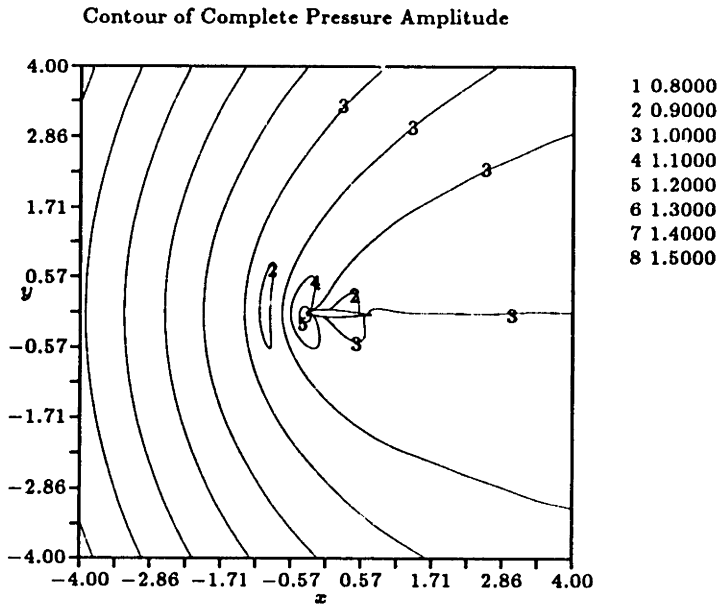

Figure 7-24: Amplitude of Combined Acoustic Pressure, $M_0 = 0.3$, $\alpha = 2°$

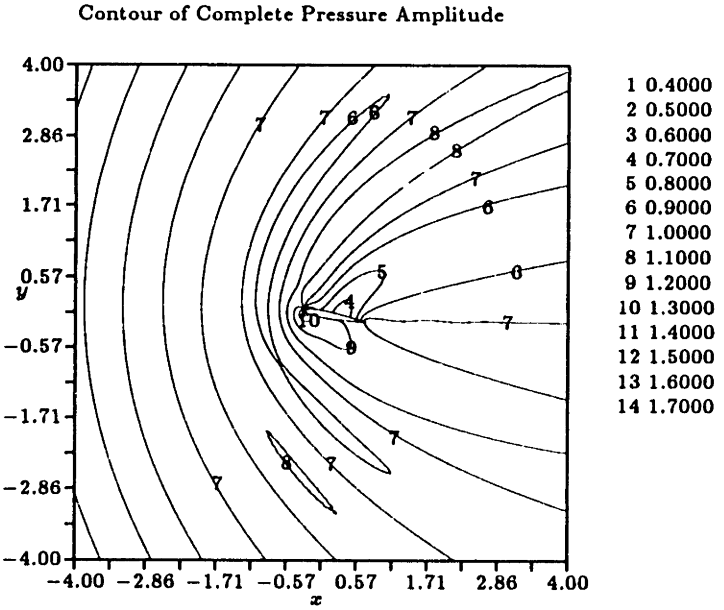

Figure 7-25: Amplitude of Combined Acoustic Pressure, $M_0 = 0.3$, $\alpha = 11°$

7.3 Summary

In this chapter we have studied some aspects of plane sound wave scattering by a thick airfoil in a nonuniform flow.

The scattered sound is a function of the free stream Mach number. In no lift situations, a NACA0012 airfoil in a low Mach number flow subject to a plane sound wave can be adequately modeled by the convective wave equation for far field sound values. The near field values, however, cannot be computed by the linear method because of the additional diffraction by mean velocity gradients. As the Mach number increases, the convective wave equation becomes invalid even at the far field. The actual scattered sound amplitudes are significantly higher than those values predicted by the linear method.

The scattered sound is also a function of the angle of attack. At a small angle, the scattered sound amplitude increases slightly, and the directivity is rotated incrementally in the counterclockwise direction. The sharp trailing edge also creates a noncompact scattering pattern in the downstream direction, but the overall sound levels at the far field do not differ significantly from those predicted by the no lift computations. At a higher angle, the rotation is more pronounced and the noncompact lobes created by the diffraction of sound at the sharp trailing edge appear in the entire domain. The linear method would be valid only at the far field and for a small angle of attack.

The impinging pressure wave also creates an unsteady lift about the airfoil and a vorticity sheet trailing the airfoil. If there is no transfer of energy from the mean flow to the acoustic mode, there must be a conversion of acoustic wave energy into vortical energy, and as shown in Figure 7-21, this conversion of acoustical into vortical mode can lead to an attenuation of sound.

Chapter 8

Concluding Remarks

The purpose of the current thesis was two–fold. The first was to develop an accurate and general numerical method of computing acoustic values. To that end, we have attempted to adopt the current state of CFD wherever possible, but the very nature of the small length and time scales involved meant that the numerical scheme had to be, to a some extent, newly developed. The most important numerical improvements were in the formulation of the nonreflecting far field boundary conditions. Very early on it was realized that the far field boundary conditions were crucial to the overall accuracy of the numerical scheme, and that the most commonly used methods would not suffice. The thesis devotes a better part of an entire chapter on the development of the nonreflecting conditions, but as a percentage of the total time committed, it should be about 5 chapter in length.

In acoustics the far field values are as important as the near field solution, and in some sense, even more important. A key aeroacoustic problem is to discern an accurate sound level heard by a distant listener as an aircraft flies by. Such a necessity meant that we needed to have a fine enough grid to resolve the relevant length scales everywhere in the domain, and thus the numerical method was further refined such that the memory and time requirements were within practical limitations of the computer resources available. The use of higher order compact differencing in the azimuthal direction reduced the grid size requirement by a factor of about 2.

The second purpose of the thesis was to apply the numerical method to a few model

aeroacoustic problems. The intent was not to apply the method in *actual* engineering cases, but rather to ascertain, in a parametric sense, the relevance/limitations of the currently available linear methods and to quantify the newly acquired capabilities. We wanted to use the numerical method as a tool to understand the effects of some key parametric variations on the radiated sound.

8.1 Summary of Results

The amplitude and phase of sound radiating from an isolated airfoil are functions of the thickness, the angle of attack, the Mach number and the compactness ratio. In the thesis we have attempted to analyze the parametric dependence for 3 model aeroacoustic problems.

8.1.1 Gust–Airfoil Interaction

An airfoil impressed with a compact ($K < 1$) transverse vortical gust appears as a single dipole radiating in phase, and at a constant Mach number, an increase in compactness ratio increases the retarded time differences which appear as additional lobes in directivity.

Thickness creates a varying mean velocity field which alters the sound propagation direction. The specific level of diffraction is a function of the compactness ratio (i.e. wavelength) and the maximum thickness of the airfoil. When the airfoil is disturbed by a noncompact ($K > 1$) gust, the changes in thickness affect the directivity of sound such that sound is directed away from the center region towards the up and downstream directions. Thickness may also affect a compact airfoil when it exceeds the constraint,

$$|1 - M_0| \gg \tau^{2/3}. \tag{8.1}$$

An airfoil at an angle of attack creates a nonuniform velocity field, and the gradient of velocity affects the direction of sound travel. An airfoil at an angle of attack subjected

to an unsteady vortical disturbance also has a trailing vorticity sheet associated with it; and because the problem is no longer symmetric, the wake can extract energy from the mean flow to the perturbation mode, and through the imposition of the Kutta condition, the extraction may create a higher overall acoustic energy level.

A compact source at a small angle of attack has its far field directivity rotated in the counterclockwise direction due to the leading edge suction effect. The reduction of projected airfoil length also creates a slight decrease in the amplitude of lift and the radiated sound energy. As the angle increases, the directivity is similarly rotated, but in addition, there is an extraction of energy from the mean flow which creates an overall higher noise level. The effect of angle of attack on a noncompact source is similar except that the rotation of directivity at the far field is in the clockwise direction. This is believed to be caused by the bound vorticity and its clockwise rotational flow. Simple methods based on the convective wave equation are generally ineffective when the airfoil is at an angle to the mean flow.

8.1.2 Oscillating Airfoil

A moving airfoil must necessarily 'carry' its surrounding fluid with it, and therefore, the surface boundary conditions become a function of the local normal mean velocity gradient.

A thick symmetric airfoil at a zero incidence angle and in a compact oscillation has a significantly higher acoustic energy level than a flat plate case. Evidently there is a transfer of energy from the mean flow to the acoustic mode. Because of the symmetry of the problem, however, the transfer path is not through the vortical wake and the Kutta enforcement, but instead the energy cascade is via a direct increase in the source distribution through interactions of the mean flow gradient and the oscillating airfoil. A large mean velocity variations in the local surface normal direction translates directly to a stronger distribution of surface acoustic source strengths. The diffractive effect of the thickness is small for the long wavelength case, but there is a distinct upstream tilting

of the directivity lobes.

The energy extraction (in terms of percentage) is less for the same airfoil in a non-compact oscillation. However, the diffractive effect of the varying mean velocity is more pronounced in the shorter wavelength case, particularly in the upstream direction where additional lobes appear.

The overall sound level from a thick symmetric airfoil at an angle of attack and in a compact oscillation is only slightly higher than the same airfoil at zero incidence. Evidently the energy transfer from the vortical wake is insignificant when compared to the direct energy transfer through the mean flow–moving airfoil interaction. The effect of leading edge suction creates a far field sound field which has amplified sound pressure levels in the lower $180° < \theta < 270°$ zone.

The same airfoil in a noncompact oscillation has moderately higher energy level than either the airfoil at zero incidence and in a noncompact oscillation or the angled airfoil in a compact oscillation. The diffraction of sound from the mean bound vortex dominates at the far field and there appears a new upstream directed sound lobe at the far field.

The linear theory must necessarily assume a uniform mean flow, and it does not incorporate the diffractive effect of the varying mean flow or the increase in the overall sound pressure levels from the mean flow energy transfer. Thus the linear method would only be applicable if the thickness, the angle of attack and the compactness are all small.

8.1.3 Scattering Effects

The diffraction and scattering of plane acoustic waves by rigid bodies in various flow fields were investigated.

An airfoil with no lift and with a thickness within the constraint of Equation 8.1 can be adequately modeled by the convective wave equation for far field sound values. The near field values, however, cannot be computed by the linear method because of the additional diffraction by mean velocity gradients. The scattered sound from the

same airfoil which is outside of the constraint of Equation 8.1 cannot be computed by the convective wave equation, even for far field values. The actual scattered sound amplitudes are significantly higher than those predicted by the linear method.

The mean and unsteady lift also affect the scattered sound. At a small angle, the scattered sound amplitude increases slightly in the upstream direction, and the acoustic phase is rotated incrementally in the counterclockwise sense. The sharp trailing edge also creates a noncompact scattering pattern in the downstream direction; nevertheless, the combined (incident + scattered) sound levels at the far field do not differ significantly from those of the no lift computations. At a higher angle, the rotation of phase is more pronounced, and the noncompact lobes from the trailing edge dominate the entire scattered field. In addition, the conversion of acoustic energy into that of the wake creates an attenuated sound field. The linear methods would be effective only if the angle of attack is small and if the disturbance is also compact.

8.2 Suggestions for Future Research

8.2.1 Numerical Improvements

There are a number of improvements we can suggest to improve the accuracy and the efficiency of the current method. A multigrid time integration method can be implemented; such a refinement will offer the accuracy level of a dense grid and the convergence rate of a coarse grid (at the expense of an increased memory use).

Away from the surface, say 2 chord lengths, the numerical domain is nearly circular, and given such a geometry, we could discretize in space using the spectral method. The Fourier spectral method requires only 2 points per length scale and thus could offer large efficiency improvements. A 'zonal' grid approach which maintains a fine grid near the surface but has a much coarser grid away from it could be implemented. In such an approach, the discretization in the near zone would remain a finite difference type, while we would discretize the coarse grid zone using a Fourier spectral method.

The far field boundary conditions can be further refined. An improvement in the accuracy of the far field conditions improves both the accuracy (less reflection) and efficiency (smaller domain).

8.2.2 General Improvements

While we have attempted to include as much of the physical parametric effects as possible, the financial and time constraints have forced us to limit the actual number of case studies. Some important and interesting parametric questions remain for the 3 model problems, particularly for the scattering study.

Consider an airfoil in M_0 flow and at an angle of attack of α which encounters a plane sound wave of the form in Chapter 7. We have found that when the angle is sufficiently high, the incoming acoustic energy is transferred to the unsteady wake and the overall sound level decreases. Several investigators [17, 62], however, have suggested that given the same airfoil, the radiated sound power can also be *higher* than in the no lift case. Section 2.4 demonstrated that if the mean velocity $\mathbf{u_0}$ is not parallel to the perturbation velocity $\mathbf{u}'$, there can be a transfer of energy from the mean flow to the perturbation vortical flow. (We have seen this phenomenon in the Chapters 6 and 7) It turns out that the Kutta condition can, in turn, convert this additional vortical energy into acoustic energy [17, 62]; evidently the Kutta condition converts energy both to/from acoustic from/to vortical. The radiated sound, thus, can be actually higher with the enforcement of Kutta condition [62].

One issue is then 'is the radiated sound power higher or lower?' with the Kutta condition. It appears that the answer is not a simple one, and that the radiated sound power is dependent at least on the parameters M_0, α and the angle of the incident wave [62] and may also depend on the frequency ω.

We have purposely restricted our case studies to those situations in which the local Mach number does not exceed unity. A shock wave which is subjected to an unsteady disturbance will generally oscillate and thereby create a radiating sound field of its own.

This is thought to be an important source of sound and cannot be ignored in many transonic flow situations [31]. Unfortunately the unsteady shock location problem is a nontrivial one, and to date, we know of no linearized Euler solutions for a general two dimensional case. Hall [30] has provided an unsteady shock 'fitting' method for the one dimensional set, but its applicability to a general two or three dimensional geometry is probably limited. Recently Lindquist [47] showed that an unsteady shock 'capturing' method can be applied for the linearized Euler equations in one dimension. A capturing scheme offers a possibility of general geometric application, and it would be interesting to apply her contribution to the current method.

Bibliography

[1] Abramowitz, M. and Stegun, I., *Handbook of Mathematical Functions.* New York: Dover, 1972.

[2] Agarwal, R. K. and Deese, J. E., "Computation of Viscous Airfoil, Inlet, and Wing Flowfield," AIAA Paper 84-1551, 1984.

[3] Amiet, R. K., "Compressibility Effects in Unsteady Thin-Airfoil Theory," AIAA Journal, Vol. 12, No. 2, pp. 252-255, 1974.

[4] Anderson, D. A., Tannehill, J. C. and Pletcher, R. H., *Computational Fluid Mechanics and Heat Transfer.* New York: Hemisphere Publishing Corporation, 1984.

[5] Andreev, N. N., "Concerning Certain Second Order Quantities in Acoustics," Soviet Phys. Acoust., **1**, 2, 1955.

[6] Atassi, H. M. and Dusey, M. P., " Acoustic Radiation from Thin Airfoils in Nonuniform Subsonic Flow," AIAA Paper 90-3910, 1990.

[7] Atassi, H. M., Subramaniam, S., and Scott, J. R., " Acoustic Radiation from Lifting Airfoils in Compressible Subsonic Flow," AIAA Paper 90-3911, 1990.

[8] Batchelor, G. K., *An Introduction to Fluid Dynamics.* Cambridge, England: Cambridge University Press, 1967.

[9] Baumeister, K. J., "Numerical Techniques in Linear Duct Acoustics, 1980-81 Update," NASA TM-82730, 1981.

[10] Bayliss, A. and Turkel, E., "Radiation Boundary Conditions for Wave-Like Equations," Communications on Pure and Applied Mathematics, Vol. XXXIII, pp. 707-725, 1980.

[11] Bayliss, A. and Turkel, E., "Far Field Boundary Conditions for Compressible Flows," Journal of Computational Physics 48, 182-199, 1982.

[12] Bayliss, A. and Turkel, E., "Outflow Boundary Conditions for Fluid Dynamics," SIAM J. SCI. STAT. COMPUT., Vol. 3, No. 2, June 1982.

[13] Bisplinghoff, R. L. and Ashley, H., *Principles of Aeroelasticity.* New York: Dover, 1962.

[14] Bussing, T. R. and Murman, E. M., "A Finite Volume Method for the Calculation of Compressible Chemically Reacting Flows," AIAA Paper 85-0331, 1985.

[15] Colonius, T., Lele, S. K., Moin, P., "Scattering of Sound Waves by a Compressible Vortex," AIAA Paper 91-0494, 1991.

[16] Courtier & Arnoux, "Overview of Computational Aeroacoustics in Aerodynamics," AIAA Professional Study Series, Nevada, January 10-11, 1992.

[17] Crighton, D. G., "Basic Principles of Aerodynamic Noise Generation," Prog. Aerospace Sci., Vol. 16, No. 1, 31-96, 1975.

[18] Crighton, D. G., "Acoustics as a Branch of Fluid Mechanics," Journal of Fluid Mechanics, Vol. 106, pp. 261-298, 1981.

[19] Dowling, A. P. and Ffowcs Williams, J. E., *Sound and Sources of Sound.* Chicester, England: Ellis Horwood Limited, 1983.

[20] Drazin, P. G. and Reid, W. H., Hydrodynamic Stability. Cambridge: Cambridge University Press, 1981.

[21] Engquist, B. and Majda, A., "Radiation Boundary Conditions for Acoustic and Elastic Wave Calculations," Communications on Pure and Applied Mathematics, Vol. XXXII, pp. 313-357, 1979.

[22] Ferm, L., "Open Boundary Conditions for External Flow Problems," Department of Computing Science Report 108, Uppsala University, 1987.

[23] Fletcher, C. A. J., *Computational Techniques for Fluid Dynamics.* Vol. II, New York: Springer-Verlag, 1988.

[24] Giles, M., A Technical Conversation with, 1990.

[25] Giles, M., "Non-Reflecting Boundary Conditions for the Euler Equations," CFDL-TR-88-1, MIT Department of Aeronautics and Astronautics, 1988.

[26] Giles, M., "Non-Reflecting Boundary Conditions for Unsteady Airfoil Calculations," CFDL-TR-90-1, MIT Department of Aeronautics and Astronautics, 1990.

[27] Goldstein, M. E., *Aeroacoustics.* New York: McGraw-Hill, 1976.

[28] Goldstein, M. E. and Atassi, H., "A Complete Second-Order Theory for the Unsteady Flow About an Airfoil Due to a Periodic Gust," Journal of Fluid Mechanics, Vol. 74, Part 4, pp. 741-765, 1976.

[29] Gustafson, B., "Far Field Boundary Conditions for Time-Dependent Hyperbolic Systems," Center for Large Scale Scientific Computation, CLaSSiC-87-16, Stanford University, 1987.

[30] Hall, K. C., *A Linearized Euler Analysis of Unsteady Flows in Turbomachinery.* ScD. Thesis, Massachusetts Institute of Technology, 1987.

[31] Hardin, J. "Overview of Computational Aeroacoustics in Aerodynamics," AIAA Professional Study Series, Nevada, January 10-11, 1992.

[32] Hariharan, S. I. and Bayliss, A., "Radiation of Sound from Unflanged Cylindrical Ducts," SIAM J. SCI. STAT. COMPUT., Vol. 6, No. 2, April 1985.

[33] Hariharan, S. I., "Numerical Solutions of Acoustic Wave Propagation Problems Using Euler Computations," NASA Contractor Report 172434, ICASE Report No. 84-39, August 1984.

[34] Hildebrand, F. B., *Advanced Calculus for Applications.* Second Edition, New Jersey: Prentice–Hall, 1976.

[35] Howe, M. S., "On the Absorption of Sound by Turbulence and Other Hydrodynamic Flows," *Recent Advances in Aeroacoustics.* New York: Springer-Verlag, 1986.

[36] Huh, K. S. Agarwal, R. K. and Widnall, S. E., "Numerical Simulation of Acoustic Diffraction of Two–Dimensional Rigid Bodies in Arbitrary Flows," AIAA Paper 90-3920, 1990.

[37] Jameson, A., Schmidt, W. and Turkel, E., "Numerical Solutions of the Euler Equations by Finite Volume Methods Using Runge-Kutta Time-Stepping Schemes," AIAA Paper 81-1259, 1981.

[38] Jameson, A. and Baker, T. J., "Solution of the Euler Equations for Complex Configurations," AIAA Paper 83-1929, 1983.

[39] Karamcheti, K., *Principles of Ideal–Fluid Aerodynamics.* New York: John Wiley and Sons, 1966.

[40] Khan, M. M. S., Brown W. H. and Ahuja, K. K., "Computational Aeroacoustics as Applied to the Diffraction of Sound by Cylindrical Bodies," AIAA Paper 86-1879, 1986.

[41] Landahl, M. and Mollo–Christensen E. *Turbulence and Random Processes in Fluid Mechanics.* Cambridge: Cambridge University Press, 1986.

[42] Landahl, M., *Unsteady Transonic Flow.* New York: Pergamon Press, 1961.

[43] Lele, S. K., "Compact Finite Difference Schemes with Spectral-like Resolution," submitted to Journal of Computational Physics, 1990.

[44] Lighthill, M. J. "On Sound Generated Aerodynamically. I. General Theory," *Proc. Roy. Soc.*, **211A**, 1107, pp. 564-587, 1952.

[45] Lilley, G. M., AFAPL TR-72-53, Vol. 4, 1972.

[46] Lin, C. C., *The Theory of Hydrodynamic Stability.* Cambridge: Cambridge University Press, 1966.

[47] Lindquist, D. R., *Computation of Unsteady Transonic Flowfields Using Shock Capturing and the Linear Perturbation Euler Equations.* PhD Thesis, Massachusetts Institute of Technology, 1992.

[48] Mack, L. M., "Boundary-Layer Linear Stability Theory," Lecture Notes of VKI/AGARD Special Course on Stability and Transition, Von Karman Institute of Fluid Dynamics, Rhode-St-Genese, Belgium, 1984.

[49] Markham, J. J., "Second Order Acoustic Fields: Energy Relations," Phys. Rev., **86**, 712, 1952.

[50] Morse, P. M. and Ingard, K. U., *Theoretical Acoustics.* New York: McGraw-Hill, pp. 401-403 & 450-455, 1968.

[51] Morfey, C. L., "Acoustic Energy in Non-Uniform Flows," Journal of Sound and Vibration, **14**(2), 159-170, 1971.

[52] Myers, M. K., "An Exact Energy Corollary For Homentropic Flow," Journal of Sound and Vibration, **109**(2), 277-284, 1986.

[53] Myers, M. K., "Generalization and Extension of the Law of Acoustic Energy Conservation in a Nonuniform Flow," AIAA Paper 86-0471, 1986.

[54] Ni, R. H., *Nonstationary Aerodynamics of Arbitrary Cascades in Compressible Flow.* PhD Thesis, Stevens Institute of Technology, 1974.

[55] Nystrom, P. A. and Farassat, F., "A Numerical Technique for Calculation of the Noise of High-Speed Propellers with Advanced Blade Geometry," NASA Technical Paper 1662, 1980.

[56] Orszag, S. A. and Israeli, M., "Numerical Simulation of Viscous Incompressible Flows," *Annual Review of Fluid Mechanics*, Vol. 6, pp. 281-318, Palo Alto, California: Annual Reviews, Inc., 1974.

[57] Panton, R. L., *Incompressible Flow.* New York: John Wiley & Sons, 1984.

[58] Pierce, A. D., *Acoustics, An Introduction to Its Physical Principles and Applications.* New York: McGraw-Hill, 1981.

[59] Powell, A., "Theory of Vortex Sound," J. Acoust. Soc. Am., 36, pp. 177-195, 1964.

[60] Ribner, H. S., "Aerodynamic Sound from Fluid Dilations," UTIA Rep. No. 86, AFOSR TN 3430, 1962.

[61] Ridder & Beddini, "Overview of Computational Aeroacoustics in Aerodynamics," AIAA Professional Study Series, Nevada, January 10-11, 1992.

[62] Rienstra, S. W., "Sound Diffraction at a Trailing Edge," Journal of Fluid Mechanics, Vol. 108, pp. 443-460, 1981.

[63] Roberts, T. W., *Euler Equation Computations for the Flow Over a Hovering Helicopter Rotor.* PhD Thesis, Massachusetts Institute of Technology, 1986.

[64] Rudy, D. and Strikwerda, J., "Boundary Conditions for Subsonic Compressible Navier-Stokes calculations," ICASE Report No. 79-18, 1979.

[65] Ryshov, O. S. and Shefter, G. M., " On the Energy of Acoustic Waves Propagating in Moving Media," Translated in J. Appl. Math. Mech. **26**, 1293, 1962.

[66] Schlichting, H., *Boundary-Layer Theory*. New York: McGraw-Hill, pp. 638, 1955.

[67] Sears, W. R., "Some Aspects of Non-Stationary Airfoil Theory and Its Practical Application," Journal of the Aeronautical Sciences, **8**, 3, 104-188, 1941.

[68] Thompson, K. W., "Time Dependent Boundary Conditions for Hyperbolic Systems," Journal of Computational Physics **68**, 1-24, 1987.

[69] Verhoff, A. "Numerical Computation of Derivatives Using Fourth-Order Accurate Compact Differencing," McDonnell Douglas Memorandum 341-6016, 1980.